

Dissertation
submitted to the
Combined Faculties for the Natural Sciences and for Mathematics
of the Ruperto–Carola University of Heidelberg, Germany
for the degree of
Doctor of Natural Sciences

presented by
Dipl. Phys. Tina Jurkat
born in Marburg

Oral examination: May 26th 2010

**Airborne ion trap CIMS using SF_5^- reagent ions:
Atmospheric trace gas detection in the
tropopause region and in aircraft exhaust plumes**

Referees:

Prof. Dr. Frank Arnold

Prof. Dr. Ulrich Platt

**Flugzeuggetragene Ionenfallen-CIMS mit SF_5^- Reagenzien:
Atmosphärische Spurengasmessungen in der Tropopausenregion und im
Abgas von Flugzeugen**

Gegenstand der vorliegenden Arbeit ist die Untersuchung schwefelhaltiger Luftmassen in der Tropopausenregion. Ein flugzeuggetragenes Ionenfallen Massenspektrometer (ITCIMS) wurde erstmalig mit einer SF_5^- Ionenquelle ausgestattet zum Nachweis von SO_2 , HCl , HNO_3 und HONO . Diese neuartige Kombination wurde im Labor untersucht und während der CONCERT (CONtrail and Cirrus ExpeRimenT) Kampagne auf dem Forschungsflugzeug Falcon eingesetzt. Messungen im Oktober 2008 in der unteren Stratosphäre wiesen großräumige SO_2 Erhöhungen (bis zu 510 pptv) auf, die auf die Vulkaneruption des Mt. Kasatochi (Aleuten) im August 2008 zurückzuführen sind. Korrelationsanalysen zeigen eine Erhöhung der Molfraktionsverhältnisse HCl/O_3 und HNO_3/NO_y von 19 % und HNO_3/O_3 von 50 % in der SO_2 -Schicht. Es wurde eine Obergrenze von 60 Tagen für die Lebensdauer von SO_2 in der unteren Stratosphäre nördlicher Breiten bestimmt. Neben natürlichen Schwefelquellen wurde auch der Eintrag von anthropogenen Schwefel- und Stickoxidverbindungen durch den Luftverkehr untersucht. SO_2 und HONO wurden in jungen Abgasfahnen von zehn kommerziellen Flugzeugen gemessen und erstmals durch Laborkalibrierungen von HONO unterstützt. Über das gemessene Molfraktionsverhältnis HONO/NO von 0.042 ± 0.010 konnte indirekt eine effektive Konversionseffizienz des Treibstoffschwefels zu Schwefelsäure bestimmt werden, die mit früheren Messungen gut übereinstimmt.

**Airborne ion trap CIMS using SF_5^- reagent ions: Atmospheric trace gas
detection in the tropopause region and in aircraft exhaust plumes**

This work aims at the investigation of sulfur containing plumes in the tropopause region. For the first time an ion trap chemical ionization mass spectrometer (ITCIMS) was equipped with an SF_5^- ion source for the detection of SO_2 , HCl , HNO_3 and HONO . This novel combination was tested in the laboratory and deployed on the research aircraft Falcon during the CONCERT (CONtrail and Cirrus ExpeRimenT) campaign. In October 2008 an SO_2 layer in the lower stratosphere with mole fractions up to 510 pptv was detected, originating from the Mt. Kasatochi (Aleutian island) eruption in August 2008. Correlation analysis show an enhancement of the molar abundance ratios HCl/O_3 and HNO_3/NO_y of 19 % and HNO_3/O_3 of 50 % inside the SO_2 plume. The data were used to derive an upper limit of the e-folding lifetime of SO_2 in the lower stratosphere at northern latitudes of 60 days. Besides natural sources, anthropogenic emissions of sulfur and nitrogen oxides from aircraft are discussed. SO_2 and first laboratory-calibrated HONO measurements in young aircraft exhaust plumes of ten commercial airliners were conducted. Employing the measured HONO/NO molar abundance ratio of 0.042 ± 0.010 , the effective conversion efficiency of fuel sulfur to sulfuric acid was indirectly inferred. It compares well to former measurements.

Contents

Abstract	i
Contents	iii
1 Introduction and overview	1
2 Chemical Ionization Mass Spectrometry (CIMS)	5
2.1 Measurement principle	5
2.2 The Ion Trap Chemical Ionization Mass Spectrometer (ITCIMS) . . .	8
2.3 SF ₅ ⁻ ion chemistry	13
2.3.1 Ion generation	18
3 Calibration	21
3.1 The calibration factor	21
3.2 Calibration of HCl	22
3.3 Calibration of HNO ₃	25
3.4 Calibration of SO ₂	27
3.5 Calibration of HONO	30
3.6 Mass analysis in the ion trap	35
3.7 Comparison of fragmentation and consecutive reactions	35
3.8 Precision, accuracy and detection limit	38
3.9 Calibration with isotopically labeled standards	43
4 Interfering trace gases	47
4.1 Water vapor	47
4.2 NO and NO ₂	52
4.3 Ozone	54
5 Experimental setup during CONCERT	57
5.1 Ion trap mass spectrometer settings	57
5.2 Flow configuration	58
5.2.1 Inlet system: Passive and active flow configurations	58
5.3 Other instrumentation on the Falcon	64

6	Measurements in the aged plume of volcano Kasatochi	67
6.1	Scientific background: SO ₂ , HCl and HNO ₃ in volcanic stratospheric plumes	67
6.2	Volcanic eruptions in July and August 2008	73
6.3	Measurements during the CONCERT-Chemistry campaign	75
6.4	Meteorological situation on 31 October 2008	75
6.5	CIMS measurements on 31 October 2008	77
6.6	Time sequences and altitude profiles	78
6.7	Location of the air mass with respect to the tropopause	80
6.8	Evidence for volcanic origin	84
6.9	Correlation analysis	85
6.9.1	Correlation of HCl with ozone	87
6.9.2	Correlation of HNO ₃ and NO _y with ozone	90
6.10	Aerosol composition	92
6.11	Partitioning of volcanic sulfur species	93
7	Measurements of HONO and SO₂ in young aircraft exhaust plumes	95
7.1	Scientific background: HONO and SO ₂ in aircraft exhaust plumes . .	95
7.2	Measurements during the CONCERT-2-Contrails campaign	103
7.3	Plume ages	104
7.4	The NO _x Emission Index	107
7.5	ITCIMS measurements in aircraft exhaust plumes	110
7.6	Abundance ratios of HONO/NO and HONO/NO _y	112
7.7	Sulfur conversion efficiency	116
7.7.1	The ratio of effective reaction rate coefficients	118
7.8	Spatial distribution of trace gases inside the exhaust wake	123
7.9	Dilution of SO ₂	126
8	Conclusion and outlook	129
	List of Figures	133
	List of Tables	135
	A	137
	Bibliography	147
	Acknowledgement	161

Chapter 1

Introduction and overview

Aviation has a profound impact on intercontinental relationships and politics, the global economy and world awareness. At the same time its environmental impact affects society and ecosystems now and in the future. The growth of the aviation sector in the recent years reflects the rising popularity of this class of transportation. With a current estimated contribution of 4.9 % [Lee et al., 2009] to the total anthropogenic radiative forcing (RF) the impact may be relatively small as compared to other transportation sectors however the uncertainties (particular in the non-CO₂ effects) allow for estimates that may be 2.5 times as high. In addition the trend of aviation of 5.3 %/a growths in RPK (Revenue Passenger Kilometers) will lead to a doubling in aviation in less than 20 years. Therefore efforts on minimizing the uncertainties of the various environmental impacts of aviation on the climate are fundamental requirements for comprehensive mitigation policies.

Investigation of trace gas abundances from natural and anthropogenic sources starts in regions where aircraft mainly operate: The tropopause region represents a sensitive and variable boundary between the troposphere and the stratosphere, which differ greatly in the trace gas abundances and as a consequence in the radiative properties. Aircraft influence the tropopause region through emission of gaseous species mainly CO₂, H₂O, oxides of nitrogen (NO_x) and sulfur (SO_x) and particles like soot and volatile aerosols. Formation of linear contrails in the wake of aircraft and subsequent aviation induced cloudiness contribute positively to the RF on the system earth-atmosphere [Penner et al., 1999; Minnis et al., 1999]. Linear persistent contrails and induced contrail cirrus increase the earth's albedo and trap outgoing longwave radiation from the earth's surface, resulting a net heating of the system. In addition, the contrail and contrail-cirrus ice crystals serve as activation sites for heterogenous processes involving for example hydrochloric acid (HCl) disturbing the upper troposphere and lower stratosphere (UT/LS) ozone budget [Meilinger et al., 2001].

Trace gas measurements in this region are rare. Particularly the distribution of halogen and nitrogen oxide reservoirs are lacking highly resolved measurements, pre-

venting a quantitative estimate of their counteracting influence on the ozone budget. While NO_x catalyzes ozone production in the upper troposphere, halogen activation on aerosols and contrail ice particles is the driving process for ozone destruction in the lower stratosphere. The impact on the ozone budget of these and other heterogeneous processes induced by aircraft emissions therefore depends on the region of injection.

Sulfur is one of the key components in atmospheric chemistry. Particularly sulfuric acid (H_2SO_4) formed by oxidation of sulfur dioxide (SO_2) by the hydroxyl radical OH induces particle formation and growth [Reiner and Arnold, 1993]. It is directly emitted by aircraft engines and the sulfate particles formed through condensation and coagulation in the wake of aircraft dominate under certain atmospheric conditions the number concentrations of aerosols [Kärcher and Yu, 2009]. Additionally, it influences contrail formation through coating of soot particles. However, effective emission of H_2SO_4 and nitrogen oxide reservoir gases (such as nitrous acid (HONO) and nitric acid (HNO_3)) by aircraft at flight altitude are rarely measured.

Long term effects of aviation are difficult to quantify due to large scale variabilities in the atmosphere overlapping the small scale perturbation. Large-scale effects of sulfur are more likely induced by ground based emissions into the tropopause region mainly through volcanic activity. Injection of large amounts of sulfur into the stratosphere, predominantly in the form of sulfur dioxide (SO_2), enhances the aerosol budget [WMO, 2006]. The aerosol enhancement can be used to study qualitatively the effects of sulfur emissions as for example those by aircraft on the local trace gas fields in the lower stratosphere. Changes in the ozone abundance, nitrogen oxide and halogen partitioning have been observed as a consequence of the enhanced aerosol surface area density after major volcanic eruptions in the last century [Solomon, 1999].

Seen from a different perspective volcanic emissions may change the inherent stratospheric trace gas distribution dramatically such that long term effects from aircraft are exceeded by this variable bias. Therefore consideration of both anthropogenic and non-anthropogenic contributions is necessary for a profound understanding of the complex tropopause region chemistry.

A controversial method proposed by Crutzen [2006] suggests an artificial enhancement of the earth's albedo by injection of sulfur into the stratosphere. With a residence time of 1 to 2 years, sulfate particles would lead to a surface cooling partly counteracting the global warming from greenhouse gases. However, the adverse effects of this and other methods referred to as "climate engineering", such as acidification of the ocean and ozone depletion in the stratosphere, are difficult to predict.

Airborne measurements have recently gained revitalized interest through new altitude aircraft extending the measurement region to higher altitudes and longer

ranges. Sensitive and fast measurement techniques that allow for trace gas detection over a wide range of different atmospheric conditions are needed for a fundamental understanding of the chemical composition of the atmosphere. In addition in-situ measurements are needed for validation of satellite based measurements.

This work presents a new combination of the measurement technique of chemical ionization mass spectrometry (CIMS) with an ion-trap chemical ionization mass spectrometer (ITCIMS) [Kiendler et al., 2000; Aufmhoff, 2004; Speidel et al., 2007; Nau, 2008; Fiedler et al., 2009] previously developed and deployed by an MPI-K/DLR collaboration and a new ion chemistry using SF_5^- reagent ions measuring SO_2 , HONO, HCl and HNO_3 [Marcy et al., 2005]. The aim of this work was to configure the sampling system and calibrate the instrument for fast and sensitive airborne trace gas measurements of SO_2 and HONO in aircraft exhaust plumes of commercial airliners, and for gas phase measurements of SO_2 , HNO_3 and HCl in the tropopause region.

In **chapters 2, 3 and 4** the measurement technique will be introduced focusing on the calibration procedures for the airborne measurements. A particular focus is laid on the newly employed reactions of SO_2 and HONO with SF_5^- reagent ions and an optimized transmission efficiencies for the adhesive gases HNO_3 and HCl. The instrument with the new reagent ion and an improved sampling line was deployed on the research aircraft Falcon during the CONcert and Cirrus ExpeRimenT (CONCERT) in October/November 2008 [Voigt et al., 2010] and the setup will be presented in **chapter 5**.

The **second part** of this work concentrates on measurements during CONCERT in the lowermost stratosphere over Western Europe. A large-scale SO_2 enhancement has been detected with the ITCIMS. Trace gas distributions of HNO_3 and HCl in the SO_2 -plume are compared to outside plume conditions. The main questions are centered around the origin of the SO_2 enhancement and the effects of heterogeneous reactions involving HNO_3 , HCl and sulfate particles in the stratosphere. These measurements will be presented in **chapter 6** with a detailed introduction on the scientific background.

The **third part** deals with HONO and SO_2 measurements in the wake of commercial airliners. An extensive data set of measurements of HONO, SO_2 , NO and NO_y (total reactive nitrogen oxides) in young aircraft exhaust plumes has been collected during CONCERT, allowing for analysis of oxidation processes and conversion efficiencies of NO and SO_2 in aircraft engines and exhaust plumes at flight altitude. The data are presented in **chapter 7** with an introduction on exhaust chemistry and an overview on earlier measurements in aircraft exhaust.

Chapter 2

Chemical Ionization Mass Spectrometry (CIMS)

The measurement principle of chemical ionization mass spectrometry is explained in this chapter. The reaction scheme of the ion-molecule reaction using SF_5^- educt ions is assessed in detail with a focus on the relevant ion-molecule reactions of HCl , HNO_3 , SO_2 and HONO . Additional reactions that cause interferences and consecutive reactions are discussed.

2.1 Measurement principle

Active Chemical Ionization Mass Spectrometry (ACIMS) uses artificially produced educt or reagent ions that are formed by flushing small amounts of a neutral trace gas transported by a carrier gas through a radioactive or electrical discharge source [Arnold and Fabian, 1980; Arnold and Hauck, 1985; Arnold and Spreng, 1994]. Here, free electrons are produced that attach to highly depolarized molecules to form reactive so called reagent or educt ions. Inside a flow tube trace gas molecules react with these educt ions selectively to form product ions, both can be analyzed by a mass spectrometer.

Due to permanent or induced dipole moments of neutral reagent molecules, ion-molecule reactions have a large cross-section, thus reaction rate coefficients are larger compared to neutral molecule-molecule reactions. For most reactions the reaction rate is assumed to be close to the collision rate. The trace gas concentration in the sample flow can be quantified in absolute terms if the residence time and the reaction rate coefficient is known.

If only one type of product ion is produced, the ion-molecule reaction is generally described by



where A is the neutral trace gas to be measured, E is the educt ion, P is the product ion and B is a neutral reaction product. The reaction efficiency is in first order

linearly dependent on the concentration of the neutral trace gas reactant A and of the educt ions, $[E^\pm]$:

$$R(t) = \frac{d}{dt}[E^\pm] = -\frac{d}{dt}[P^\pm] = -k[E^\pm][A] \quad (2.2)$$

in which k is the temperature dependent reaction rate. Additionally the reaction is more efficient at higher pressures due to a higher collision rate of the ions and molecules. The temperature dependence is given by the Arrhenius equation [Atkinson and de Paula, 2006]. Backward reactions are neglected. The trace gas is in excess over the educt ion ($[A] \gg [E^\pm]$) and assumed to be constant ($[A](t) = [A]$), thus a pseudo-first-order reaction. The integration of equation (2.2) yields

$$[E^\pm] = [E^\pm]_0 \cdot e^{-k[A]t} \quad (2.3)$$

with $[E^\pm]_0$ being the initial educt ion concentration.

The fundamental laws on conservation of charge and mass lead to

$$[P^\pm] = [E^\pm]_0 \cdot (1 - e^{-k[A]t}). \quad (2.4)$$

Equation (2.4) divided by equation (2.3) leads to an expression for the concentration of the neutral trace gas concentration A, the so-called ACIMS-formula

$$[A]_{t_r} = \frac{1}{k \cdot t_r} \ln \left(1 + \frac{[P^\pm]_{t_r}}{[E^\pm]_{t_r}} \right) \quad (2.5)$$

in which t_r is the residence time in the flow reactor.

Since the educt ions usually react with several different molecules,



the above derived ACIMS-Formula, which presumes the bimolecular case, needs to be modified. Thus, if reactions with other molecules cannot be neglected, and consecutive reactions occur, the concentration of A is determined by the Parallel-ACIMS-Formula

$$[[A_i]] = \frac{1}{k \cdot t_r} \cdot \frac{[P_i^\pm]}{\sum_{j=1}^n [P_j^\pm]} \cdot \ln \left(1 + \frac{\sum_{j=1}^n [P_j^\pm]}{[E^\pm]} \right) \quad (2.7)$$

A detailed derivation is given in Wohlfrom [2000]. Here all product ions are formed by the reaction with one educt ion. Therefore the relative abundance of all product ions formed through reaction with the educt ion needs to be taken into account otherwise an overestimation of the trace gas concentration is perceived. Consecutive reactions involving the primary product ion may become dominant at high trace gas concentrations and have to be considered additionally



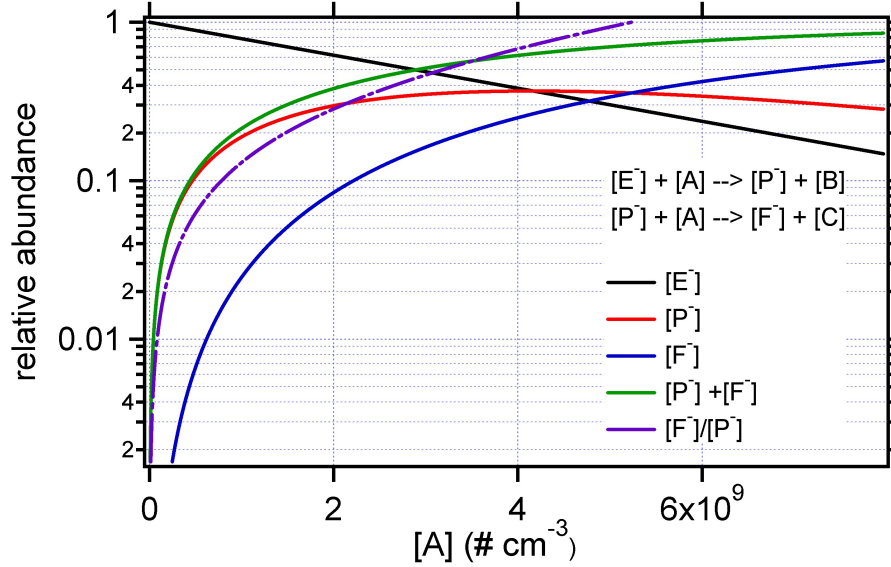


Figure 2.1: The theoretical normalized educt, primary and secondary product yield as a function of trace gas concentration, calculated with a rate coefficient of $2 \cdot 10^{-9} \text{ cm}^3 \text{ s}^{-1}$ for both reactions and a residence time t_r of 0.12 s in the flow reactor.

The dependence of the secondary product on the trace gas concentration is given by the solution of the set of differential equations

$$\frac{d}{dt}[\text{E}^\pm] = -k[\text{E}^\pm][\text{A}] \quad (2.9)$$

$$\frac{d}{dt}[\text{P}^\pm] = k[\text{E}^\pm][\text{A}] - k[\text{P}^\pm][\text{A}] \quad (2.10)$$

$$\frac{d}{dt}[\text{F}^\pm] = k[\text{P}^\pm][\text{A}] \quad (2.11)$$

The yield for the primary and secondary product is

$$[\text{P}^\pm] = [\text{E}^\pm]_0 \cdot t_r k [\text{A}] (1 - e^{-k[\text{A}]t_r}) \quad (2.12)$$

$$[\text{F}^\pm] = [\text{E}^\pm]_0 \cdot (1 - (1 + t_r k [\text{A}])e^{-k[\text{A}]t_r}) \quad (2.13)$$

The residence time in the flow reactor is given by the distance from the area of ionization into the spectrometer and the velocity of the total flow. As an example the theoretical dependence of the educt, the primary and secondary products from a consecutive reaction on the concentration of the trace gas A is shown in Fig. 2.1. The plot shows theoretical relative ion abundances calculated with a typical reaction rate coefficient of $2 \cdot 10^{-9} \text{ cm}^3 \text{ s}^{-1}$ and a residence time of 0.12 s.

2.2 The Ion Trap Chemical Ionization Mass Spectrometer (ITCIMS)

Ion traps or "Paul Traps" named after their creator are generally used for storage and subsequent analysis of charged particles and their physical properties. Their application to atmospheric measurements has been demonstrated in previous studies of MPI-K atmospheric physics division and more recently by an MPI-K/DLR collaboration [Kiendler et al., 2000; Fiedler et al., 2005; Speidel et al., 2007; Aufmhoff, 2004; Fiedler et al., 2009; Katragkou et al., 2004; Hanke, 1999].

Ion traps as compared to linear quadrupole mass spectrometers have great advantages which become especially useful if the nature and composition of ions for a new reaction scheme have to be characterized. These advantages are:

- mass analysis when being operated in the fragmentation mode
- multi-interactions of molecules and ions of positive and negative charge
- a broad dynamic range of trace gas mole fractions
- fast acquisition
- quasi-simultaneous trapping of masses with a broad mass range (15-2000 amu) which is especially needed if the reagent ion is very reactive and many product ions are formed (e.g. in exhaust plume measurements)
- high mass resolution for a safe detection of neighboring masses
- excellent duty cycle

The ion trap mass spectrometer (Fig. 2.2) used during CONCERT is a commercially purchased instrument (Finnigan LCQ, Finnigan Company, USA) configured for airborne trace gas measurements. The inlet system was exchanged by a stainless steel adapter to fit a 40 mm tubing [Hanke, 1999; Kiendler et al., 2000]. The mounted inlet system, originally used for detection of high molecular weight biopolymers, was replaced by a sampling electrode with a diameter of 0.02 cm used as a critical orifice for atmospheric measurements. The 40 mm tube is connected to a flow reactor that contains the ion source and guides the ions into the spectrometer. A defined flow through the flow reactor enters the pre-chamber of the mass spectrometer via an ion cone directed towards the sampling electrode. The bulk of the gas stream leaves the system through an exhaust tube where additional data such as temperature, flow velocities, pressure and humidity are measured. The ions in the pre-chamber are pumped through an inter-octapole lens into the analyzer region. The main chamber, where the ion trap is housed, is pumped by a Balzers Pfeiffer TMH 260/130 turbo-molecular pump backed by a membrane pump.

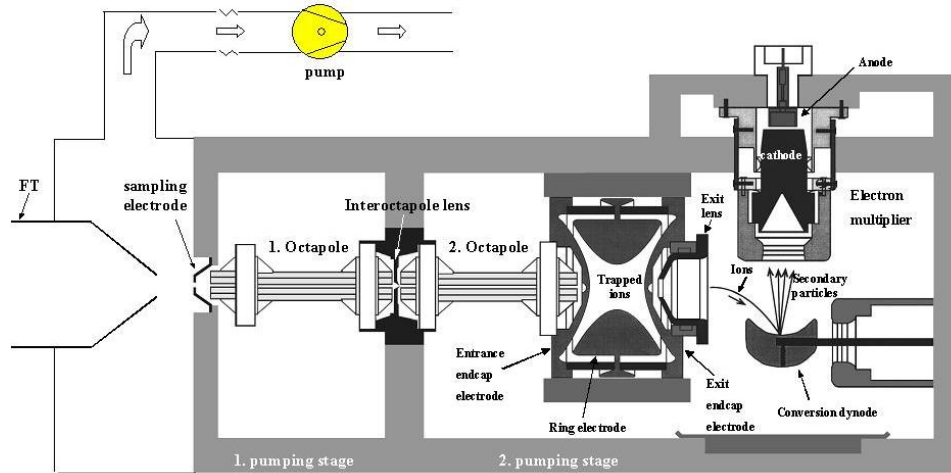


Figure 2.2: Internal setup of the ion trap mass spectrometer. Taken from Hanke [1999].

The ions are accelerated through three different pumping stages: The flow tube is typically operated at pressures between 40 and 120 hPa and separated from the first octapole region by a critical orifice with pressures of the order of 10^{-3} hPa. The pressure inside the main chamber is controlled by the helium pressure, the inlet pressure and the diameter of the critical orifice. The main chamber contains a second octapole lens, the ion trap and the detection unit: the conversion dynode and the electron multiplier. The quadrupole ion-trap is built of two hyperboloid end-cap electrodes and one ring electrode in the center. The ions are confined by application of an appropriate radio frequency (2.45 MHz) and DC voltage (± 10 V) at the ring electrode. AC and DC voltages applied to the end caps generate a quadrupole field that is zero in the center and increases with increasing distance to the center, stabilizing the selected ions on trajectories close to the center.

The motion of ions in a quadrupole field can be described mathematically by the solutions of the second-order linear differential equations described originally by Mathieu which are described in detail in March and Hughes [1989].

The number of ions that enter the ion trap is controlled by the opening and closing time of the interoctupole lens. The lens is set to a certain voltage that is attractive or repulsive and serves as a gate to the trap. The trapping time as well as the number of ions can be controlled by a so called "automatic gain control" (AGC). A fast pre-scan is performed to derive the ion current into the trap. According to this pre-scan the trapping time is changed to achieve the pre-set ion density inside the trap. If the ion density is too high the resolution may be affected due to space charge effects. This should be avoided. A maximal injection time can be set to achieve comparable sampling times and anticipate sampling over longer time intervals. The instrument is supplied with a software (LCQtune) where these parameters can be set manually.

For cooling or deceleration of the ions as well as for the removal of water clusters helium is injected into the trap as a damping gas.

A scan can be divided into the following steps:

1. the pre-scan gives an estimate of the total number of ions inside the trap
2. according to the pre-scan the ion injection time is chosen
3. injection into the ion trap followed by cooling and declustering by helium atoms
4. stabilization and trapping inside the ion trap
5. successive destabilization of the ion trajectories
6. acceleration towards the conversion dynode and generation of secondary electrons
7. amplification of the electron current by the electron multiplier
8. measurement of a voltage drop over a resistor by an electrometer
9. digitalization of the measured voltage

These so called micro-scans are averaged (between 5-20 micro-scans) to reduce the noise. The total time resolution of one averaged spectrum is mainly dominated by the trapping time but for the present measurements approximately the same time for read out and mass analysis has to be added to obtain the total spectrum time. The measured voltage is proportional to the number of ions in the flow tube with an unknown scaling factor. Due to this unknown amplification and unknown read out time the obtained signal is given in arbitrary units (a.u.). The relative abundance of ions with a different mass, which is essential to the present measurements, is however not affected by the conversion, amplification and digitalization unit. Thus the relative abundance of the ion signals are the same as the relative ion abundance at the end of the flow tube. A correction for mass discrimination due to a mass dependent sampling efficiency of the ion trap MS, the octapoles or the front electrode has to be applied additionally and will be explained below.

Tuning and mass discrimination

The tuning for the ion trap was obtained by a semi-automatic tuning procedure supplied by the instrument manufacturer. The tuning procedure adjusts the octapole, front plate and inter-octapole lenses as well as the multipole radio frequency to obtain the best sensitivity for a specific mass. Using the semi-automatic tuning the operator can choose the order of components that are tuned in a sequence. For an optimized tune file the tuning procedure can be repeated several times and should only be used for the pressure and flow configurations set during the tuning. The

date	discrimination
10.11.2008	0.31
18.11.2008	0.33
02.12.2008	0.28

Table 2.1: Measured mass discrimination values during the CONCERT campaign for the mass 127 (SF_5^-) with respect to mass 83 (FSO_2^-).

tuning as well as the spectral range has a profound effect on the relative sensitivity of different masses. Therefore it should not be changed between the calibration and the application of the calibration parameters (e.g. for determination of atmospheric trace gas concentrations).

Tuning on a lower mass causes a discrimination of higher masses such as for example the educt mass. This discrimination has to be accounted for in the ACIMS formula.

$$[\text{A}]_{\text{tr}} = \frac{1}{k_{\text{tr}}} \cdot \ln \left(1 + \kappa \cdot \frac{[\text{P}^\pm]_{\text{tr}}}{[\text{E}^\pm]_{\text{tr}}} \right) \quad (2.14)$$

Due to the non-linear relationship of the trace gas concentration on the discrimination factor κ , neglecting the discrimination factor would particularly influence the accuracy of the measurement if the calibration is done at a higher trace gas concentration than the atmospheric measurements, that means if $\ln(1+R) \neq R$. $\kappa = \frac{1}{b}$, where b is the correction factor for the discriminated mass, can be derived given the following relationship (conservation of charge):

$$[\text{P}^\pm]_0 + b \cdot [\text{E}^\pm]_0 = [\text{P}^\pm]_{\text{A}} + b \cdot [\text{E}^\pm]_{\text{A}} \quad (2.15)$$

the index 0 indicates the ion concentration at background conditions and the index A the ion concentration when the trace gas is injected. The discrimination is given by

$$b = \frac{1}{\kappa} = \frac{[\text{P}^\pm]_0 - [\text{P}^\pm]_{\text{A}}}{[\text{E}^\pm]_{\text{A}} - [\text{E}^\pm]_0} \quad (2.16)$$

and it is only a measure of the relative sampling and transmission efficiency for the two masses and has to be determined whenever the tuning is changed. Depending on the ion chemistry it is very difficult to determine the discrimination because consecutive reactions and fragmentation to other masses reduce the ion signal of the primary product mass and shift it to other masses. For SO_2 the discrimination has been determined three times during the campaign (Table 2.2) for three different calibrations using the above relationship for ion signals at background injection and when high concentrations of SO_2 were injected.

An average value of 0.307 ± 0.022 was used for the discrimination of the ion signal of the educt mass (127 amu) with respect to the ion signal of the product

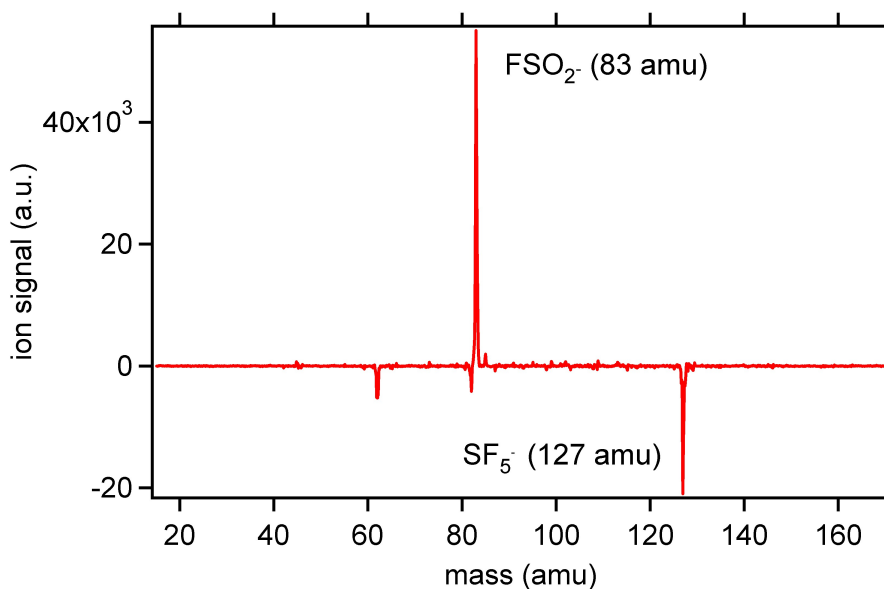


Figure 2.3: The difference of two mass spectra. A spectrum obtained when SO_2 was injected and one obtained under background conditions (only dry N_2 injected) were subtracted. The decrease in the educt ion signal compared to the increase in the product ion signal differs by a factor of ~ 3 .

mass FSO_2^- . The effect is demonstrated in Fig. 2.3. For adjacent product masses such as mass 82 (FHNO_3^-) and mass 66 (FHNO_2^-) the discrimination was assumed to be the same with respect to the educt mass (SF_5^-). For the product mass FHCl^- no discrimination factor κ was applied because consecutive reactions and fragmentation depleting the mass 55 and forming lighter or heavier ions made the above described procedure impossible for HCl .

The MS^n mode

The ion trap mass spectrometer can store a selected mass for constitutional analysis of the corresponding ions. The ions are stored in the trap and excited by a voltage applied to the end caps of the trap, oscillating at the resonant frequency of the ions. By collision of the excited ions with helium the ions are fragmented. This process is called collision induced dissociation. The fragments are trapped and read out. They can also be stored and analyzed in the same manner for a sequential fragmentation of large ions with unknown constitution. The so called MS^n mode is particularly important if a new ion-molecule reaction scheme is used with unknown reaction products of a high mass.

2.3 SF_5^- ion chemistry

The trace gases to be measured determine the choice of the reagent ion or vice versa. However other effects on the reaction scheme have to be considered such as water vapor influences, inferences of other more abundant trace gases, stability of the ion signal and contaminations that are inherent to the system such as contaminations of the ion source or other parts of the setup. CIMS methods employing other educt ions such as CO_3^- [Möhler and Arnold, 1991; Reiner and Arnold, 1993; Aufmhoff, 2004; Speidel et al., 2007], NO_3^- [Arnold and Spreng, 1994], CF_3O^- [Huey et al., 1996] and SF_6^- [Kim et al., 2008] have been proven to be very sensitive and efficient for measurements of HONO, HCl, HNO_3 and SO_2 .

Early balloon-borne CIMS measurements of HCl and HF using $NO_3^-(H_2O)$ were performed by [Arnold and Spreng, 1994]. NO_3^-HCl product ions are generated by a switching reaction. The $NO_3^-H^{35}Cl$ isotope is masked by the second water cluster ($NO_3^-(H_2O)_2$), thus the sensitivity is given by the ion signal of the less abundant heavy isotope $NO_3^-H^{37}Cl$. Atmospheric measurements with $NO_3^-(HNO_3)$ educt ions for measurements of sulfuric acid and OH are reported for example in Curtius et al. [1998]; Hanke [1999]; Aufmhoff [2004]; Fiedler et al. [2005]

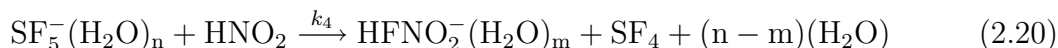
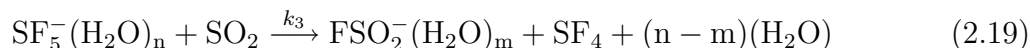
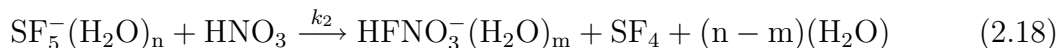
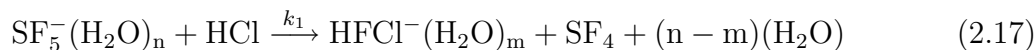
CO_3^- reagent ions are generated by flushing O_2 through an electrical discharge source and have been employed by MPI-K for a number of measurements in recent years [Möhler and Arnold, 1991; Reiner and Arnold, 1993; Aufmhoff, 2004; Speidel et al., 2007; Nau, 2008; Fiedler et al., 2009]. CO_3^- ions were tested for measurements of HCl producing the fragment ions Cl^- and clusters of the form Cl^-HCl . Additionally NO_3^-HCl product ions were detected. The sensitivity was too low for atmospheric measurements in the tropopause region where HCl mole fractions are of the order of a few hundred pptv. Further laboratory work is needed for a quantitative analysis. At higher trace gas concentrations as observed in young volcanic eruption plumes CO_3^- educt ions have been used for the detection of H_2SO_4 , HF, HCl, H_2S and SO_2 [Hunton et al., 2005].

Previous measurements of HONO and HNO_3 in aircraft exhaust plumes used CO_3^- educt ions [Arnold et al., 1992]. The measurements assumed the same reaction rate coefficient for HONO as for HNO_3 with CO_3^- ions ($1.6 \cdot 10^{-9} cm^3 s^{-1}$) which was measured by Möhler and Arnold [1991]. Measurements of SO_2 with the ITCIMS in combination with CO_3^- ions and an in-flight-calibration proved to be very sensitive with a low detection limit (approx. 20 pptv) [Speidel et al., 2007; Fiedler et al., 2009]. Simultaneous measurements of HONO and SO_2 using the same CIMS method have been carried out in a lightning laboratory, however no calibration of the HONO measurement was reported [Nau, 2008].

SF_5^- was tested and compared to other educt ions, such as CF_3O^- , $CH_3SiF_4^-$, SiF_5^- by Marcy et al. [2005] and proved to be of specific advantage for measurements of HCl and HNO_3 under UT/LS conditions with a high sensitivity and low detection limit. In addition it allowed for simultaneous measurements of HONO and SO_2 in

young exhaust plumes of commercial aircraft at cruise altitude.

SF_5^- educt ions possess the ability of F^- abstraction and therefore react efficiently with strong acids to form the product ions through fluoride transfer. The following reactions are observed with the trace gases HCl , HNO_3 , SO_2 and HNO_2 :



The values n and m denote the water molecules attached to the ions. Reactions (2.17), (2.18), (2.19) and (2.20) all go through an intermediate state where an excited cluster ion forms which then evolves into the respective product ion and uncharged molecule. These clusters are short lived and unstable and therefore cannot be detected by the ion trap. The reaction rate coefficients k_1 to k_4 are effective reaction rate coefficients that depend on the water clusters forming in the ion-molecule reactor. The amount of clustering depends on the water vapor abundance and the thermodynamic state. The change in reaction rate coefficient can be both correlated or inversely correlated to the water vapor abundance.

At low water vapor concentrations the reactions (2.17) and (2.18) and the respective reaction rates have been measured and employed during atmospheric measurements by Marcy et al. [2005]. The reaction rate coefficients are

$$k_1 = 1.2 \pm 0.2 \cdot 10^{-9} \text{cm}^3 \text{s}^{-1} \quad (2.21)$$

$$k_2 = 2.1 \pm 0.3 \cdot 10^{-9} \text{cm}^3 \text{s}^{-1} \quad (2.22)$$

The reaction rate coefficient for reaction (2.19) has been determined indirectly by generating SF_6^- , F_2SO_2^- and SF_5^- simultaneously, measuring their abundance separately with a quadrupole ion trap mass spectrometer and comparing it at equal SO_2 concentrations Lovejoy and Wilson [1998]. The first order kinetic reaction rate coefficient is

$$k_3 = 0.6 \pm 0.12 \cdot 10^{-9} \text{cm}^3 \text{s}^{-1} \quad (2.23)$$

The reaction rate coefficient k_3 is small compared to the k_2 which is close to the collision rate. Reaction (2.20) has not been reported in literature before, thus reaction rate coefficients are not available for this reaction. An attempt to determine a rate coefficient for this reaction is described in chapter 3. Interfering reactions regarding these four trace gases will be discussed in chapter 4.

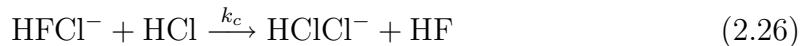
In the following section the relations derived above will be applied exemplarily on the HCl reaction with SF_5^- . At low concentrations and if no other trace gases are present, the upper ion-molecule reaction (2.17) is a bimolecular reaction, therefore the ACIMS-formula (2.5) can be applied:

$$[HCl] = \frac{1}{kt_r\chi} \cdot \ln(1 + \kappa R) \quad (2.24)$$

$\kappa=1$ and

$$R = \frac{\sum_m [HFCl^-(H_2O)_m]}{\sum_n [SF_5^-(H_2O)_n]} \quad (2.25)$$

where k is the weighted average of the rate coefficients for different water clusters of the educt ion and is assumed to be the same for the consecutive reactions as for the primary reactions. At higher mole fractions consecutive reactions involve the product ion $HFCl^-$ and HCl



and as a consequence the mole fraction can be determined using:

$$[HCl] = \frac{1}{k \cdot t_r\chi} \cdot \ln(1 + \kappa R) \quad (2.27)$$

$$R = \frac{\sum_m HFCl^-(H_2O)_m + \sum_l HClCl^-(H_2O)_l}{\sum_n SF_5^-(H_2O)_n}. \quad (2.28)$$

An overview on the four main reactions and consecutive reactions is given in Fig. 2.4.

The proportionality factor or calibration factor $CF := (kt\chi)^{-1}$, where χ is the transmission efficiency, can be derived experimentally by use of an artificial source which delivers a known concentration of the trace gas. This calibration procedure will be described in chapter 3. It is particularly needed if losses of the trace gas to the walls of the sampling line occur and should ideally be measured at different water vapor abundances due to a changing reaction rate coefficient.

Measurements of very low concentrations exhibit a difficulty. Either large residence times or a large amount of educt ions is required. At large residence times t_r a competing effect may lead to the contrary: Ion-ion recombination and losses of ions to the walls may diminish the number of ions that enter the mass spectrometer and thereby decrease sensitivity. These effects have to be balanced in order to obtain an optimized t_r .

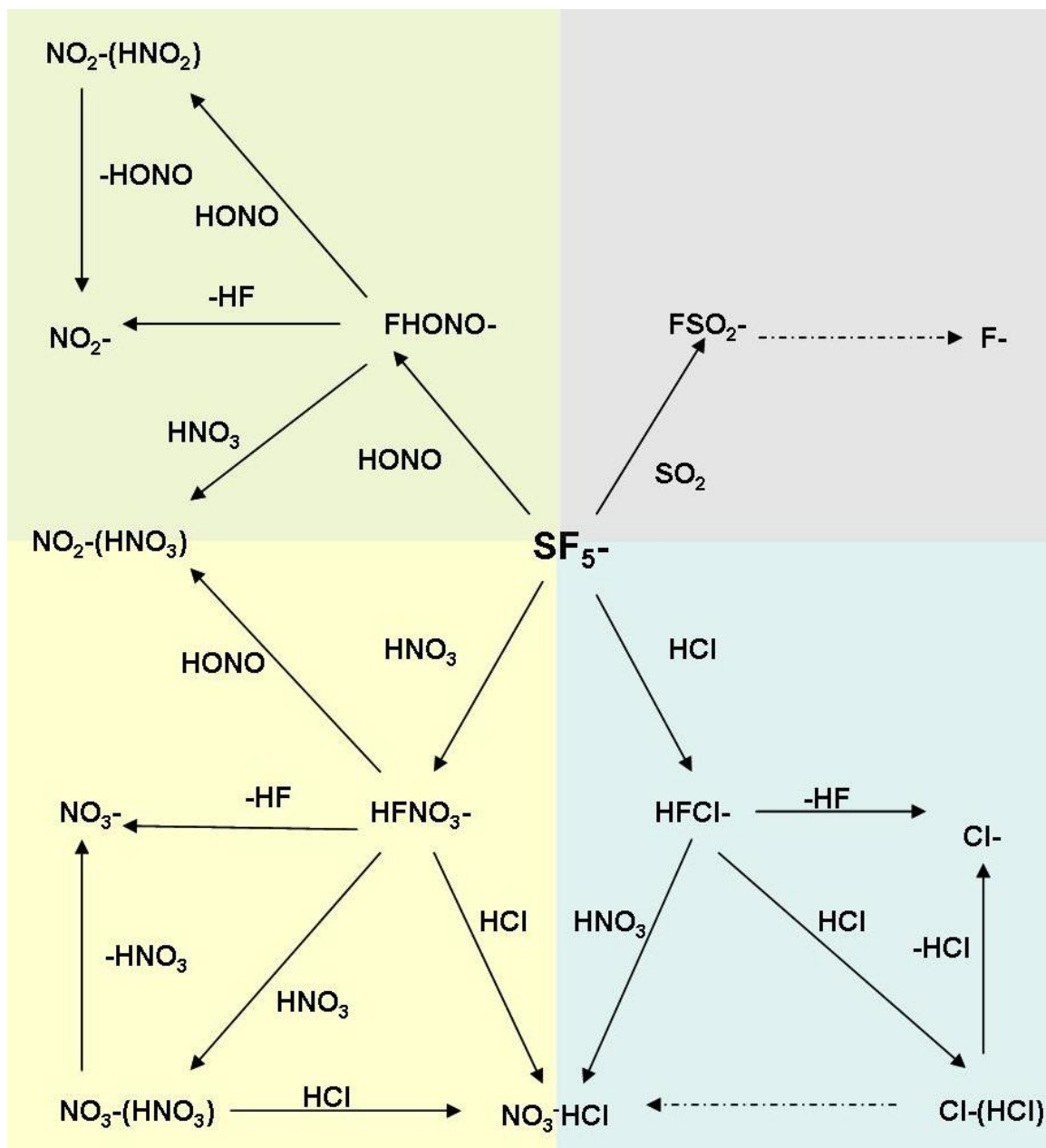


Figure 2.4: The main reactions of HONO, SO₂, HNO₃ and HCl (shaded with different colors) with SF_5^- educt ions and secondary reactions of primary product ions.

mass	ion	source / reaction
19	F^-	fragmentation
35	Cl^-	fragmentation of $HFCI^-$
37	FH_2O^-	reaction with water
39	FHF^-	reaction with water
46	NO_2^-	fragmentation of $FHONO^-$
48	O_3^-	electron attachment
55	$HFCI^-$	$SF_5^- + HCl \rightarrow HFCI^- + SF_4$
57	$FHF(H_2O)^-$	reaction with water
57	$HFCI^-$	chlorine 37 isotope
59	$F(HF)_2^-$	reaction with water
62	NO_3^-	$HFNO_3^-$ fragmentation, ion source
66	$FHONO^-$	$SF_5^- + HNO_2 \rightarrow HFNO_2^- + SF_4$
69	CF_3^-	electron attachment to fragmented ion source gas
71	$HCICl^-$	$HFCI^- + HCl \rightarrow HCICl^- + HF$
73	$HCICl^-$	heavy isotope
75	$HCICl^-$	heavy isotope
79	$F(HF)_3^-$	reaction with water
82	$HFNO_3^-$	$SF_5^- + HNO_3 \rightarrow HFNO_3^- + SF_4$
83	FSO_2^-	$SF_5^- + SO_2 \rightarrow FSO_2^- + SF_4$
83	$HF^{15}NO_3^-$	$SF_5^- + H^{15}NO_3 \rightarrow HF^{15}NO_3^- + SF_4$
85	$F^{34}SO_2^-$	$SF_5^- + ^{34}SO_2 \rightarrow F^{34}SO_2^- + SF_4$
89	$C_2HO_4^-$	oxalic acid (contamination in PFA)
93	$NO_2(HNO_2)^-$	$FHONO^- + HONO \rightarrow HF + NO_2(HONO)^-$
108	SF_4^-	electron attachment to SF_4
109	$NO_3(HNO_2)^-$	$HFNO_3^- + HONO \rightarrow NO_3(HONO)^- + HF$
109	$C_2O_4H_2F^-$	oxalic acid (contamination in PFA)
125	$NO_3(HNO_3)^-$	$HFNO_3^- + HNO_3 \rightarrow NO_3(HNO_3)^- + HF$
126	$^{15}NO_3(HNO_3)^-$	heavy isotope
127	SF_5^-	ion source, ionization of SCF_8
129	SF_5^-	sulfur 34 isotope
143	$FClNO_3^-$	$ClONO_2 + SF_5^- \rightarrow FClONO_2^- + SF_4$
146	SF_6^-	contamination in the ion source / source gas

Table 2.2: Compilation of ion mass numbers and identification of detected ions

High reactivity of the SF_5^- educt ion leads to a number of unwanted product ions and neutral products e.g. HF mainly due to reaction with water. Table 2.3 gives an overview on the reactions.

2.3.1 Ion generation

SF_5^- ions were generated using an α particle emitting inline ionizer supplied by NRD Incorporate with a maximal activity of 20 mCi (740 MBq). It is a polonium (^{210}Po) compound condensed onto a gold foil with a half-life of 138 days. The activity of the polonium source was sufficient over the time of employment (~ 1.5 years) but longer storage at standard pressure caused high contamination of the source with HNO_3 and therefore should be avoided. A screw-coupling to a modified KF 40 flow tube (a stainless steel tube of 40 mm diameter) assured a short distance to the ionization region.

A mixture of 5 sccm of 600 ppmv SCF_8 in N_2 and the main source gas flow of 2 slm N_2 (purity 5.0) were flushed through the capillary-like ion source. SCF_8 (Trifluoromethyl-sulfur pentafluoride) is an odorless, colorless, non-flammable, non-toxic gas and was supplied by Apollo Scientific, UK and thereafter mixed with dry nitrogen by the company Deuste-Steiniger, Germany. It should not be inhaled since no long term effects on the human body are known.

SCF_8 is fragmented by the α particles in the ion source. Free electrons, formed by collision of alpha particles with the nitrogen molecules, attach preferably to the fraction with the higher numbers of electronegative F which is SF_5 to form SF_5^- ions. Due to a lower electron affinity of N_2 and CF_3 only a small amount of ions of the second mass (69 amu) and non on mass 28 were observed.

The ion signal of the educt ion did not show a significant dependence on the SCF_8 concentration as shown in Fig. 2.5. It reached saturation even at the lowest mole fraction of approx. 1 ppbv. SCF_8 proved to be a "sticky" substance. A slow decay (approx. 1 h) of the SF_5^- ion concentration was observed after the gas flow was turned off.

Changing the nitrogen source gas flow had a very profound impact on the educt ion signal. At a constant pressure and total gas flow of 7.5 slm, the gas flow through the ion source was increased from 1.4 to 2.5 slm. The educt ion signal (mass 127) increased by more than a factor of two. This observation suggests that a higher flow rate in the ion source is needed to keep the production of ions at a high level. However, by adding more nitrogen to the constant total flow the sample flow was reduced and more diluted. Dilution of the sample flow means a dilution of the trace gas concentration in the flow reactor and consequently less reactions with SF_5^- . It also means that the detection limit is increased because the smallest concentration detectable is changed with the dilution. The measurements imply that a constant flow of nitrogen through the ion source for the given flow configurations is crucial. The flow configurations for the sampling line applied for the CONCERT campaign are described in chapter 5. The following discussion deals with the flow configurations in the ion-molecule reactor. The ion source gas flow was injected perpendicular to the main gas flow, thereby causing a disturbance of the laminar flow profile inside the flow reactor. The residence time t_r was derived according to Wohlfrom [2000]

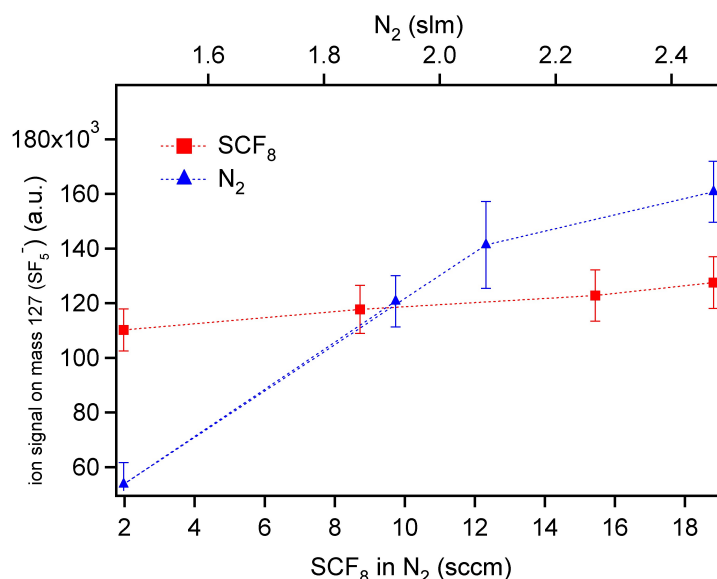


Figure 2.5: The educt ion signal (mass 127, SF_5^-) for a sampling time of 200 ms is plotted versus the source gas flow components: 600 ppmv SCF_8 in N_2 (with $N_2=2$ slm added constantly) and N_2 (with $SCF_8/N_2=4$ sccm added constantly).

assuming a turbulent plug flow, thus assuming the gas flow carrying the ions and the sample gas flow are instantly well mixed. It is given by the relation

$$t_r = \frac{As}{Q} \frac{p}{p_0} \frac{T_0}{T} \quad (2.29)$$

where A is the cross section area of the flow tube, s is the distance from the ion source to the entrance of the mass spectrometer, Q is the total gas flow in standard liter, p and T are the pressure and temperature in the flow reactor and p_0 and T_0 are the pressure and temperature at standard conditions. The residence time can therefore be varied by a pressure change, a change in total mass flow or a change in the distance between the ion source and the mass spectrometer.

Uncertainties remain about the mixing state and propagation of the two gas flows. The jet-like gas beam from the sampling gas flow was a factor of 2.5 times larger than the source gas flow, thus the latter may not have penetrated the entire beam. This might result in a smaller residence time for ion-molecule reactions.

The dependence of the ion signals on different pressures is given in Fig. 2.6. During a background measurement the pressure in the flow tube was increased from 30 to 60 hPa in steps of 10 hPa. The total gas flow and the source gas flow were kept constant. The educt ion signal increases with increasing pressure due to an enhanced rate of ionization in the ion source and flow of ions into the spectrometer. Therefore the sensitivity is increased at higher pressures.

A high pressure causes a longer residence time and elevated background ion signals. For a latent nitric acid contamination from the ion source this resulted in an absolute

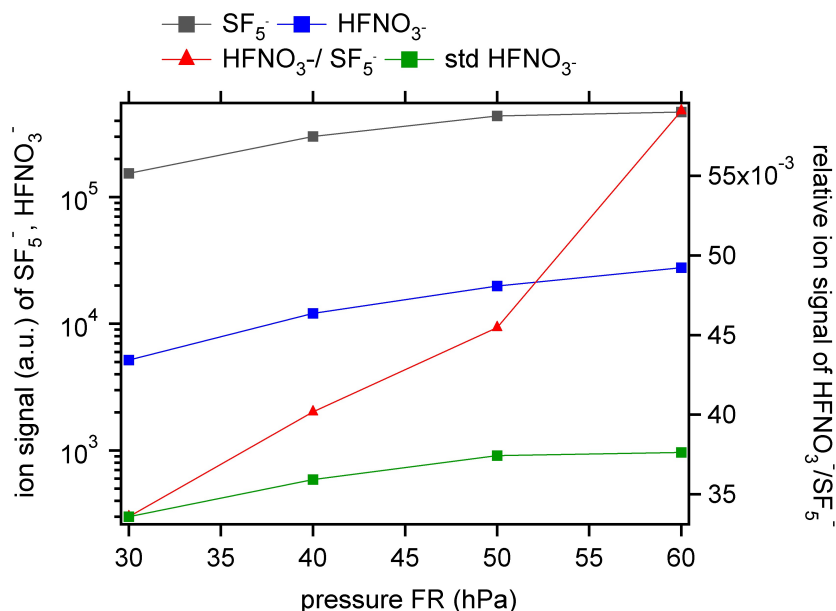


Figure 2.6: The absolute ion signals for SF_5^- , HFNO_3^- (product of the reaction with HNO_3) and its standard deviation for background conditions are plotted versus the pressure in the flow tube. The red curve represents the ratio of product and educt ion signal at different pressures. The total standard gas flow was constant.

increase of the background ion signal of a factor of 5 and a relative increase (product/educt) of a factor of 2. Therefore a pressure of 40 hPa was chosen which was a trade-off between a stable pumping efficiency and a comparably low background, thus a reduced detection limit.

Alternatively to the nitrogen ion source gas, nitrogen of a higher purity (6.0) and argon were tested. No significant improvement of the background and the detection limit was observed. In case of the inert gas argon a reduction of approx. 10 % in the educt ion signal was observed suggesting that less free electrons are produced followed by a reduced ion signal.

A high frequency discharge source described in Aufmhoff [2004] and Speidel et al. [2007] was installed during laboratory tests with an SCF_8 source gas flow. The high energies produced in the discharge however caused a number of unidentifiable ions and proved to be unsuitable for this ion reaction scheme.

Chapter 3

Calibration

This chapter will give insight into the various calibration procedures of the trace gas measurements of SO₂, HCl, HNO₃ and HONO. The generation of the standards and the calibration procedure will be explained. The laboratory tests were substantial for a profound understanding of the ion-molecule reaction scheme as well as for the application to the atmospheric measurements performed during CONCERT. They represent a central aspect of this thesis.

3.1 The calibration factor

A calibration factor (CF) was derived for all four trace gases in the laboratory and for nitric acid additionally in flight. CF is the proportionality factor which relates the ion abundance ratios of the product and educt ions measured by the mass spectrometer with the trace gas mole fraction in the atmosphere

$$CF = \frac{[A]}{\ln(1 + \kappa \frac{P^\pm}{E^\pm})} = \frac{d}{kt_r\chi} \quad (3.1)$$

where $[A]$ is the mole fraction of the calibration gas standard, P and E are product and educt ion signals, k is reaction rate coefficient and κ the mass discrimination as introduced in chapter 2. χ is the transmission and d the dilution of the sample flow with the nitrogen flow from the ion source. CF was derived through a linear correlation of the $\ln(1 + \kappa \frac{P^\pm}{E^\pm})$ and the 3 to 6 different mole fractions of the trace gas in the sampling line. For SO₂, HNO₃ and HCl only primary products were included to avoid additional background noise from the secondary products and fragments. HONO was calibrated differently which will be explained in section 3.5. A high calibration factor means a low sensitivity and vice versa.

The transmission can be quantified by

$$\chi = \frac{dRT}{kt_rCFpN_a} \quad (3.2)$$

with t_r in s, p in Pa, T in K, R is the universal gas constant in J K⁻¹ mol⁻¹, CF in mole fraction, N_a is the Avogadro constant and k in cm³s⁻¹, if all other values

are well known. For the present consideration $t_r = 0.1$ s and k , the effective rate coefficient given in chapter 2, are used.

3.2 Calibration of HCl

Generation of the standard

Calibration of HCl was performed using a permeation tube provided by the company VICI. Permeation devices for calibration of CIMS measurements have found a wide range of application during the recent years [Hanke, 1999; Neuman et al., 2000; Jost, 2004]. Some of the several advantages over bottled standards are: Generation of a wide range of precise concentrations, easily exchangeable by other components, reduced weight and size if housed in small permeation oven and limited losses on the wall of the container (e.g. stainless steel bottles).

The permeation source is built of a small, inert capsule, a teflon tube containing a liquid mixture of the chemical compound in a two phase equilibrium between the gas phase and liquid phase. For the present calibration a mixture of 20 % HCl in water was used. The amount of HCl entering the gas phase depends on the HCl saturation vapor pressure thus exponentially on the temperature of the permeation source. A well temperate environment is therefore mandatory and was provided by a commercial permeation oven of the company MCZ Umwelttechnik. This permeation oven is built of a glass container embedded in a metal block that is temperature controlled. A mass flow controller (MFC) upstream of the glass container controls a dry nitrogen flow guided over the permeation source and the flow carries a well defined mole fraction of HCl into the sample flow. Given the temperature dependent permeation rate the mole fraction in ppbv can be calculated according to

$$[\text{HCl}] = \frac{PR V_0}{M Q} \quad (3.3)$$

where PR is the permeation rate in ng/min, M is the molar mass (g/Mol), V_0 is the mole volume at standard conditions in slm mole⁻¹ and Q is the nitrogen flow over the permeation source in standard liter per minute (slm). Dilution of this enriched flow occurs downstream of the permeation oven. The flow over the permeation source and inside the glass container should be kept constant due to varying wall effects that change the concentration abruptly if a higher or lower flow is applied. Additionally some permeation sources are sensitive to pressure changes [Jost, 2004]. Alternative calibration standards have been tested in the laboratory and will partly be explained in section 3.9 of this chapter. Calibration with a bottled gas standard as discussed in [Marcy et al., 2005] was unsuccessfully tested: HCl can be ordered commercially in a gaseous mixture with N₂ at a minimal mole fraction of 5 ppmv. Using a pressure reducer and a mass flow controller a defined flow into the sampling line can be generated. However metallic surfaces on the pressure reducer and the

MFC made it impossible for HCl to exit the bottle and reach the sampling line especially at low flow rates of a few standard milliliters. Only at higher flow rates that were unpractical for the calibration of the mass spectrometer a stable value of the HCl concentration was reached. This experiment demonstrates the particularly sticky nature of HCl which is effectively and irreversibly removed by non PFA - surfaces such as tested by Neuman et al. [1999]. Therefore it is not recommended to leave any metallic surfaces in the sampling tube as well as in the supply unit of the calibration standard.

Calibration of the permeation source

The manufacturer assigns a permeation rate for one temperature to the delivered tube but often with large uncertainties. In principal there are two ways of an absolute and independent measurement of the permeation rate: It can be determined gravimetrically or by means of an ion chromatography. In both cases the permeation source has to be operated during several days continuously. The gravimetrical method determines the difference in weight before and after a specific run period. The decrease in g per run time gives the total permeation rate. An active HCl permeation rate, that means exclusively the permeation rate of HCl, has to be derived taking into account the vapor pressure of the HCl/water solution. This method requires a precise measurement of small masses and may be very imprecise for low permeation rates. Furthermore it is only valid under the assumption that the mixture of HCl and water in the tube is azeotrope at this temperature.

The second method uses an ion chromatographic analysis which has been carried out by the company CURRENTA (former Bayer Industries) with an accuracy of 10 %. Ion chromatography uses the interaction of ions in a solute with ions that are located on a stationary phase. Negative ions as for example Cl^- and NO_3^- can be separated by their different retention due to interaction with the positively charged ions on the stationary phase. The concentration is measured by the conductivity of the solute.

The liquid samples were generated by passing the gaseous nitrogen flow enriched with HCl into a graduated wash bottle of deionized ($18 \text{ M}\Omega \text{ cm}^{-1}$) water. The water volume can be derived by measuring the weight of the solution at the temperature dependent density. Under the assumption that all HCl in the gas flow was taken up by the water the amount of Cl^- can be related to the active PR. The uncertainty of this procedure is governed by the uncertainty of the ion chromatography and therefore lies in the same range of 15 %. Before and during the aircraft campaign several samples have been taken for one HCl permeation tube operated at a temperature of 70°C and analyzed to monitor a time dependent decay of the permeation tube. The measurements with the active PR are listed in Table 3.1. The active PR denotes the rate of mass permeation by a specific substance (e.g. HCl) in a solution (e.g.

temperature (°C)	date	permeation rate (ng/min)
70	26.03.2008	39.3
70	21.06.2008	50.7
70	18.10.2008	50.1
70	10.11.2008	49.1

Table 3.1: Active permeation rates (definition see text) of HCl of four different ion chromatographic analysis.

HCl/H₂O), thus it only comprises a fraction of the total permeation rate. The high temperature was chosen because only at high temperatures the permeation source produced enough HCl for the calibration procedures of the ITCIMS. Except for the first PR the three others show very good agreement within the measurement uncertainties. No decay of the PR was observed. The low permeation rate of the first measurement may be attributed to wrong handling of the sampling procedure such as a long transfer tubing, insufficient lead time or a relatively long time period between the sampling and the analysis of the probes.

Two additional samples have been obtained for each sampling: A background sample with only the filtered water and a "check" sample which consisted of a second wash bottle downstream of the actual probe to assure that all HCl was solved in the first wash bottle. Neither of the two showed an enhancement above the detection limit of 0.1 mg l⁻¹.

Calibration procedure during the campaign

Before each calibration the oven with the permeation source was operated for several hours, preferably over night. An exemplary calibration curve is shown in Fig. 3.1. For the campaign a calibration factor of 42 ± 4 ppbv was inferred to derive the HCl concentration during flight.

However, HCl showed quick response times when compared to other substances as for example HNO₃, that means fast transmission of changes in the concentration from the calibration unit into the mass spectrometer. Comparison of measured values of the calibration factor with the theoretical $\frac{d}{kt_r}$ however revealed a high irreversible loss to the walls of approx. 75 %. These losses may partly be attributed to a reduced sampling efficiency of the ion trap for the small mass (55 amu) but mainly due to removal in the sampling line.

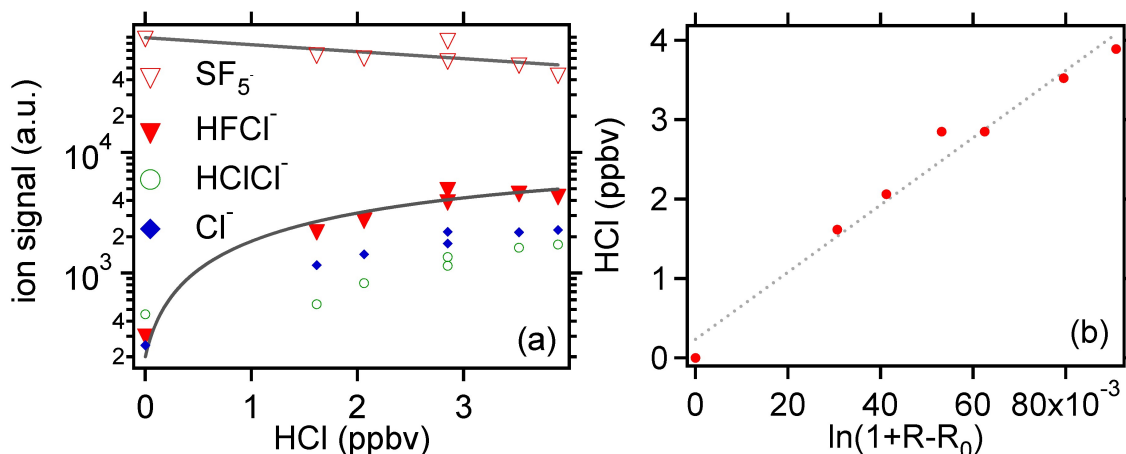


Figure 3.1: (a) The educt, primary and secondary ions and fragments are plotted as a function of the HCl mole fraction in the sample flow. (b) The calibration factor can be determined by the slope of HCl (ppbv) versus $\ln(1+R-R_0)$, R_0 being the ratio of product to educt ion at background conditions.

3.3 Calibration of HNO_3

Setup of the in-flight permeation oven

Nitric acid calibration was performed using a newly built permeation oven specifically designed for in-flight calibration. A schematic setup is given in Fig. 3.2. The oven housed a glass container where the nitric acid permeation standard was heated to 325 K and maintained at a constant pressure of 2 bar. The glass container was embedded in a latent heat storage which maintained the temperature for 45 min in case of power shortage e.g. during times when there is no power on the aircraft. The latent heat capacitor named Rubitherm PX, provided by Rubitherm Technologies GmbH is based on a paraffin basis. It uses the phase transition and the latent heat release to maintain the temperature between 46 and 55 °C if the heating is turned off.

The oven had an inlet and outlet quick connection fabricated of PFA that allowed a fast and uncomplicated deployment before and after the flights. This feature allowed for a continuous operation of the permeation standard.

Generation of the standard

A calibration flow of 110 sccm was injected through a critical orifice made of glass into the 5 slm sampling flow at the upper part of the sampling line in front of a PFA back-pressure valve. For further details on the setup see chapter 5. A stable maintenance of the calibration source had to be assured not only regarding the temperature but also regarding the pressure and the flow around the permeation

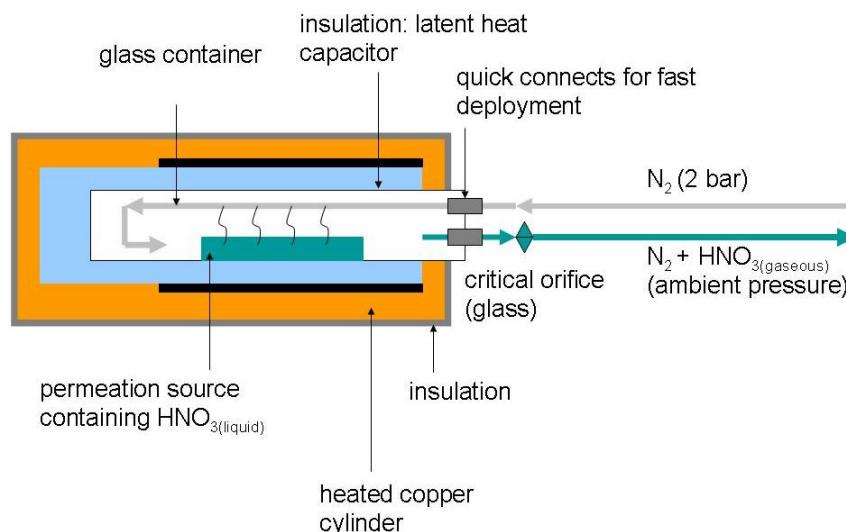


Figure 3.2: The schematic drawing of the permeation oven built for in-flight calibration. The permeation source is embedded into a latent heat storage that keeps a constant temperature for 45 min in case of power shortage.

source. A possible pressure dependence of the permeation rate discussed by Jost [2004] was investigated during laboratory experiments. A change of pressure by a factor of 2 starting at 2 bar had no influence on the permeation rate for nitric acid. A stable environment not only with respect to pressure but also to water vapor is desirable and was achieved by a critical orifice downstream of the oven. The permeation source was therefore not in contact with the ambient air. Another advantage of the critical orifice instead of an MFC was that the nitrogen flow was active even if the instrument had no power.

Calibration of the permeation source

The permeation rate was monitored by an ion-chromatographic analysis described in section 3.2. Additionally it was cross-checked by the use of a chemiluminescence detector (CLD). The detailed description is given in chapter 5. Additional emissions from the permeation source such as NO_2 were quantified using a blue light converter that uses an array of ultraviolet light emitting diodes to photolyze NO_2 to NO , which may be subsequently measured by the CLD. 5 % of the total NO_y emission comprised NO , 24 % were in the form of NO_2 . The NO_x fraction was subtracted from the total NO_y value assuming that no other emissions than HNO_3 came from the permeation source.

During later experiments a nylon-filter was used to remove HNO_3 from the total gas flow. By subtracting the signal without filter from the signal with a filter the HNO_3 concentration was inferred assuming that all HNO_3 was removed by the filter. The comparison for different dilution rates is shown in Fig. 3.3 and shows good

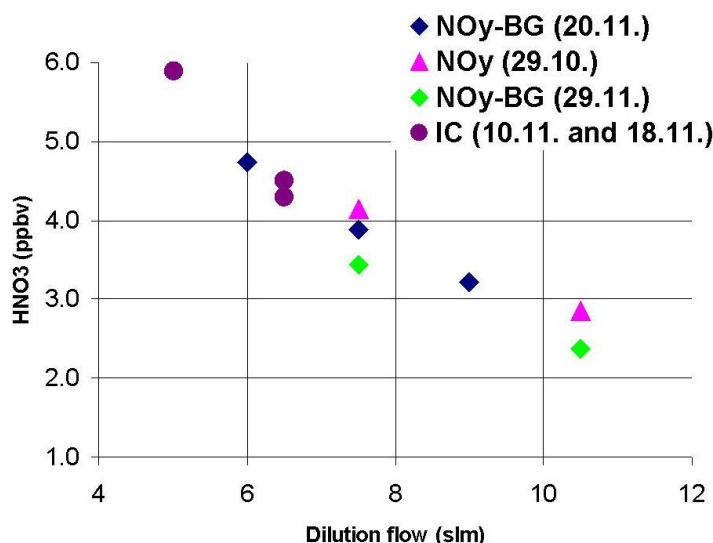


Figure 3.3: The nitric acid mole fraction measured by the CLD (ChemiLuminescence Detector) and IC (Ion Chromatography) plotted as a function of the diluted gas flow. The PR of the nitric acid permeation source was determined with the CLD measuring NO_y and NO_y-HNO₃ and IC sample analysis.

correlation and agreement for the two different methods.

Calibration procedure during the campaign

Nitric acid was injected three to five times into the sample flow during the flights. It was added in addition to the atmospheric concentration therefore the atmospheric background (BG), measured before the calibration, was subtracted. A typical calibration peak obtained during the flight on 17 November 2008 is shown in Fig. 3.4. The fast adjustment of the signal to a saturation value is a good demonstration of the fast sampling line. However the slow decay of the signal due to memory effects results in significant loss of measurement time (approx. 4 min) and spatial resolution. Additional use of a chemical reaction, binding HNO₃ to the walls is recommended in the future [Neuman et al., 2000]. As an example for the stability of the calibration factor the average for the flight on 17 November 2008 was 19.3 ppbv with a standard deviation of 1.85 ppbv.

3.4 Calibration of SO_2

Generation of the standard

Calibration of SO_2 was performed using a mixed standard of 2.12 ± 0.064 ppmv $^{32}\text{SO}_2$ in dry nitrogen provided by the company Air Liquide, Germany. The gas was injected into the sampling line in front of the back-pressure valve by the use of a 20

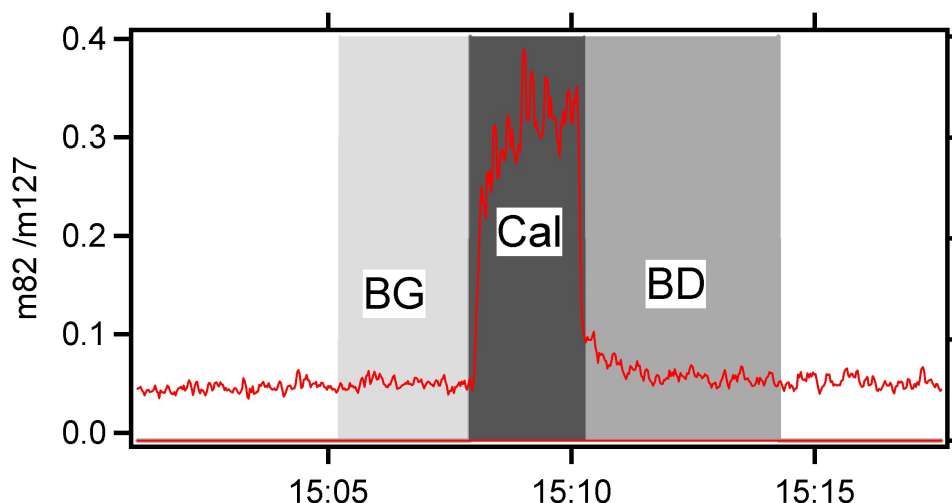


Figure 3.4: A calibration peak (Cal), expressed by the ratio of the nitric acid product ion HFNO_3^- (mass 82) and the educt ion with mass 127 amu obtained in-flight at an altitude of 10 km. The plateau of the ratio was used after background subtraction. The shaded area before the calibration peak is the atmospheric background (BG) that was subtracted. The shaded area after calibration is declared as bad data (BD) because of memory effects that enhance the atmospheric measurements artificially and therefore cannot be used.

sccm MFC (Bronkhorst). The MFC was operated and therefore passivated at least one hour before the calibration was performed. The standard was not compared or cross-checked with a second standard thus a higher error was assumed (see chapter 3.8).

FSO_2^- is a primary product of the reaction of SO_2 with SF_5^- as demonstrated in Fig.3.5. Fragmentation of the ion in the ion trap was not achieved which either indicates a high stability of the ion or results from reduced sampling efficiency of the F^- ion. Consecutive reactions to higher masses were not observed and therefore the reaction became particularly important for measurements of the mass discrimination by the ITCIMS which is explained in chapter 2.2. Calibration with an isotopically labeled standard is discussed in section 3.9.

Calibration procedure during the campaign

SO_2 calibration was performed during and after the campaign. A calibration factor of 24 ± 4 ppbv for the first part of the campaign and 20.2 ± 2 ppbv for the second part of the campaign was employed.

SO_2 is less susceptible to wall effects, particularly if PFA is used. Within a few seconds the ion signal rises to 90 % of the maximal signal. Comparison of the calibration factor with the theoretical value $\frac{d}{kt}$ revealed 40 % loss in the sampling line. For stainless steel surfaces substantial passivation has to be pursued to achieve

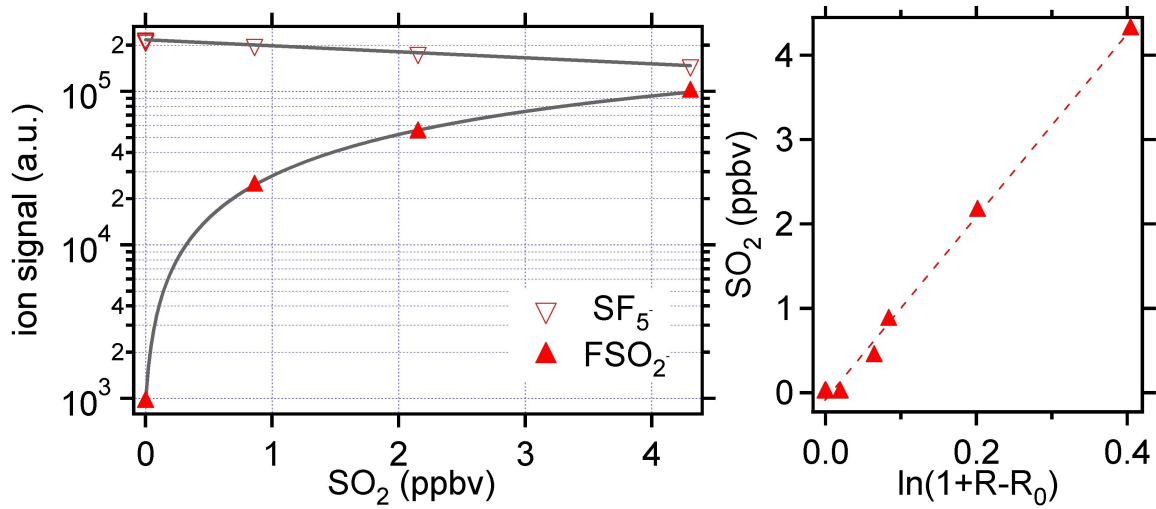


Figure 3.5: (a) The educt and primary product ion signals are plotted as a function of the SO_2 mole fraction in the sample flow. (b) The calibration factor was determined by the slope of the fit SO_2 (ppbv) versus $\ln(1+R-R_0)$, where R is the ratio of the ion signals.

a stable signal and changing water vapor conditions can alter the passivation. An increase of the background signal in the presence of O_3 as previously reported by Nau [2008] was not observed and will be discussed in chapter 4.

Comparison of isotope ratios

A valuable prove of a consistent measurement gives the comparison of the isotopy of the ion signal during atmospheric measurements with the natural abundance. The ion signals of all isotopes are monitored quasi-simultaneously by the mass spectrometer and can therefore be compared to the natural abundance ratio. This comparison has been carried out for HCl and SO_2 at three different measurement sites: in the stratospheric SO_2 -plume (see chapter 6), during measurements of aircraft emission (see chapter 7) and in the laboratory.

All values were background-corrected with a background measurement performed with dry nitrogen. The measured isotope ratios agree well within the measurement uncertainties with the expected ratios. The deviation and the high uncertainty arises mainly from the change of the background conditions that change with different water vapor mole fractions. This is discussed with respect to measurements of isotopically labeled standards in section 3.9.

	$^{34}\text{S}/^{32}\text{S}$	$^{35}\text{Cl}/^{37}\text{Cl}$
natural abundance ratio	0.044	3.13
stratospheric SO_2 plume	0.039 ± 0.025	2.8 ± 1
aircraft exhaust	0.04 ± 0.01	-
laboratory (see Fig. 3.7)	0.039 ± 0.01	3.23

Table 3.2: Abundance ratios of sulfur and chlorine isotopes during measurements in the UT/LS, in aircraft exhaust plumes, and in the laboratory.

3.5 Calibration of HONO

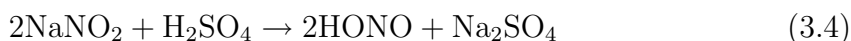
The LOPAP instrument

HONO calibration was performed with a LOPAP (LOng Path Absorption Photometer) instrument [Heland et al., 2001; Kleffmann et al., 2006] operated by the University of Wuppertal. The detection principal is based on a wet chemical reaction of HONO with a light acidic fluid of sulfanilamid forming a diazonium salt. It is a fast, selective chemical reaction that occurs in a stripping coil. Afterwards the solution is converted into an azo dye, a strong absorbing complex at a wavelength of 540 nm. The concentration is photometrically detected in a long path absorption cell made of teflon. A mini spectrometer at the end of the absorption cell measures the light absorption. A schematic of the detection unit is shown in Fig. 3.6. The measurement is absolute and does not need a standard.

The instrument has a detection limit of 0.2 - 2 pptv at a time resolution of 7 - 2 min. The time resolution is mainly given by the sample gas and liquid flow rates and the length of the absorption cell which affects the time that the solution needs to be totally exchanged. Instrument inter-comparison with other absorption techniques such as DOAS (Differential Optical Absorption Spectroscopy)[Platt et al., 1980] revealed the excellent performance of the instrument [Heland et al., 2001].

Generation of the standard

HONO is chemically very instable and therefore permeation devices cannot be used to generate a standard. HONO was generated using a solution of sodium nitrite (NaNO_2) and water which reacts with sulfuric acid to form HONO.



Given a molarity M of NaNO_2 in the solute the reaction evolves in stoichiometric manner to 1 M HONO. The aqueous HONO is injected into a stripping coil and a

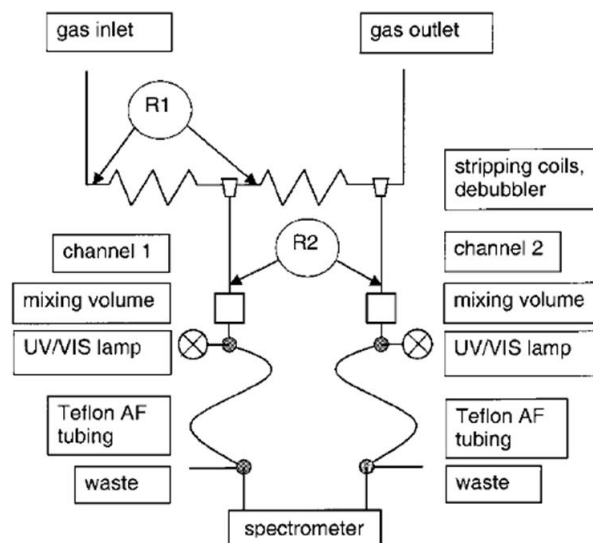


Figure 3.6: The schematic diagram of the LOPAP instrument taken from Heland et al. [2001]. Two stripping coils in a series are used to account for interfering reactions of other gases with the solute. By comparison of the two channels the interferences can be quantified.

dry nitrogen flow is passed through the coil that saturates at the given saturation vapor pressure. Therefore the stripping coil needs to be temperature stabilized. A similar HONO source with HCl used instead of H_2SO_4 is explained in Febo et al. [1995].

Ion-molecule reaction of HONO with SF_5^-

Calibration of the instrument for the CONCERT measurements took place in October 2009 with a second ion trap, identical in construction. The LOPAP instrument and the ITCIMS measured simultaneously the HONO concentration in the same gas flow. A sampling line of approx. 10 m was used between the HONO source and the instruments to account for complete mixing. The same sampling line, flow reactor, ion source, MFCs, HNO_3 and SO_2 standards were used for the calibration as during the campaign to avoid adverse effects that prevent the applicability of the calibration. Nevertheless the exchange of the ion trap mass spectrometer may have an influence on the detection efficiency. Possible deviations will be discussed in the following section.

A spectrum measured by the ion trap during calibration is shown in Fig. 3.7. The calibration spectrum is given for 1.7 ppbv HONO together with one constant SO_2 mole fraction. The background spectrum (grey) was obtained under similar conditions of 230 ppmv water vapor. The predominant masses are mass 83 (FSO_2^-), the

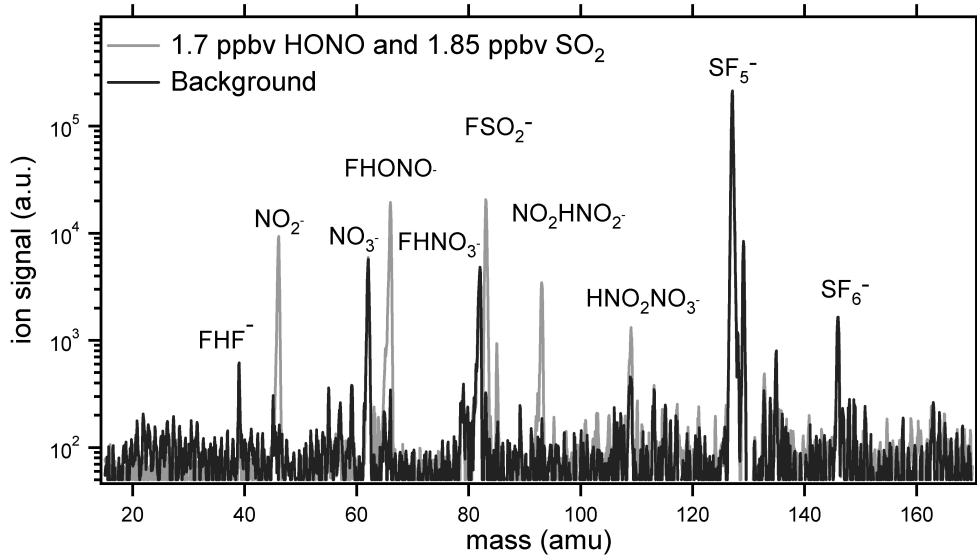
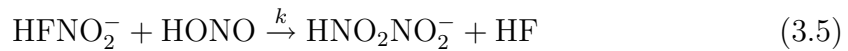
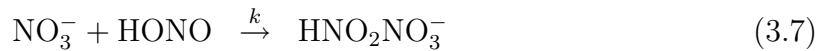
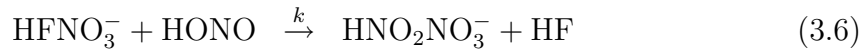


Figure 3.7: A calibration spectrum with 1.7 ppbv HONO and 1.85 ppbv SO₂ is compared to a background spectrum at the same water vapor mole fraction.

HONO products mass 46 (NO₂⁻), mass 66 (FHNO₂⁻) and mass 93 (HNO₂NO₂⁻) (Fig. 3.8). FHNO₃⁻ is present due to contamination from the ion source which will be discussed in section 3.8. Water vapor injected from the HONO calibration source produces FHF⁻ clusters with mass 39. Mass 46 and 66 behave similar in their dependence on the HONO mole fraction; they can be fitted to an exponential curve proving a first order kinetic reaction. Mass 93 versus HONO cannot be fitted by an exponential function but it shows a quadratical dependence on the HONO mole fraction, thus it is a secondary product of the reaction. It is produced by a ligand exchange with the primary product FHNO₂⁻.



The secondary product HNO₂NO₃⁻ is similarly produced through ligand switching if HNO₃ or NO₃ is present via



The sensitivity of the instrument was obtained by measuring the educt ion signal at a given HONO mole fraction. The decrease of the educt ion signal with increasing concentration of HONO is given by the exponential expression

$$[\text{SF}_5^-] = [\text{SF}_5^-]_0 \cdot e^{-kt_r\chi[\text{HONO}]}. \quad (3.8)$$

If the ion signal is measured for at least two concentrations of HONO the factor in the exponential argument $kt_r\chi$ can be derived. The factor is a combination of the

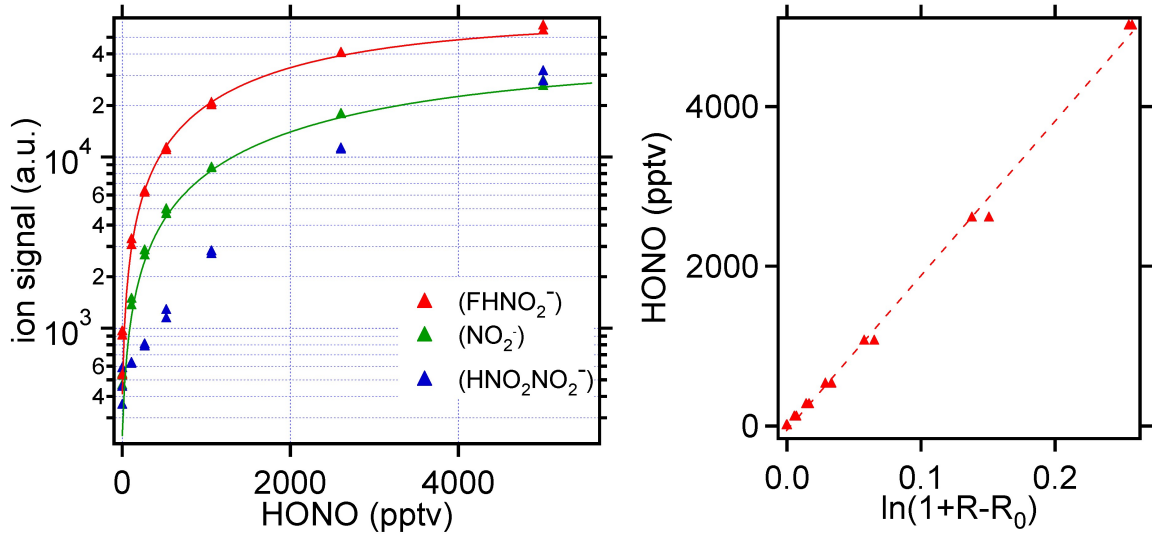


Figure 3.8: Primary and secondary products as a function of the HONO mole fraction in the sample flow. HONO mole fraction are plotted as a function of $\ln(1+\kappa(R-R_0))$ where R is the ratio of the primary product mass 66 (FHNO_2^-) and the educt mass and R_0 is the ratio under background conditions

inherent rate coefficient of the reaction that changes with water vapor abundance and the inherent residence time t_r and transmission χ of the setup.

The method is independent of the tuning, discrimination and of the rate of consecutive reactions therefore it was particularly useful for the HONO calibration with a different instrument but the same inlet configurations and similar transmission effects. It can only be applied under the assumption that no additional reactions affect the educt ion signal. All other parameters such as pressure, temperature and other trace gas concentrations (such as water vapor) are maintained constant during the measurement.

Fig. 3.9 shows the logarithmic SF_5^- ion signal versus the HONO, SO_2 and HNO_3 mole fraction. The fit function of the two HONO fit curves is given by

$$\ln[\text{SF}_5^-] = (-0.157 \pm 0.002) \cdot [\text{HONO}] + (12.522 \pm 0.002) \quad (3.9)$$

$$\ln[\text{SF}_5^-] = (-0.144 \pm 0.036) \cdot [\text{HONO}] + (12.268 \pm 0.021) \quad (3.10)$$

The first one is obtained for a water vapor mole fraction of 595 ppmv in the flow reactor. The second at a mole fraction of 160 ppmv. The different slopes suggest a positive water vapor dependence of the rate coefficient thus a better sensitivity for higher water vapor content. Assuming a residence time t_r of 100 ms and no transmission effects the rate coefficient can be determined.

$$k_{dry} = 1.45 \cdot 10^{-9} \text{cm}^3 \text{s}^{-1} \quad (3.11)$$

$$k_{humid} = 1.59 \cdot 10^{-9} \text{cm}^3 \text{s}^{-1} \quad (3.12)$$

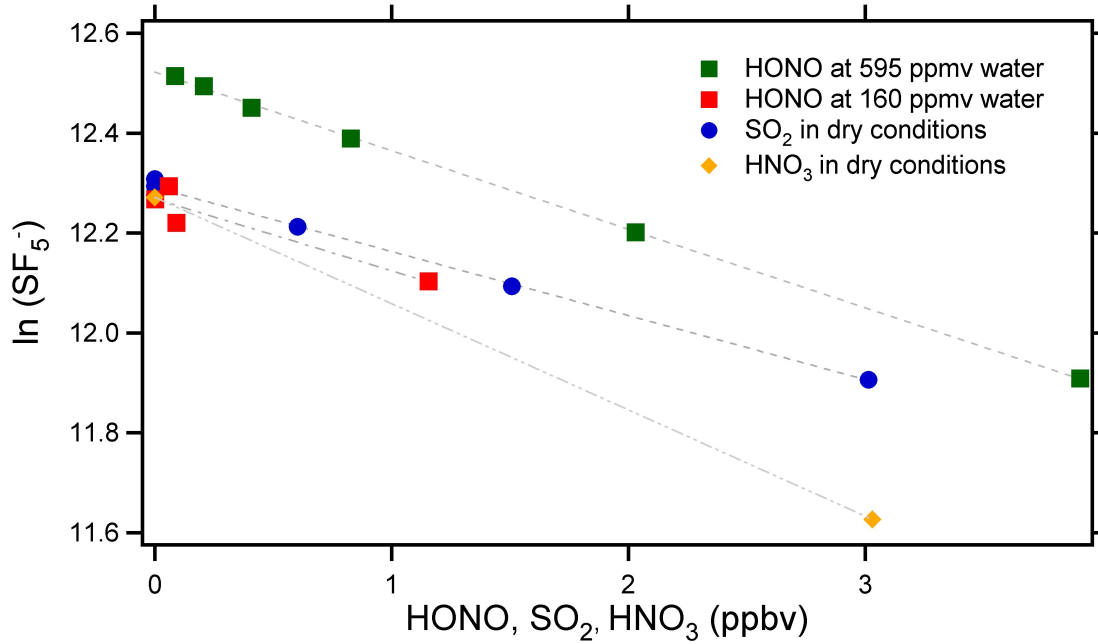


Figure 3.9: The calibration factor for HONO was derived by fitting the logarithmic SF_5^- ion signal versus the HONO mole fraction. For comparison a similar method has been employed for SO_2 and HNO_3 .

These values may only give a relative dependence on the water vapor mole fraction but are absolutely poorly constrained due to a lacking knowledge of the residence time for ion-molecule reaction. The error of the residence time may be as high as 100 % due to unknown mixing effects (see chapter 5).

A similar argument holds if comparing the rate coefficient with the literature values for SO_2 : At dry conditions the rate coefficient was $1.3 \cdot 10^{-9} \text{ cm}^3 \text{ s}^{-1}$ thus a factor of two higher than the rate coefficient measured by Lovejoy and Wilson [1998]. The nitric acid reaction rate coefficient of $2.09 \cdot 10^{-9} \text{ cm}^3 \text{ s}^{-1}$ compares well within the errors to the rate coefficient measured by Marcy et al. [2005]. But wall effects were dominant thus no direct comparison can be done. The calibration factor for HONO is given by $CF_{HONO} = (kt_r\chi)^{-1}d$. A factor of 9.9 ppbv was obtained.

The error of this calibration factor can only roughly be estimated since the instrument was exchanged between the campaign and the calibration. The system was more sensitive during calibration in the laboratory mainly due to less contamination from the ion source. However the method itself is independent of the instrument thus an error of less than 50 % is assumed. The atmospheric mole fraction was derived with the parallel ACIMS formula (2.7)

$$[HONO] = CF_{HONO} \frac{^{46} + ^{66} + ^{93}}{^{46} + ^{66} + ^{82} + ^{83} + ^{93}} \cdot \ln\left(1 + \kappa \frac{^{46} + ^{66} + ^{82} + ^{83} + ^{93}}{^{127}}\right) \quad (3.13)$$

The numbers represent for simplicity the ion signal for the mass in amu after background correction. The water vapor dependence and other interfering reactions that may disturb the measurement are discussed in chapter 4.

3.6 Mass analysis in the ion trap

The MS^n mode of the ion trap allows for selective trapping and subsequent fragmentation of the ions as described in chapter 2. The fragments of the trapped ions are thereafter trapped and can be fragmented as well. Mass analysis is of specific importance if the composition of the ions is not known and the reaction scheme of the educt is unfamiliar. For smaller ions only a limited number of combinations is possible but it becomes more difficult for large ions such as long chains of hydrocarbons.

The MS^2 mode was used for mass analysis of the primary and secondary products and gave the final prove for the composition of the ions. The fragment F^- with mass 19 has not been observed in the ion trap because of the mass discrimination for small masses. With a linear quadrupole mass spectrometer [Huey et al., 2004], the F^- ion has been observed however not as a potential educt ion reacting with e.g. SO_2 . The amount of F^- depends on the fragmentation taking place in the collision dissociation chamber, thus F^- is mainly formed as fragment. Additionally due to a high proton affinity of the ion a fast reaction with acids of high gas phase acidity to HF may explain the depletion of the ion concentration of F^- .

3.7 Comparison of fragmentation and consecutive reactions

Fragmentation in the ion trap can be reinforced by changing the RF on the end cap electrodes with subsequent collision with helium. However fragmentation cannot be avoided completely because helium is injected as a dampening gas continuously into the trap and will continuously initiate fragmentation.

A comparison of the continuous fragmentation of the primary product for HONO, HNO_3 and HCl is given in Fig. 3.11. The fragmentation for the HNO_3 product ions appears to be more efficient than for the HONO product ions. The slope varies by a factor of 4. A simple explanation can be given by comparing the gas phase acidities of the acids involved. Gas phase acidities and proton affinities [Manion et al., 2008] of the respective anions are listed in the following Table 3.3. The gas phase acidity is the Gibbs free energy change of the reaction $HA \rightarrow H^+ + A^-$. Thus the higher the ΔG the weaker is the acid. The enthalpy change ΔH of this reaction is the proton affinity of the anion.

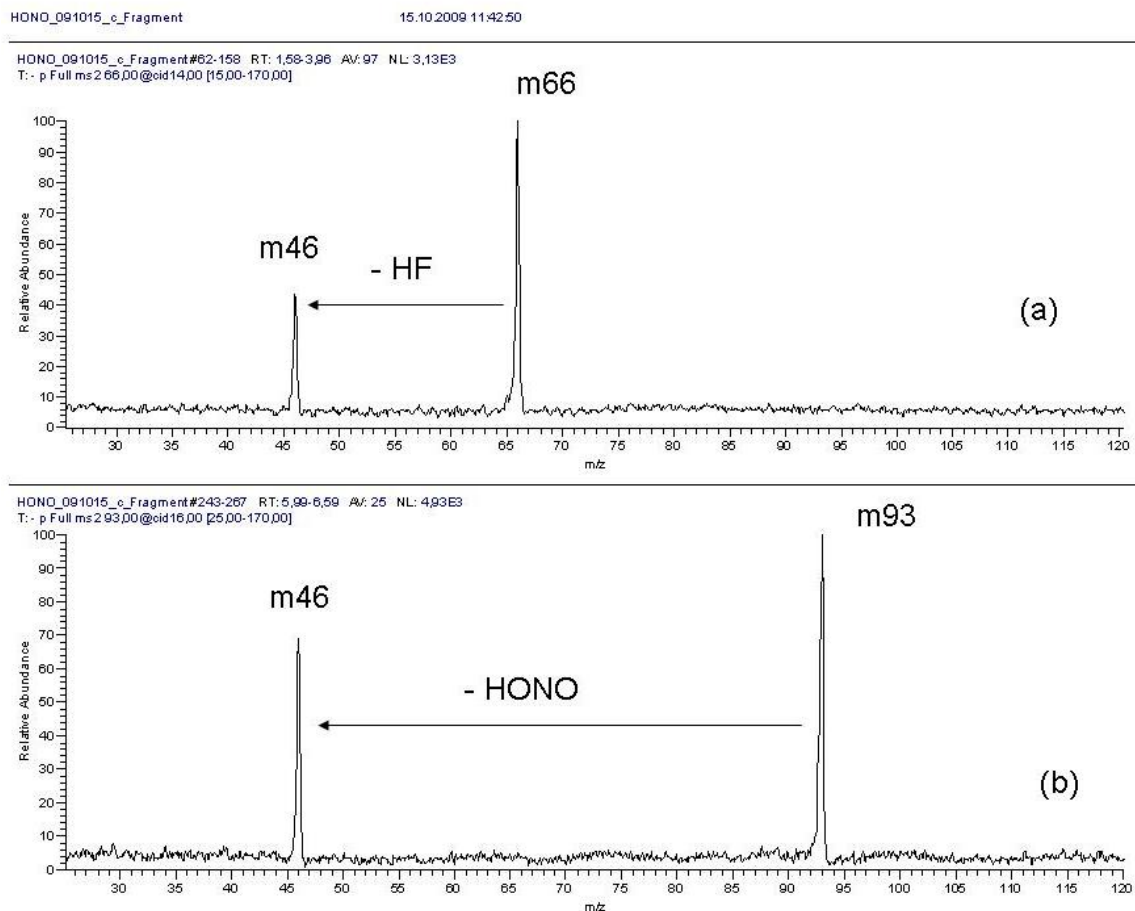


Figure 3.10: The spectra of the fragmentation of mass 66, the primary product (Panel (a)) and the fragmentation of mass 93, the secondary product (Panel (b)) of the reaction of HONO with SF_5^- . In the first case HF is abstracted in the second HONO.

molecule/anion	ΔG (kJ mol ⁻¹)	ΔH (kJ mol ⁻¹)
HF/F ⁻	1529	1554
HONO/NO ₂ ⁻	1396.2 ± 1.3	1423.4 ± 0.84 kJ/mol
HCl/Cl ⁻	1372.8 ± 0.42	1395.0
HNO ₃ /NO ₃ ⁻	1329.7 ± 0.84	1357.7 ± 0.84

Table 3.3: Gas phase acidities and proton affinities (of the anion) for HF, HONO, HCl and HNO₃. Taken from Manion et al. [2008].

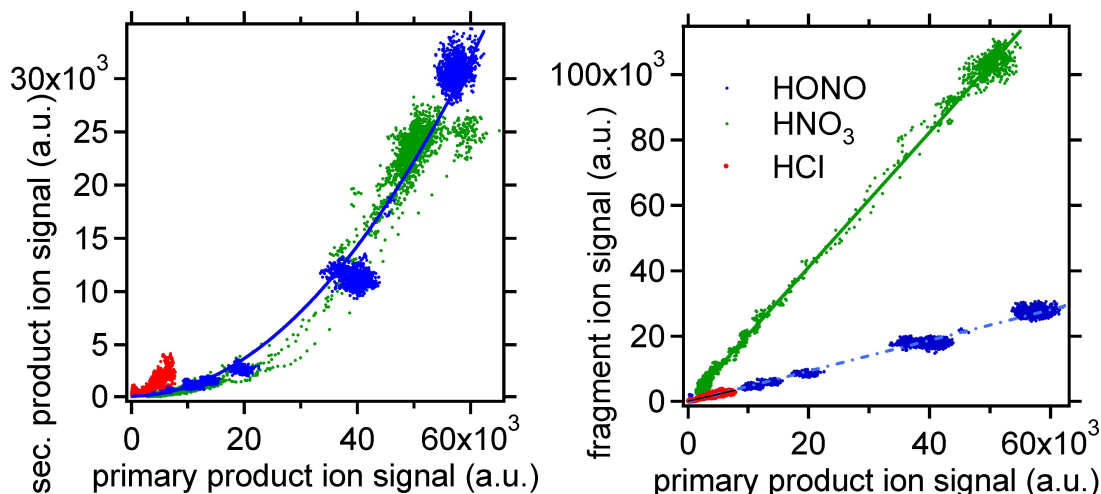
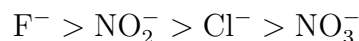


Figure 3.11: The ion signal of the fragments plotted versus the primary product ion signal is compared if either HONO, HCl or HNO₃ is injected into the sample flow.

The proton affinity of the anions compares as follows:



The higher fragmentation of the FHNO_3^- ion compared to the FHNO_2^- can be explained by the proton affinities of the anion: the proton has a stronger bond with the NO_2^- than with the NO_3^- ion. The ratio of fragmentation of FHCl^- leading to Cl^- relatively to the other two acidic gases does not seem to fit into the picture and the argument given above. However discrimination of the small mass 35 (Cl^-) in the ion trap may have shifted the slope substantially to lower values. Therefore the ratios have to be taken with caution.

The electron affinities (eV) [Manion et al., 2008] of the neutral radicals show a different behavior and may give additional insight into the structure of the ions:

$$\begin{aligned} \text{NO}_3 > \text{Cl} > \text{F} > \text{NO}_2 > \text{SO}_2 \\ 3.937 > 3.614 > 3.401 > 2.273 > 1.107 \end{aligned}$$

The location of the additional electron in the ion is given by the above order: The higher electron affinity of Cl and NO₃ compared to F suggests that in a simplified picture the electron is located with a higher probability at the Cl and NO₃ than at the F atom. Comparing NO₂ and SO₂ with F, the probability density of the electron position is higher at the F atom.

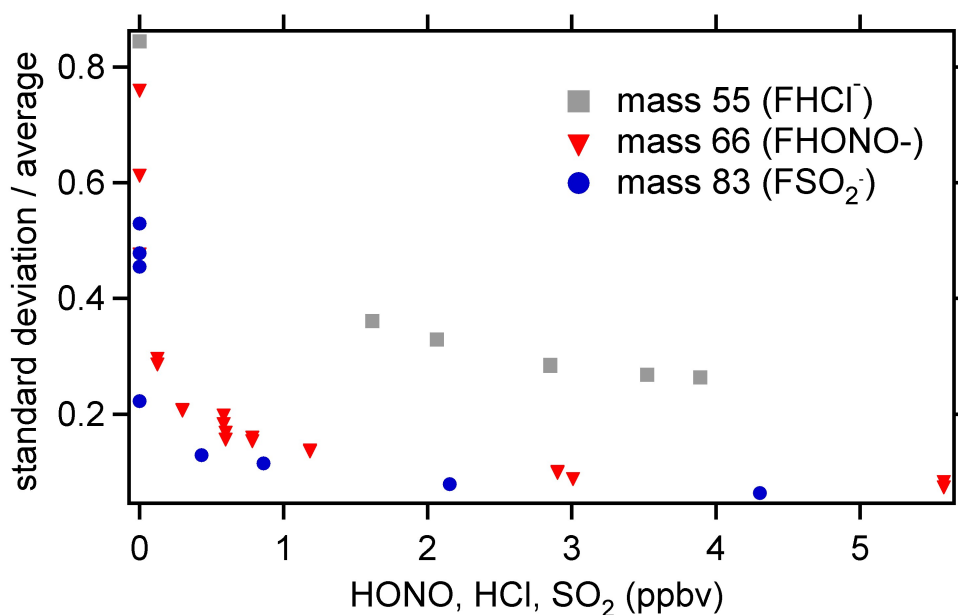


Figure 3.12: Relative errors of the ion signal for FHONO^- , FSO_2^- and FHCl^- for a total time resolution of 1.6 s and a trapping time of 200 ms.

3.8 Precision, accuracy and detection limit

The ion trap signal has a statistical scatter influencing the precision of the measurement. The accuracy is mainly given by the uncertainty of the calibration factor and the background measurement. Memory effects due to reactions of the trace gas with the walls additionally effect the accuracy. Both have to be characterized in order to give a quantitative and qualitative statement on the measurement.

Precision

The ion signal in case of a large number of measurements N follows a gaussian probability distribution where the error of the mean is given by σ/\sqrt{N} , σ being the standard deviation of the ensemble. The precision for this measurement is regarded as the error of the mean. It can be improved by averaging over a larger sample of data points but simultaneously the time resolution of the measurement would be degraded. These two aspects have to be balanced to meet the demands of the measured air mass. Therefore smoothing of the time series was done mainly during measurements of relatively constant concentrations as encountered in the UT/LS region. Here a running average over 30 (HCl) and 10 (SO_2 and HNO_3) data points was applied.

The relative error σ/\bar{x} of the ion signal as a function of the injected trace gas mole fraction is given in Fig. 3.12, where \bar{x} is the averaged ion signal. The relative error exhibits a power-law dependence on the concentration of the trace gas, thus on the

product ion signal. At the maximal concentrations used for this measurement the value settles at 10 % for FSO_2^- and FHONO^- . Three influences may add up to the signal noise:

- mixing of the ions with the gas flow; variations in the ion signal may evolve from inhomogeneous mixing in the flow tube
- electronic noise from e.g. the electron multiplier
- fast read out procedure of the ion trap

The last aspect has to be explained in detail: Due to a high mass resolution of 0.3 amu the shape of the ion signal does not have a gaussian form where the maximum is well defined but it appears more like a peak with sharp edges. This shape does not reflect the statistical scatter of the ion signal authentically. The peak of the ion signal is recorded at a varying distance with respect to the center. Depending on where the ion trap read-out is performed on the gaussian distribution it may even represent a tail of the distribution rather than the maximum. This causes a high signal noise. It is a trade off because a high mass resolution is needed for safe separation of the two masses 82 (HFNO_3^-) and 83 (FSO_2^-).

Additional trapping effects cause the scatter for the FHCl^- ion signal. With a lighter mass the relative error seems to settle at a higher value of approx. 30 %. This effect may be attributed to an ion specific mass and collision efficiency at lower masses. The "low mass cut-off" which is a threshold given by the RF, marks a lower limit of the ions that can be stabilized in the ion trap. In general smaller ions are less efficiently trapped in the ion trap. Fragmentation of the F^- bounded ions has not been observed mainly due to the trapping efficiency at m/z 19. Similar reasons explain that the signal to noise ratio for m/z 55 is higher than for m/z 66 or 83.

Accuracy

The accuracy mainly depends on the calibration factor which in turn depends on pressure, temperature, tuning of the ion trap, total sample flow rate, water vapor content and source gas flow. In general the calibration factor should always be determined at conditions as close as possible to the conditions of the atmospheric measurements. Table 3.4 gives estimated contributions to the error of the calibration factor. In general in-flight calibration improves the accuracy.

The source gas flow of 2 slm was controlled by a new 5 slm Bronkhorst mass flow controller calibrated for N_2 with very high accuracy and precision. The total mass flow rate is controlled by a critical orifice in the exhaust and given by

$$Q = Cd^2p\sqrt{T_0/T} \quad (3.14)$$

Parameter	estimated accuracy
source gas flow	2 %
pressure	5-10 %
temperature	2-3 %
uncertainty of the standard	5 - 15 %
tuning of the ion trap	0 % if not altered
water vapor content	negligible for H ₂ O < 200 ppmv

Table 3.4: The estimated accuracies of the various measurement parameters contributing to the total accuracy of the measurement.

where C is a constant, T_0 is the temperature during calibration, p [hPa] is the pressure upstream of the critical orifice and d [cm] is the diameter of the orifice. Thus the error of the flow is $\propto T^{-3/2}$ and for variations of ± 10 K negligible. The pressure dependence is linear therefore pressure variations have to be accounted for in the error calculation. The pressure varied within ± 1 hPa which results in an error of max. 6 %. During ascent and descent of the aircraft errors were higher mainly due to a fast changing pressure and changing water vapor content which has a profound influence on the rate coefficient. Only data obtained for H₂O < 200 ppmv were used. The tune file, which predetermines the voltages on the octapoles for an optimized sensitivity, was the same for all flights.

The uncertainty of the standard depends on the accuracy of the method that is used to determine the absolute concentration. The anion concentration of a solution with solved HCl and HNO₃ is measured absolutely by the ion chromatographic method described above with an accuracy of 15 %. For SO₂ the uncertainty is given by the uncertainty of the mixture supplied by the gas distributor. For the SO₂ calibration a gas cylinder with 2.12 ± 0.064 ppmv ³²SO₂ was used. However the SO₂ stability was neither monitored nor compared to a second standard therefore a higher error of 8-10 % is applied to account for a possible decay of the concentration in the bottle. The error also includes wall effects of SO₂ that take place inside the MFC that may not be negligible if it was not passivated properly.

The accuracy of the HONO mole fractions is high due to calibration with an instrument of high precision such as the LOPAP instrument. The LOPAP instrument has an accuracy of 7 % and a precision of 1 %.

Another aspect that has to be taken into account is the accuracy of the background measurement. The background signal is the ion signal at a specific mass in the absence of the trace gas. It is governed by the instrumental electronic noise but for nitric acid for example to a greater extent by contaminations in the sampling line. For "sticky" gases such as HNO₃ and HCl that attach and detach continuously to and

from the walls because of their polarity, measurements of the background signal involve a certain detention time. This is especially disturbing during flights where long background measurements cost valuable measurement time. The detention time for a 90 %-signal-decay was measured in the laboratory and employed during background measurements in flight and extrapolated to the "real" background measurement in order to save time. For the flight measurements this time was approximately 3 min as shown in Fig. 3.13.

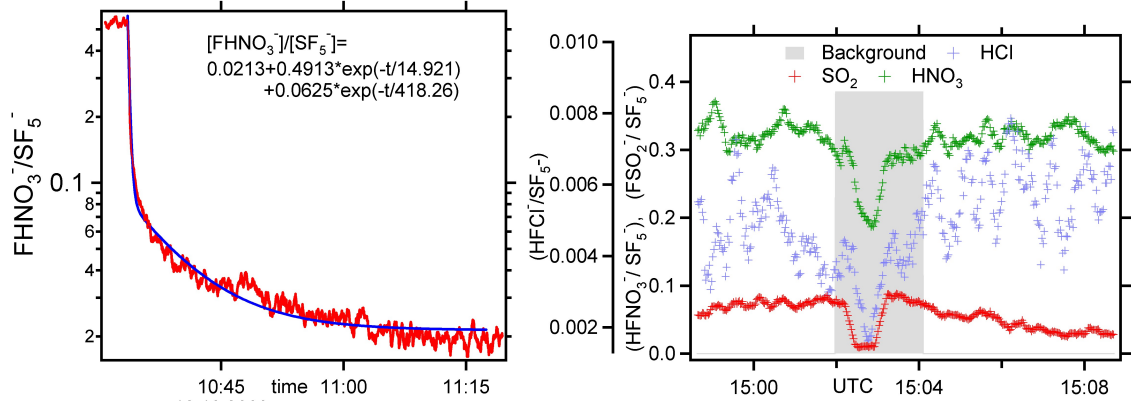


Figure 3.13: Left: The decaying signal of the ratio $\text{FHNO}_3^-/\text{SF}_5^-$ after removal of HNO_3 from the sample flow. The double exponential fit has been applied to account for a fast decay caused by the HNO_3 decrease in the center of the main flow and a slow decrease accounting for HNO_3 slowly detaching from the walls. Right: Ratio of the product to educt ion signal during an in-flight background measurement of HNO_3 , HCl and SO_2 inside the stratospheric plume with volcanic influences (see chapter 6). The shaded area demonstrates the approximate time span that is needed for a background calibration.

Background and detection limit

The detection limit is derived by taking the standard deviation of the background signal of the products and calculating the mole fraction with the ACIMS formula (2.5) at a given calibration factor

$$DL = CF \cdot \ln\left(1 + \kappa \sigma \left(\frac{BG}{\text{SF}_5^-}\right)\right) \quad (3.15)$$

The background was measured on the ground-level and in-flight by occasional injection of dry nitrogen (5.0 purity standard). An example of an in-flight background measurement in stratospheric air is shown in Fig. 3.13. SO_2 shows fast a response and decrease to a laboratory background within seconds. HCl shows a slower decay and stabilizes at a later time but nitric acid shows a continuous decay throughout the measurement and no plateau was reached.

The background signals and standard deviation for nitric acid differed between the

flights due to nitric acid contamination from the ion source. The background signal decreased during flight by approx. 10 % due to a decay of nitric acid concentration initially caused by the ion source. This adds to the total accuracy. Additionally it showed a water vapor dependence such that at higher dew points the background signal decreased. This may be due to other reactions taking place in the flow reactor at higher water vapor mole fractions and a water vapor dependent rate coefficient. Therefore only the dry background was used.

Nitric acid is produced in the ion source by collision of the α particles with N_2 and other impurities in the source gas flow, such as water vapor and O_2 . Radicals are produced and react to form HNO_3 . If the ion source is exposed to these gases at higher pressures the production of HNO_3 increases accordingly. A film of HNO_3 absorbs to the walls of the metallic capillary ion source. It can only be removed slowly through pumping and/or heating. Thus the system should be pumped and kept clean to minimize these contaminations. During the CONCERT campaign the system was deployed over-night in the aircraft and could therefore not be pumped continuously. Different procedures have been applied to minimize the contamination:

- running and therefore pumping the system for several hours before the flights
- pressurize the ion source with nitrogen if no pumping was possible to prevent O_2 and other gases from entering into the flow tube
- flushing the ion source continuously with a small flow of N_2 particularly during the night when no power was on the aircraft

Other common chemical methods such as injection of NH_3 [Marcy et al., 2005; Neuman et al., 2000] that reacts with HNO_3 to form NH_4NO_3 which is inert to reactions with SF_5^- where not applied. A decrease in sensitivity for HCl and HNO_3 , contamination of the system and unforeseen adverse effects may have disturbed the measurement and therefore were not considered.

During laboratory tests a substantially smaller background was achieved by maintaining the system at a lower pressure and pumping for several days. The high background signal of HNO_3 of 0.5 to 1 ppbv caused a higher detection limit compared to the SO_2 and $HONO$ measurements. This was specifically problematic during the measurements in the wake of commercial airliners where the increase of HNO_3 mole fraction was insignificant above the background and transmission was affected due to more humid air in the upper troposphere than during measurements in the lower stratosphere. The detection limits (in pptv) for a 2σ standard deviation for $HONO$ and SO_2 at a time resolution of 1.6 s and for HNO_3 averaged over three spectra for the three tropospheric flights is given in Table 3.5. For the stratospheric flight on 31 October 2008 where the aircraft cruised in a more stable environment with respect to the trace gas concentration the time resolution was decreased by averaging over 10 spectra for SO_2 and HNO_3 , and 30 for HCl . Thus the detection limits for a 1σ standard deviation were 18 pptv, 36 pptv and 22 pptv, respectively.

day	HONO	SO ₂	HNO ₃
17.11.2009	71	66	275
19.11.2009	72	67	285
20.11.2009	59	42	200

Table 3.5: Detection limits of HONO, SO₂ HNO₃ in pptv on 17, 19 and 20 November 2008

3.9 Calibration with isotopically labeled standards

The use of isotopically labeled standards has become very common in combination with the CIMS method [Speidel et al., 2007; Fiedler et al., 2009; Zondlo et al., 2003; Kim et al., 2008]. Adding a standard of the same chemical nature but with a different physical behavior due to a difference in mass is very elegant and practical in many aspects of mass spectrometry. Such advantages are

- the standard can be added continuously during operation without interfering with the ambient isotope
- rate coefficients depending on temperature and water vapor are monitored continuously
- the transmission is monitored because the two isotopes are expected to behave similarly
- parameters such as rate coefficient, discrimination and other trapping efficiencies depending on the mass are negligible if the relative mass difference of the two isotopes reaches only a few percent.

For the present work three heavier isotopes of HCl (deuterium chloride (DCl)), HNO₃ (H¹⁵NO₃) and SO₂(³⁴SO₂) have been tested in the laboratory. Neither was used during atmospheric measurements due to interferences with other product ions. HCl is a small and "uncomplicated" molecule with only two options for isotopic labeling, chlorine or hydrogen. The chlorine isotopy was already used for a consistency check of the measurement (see section 3.4). A labeled chlorine standard is very costly and difficult to obtain. Therefore an unsuccessful effort for calibration with DCl was made. It may serve as background information for future efforts on HCl calibration with an isotopically labeled standard.

The DCl solution with 38 % DCl in D₂O was supplied by Sigma Aldrich. The solution was sent to VICI (Metronics) to built a calibration standard similar to the calibration standard for HCl. However their experience with the solution and the substance was limited so an adequate treatment of the substance (e.g. no contact

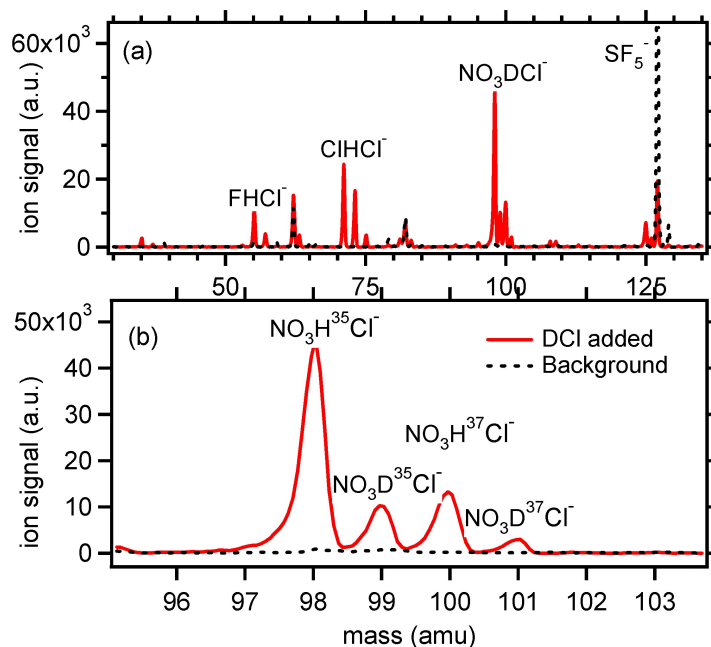


Figure 3.14: Mass spectrum obtained when several ppbvs of DCl were added to the sample flow through a PFA tube with a specifically built DCl calibration source. No primary products (DFCl^- , mass 56 and mass 58) were observed.

with water) could not be guaranteed. A permeation device with a high output rate of 508 ng/min at 323 K was supplied and tested. The expected reaction was:

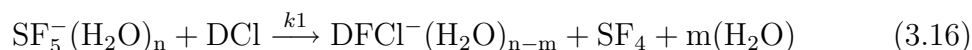


Fig. 3.14 shows a spectrum where the above described calibration standard was used. Consecutive reactions are dominant due to a high concentration. However primary products comprise exclusively the ambient HCl product ions and none of the expected products of 56 and 58 amu are observed. NO_3^- reveals a reaction path with the heavy isotope to form NO_3^-DCl but even this path is more efficient for the ambient HCl isotope.

This may be attributed to a fast reaction of D_2O with the ambient water vapor inside the calibration standard but also in the teflon tube and the flow reactor. The exchange of the deuterium atom with the hydrogen atom is efficient in the solution where the acid is present in ionic form. Water may enter the diffusive Furthermore for light molecules and atoms the last aspect on the list above has to be considered: The relative mass difference is larger than for heavy molecules even if the absolute difference is only of the order of a few amu. For deuterium and hydrogen the effect is the largest. Due to the higher mass of deuterium the zero-point energy is lower. Therefore the activation energy for reactions with deuterium molecules is decreased compared to equivalent bonds with hydrogen [Atkinson and de Paula,

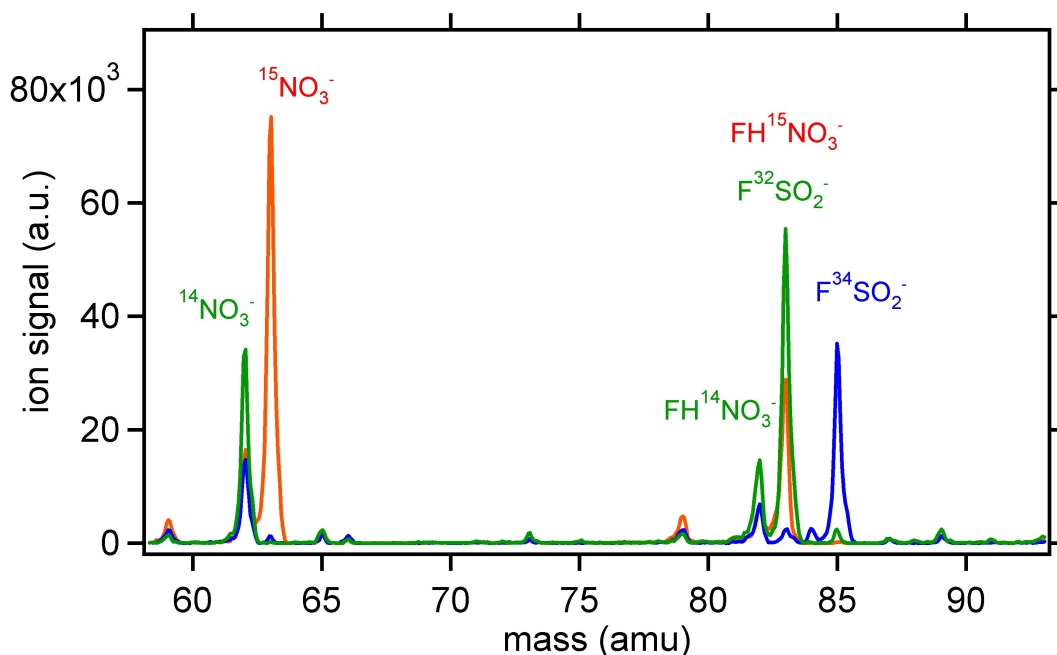
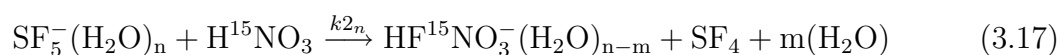


Figure 3.15: Mass spectrum with isotopically labeled trace gases. The red curve shows a spectrum when H^{15}NO_3 is injected. The green curve that peaks at the same mass was measured when $^{32}\text{SO}_2$ was injected, interfering with the isotopic calibration of nitric acid. The blue curve shows a spectrum where the isotopically labeled standard $^{34}\text{SO}_2$ is injected.

2006]. The change in the reaction kinetics due to the deuterium bond may be as large as a factor of seven, which can be observed in the reaction kinetics for C-H and D-H bonds.

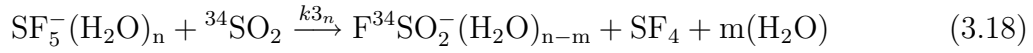
This effect is negligible for calibration of nitric acid with the heavy isotope of the nitrogen atom ^{15}N , with a relative mass difference of 7%. Measurements of Zondlo et al. [2003] described the use of the same calibration standard reacting with deprotonated methanesulfonic acid as a reagent ion. For SF_5^- the reaction with H^{15}NO_3 is the following:



In Fig. 3.15 a section of a spectrum with the isotope injected is shown (red curve). Additionally to the primary product ion with mass 83 the fragment $^{15}\text{NO}_3^-$ (mass 63) appears.

The spectrum also reveals the problematic interference with the SO_2 measurement: The product mass of the calibration is the same as for the $\text{F}^{32}\text{SO}_2^-$ product. Using the standard would therefore either degrade the SO_2 measurements or make the calibration more imprecise if SO_2 is present in the ambient air because it would add to the calibration signal.

Adding $^{34}\text{SO}_2$ the product ion on mass 85 is formed via:



and shown in Fig. 3.15. The relative abundance of the two mass peaks can therefore be compared continuously during ambient measurements. A correction for the ambient sulfur isotopy, the artificially produced isotopy of the standard and a background correction has to be done. The mole fraction can be derived with the "Bandy formula" [Bandy et al., 1993; Fiedler et al., 2009], where these corrections are considered.

Interfering reactions with water vapor represent an additional issue to this measurement. The background at higher water vapor mole fractions has to be corrected in the spectra. The ratio of mass 85 to mass 83 changes with water vapor due to an additional unknown reaction with a product of mass 83. This background measurement can alternatively be done in-flight in uncontaminated air by simply turning of the standard. It can also be done on the ground by injection of different water vapor mole fractions.

For measurements in the UT/LS no water vapor dependent background correction was applied because of low water vapor concentrations.

Chapter 4

Interfering trace gases

This chapter discusses additional laboratory experiments with interfering gases that change the reaction kinetic or influence the background. Particularly the water vapor dependence of the measurements is discussed. Nitrogen oxides that may interfere with the measurements in aircraft plumes and ozone which is abundant in the lower stratosphere were tested for interfering reactions.

4.1 Water vapor

Water vapor is one of the most abundant trace gases in the atmosphere. Water vapor mole fractions can vary by a few orders of magnitude within the horizontal and vertical measurement range of the aircraft. A thorough investigation of the water vapor dependence of the reactions and interfering reactions is therefore a liability.

Water vapor influences the ion detection scheme in several ways:

- It may change the effective rate coefficients of the ion-molecule reaction
- It enhances the background ion signal through interfering products such as hydrated products and HF clusters
- It depletes the educt ions thereby lowering the sensitivity
- It forms multiple product and educt ions
- It influences the collision cross section therefore the trapping efficiency

In addition to the effects on the reaction scheme it may influence the transmission of the sampling line by exchange of polar molecules attached to the walls.

Under UT/LS conditions the water vapor mole fraction of maximal 200 ppmv as encountered during the CONCERT campaign is too low to cause server interfering reactions or depletion of the educt ion. However it may become disturbing for other

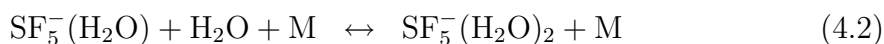
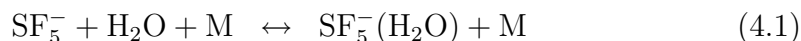
measurement sites. One way to reduce the water vapor effects is to reduce the residence time, thus reaction with water vapor is less efficient or / and the pressure in the flow tube to downsize the absolute water vapor concentration. An increase of the temperature in the flow tube causes an increase in relative humidity and depending on the reaction scheme this lowers the formation of water cluster ions [Huey, 2007].

The water vapor mole fraction was generated by the CEM (Controlled Evaporator Mixer) system supplied by Wagner Mess- und Regeltechnik. A water flow, measured and controlled by a liquid flow meter, and 2 slm of dry nitrogen, used as a carrier gas, are injected into a heated chamber where the water evaporates. The water-saturated nitrogen flow is then diluted by a higher nitrogen flow. Due to a lower limit of 0.05 g/h for the liquid flow meter water vapor mole fractions between 10 and 200 ppmv could only be generated with a high N₂ dilution flow. These flow rates were very unstable and therefore no measurements below 200 ppmv were included in the plots. The measurements for background and 500 ppmv water vapor can be interpolated to obtain the dependence of the product and educt ion signal at lower water vapor mole fractions.

The water vapor was measured by a cryogenic frost point hygrometer (CR-2)(Buck Research Instruments, LLC). The instrument measures the dew point temperature by maintaining a thin ice layer on a mirror that is in equilibrium with the gas phase water vapor. The reflectivity of the mirror is measured with an optical detector. The uncertainty of the measured mixing ratios is between 3 and 5 % [Voigt et al., 2010].

Despite the high precision of the water vapor measurement the laboratory experiments with water vapor can only be considered as a qualitative investigation of the reaction scheme. The sampling line was designed for aircraft measurements and comprised a length of at least 1.5 m of PFA. Removal of water vapor due to sampling effects or diffusion of water vapor through the PFA sampling line was not taken care of. The aim of the laboratory tests was to show that no effects for water vapor mole fractions below 200 ppmv appear.

Due to the polar structure of the H₂O molecule multiple educt ions evolve in the flow reactor with a thermodynamic distribution:



Helium injected into the ion trap dissociates these clusters. Therefore the information on the distribution of the hydrated educt ions is lost. On their way into the mass spectrometer these clusters undergo a rearrangement followed by decomposition into stable ions of the form F[−](HF)_{*n*}. The clusters were fragmented in the ion trap revealing the simple structure: The mass difference between daughter and

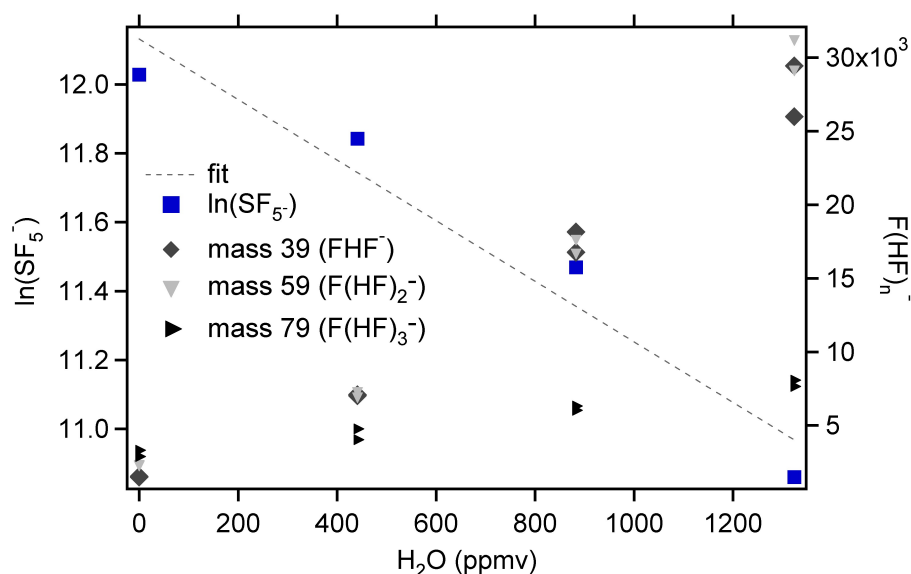


Figure 4.1: The logarithm of the SF_5^- educt ion signal (a.u.) is shown versus the water vapor mole fraction in the FR. While the SF_5^- educt ion signal decreases, the ion signals of $\text{F}^-(\text{HF})_n$ clusters (mass 39, mass 59, mass 79) increase with increasing water vapor mole fraction. The two dominant masses are $\text{F}^-(\text{HF})$ (mass 39) and $\text{F}^-(\text{HF})_2$ (mass 59). The measurement was performed at modified conditions with a pressure of 35 hPa in the FR and a total flow of 5 slm.

mother ion is 20 amu and can only be attributed to an HF abstraction.

These reactions though generally occurring at a lower rate coefficient (of the order of $10^{-14} \text{cm}^3 \text{s}^{-1}$ measured for CF_3O^- [Huey et al., 1996]) are very effective in depleting the educt ions because water vapor mole fractions are approx. 3-6 orders of magnitude higher than competing trace gas mole fractions. A list of product and educt ions is already given in chapter 2.

The logarithm of the educt ion signal is plotted as a function of the water vapor mole fraction in the flow tube (after dilution by the ion source gas flow) in Fig. 4.1. The slope of the plot can be used to derive the reaction rate coefficient for the reaction of $\text{SF}_5^-(\text{H}_2\text{O})_n$ with water vapor. As discussed in chapter 3 the residence time is not well known. Assuming a residence time t_r of 100 ms the reaction rate coefficient is $1.0 \cdot 10^{-14} \text{cm}^3 \text{s}^{-1}$, thus comparable to the reaction of CF_3O^- with water vapor considering the error of the measurement which may be up to 100 %. This investigation should be pursued if measurements in humid air are considered and comparison to other reagent ions are made.

Spectra with 3 different water vapor mole fractions added to the sampling flow and under background conditions (dry nitrogen) are shown in Fig. 4.2. The dominant masses are $\text{F}(\text{HF})_n^-$ clusters. Additionally a high background ion signal on mass 83, mass 37 and mass 57 appears which cannot be linked to the reactions of HCl and

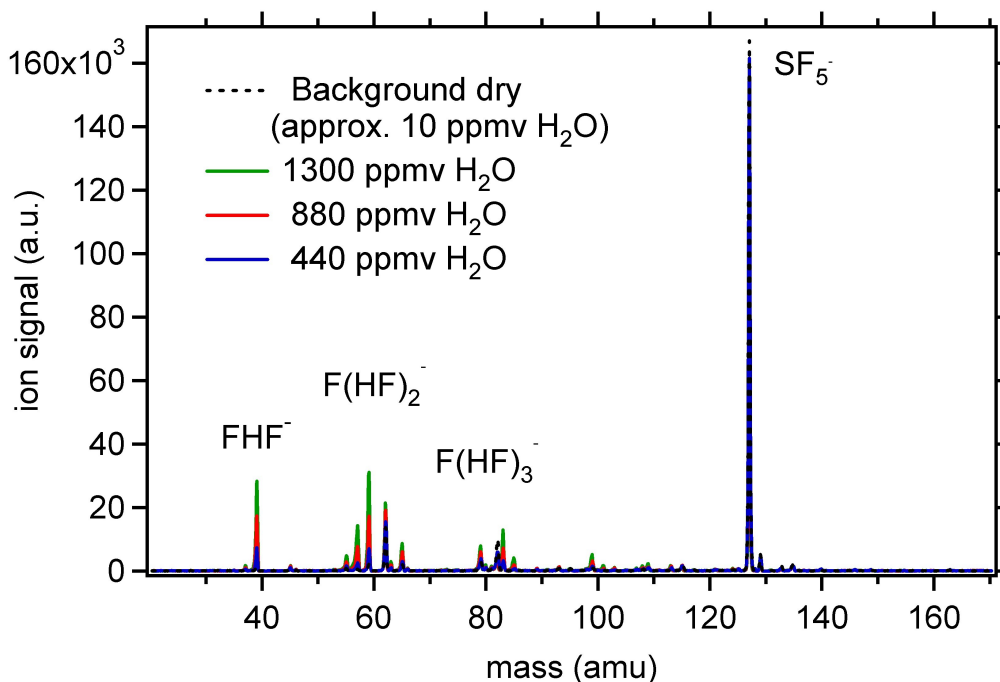


Figure 4.2: Mass spectrum for 3 different water vapor mole fractions in the sample flow (black) and under background conditions (red). The pressure in the flow reactor was 35 hPa and a total flow of 5 slm was used.

SO₂ because of a different ratio with mass 85 and mass 55 compared to the natural isotopic abundance. Possible candidates for mass 37 and mass 57 are FH₂O⁻ and FHF(H₂O)⁻.

Other unidentified ions appear with an m/z ratio of 113, 109 and 101 amu. An increase of the sum of all ions detected in the mass range between 15 and 170 amu for dry and humid conditions was not observed. This observation may however be affected by the mass dependent sampling efficiency of the ion trap. If nitric acid is introduced in the sampling flow an increase in total ion signal is observed which can be attributed to the discrimination of mass 127.

HNO₃ and SO₂ under humid conditions

The change in reaction rate of HNO₃ and SO₂ at different water vapor mole fractions was investigated by adding one constant mole fraction of the trace gas and thereafter varying the water vapor mole fraction. The main gas flow (dry nitrogen) and pressure in the flow reactor was the same as during the atmospheric measurements and constant at all times. The background was measured at these water vapor mole fractions and subtracted from the ion signals. It appears that the product ion formation behaves differently for SO₂ and HNO₃ in the presence of water vapor: for nitric acid a decrease of the primary product ion signal is observed while the sum of FHNO₃⁻ and NO₃⁻ stays constant. Marcy et al. [2005] observed a similar tendency

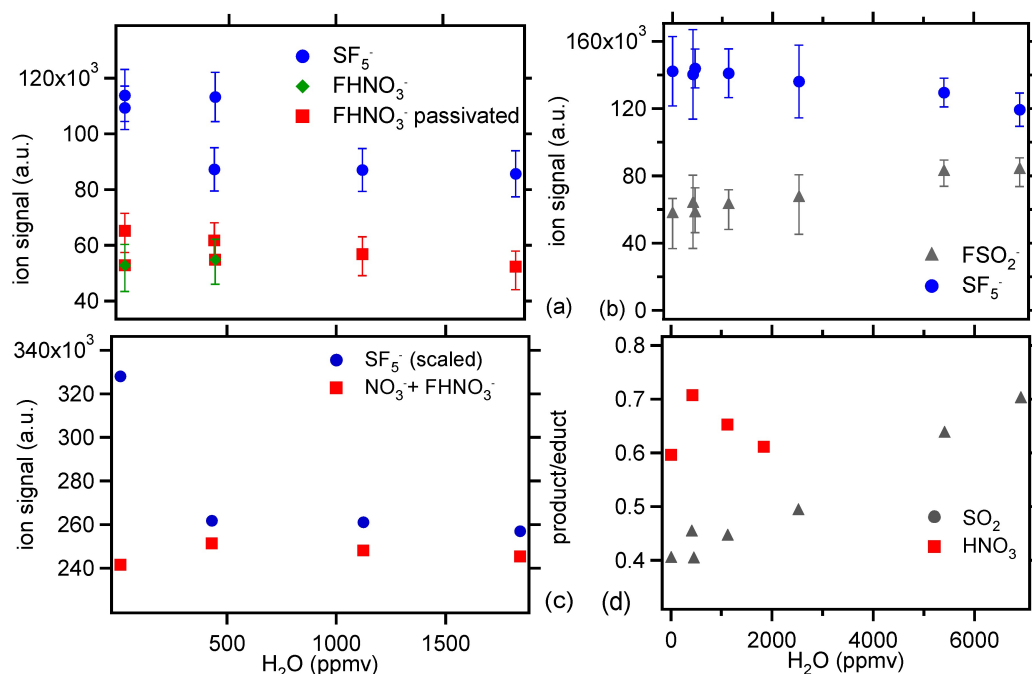


Figure 4.3: The product and educt ion signals for 4.3 ppmv HNO_3 and 2.75 ppmv SO_2 added are shown as function of water vapor mole fraction. Relative (d) and absolute ion signals for HNO_3 (a,c) decrease and increase for SO_2 (b).

for the primary product ion when adding 100 ppmv of water. SF_5^- decreases mainly due to depletion by reactions with water vapor. In contrast FSO_2^- increases with increasing water vapor. This observation stands in contrast to findings of Kim et al. [2008]. They worked with SF_6^- reagent ions and found that due to hydrolysis of the product ion F_2SO_2^- the sensitivity is reduced at higher dew points. One possible explanation for the deviating observations is that the polarity of the two product ions differs (due to one additional fluorine atom of high electronegativity) such that water vapor clusters form faster for the F_2SO_2^- ion. A second explanation might be that H_2O cluster ions are dissociated in the ion trap and therefore no shift to higher masses is observed.

HONO under humid conditions

The effect of water vapor on the HONO sensitivity was partly discussed in chapter 3 with a comparison of the rate coefficients at different water vapor mole fractions. An increase of the rate coefficient of approx. 10 % was observed if the water vapor was enhanced by a factor of 3.7, thus there is only a light dependence on the water vapor mole fraction.

The educt and product ion signals and the fragments are plotted for two different water vapor mole fractions (below and above 800 ppmv) as a function of HONO in Fig. 4.4. The educt ion signal decreases dramatically at higher water vapor again

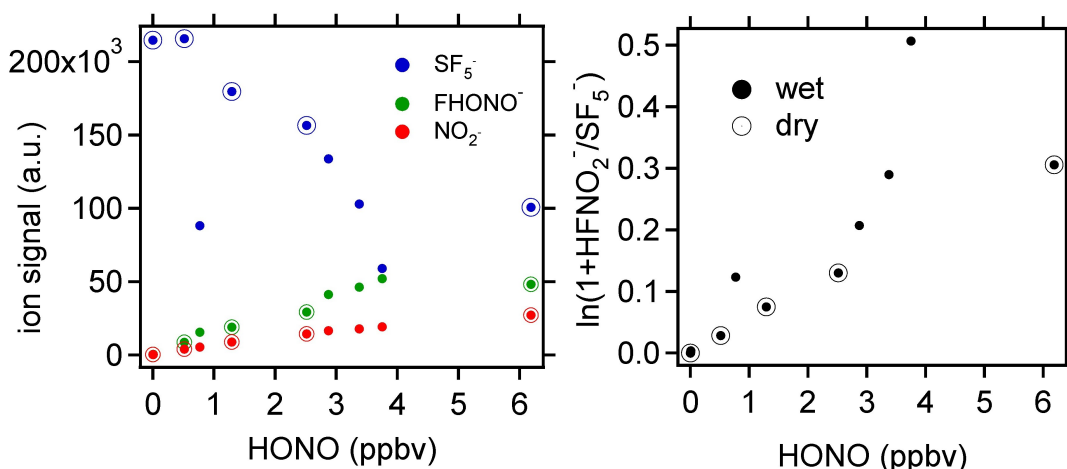


Figure 4.4: The product and educt ion signals are plotted as a function of different HONO mole fractions for wet ($\text{H}_2\text{O} > 800$ ppmv, full circles) and dry ($\text{H}_2\text{O} < 800$ ppmv, open circles) conditions.

due to depletion by concurring reactions with water. The product ion signals are also enhanced above their reference points at dry conditions. The dependence of the fragment on the HONO mole fraction is not affected by the different conditions and so is the secondary product (not included in the figure for simplicity). This implies that NO_2^- is mainly a descendent of the mass $(\text{HONO})\text{NO}_2^-$. As a consequence the $\ln(1 + R - R_0)$ is higher under humid conditions, resulting in a smaller calibration factor.

However these laboratory investigations are a qualitative consideration and have no effect on the measurements performed during CONCERT in the UT/LS where water vapor mole fractions were below 200 ppmv during contrail encounters.

4.2 NO and NO_2

Interferences with NO_x (NO and NO_2) that is particularly abundant in young aircraft exhaust plumes were tested in the laboratory. Heterogeneous reactions as discussed by Kleffmann et al. [1998]; Kleffmann and Wiesen [2008] of NO_2 and H_2O on water/sulfuric acid surfaces or on PFA forming HONO and HNO_3 may cause an interfering HONO background signal.

Ion signals were monitored when NO and NO_2 were added to the sample flow. NO_2 is generated by titration of NO with O_3 with a gas phase titration unit (GPT) supplied by Ansycho. O_3 was produced by means of a UV-lamp. NO was supplied in a steel cylinder with a calibrated mixture of 3 ppmv NO (2.5 purity) in N_2 (5.0 purity). The optimized gas phase titration occurs at a mixing ratio of O_3 and NO of 7 : 8, at higher O_3 mixing ratios higher oxidants of NO_x would be produced. The output was measured with a blue-light converter before employing it for the CIMS

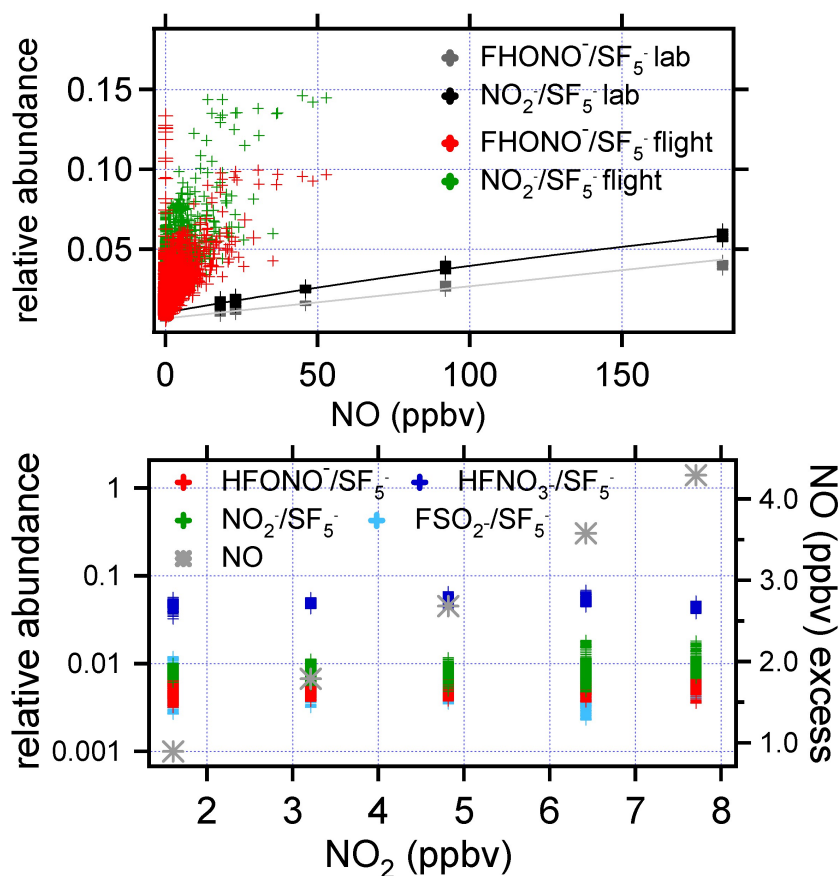


Figure 4.5: The product to educt ion signal ratio is plotted versus NO₂ (upper panel) and NO (lower panel) mole fractions. No interfering reactions on the masses of interest were observed for mole fractions between 0 and 7.7 ppbv NO₂. For NO a linear increase of the background was observed.

measurement. Due to this initial mixing ratio, excess-NO entered the sample flow simultaneously which is plotted on the right axis of Fig. 4.5 (upper panel).

During the CONCERT campaign no NO₂ was measured in-flight. However the second most abundant trace gas in aircraft exhaust plumes is NO₂ with an initial ratio [NO₂]/[NO_x] of 0 to 15% [Schulte et al., 1997]. Assuming that all NO_y with maximum values of 60 ppbv detected in the young aircraft plumes was NO_x maximal 9 ppbv would be in the form of NO₂, which is covered by the laboratory experiment (Fig. 4.5, upper panel). For a dependence of the background on higher mole fractions than 7.7 ppbv additional laboratory tests are required.

NO was tested for higher mole fractions up to 183 ppbv (Fig. 4.5, lower panel). The mixture was generated by the same gas standard as the one used for the titration of O₃. A linearly increasing background of the two product masses 66 and 46 with the NO mole fraction was observed. Possibly this enhancement was

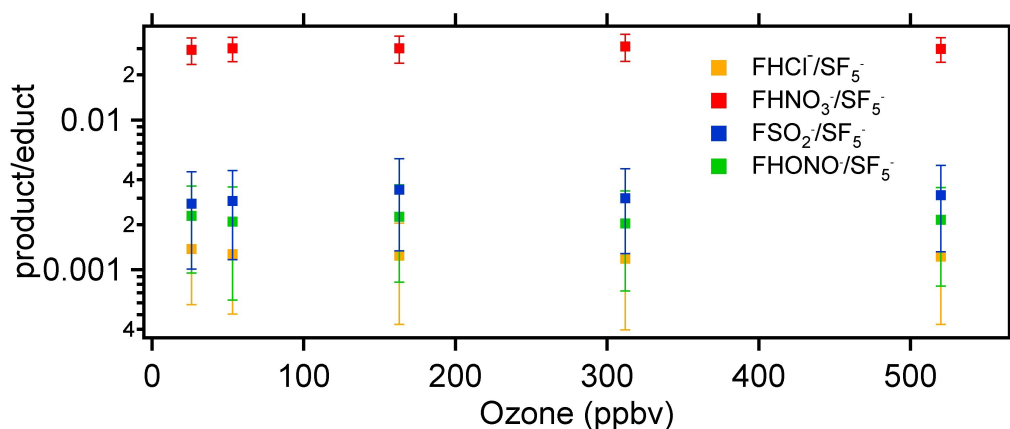


Figure 4.6: The product to educt ratio for the main reactions are plotted versus the ozone mole fraction. No interference with ozone was detected for mole fractions up to 520 ppbv in the sampling line.

caused by heterogenous reactions occurring on PFA surfaces in the presence of water. The increase is given by $2.6 \cdot 10^{-4} \cdot \text{NO}[\text{ppbv}] + 0.012$ for the ratio of $\text{NO}_2^-/\text{SF}_5^-$ and $2.0 \cdot 10^{-4} \cdot \text{NO}[\text{ppbv}] + 0.007$ for $\text{FHONO}^-/\text{SF}_5^-$. For maximum NO mole fractions encountered during CONCERT the background increase caused by NO would correspond to approx. 50 pptv or 5-8 %. Such high mole fractions were rarely encountered as can be seen in the Fig.4.5. That implies that only few data points contribute to the error and might suffer from a systematic overestimation. This background effect lies within the uncertainty of the measurement and is considered as a negligible effect.

4.3 Ozone

Interfering reactions that might cause a background enhancement or an educt ion depletion were tested for mole fractions up to 520 ppbv ozone. Slusher et al. [2001] reported on the reaction of SF_6^- with ozone to form O_3^- (mass 48) and inferred a reaction rate coefficient of $1.7 \cdot 10^{-10} \text{cm}^3 \text{s}^{-1} \pm 20\%$ relative to the reaction with SO_2 . CO_3^- educt ions as used in the work of Möhler and Arnold [1991] are formed in the flow reactor via the reaction of CO_2 and O_3^- . O_3^- is initially produced in the ion source through O^- and O_2^- by electron attachment on the electron affine O_2 (0.5 eV) molecule which is used as ion source gas. This would cause an enhancement on mass 60.

Fig. 4.6 shows the dependence of the main product to educt ratios (HCl , HNO_3 , SO_2 and HONO) as a function of the ozone mole fraction in the sampling line. The ozone mole fraction was simultaneously measured by an UV absorption photometer, explained in chapter 5. The mole fraction was increased from background values to 520 ppbv. No enhancement of the main product ion signals was observed. Educt ion

signals were stable at all ozone concentrations. In general no significant enhancement above the background of any product ion within the measurement range of 15 to 170 amu was detected, thus no production of O_3^- and CO_3^- was observed. This may be attributed to the fact that reactions with SF_5^- occur via fluoride transfer as compared to SF_6^- that also reacts through electron de- and attachment. Earlier measurements with CO_3^- educt ions in the stratosphere [Fiedler et al., 2009; Nau, 2008] have shown an enhanced background ion signal on the SO_2 product mass SO_5^- which was attributed to reactions with O_3 on the stainless steel walls of the flow tube. SO_2 may be released by the steel in the presence of O_3 . Due to a teflon coating applied on the walls of the flow reactor these effects were suppressed in the present measurement.

Chapter 5

Experimental setup during CONCERT

The experimental setup during the campaign is explained in detail in this chapter. Two aspects had to be optimized for airborne measurements of HNO_3 and HCl : Specific requirements to the inlet system had to be fulfilled to minimize wall effects such as losses or memory effects. And secondly specific optimization of the ion trap performance, the ion generation and reaction efficiency had to be performed.

5.1 Ion trap mass spectrometer settings

The ion trap mass spectrometer shown in Fig 5.1 was originally integrated into a Falcon rack by an MPI-K/DLR collaboration. The mechanical integration as well as electrical components like power supply and sensors were supplied by MPI-K. Several aircraft missions around the globe have been performed with the instrument, mainly in combination with CO_3^- educt ions. Measurements of SO_2 , HNO_3 , HCN and HONO conducted with the Falcon-instrument are in detail described in Speidel et al. [2007]; Aufmhoff [2004]; Fiedler et al. [2009]; Nau [2008]. Negative and positive chemiions measurements in aircraft exhaust with the ITMS are described in Katragkou et al. [2004]; Kiendler et al. [2000]; Kiendler and Arnold [2002a].

For the CONCERT campaign the ITMS had to be adjusted for measurements of small masses. The sampling time, the AGC, the multipole voltages as well as the mass range had to be optimized. The ion trap tuning was obtained as described in chapter 2 by the LCQ-tune programm supplied by Thermo Finnigan. Optimization was achieved for the ion signal on mass 55 (HFCI^-). Typical settings are given in Table 5.1. The potential changes from negative to positive values thus the negative ions are accelerated towards the ion trap. The repulsive potential of the front electrode and first octapole prevents losses of the ions to the aperture. The instrument was calibrated with a specific calibration substance containing Ultramark, (922 amu), caffeine (194 amu) and peptide with different amino acids (524 amu to

setting	value
AGC	$8 \cdot 10^7$ ions
microscans	5
injection time	200ms
mass range	15-170 amu
front aperture diameter	0.2 mm
Capillary Voltage	-4.17 V
Multipole 1 Offset	-2.93 V
Lens Voltage	(55.65 V)
Multipole 2 Offset	4.02 V
Multipole RF Amplitude	350.00 Vp-p
Coarse Trap DC Offset	9.8 V
multiplier actual	- 1070 V

Table 5.1: Ion trap mass spectrometer settings during CONCERT

1300 amu) before the campaign. Optimization was achieved for the mass calibration with regard to the center of the mass peak and the broadening of the peak (full-width-at-half-maximum).

5.2 Flow configuration

The main challenge for measurements of nitric acid under highly variable conditions is the setup of a reliable transmission line for the gas into the spectrometer. A distance of approx. 2 m from the unperturbed air outside the aircraft down to the ion source has to be surmounted. High flow velocities, stable flow conditions and inert tubing material have to be employed to reduce the residence time in the transmission line and losses to the walls.

A schematic drawing of the two setups used during CONCERT is shown in Fig. 5.2.

5.2.1 Inlet system: Passive and active flow configurations

Two alternative flow configurations were used: One employed only active pumping from the top of the inlet into the spectrometer, the other one used a bypass with a passive flow connected to a smaller actively pumped flow through a shorter PFA tubing. Generally the active pumping was employed, except for two flights, one flight on 2 November 2008 and one flight on 7 November 2008.

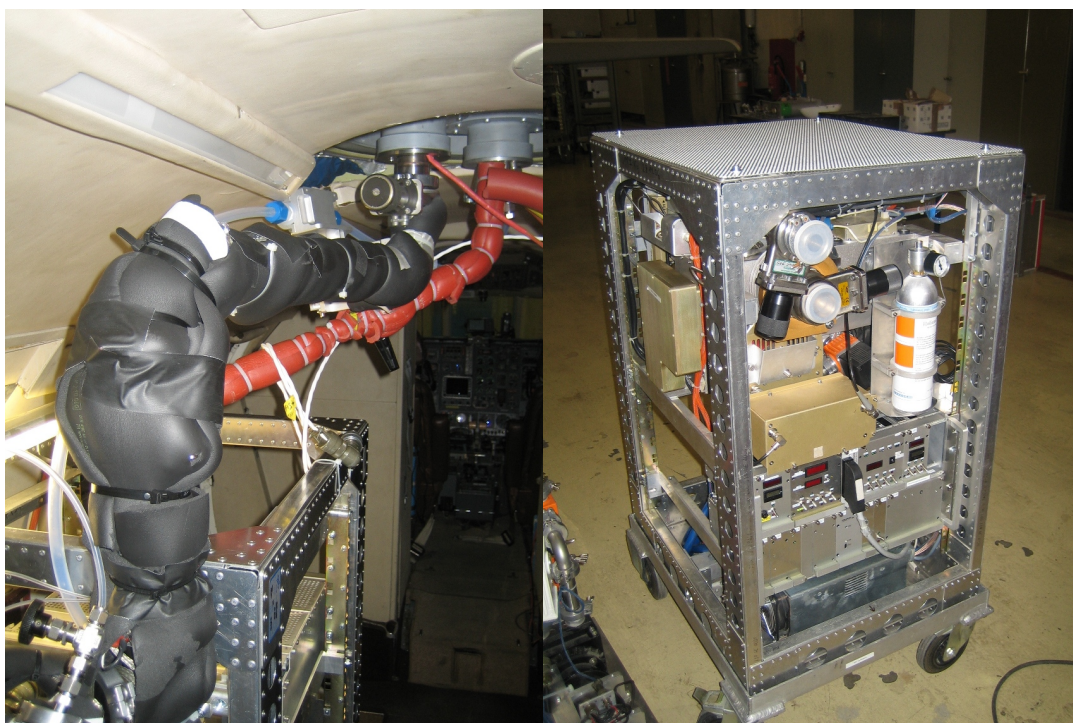
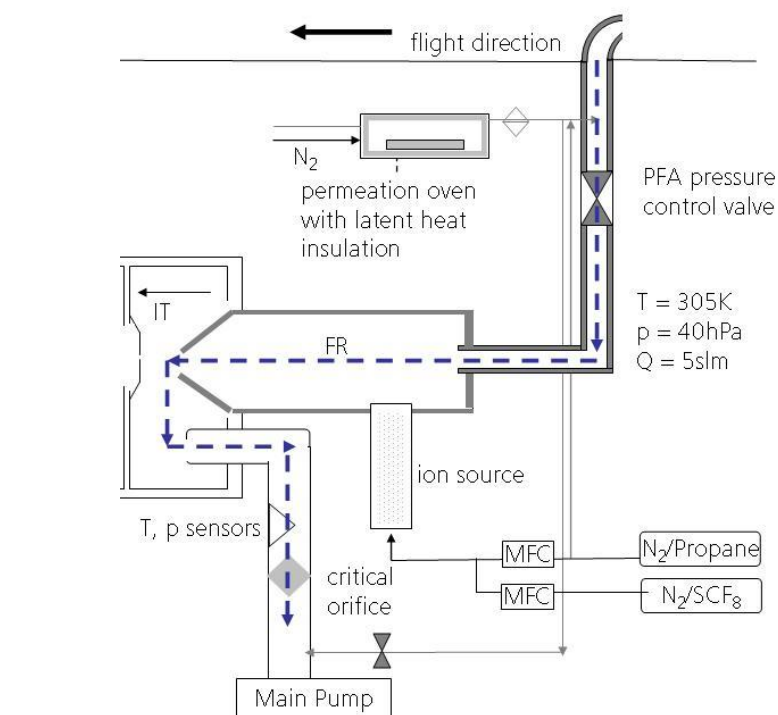


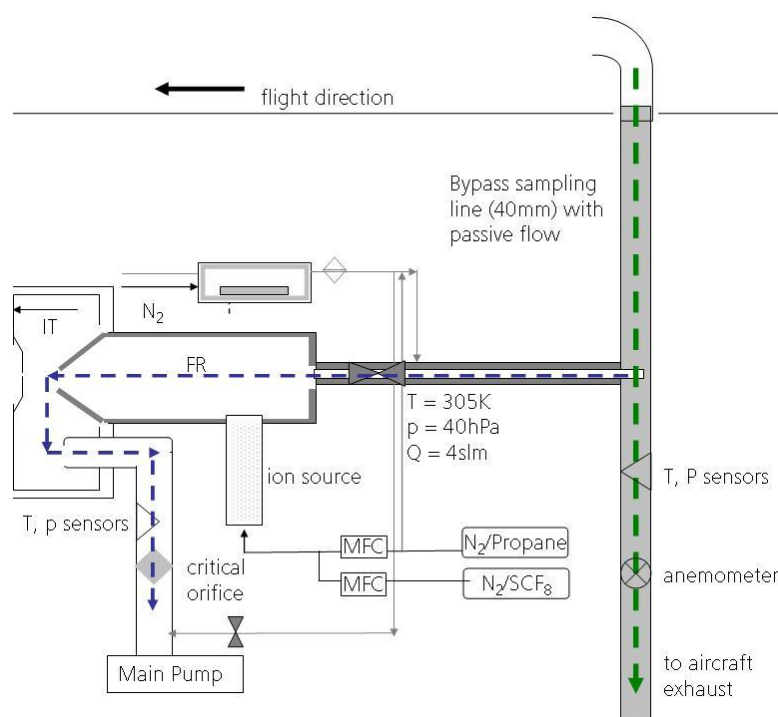
Figure 5.1: Photo (right) of the ion trap MS which was originally integrated into the Falcon rack by an MPI-K/DLR collaboration. The passive and the active sampling lines (left) installed on the Falcon. The sampling lines were heated by heating bands wrapped in insulation to improve the transmission.

Active pumping was achieved with an Alcatel oil pump with a maximal pumping volume of $25 \text{ m}^3/\text{h}$. Two critical orifices with different diameters in the exhaust were used, thus with a constant pressure of 40 hPa in front of the orifice a flow of 6.5 and 7.5 slm was obtained. The pressure valve was mounted at the upper part of the sampling line on the inside of the aircraft cabin underneath the ceiling. Keeping 3/4 of the sampling line at 40 hPa reduced the residence time of the air sample in the sampling line and the water vapor partial pressure. Heterogenous reactions occurring on wet PFA surfaces and soot in the presence of NO_2 and HNO_3 have been subject to many investigations on sampling techniques [Kleffmann and Wiesen, 2008; Kleffmann et al., 1998; Zhou et al., 2002]. Changes of water vapor in the sampling line change the passivation of the tubing with the trace gas (e.g. HNO_3) therefore low water vapor is desirable. Due to low pressures and high flow rates thus short residence times these reactions are partially suppressed. A discussion of possible interferences and supporting laboratory studies can be found in chapter 4.

All wetted parts were covered with or made of PFA, thus no contact to steel surfaces that absorb sticky gases [Neuman et al., 1999] was possible. The coating of the steel tubing and connecting pieces with PFA was done by Gutbrodt GmbH. A fluoropolymer was sprayed to the inner parts of the tube. Tests with a set of different



(a)



(b)

Figure 5.2: (a) Schematic diagram of the active flow configuration during the CONCERT campaign. The actively pumped sampling line, calibration and background tubing and the exhaust configuration are shown. The main gas flow is indicated by the blue arrow. (b) Schematic diagram of the passive bypass flow configurations. The main passive bypass flow (green) through a 40 mm tube and the active flow (blue) through a 1/4" PFA sampling line are indicated.

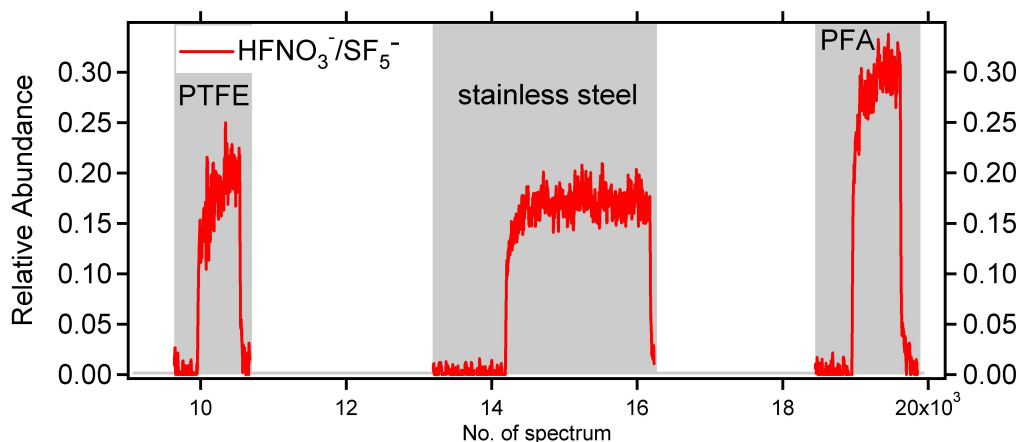


Figure 5.3: The relative abundance ratio of the nitric acid product ion signal to the educt ion signal was measured for three different flow tube coatings. PFA revealed an improved transmission by almost a factor of two compared to stainless steel tubing.

coating substances shown in Fig. 5.3 have been carried out in the laboratory. KF 40 tubes with two different coatings and one uncoated tube with a length of 25 cm were flanged upstream of the ion source, in front of the region where the air stream is mixed with the ion source gas flow. Comparison of a stainless steel flow tube with the PFA coating revealed an improved sensitivity for HNO_3 thus an improved transmission of approx. a factor of two. Comparison with a PTFE coating revealed a reduced transmission as compared to the PFA coating by approx. 30%. Therefore all metallic surfaces upstream of to the front electrode were coated with PFA.

The passive bypass flow configuration was inspired by former setups employed by MPI-K [Wohlfrom, 2000; Schneider et al., 1998]. It used a forward facing inlet with a diameter of 40 mm fabricated of stainless steel. Inside the aircraft the inlet was connected to a 40 mm stainless steel tubing covered with the described PFA coating. The sampling line extended from the top of the aircraft down to a bottom aperture with an exit for the main gas flow. Due to the back pressure drop inside the bypass tubing and the motion of the aircraft an average flow of $95 \text{ m/s} \pm 6 \text{ m/s}$ was obtained in the sampling line at around 10 km altitude. This caused a turbulent flow in the sampling line with Reynolds numbers of the order of 10^3 . The transmission for this sampling line was not measured because the large flow of the bypass would have diluted the gas standard flow to mole fractions below the detection limit.

At the height of the flow reactor a smaller sample gas flow was taken from the center of the air column with a 1/4" PFA tube. It was pumped across a pressure-control valve with an inner diameter of maximal 3/8" and, due to limited space, a reduced lateral extension. The flow, temperature and pressure parameters are given in Table 5.2.

setting	value
total flow	6.5 - 7.5 slm
N ₂ /Propane source gas	1.95 - 2 slm
600 ppmv SCF ₈ in N ₂	0.005 slm
pressure ion trap	$2 \cdot 10^{-5}$ hPa
pressure flow tube	40 hPa
temperature exhaust	309 K
residence time in the flow reactor	0.104 s
length of the reaction path	0.25 m
residence time in the bypass tubing (1/2")	~ 100 ms
bypass flow (at ~ 200 hPa)	95 ± 6 m/s (uncalibrated)
bypass temperature	238 - 263 K
residence time in the sampling line (at 200 hPa)	0.022 s

Table 5.2: Temperature, pressure and flow parameters in the sampling lines.

Ion source gas flow

A mixture of 1 % propane in N₂ and 600 ppmv SCF₈ in N₂ was flushed through the ion source. During laboratory tests a decrease in the background ion signal of mass 55 was observed. An explanation for this decrease may be the water vapor interference generating $\text{HFOH}^-(\text{H}_2\text{O})_n$ if traces of water are present in the flow tube. This reaction may be suppressed by reaction with propane scavenging particularly the OH radicals in the flow reactor. Pure propane is used for background sequences of ambient OH-measurements with CIMS [Berresheim et al., 2002] but pure propane is flammable and therefore not suited for aircraft missions.

A source gas flow of 1.95 - 2 slm allowed a sufficiently high educt ion concentrations, yet not too high for reduction of the sensitivity of the product ions due to dilution (see also chapter 2).

Pressure valve

The pressure in the flow tube was controlled by a two-way valve made of PFA, with a turning angle of 90° and a 1/2" NPT connection to a teflon tubing supplied by EM-Technik, Germany. A servo-motor with 170° turning angle was connected to the handle. The pressure signal was measured in the exhaust, upstream of the critical

orifice in front of the pump. A corresponding analog signal was sent to an USB-card (UE9- Labjack) which was connected to the computer, recording the digitized analog signals. The servo-motor was controlled using pulse-width-modulation. A signal of the actual position of the motor was sent to the USB-card. The pressure was fed into a simple proportional control taking the difference of the pressure set point and the measured pressure and multiplying it with a constant, then adding it to the actual position signal and sending it back to the motor. Thus a change of position was initiated according to sign and amplitude of the scaled pressure difference. The pressure sensor was a newly purchased pressure sensor (Bronkhorst) measuring between 0 and 100 hPa with an accuracy of 10 %. The variations of the pressure in the flow reactor were of the order of ± 1 hPa. These deviations originated mainly from the high inertia of the PFA-made valve, which needed an activation energy to overcome the internal friction. This resulted in an attenuated oscillation. Ion signals were monitored for these deviations from the set point and it affected the precision of the instrument only insignificantly. However, an improved valve in design and material would be desirable for future projects.

Background measurement

The propane/N₂ mixture used for the ion source gas flow was also used for background measurements. For this purpose the inlet and sampling line were flushed by an excess flow of the mixture of more than 7 slm. The configuration of the inlet system aimed at a minimal number of connecting pieces to avoid additional surface area for HNO₃ and HCl absorption and desorption. Milled PFA, as provided by most commercial distributors, always leaves a "sponge-like" surface that changes the transmission of the sampling line. Surfaces should ideally be treated with a liquid PFA solution that provides a smooth surface if used as a hot-melt adhesive.

As a consequence the nitrogen gas for background measurements was injected in front of the back-pressure valve using the same connection as the calibration flow. This caused occasionally problems if HNO₃, still present in the connecting PFA piece, was flushed into the sampling flow with the nitrogen flow. For future measurements a different setup is recommended.

Background measurements employing additionally a nylon filter during one flight were unsuccessful: the pressure drop over the small porous filter with a 1/4" connection was too high and caused a reduced and unstable pressure in the flow tube under UT/LS conditions.

Calibration

The flow diagram for the calibration is shown in Fig. 5.4. Calibration was performed with a modification of the so-called "suck-back-technique" [Neuman et al., 2000]. A three-way valve enabled two alternative flow directions for the calibration flow: In

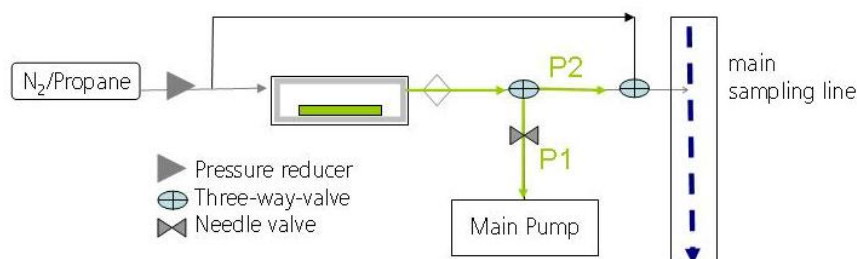


Figure 5.4: The schematic flow diagram of the calibration unit. The so-call suck-back-technique used continuous pumping (P2) of the calibration flow to maintain the passivation during non-calibration sequences. A short supply tubing into the sample flow guaranteed fast injection of the standard during calibration sequences (P1).

position 1 (P1), during non-calibration sequences, the calibration flow was guided into the exhaust line. During calibration sequences the three-way valve was turned to position 2 (P2) and thus injected HNO_3 into the sampling flow. Injection of nitrogen was blocked during atmospheric measurements and another three-way-valve was turned for background measurements. This way a constant flow through the calibration supply tubing which had approx. 1 m in length and had an 1/16" inner diameter was assured and thus a constant passivation guaranteed.

The actual "suck-back technique" uses a flow controller downstream of the teflon-tee, where the needle-valve is now placed. It is opened during atmospheric measurements measuring the diverted calibration flow that is pumped into the exhaust and it is closed to enable the small calibration flow entering the sampling flow.

Due to technical limitations, a needle - valve in front of the pump was used in this setup but proved to be difficult in handling. Pressure instabilities caused unstable pumping therefore this technique was only employed during the first flights.

The calibration mole fraction was chosen between 3.8 and 4.7 ppbv depending on the main gas flow. In the stratosphere these mole fractions are comparable to the atmospheric conditions. Under tropospheric conditions however a smaller calibration flow should be used. Due to time limits only a one-point calibration was employed.

5.3 Other instrumentation on the Falcon

Additional measurements of gas phase and particulate matter were hosted on the Falcon, measuring O_3 , CO, NO, NO_y and water vapor in the gas phase. These measurements were carried out by the Institute of Atmospheric Physics, DLR. Particle measurements comprised information on particle size distributions and number densities from particles with a diameters between 0.3 μm to several mm and particle composition, in particular the volume concentration of sulfate, nitrate, organics and

ammonia. The particle measurements were only used here to differentiate between plume and contrail-plume encounters and therefore will not be discussed in detail. For a detailed overview on the particle measurements see Voigt et al. [2010]. A frost point sensor was mounted on the aircraft for detection of water vapor. The instrument is explained in chapter 4.

Ozone was measured by means of an UV absorption photometer, measuring the absorption of O_3 at a wavelength 254 nm with a vacuum-photodiode [Brough et al., 2003]. The signal is amplified by electrometers. Two channels are used for comparison of the absorption of ozone-filtered air with the non-filtered atmospheric air according to Lambert-Beer's Law.

CO was measured by means of fluorescence detection [Brough et al., 2003]. The CO in the sampling gas is excited at a characteristic wavelength of 150 nm from a light source equipped with an argon purged optical filter system. The fluorescence is detected by a PMT at right angles to the excitation radiation. The instrument can be operated at less than 100 mbar and has been calibrated by a one-point calibration through injection of a standard. The time resolution is one second and response is linear between 0 and 1000 ppmv while the detection limit is smaller than 6 ppbv and the precision is 1.51 ppbv.

Chemiluminescence Detector

A main aspect of the campaign was the detection of NO and reactive nitrogen species NO_y ($NO_y = NO, NO_2, HONO, HNO_3, HO_2NO_2, 2N_2O_5, PAN...$) in aircraft exhaust plumes. The instrument was further used during laboratory comparisons with the ITCIMS and was deployed on the Falcon for simultaneous atmospheric measurements in the atmosphere.

The detection principle builds on the chemiluminescence technique [Fahey et al., 1985]: In the main reaction chamber NO is brought to reaction with an access of O_3 to form an excited NO_2 . Through emission of a photon the NO_2 returns to its ground state. The photon is detected by a photon-multiplier. Additionally NO_y can be measured simultaneously with NO through a second reaction chamber equipped with a gold converter. The catalytic reaction of NO_y to NO in the heated gold tube enables a simultaneous measurement at a time resolution of 1 s. The instrument was originally deployed by Feigl et al. [1999] on aircraft. A forward and backward facing inlet allows for the measurement of gas phase and particle NO_y concentrations. This technique has been employed to determine the nitric acid uptake in ice in contrails and cirrus clouds [Schäuble et al., 2009] [Voigt et al., 2006]. During the CONCERT campaign mainly gas phase NO_y and NO were measured through two backward facing inlets of the NO_y instrument [Ziereis et al., 2000, 2004]. The instrumental error

is 10 % and the detection limit for NO and NO_y is better than 1 pptv and 5 pptv. Aerosol particles with diameters < 1 μm containing trace amounts of reactive nitrogen may enter the backward facing inlets of the NO_y instrument [Feigl et al., 1999]. However at warm stratospheric conditions (T > 210 K) as encountered on 31 October 2008, model simulations [Voigt et al., 2007] indicate that the aerosol contribution of HNO₃ to the NO_y concentration is negligible.

Aerosol Mass Spectrometer

Particulate sulfate concentrations were measured with an Aerodyne Compact Time-of-Flight Aerosol Mass Spectrometer (AMS) coupled to a pressure controlled inlet (PCI) system operated by MPI-C. The AMS was deployed during the first part of the campaign and exchanged by optical particle measurements measuring the size and number of ice particles. Particulate matter is sampled through a critical orifice in front of an aerodynamic lens system which focuses the particles into a narrow beam. The aerosol is accelerated when entering the time of flight region in the vacuum recipient. At the end of this chamber the particles are flash-vaporized at approximately 600 °C and ionized by electron impact (70 eV) before the ions are extracted into a time-of-flight mass spectrometer. The instrument provides data on chemical composition and size distribution of sub-micron non-refractory aerosol particles. For further detail see Canagaratna et al. [2007] and references therein. Particulate sulfate data are reported in μg m⁻³ at standard conditions (STP). The detection limit for 10 sec average data as reported here is 0.05 and 0.03 μg m⁻³ for the two flights on 31 October 2008. The specific configuration of this AMS instrument, data analysis and results obtained during CONCERT are described in detail in Schmale et al. [2010].

Chapter 6

Measurements in the aged plume of volcano Kasatochi

This chapter provides an overview of the measurements made on 31 October 2008 during the CONCERT campaign in the aged plume of volcano Kasatochi. The timeline of the trace gas and particle measurements for both flights are presented together with the correlation analysis of these trace gases in the plume. The e-folding lifetime of SO₂, injected by the volcano during the eruption on 7/8 August 2008 in the stratosphere, is derived. Possible heterogeneous reactions taking place on volcanic sulfate particles are discussed.

The chapter starts with an overview on the scientific background of the topic.

6.1 Scientific background: SO₂, HCl and HNO₃ in volcanic stratospheric plumes

Explosive volcanic eruptions are the dominant source for sulfur in the stratosphere [Brasseur et al., 1999]. Despite their infrequent occurrence explosive eruptions have a profound influence on the earth's climate. Sulfurous gases injected into the stratosphere are mostly in the form of SO₂ and H₂S. There they are photochemically converted to gaseous sulfuric acid [Arnold and Fabian, 1980] which condenses to form sulfate particles on a time scale of weeks to months [Read et al., 1993]. The residence time for sulfate in the stratosphere may even be on the timescales of 1 to 2 years [Ansmann et al., 1996; WMO, 2006]. Thus the influence on the earth's radiative budget mainly depends on the injection, transformation and residence time of the sulfurous compounds in the stratosphere.

Stratospheric sulfate particles have diverse effects on the radiative budget: While absorption and emission of terrestrial near infra-red and long-wave radiation cause a local heating with a temperature increase in the stratosphere, the direct aerosol effect of sulfate particles leads to a surface cooling [Dutton and Christy, 1992].

Sulfate particles increase cloud reflectivity and cloud lifetimes. Downward transport

of these particles induces cloud formation, thus a change in optical properties of the clouds due to an increase in the number of droplets and a reduction in size. As a consequence the precipitation is reduced and the cloud water content and lifetime of clouds are increased. This is called the indirect radiative effect. Both the direct radiative effect and indirect radiative effects of sulfate aerosol contribute to a cooling of the earth's surface and can partly off-set anthropogenic greenhouse warming.

Sulfurous gases emitted by volcanos are mostly in the form of SO_2 and H_2S . H_2S is rapidly oxidized to SO_2 . The average annual emission of sulfur into the atmosphere (in the form of SO_2) by volcanos were 7.5 to 10.5 Tg, which comprises 7.5 to 10.5 % of the total annual sulfur emissions [Halmer et al., 2002] and only 10 to 15 % of the anthropogenic emission. Explosive volcanic eruptions contribute 60 % of the total sulfur emission while the rest is covered by quiescent degassing of volcanoes. SO_2 undergoes fast photochemical conversion to sulfuric acid within approx. 1 week in the troposphere. Furthermore in contrast to the stratospheric residence time, sulfate particles are rapidly removed through wash-out within approx. 2 weeks in the troposphere. Thus the fate of volcanic sulfate particles and their precursor gas SO_2 depends mainly on where they are injected in the atmosphere. Regarding the radiative effects of volcanic sulfur emissions their contribution is much higher compared to anthropogenic emissions because they are predominantly injected into the upper troposphere [Graf et al., 1997]. Their removal processes are not as effective as in the boundary layer where most anthropogenic sources are located.

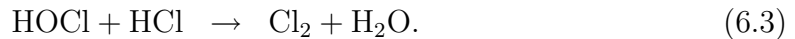
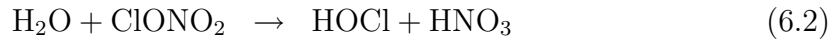
In addition to the influence on the radiative budget heterogeneous reactions taking place on sulfate aerosol change the composition of the stratospheric trace gas distribution, particularly the ozone budget.

Ozone in the stratosphere serves as an absorber of ultraviolet radiation thus enabling life on earth. With a maximum concentration at 15 to 30 km, the ozone layer determines the temperature gradient in the stratosphere through absorption of UV radiation by ozone and emission of IR radiation. Ozone is produced in the upper stratosphere by photolysis of O_2 according to the Chapman-Cycle. Additionally a number of catalytic cycles involving NO_x (NO_2 , NO), HO_x (OH , HO_2) and Cl_x (ClO , Cl) species are needed to explain the observed ozone profile in the stratosphere. Most of the chlorine in the stratosphere is bound in the reservoir species hydrogen chloride (HCl) and chlorine nitrate (ClONO_2) which are formed by reaction of Cl_x with methane (CH_4) and NO_2 in the gas phase or heterogeneous reactions.

After major volcanic eruptions local ozone depletion of up to 30 % was observed at altitudes with enhanced aerosol loadings [Hofmann et al., 1994; Ansmann et al., 1996]. Furthermore local temperature increases of up to 1.5 K in the stratosphere were observed due to enhanced absorption by the aerosol layer. Ozone depletion was attributed to heterogeneous activation of halogens. Particularly the activation of chlorine reservoir gases such as ClONO_2 and HCl is enhanced in the presence of liquid sulfate particles [Solomon, 1999]. Activated chlorine participates in catalytic ozone destruction. Reduction in ozone leads to reduced absorption of UV radiation,

thus energy is lost for stratospheric heating. The net effect however is a temperature increase in the stratosphere.

HCl, HNO₃ and O₃ abundances in the stratosphere are closely linked since they are produced at similar altitudes in the stratosphere, have long lifetimes and underly similar transport mechanisms [Plumb and Ko, 1992]. The main sources for HCl are anthropogenetic chlorofluorocarbons emitted on the ground. They reach the stratosphere unaffected where they are photochemically destroyed to form chlorine reservoir gases [Molina and Rowland, 1974]. The increase of chlorine in the stratosphere caused a decline in ozone column densities particularly in the Arctic and Antarctic spring. The discovery of heterogeneous reaction on polar stratospheric clouds (PSC) explained the fast ozone depletion [WMO, 2006] [Crutzen and Arnold, 1986]. Activation of chlorine on sulfate particles is however not restricted to particularly cold temperatures that are only encountered during polar winters. Activated chlorine forms mainly through heterogeneous reactions on the sulfate aerosol



All reaction rates depend on the composition (water content, acidity) and phase of the particles (solid or liquid) [Voigt et al., 2000][Schreiner et al., 1999] and on the environmental conditions (temperature, concentration). Formation of PSCs has been observed in explosive volcanic eruptions transporting HNO₃ and H₂O into the cold UT/LS [Rose et al., 2006]. There they may trigger fast ozone depletion.

A shift within the nitrogen oxide budget from NO_x to HNO₃ occurs via enhanced N₂O₅ hydrolysis. N₂O₅ is formed via the intermediate product NO₃ by the reaction of NO₂ and O₃. Additionally to photolytic destruction N₂O₅ reacts heterogeneously to form nitric acid:



The effect was demonstrated by the detection of a marked increase of HNO₃ in the aged stratospheric plume of the 1982 Mt El Chichón eruption at 25 to 26 km altitude [Arnold et al., 1990]. The uptake of HNO₃ on particles that sediment to lower altitudes is termed denitrification. Nitric acid condenses on particles at temperatures close to the frost point and is efficiently removed from the stratosphere in the particulate phase by sedimentation. The above described effects therefore lead to a total decline of nitrogen oxides in the stratosphere as well as a shift within the budget of reactive nitrogen species (NO_y). A reduction in NO₂ and therefore NO in the stratosphere results in a less efficient deactivation of reactive chlorine.

An illustrative overview on the effects of explosive volcanic activity is given in Fig. 6.1 taken from McCormick et al. [1995].

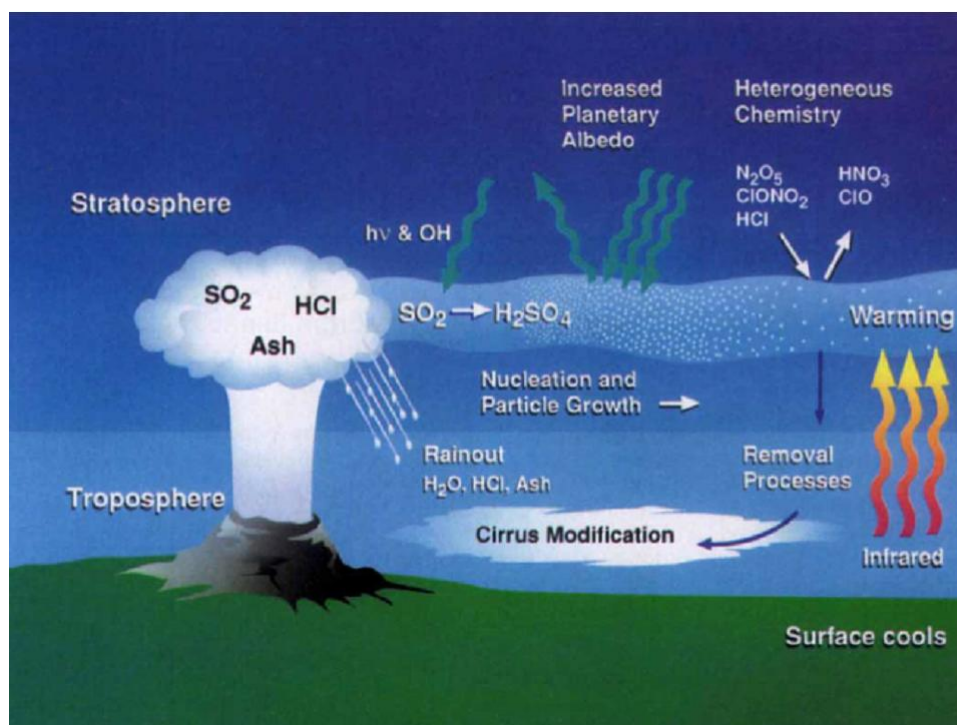


Figure 6.1: The emission of SO_2 , HCl and ash from volcanos and their effects on the atmosphere (from McCormick et al. [1995]).

Additionally ashes are a main emission product from volcanoes. It does not have a global effect on the climate due to fast removal (hours to weeks) from the atmosphere. However the local hazards for people and bio-systems cause many damages. Explosive volcanic eruptions transport particles into the regions where air traffic can be endangered. Ashes provide additional surface for condensation of water and acids and if coated with water they aggregate with hydrometeors of the environment, forming large particles [Textor et al., 2003].

Among explosive eruptions in the 20th century influencing the sulfur budget Mt. Pinatubo and El Chichón had the strongest impact on the earth's climate and due to many observations the biggest impact on scientific understanding of volcanic influences on the climate. Mt. Pinatubo erupted in the Philippines (15°N , 120°E) on 14./15. June 1991 and injected between 15 to 20 Mt SO_2 into the stratosphere. El Chichón located in Mexico (17°N , 93°W) erupted in March 1982 injecting 7-10 Mt SO_2 into the stratosphere. Both eruptions represent low latitude eruptions corresponding to a high tropopause altitude and a slow transport of volcanic emissions from the tropics into polar regions. Thus their influence on the arctic ozone-depleting mechanisms involving polar stratospheric clouds (PSCs) is limited. However due to an equator-near eruption the plumes got rapidly distributed over both hemispheres. For Mt. Pinatubo the injection height was between 20 and 27 km in altitudes where

the ozone concentration peaked [McCormick et al., 1995]. As a consequence the temperature change in the stratosphere caused vertical motion and lifting of the aerosol layer. Mean annual tropospheric temperatures declined by 0.4 K during the year 1992 and 0.25 K in 1993.

This sulfur cooling effect of volcanic eruptions has led to the idea of climate engineering by injecting anthropogenic sulfur into the stratosphere [Crutzen, 2006; Caldeira and Wood, 2008]. The idea is to continuously deploy 1 to 2 Tg of sulfur per year into the stratosphere to enhance the global albedo and counteract the anthropogenic greenhouse effect. However, the effects of such climate engineering are complex. Tilmes et al. [2009] modeled the atmospheric influence of an annual sulfur injection of 2 Tg between 2020 and 2050. According to their study, this causes a delay in global warming of 40 years, but at the same time a potential of ozone depletion at higher latitudes due to enhanced heterogeneous reactions. Additionally their models show an increase in precipitation rates and discuss unforeseen effects on the biosphere and ecosystems.

A yet open question on volcanic emissions is the injection of chlorine into the stratosphere. Besides gaseous SO₂, H₂S and the two most important gases H₂O and CO₂, high mass loadings of HCl are emitted by volcanos. The annual emission of HCl from volcanos is 0.4 to 11 Tg and it comprises up to 10 % of the total emitted mass of an eruption [von Glasow et al., 2009]. The suggested amount of HCl reaching the stratosphere is at present 0.1 to 12 Gg per year [Halmer et al., 2002]. The estimate is based on an emission ratio of HCl and SO₂ and presumed massive wash-out effects for HCl (99.99%) with no direct measurements.

While no or only a small enhancement of HCl after the Mt. Pinatubo eruption was observed in the stratosphere [Mankin et al., 1992], significantly increase of up to 40 % of the HCl column density were observed after the El Chichón eruption [Mankin and Coffey, 1984]. Airborne mass spectrometric measurements of gaseous SO₂ and HCl in the young eruption plume (35 h) of Mt. Hekla in February 2000 showed an increased HCl mole fraction of up to 80 ppbv above the background at an altitude of 11.3 km [Hunton et al., 2005]. Ozone depletion partly connected with chlorine activation was observed in the young plume [Rose et al., 2006]. Satellite measurements made by the Microwave Limb Sounder (MLS) reported of an HCl cloud at 20 km after the eruption of Soufrière Hills in May 2006 [Prata and Bernardo, 2007]. Observations of halite particles sampled during airborne measurements in the El Chichón eruption cloud in the lower stratosphere assumed a mechanism involving H₂SO₄ for secondary HCl production [Woods et al., 1985]. The process evolves on a timescale of 1 to 3 months indicated by the absence of Na₂SO₄ traces in the samples three months after the eruption. This was used as an explanation for the delayed HCl enhancement [Mankin and Coffey, 1984]. The halite particles originate either from crustal material and magma of the volcano or from sea salt entrainment.

Michelangeli et al. [1991] questioned the effectiveness of the process due to a limited amount of H_2SO_4 in the young volcanic plume but they discussed additional mechanism involving HNO_3 , NO_2 , ClONO_2 , N_2O_5 . However, in contrast to sulfuric acid, the vapor pressure of nitric acid is too high to condense at most stratospheric temperatures ($T > 210 \text{ K}$) typical for the latitudes and seasons of the eruption sides. The dynamic and chemical evolution in the eruption plume, and thus the underlying transport mechanism into the stratosphere, depends on many factors like the eruption type and duration, ambient conditions, and the composition of the magma [Textor et al., 2003]. The injection height is of critical importance for climate issues and was recently addressed by the use of the Flexpart dispersion model in combination with satellite measurements [Kristiansen, 2009; Rix et al., 2009].

Direct injection of HCl depends mainly on the scavenging thus on composition and phase of the particles in the eruption plume. Tabazadeh and Turco [1993] argue that HCl removal occurs through dissolution in the liquid supercooled water droplets which do not reach the stratosphere due to fast rain out. Model simulations of these authors indicate that less than 1 % of the released primary HCl may reach the stratosphere. Textor et al. [2003] argued based on model simulations, that the main parameter controlling the scavenging is the availability of water, in liquid or solid form, thus it can be very different for different eruption sites. They included ice scavenging through trapping of HCl and SO_2 on growing ice particles in their model. Depending on the type of eruption and the meteorological situation (stability, humidity and wind) a significant amount of up to 25 % of the initially emitted HCl may reach the stratosphere if incorporated in ice particles that form in the eruption column, and that are lifted into these altitudes. In the stratosphere they may contribute to ozone destruction depending on the fate of the ice particles. A smaller fraction of supercooled water droplets compared to the model of Tabazadeh and Turco [1993] due to lower temperatures at the top of the eruption column reduced the liquid water scavenging in their model. Lacking evidence from simultaneous reliable trace gas measurements in the stratosphere and near the volcano on the ground, the question how much HCl reaches the stratosphere is under debate.

Direct emission of reactive chlorine have been observed in the troposphere by Bobrowski et al. [2007] using DOAS. Slant column densities of BrO and SO_2 were measured in the tropospheric plumes of degassing volcanos with a ratio of the order of 10^{-4} . With growing distance to the crater the BrO/SO_2 ratio increases, suggesting BrO production. The observation of OCIO in the plume suggests the presences of ClO , which is about 20 times less abundant than SO_2 . Both bromine and chlorine influence ozone if ambient entrainment into the eruption plume occurs. The initial ozone-poor eruption column is only slightly affected. The halogen chemistry in the troposphere is however distinct from the stratospheric chemistry due to faster removal processes and different trace gas abundances.

6.2 Volcanic eruptions in July and August 2008

In summer 2008 several explosive volcanic eruptions took place at high northern latitudes (52 to 53°N) on islands in the Aleutian chain. Mt. Okmok erupted on 12 July 2008 and injected about 0.2 Mt SO₂ into the atmosphere. Mt. Kasatochi erupted three times on 7/8 August 2008 and injected about 1.5 Mt SO₂ into the atmosphere as detected by the Ozone Monitoring Instrument (OMI) on NASA's Aura satellite [Carn et al., 2008]. Compared to Okmok, Kasatochi produced a much stronger eruption. Other satellite based sensors like GOME-2 on MetOp-A monitored the eruption on 8 August and followed the global propagation of the plume [Rix et al., 2009]. The instrument is a UV/visible nadir-looking spectrometer that measures the solar radiation backscattered from the atmosphere in the 240 - 790 nm wavelength band. SO₂ total column densities were inferred using the DOAS (Differential Optical Absorption Spectroscopy) measurement principle [Platt, 1994] and measured peak values of 150 Dobson Units (DU). A comparison of the two satellite measurements approx. two weeks after the eruption is shown in Fig. 6.2. By then the plume had dispersed over the northern hemisphere. A week after the eruption the GOME-2 measurements coincided with airborne measurements of another DOAS instrument deployed on the CARIBIC (Civil Aircraft for Regular Investigation of the atmosphere Based on an Instrument Container). The measurements are reported in Heue et al. [2010] and showed good agreement with some deviation in the wind speed needed for correction of the advection of the plume during two overpass times. Aerosol filter probes were additionally collected by the CARIBIC container and showed an enhancements of sulfate up to four months after the eruption [Martinsson et al., 2009]. A measure of enhanced sulfate in the stratosphere is the ratio of sulfate to ozone. Background values for this ratio before the eruption showed average values of 0.34 ng/(m³ ppbv), and peak values of 3.4 ng/(m³ ppbv) shortly after the eruption. In October 2008 the ratio had not declined to background values but leveled out at 1.05 ng/(m³ ppbv) [Schmale et al., 2010]. Although the Kasatochi SO₂ injection relatively small compared to SO₂ injections of the previous major explosive eruptions of tropical volcanoes, the SO₂ and aerosol layer was rapidly distributed over the northern hemisphere due to strong mid-latitudinal winds. Arriving approx. on 14 August over Germany the aerosol layer was measured by many ground based remote sensing instruments [Schmale et al., 2010; Kristiansen, 2009; Steinbrecht et al., 2008] during August and September.

Additionally to the SO₂ plume, BrO was measured after the eruption of Mt. Kasatochi by GOME-2 [Theys et al., 2009]. Based on these measurements the estimated emission height of 8 to 12 km was calculated using additionally FLEXPART backward trajectories. The total mass of reactive bromine was estimated to be between 50 and 120 tons.

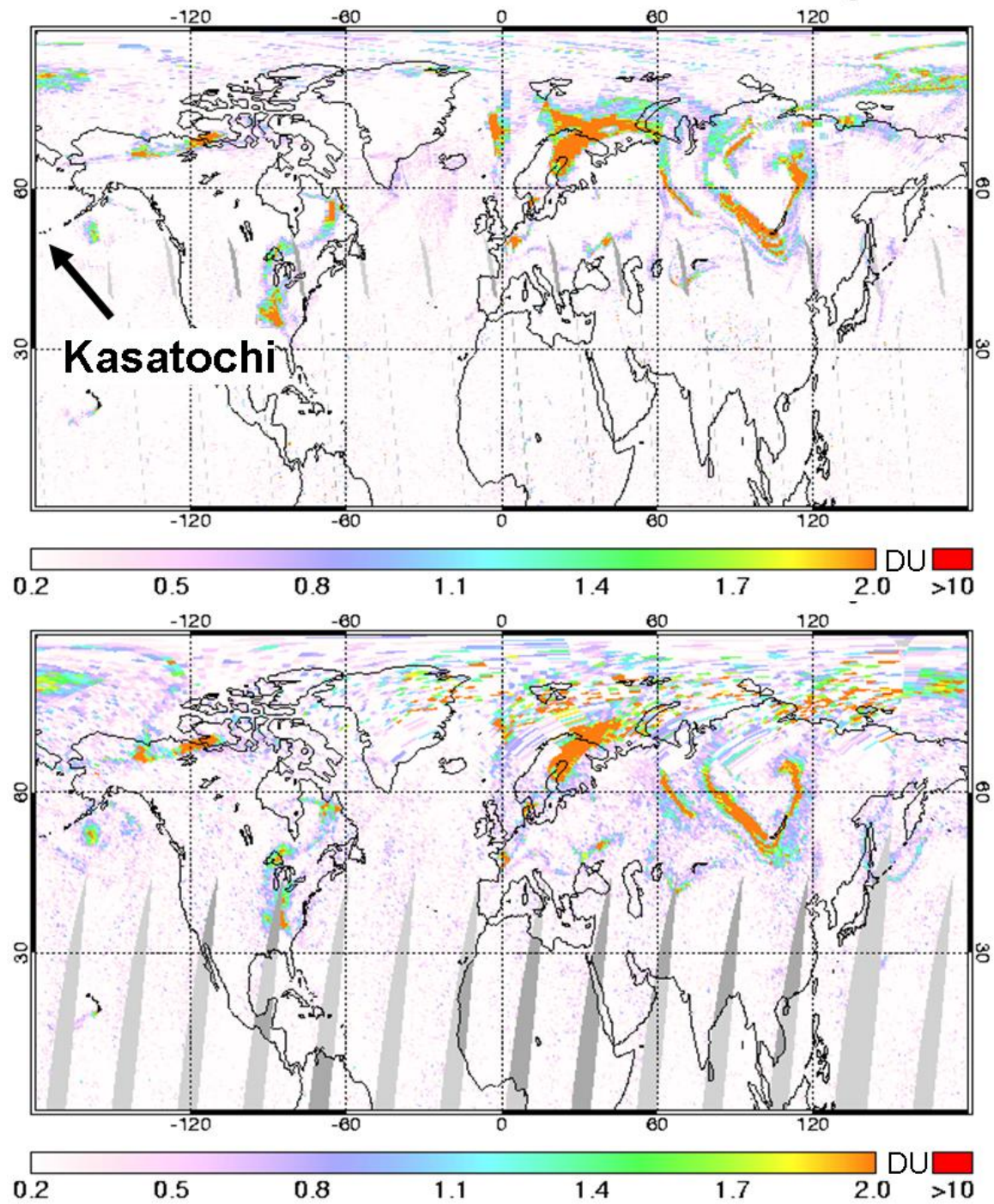


Figure 6.2: The column densities (in DU) of SO₂ on 22 August 2008 as observed by the two satellite SO₂ instruments OMI (upper panel) and GOME-2 (lower panel) approx. 2 weeks after the eruption. (graphs provided by "Support to Aviation Control Service" (<http://sacs.aeronomie.be/cases/kasatochi2.php>)). The grey shaded area was not measured by the instrument.

6.3 Measurements during the CONCERT-Chemistry campaign

The CONCERT (CONtrail and Cirrus ExpeRiment) campaign took place in October and November 2008 over Western Europe. The main aim of the CONCERT campaign was to provide in-situ observations of chemical and micro-physical particle properties as well as trace gas distributions in the mid-latitude tropopause region. Ozone trends influenced by aircraft emissions, heterogeneous reactions on cirrus clouds and troposphere-stratosphere exchange mechanisms were of particular interest. In the first part of the campaign the stratosphere was encountered during 4 flights. In total 10 flights were performed with a set of instruments deployed on the DLR research aircraft Falcon described in chapter 5. During the second part of the campaign the AMS, measuring particle composition was exchanged by particle measurements measuring the size distributions and number densities of contrail and cirrus particles.

A special focus is set on the flights on 31 October 2008. A repeating pattern of enhanced sulfate and SO₂ layers above the tropopause led to the conclusion of a broader structure that was unlikely produced by recent anthropogenic ground based emissions.

6.4 Meteorological situation on 31 October 2008

The meteorological situation encountered on 31 October 2008 was ideal for measurements in the lower stratosphere: An extended tropopause fold shaped like a tongue formed over Western Europe with particularly large tropopause pressures (up to 400 hPa, corresponding to tropopause heights as low as about 5000 m). Arctic stratospheric air had intruded to lower latitudes transporting ozone-rich, cold air into mid-latitudes. Fig. 6.3 shows the tropopause fold along with the flight tracks of the aircraft and the corresponding tropopause pressures.

The feature built up within three days prior to the measurement and extended from Scandinavia to Portugal. Also shown are the flight tracks of the two missions on 31 October 2008 with the atmospheric pressure at flight level color coded. Mission A with take off at Oberpfaffenhofen, close to Munich (Germany), and landing at Shannon (Ireland) and mission B (return flight) traversed the tongue-shaped region while cruising in the lower stratosphere, mostly at altitudes between 11000 and 11600 m (mission A) and between 9000 and 11300 m (mission B). Additionally the ozone column-density measured by the OMI-instrument on 31 October revealed the distinct feature, coinciding with the low tropopause pressures. Ozone transported from higher latitudes was enhanced up to 350 DU. O₃ was also measured in-situ onboard the Falcon in the lower stratosphere (Panel d), with clear indication that the tongue shaped feature was encounter during measurements on the 31 October.

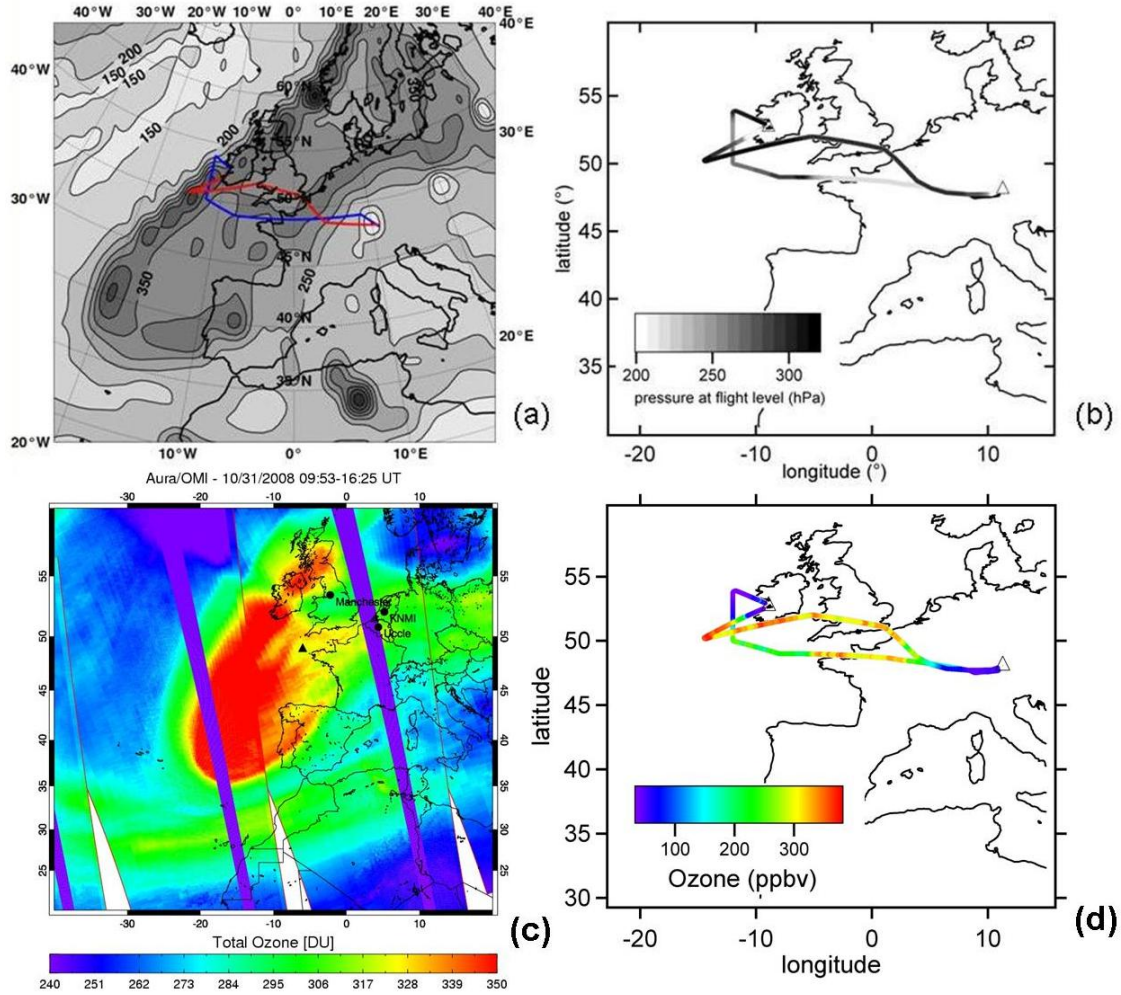


Figure 6.3: (a) Contour plot of the pressure at tropopause height. A tongue-shaped region with strong tropopause-pressure gradients at the edges formed. (b) Flight path of the two flights performed on 31 October with stop-over in Shannon, Ireland. (c) Ozone column densities on 31 October measured by OMI. (d) Same as panel (b) with the ozone mole fraction color-coded.

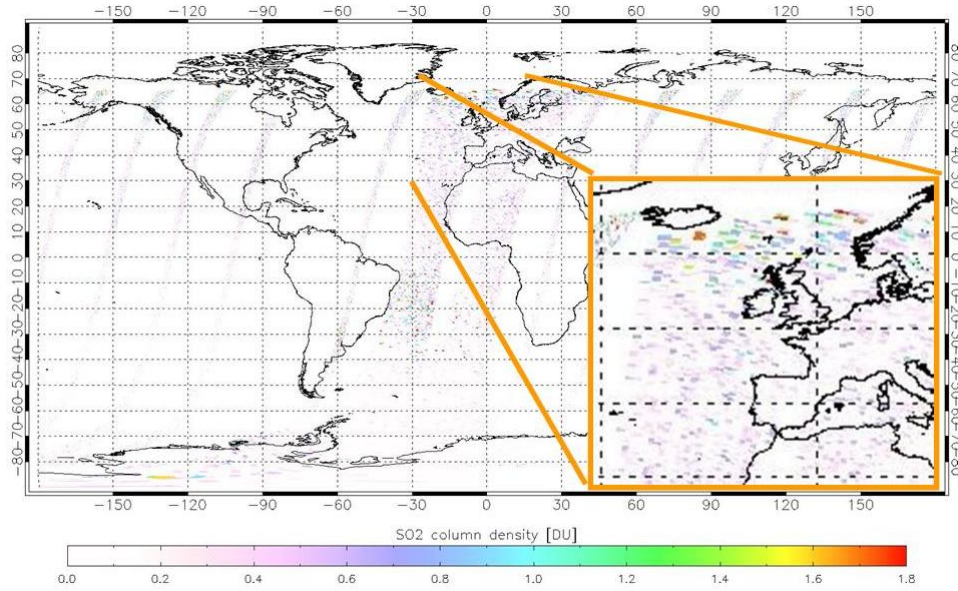


Figure 6.4: The column densities of SO_2 on 30 October 2008 as observed by the SO_2 instrument GOME-2

In Fig. 6.4 the SO_2 column density measured by GOME-2 and processed by the German Remote Sensing Data Center (DFD) [Rix et al., 2009] one day prior to the measurement is shown. North of the measurement area enhanced SO_2 is detected with a very patchy pattern. Due to a test mode run, only data with a low spatial resolution and poor coverage are available. However dilution and aging of the plume resulted in SO_2 column densities below the detection limit of the GOME-2 instrument.

6.5 CIMS measurements on 31 October 2008

Negative ion mass spectra obtained inside the plume around 9500 m altitude (14:57 UTC) and segments of that spectrum are shown in Fig. 6.5. Besides the dehydrated reagent ion SF_5^- (m/z 127), two major product ion species FHNO_3^- (82) and FSO_2^- (83) are present. NO_3^- dominates the spectrum partly as a fragment of FHNO_3^- . The lower panel shows a segment (m/z 54 to 58) of the same mass spectrum together with a background measurement during the flight. Here the HCl product ions FHCl^- (m/z 55 and 57) are clearly elevated above the background. The abundance ratio of the ions 55 and 57 is 2.8, which is within the measurement errors consistent with the terrestrial abundance ratio of the corresponding chlorine atoms ($^{35}\text{Cl}/^{37}\text{Cl} = 3.13$). The discrepancy may be due to an additional ion species appearing at m/z 57. The detection limits (1σ of the background signal) for this flight were 18 pptv for SO_2 (for a running mean over 10 spectra) and 22 pptv for HCl , and 36 pptv for HNO_3 (both with a running mean over 20 spectra).

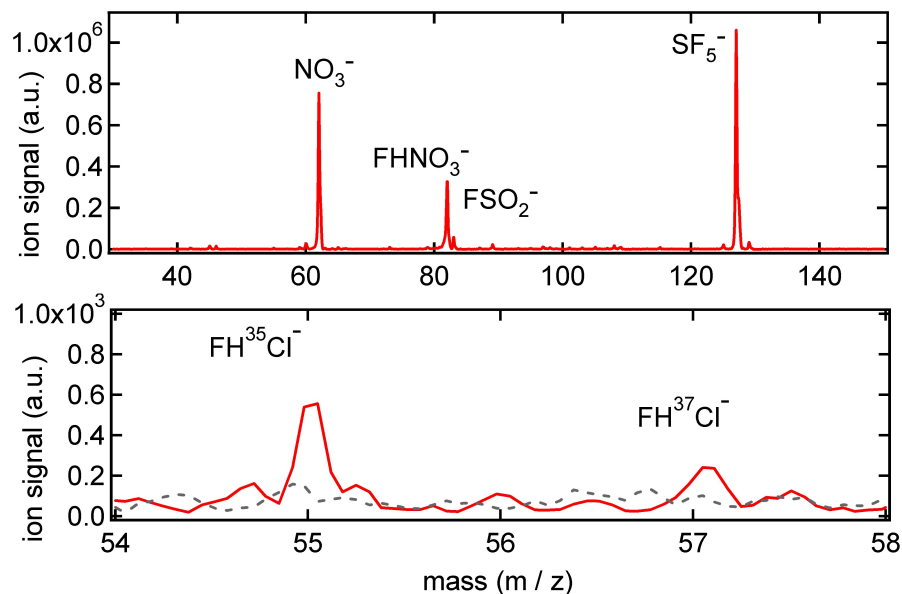


Figure 6.5: The negative ion mass spectrum inside the plume of Mt. Kasatochi (upper panel) and a segment of the spectrum (lower panel). The spectrum was averaged over 10 spectra with a time resolution of 1.6 s. No corrections for the mass discrimination has been applied.

6.6 Time sequences and altitude profiles

On 31 October 2008 during flight B, the Falcon cruised for an extended period of time (more than 2 h) in the lower stratosphere, as indicated by the dynamical tropopause altitude (grey line) derived from European Center of Medium Weather Forecast (ECMWF) analysis shown in Fig. 6.6 b. The vertical cross sections of the temperature (color coded) along the flight path together with the potential temperature (theta) isotherms (black line) mirrors a cut through the tongue-shaped region. In the lower stratosphere, an extended layer with increased SO_2 was observed as shown in Fig. 6.6 a. SO_2 was almost exclusively enhanced above the background when the aircraft reached altitudes above the 2 PVU (potential vorticity unit) iso-surface. Filaments of this stratospheric intrusion reached down to 5000 m above the ground, transporting stratospheric air to low altitudes. Around 14:10 UTC the Falcon entered the stratosphere. Here the theta isotherms crossed the dynamical tropopause, allowing transport and mixing of tropospheric and stratospheric air. A similar transport occurred at the western side of the fold where the Falcon left the stratosphere and again the isotherms crossed the dynamical tropopause. A temperature increase of 5 K was observed inside the plume as compared to outside plume conditions but could not be directly explained by absorption of radiation of the layer [Schmale et al., 2010]

The time sequences of SO_2 , HCl, and HNO_3 obtained by the ITCIMS instrument

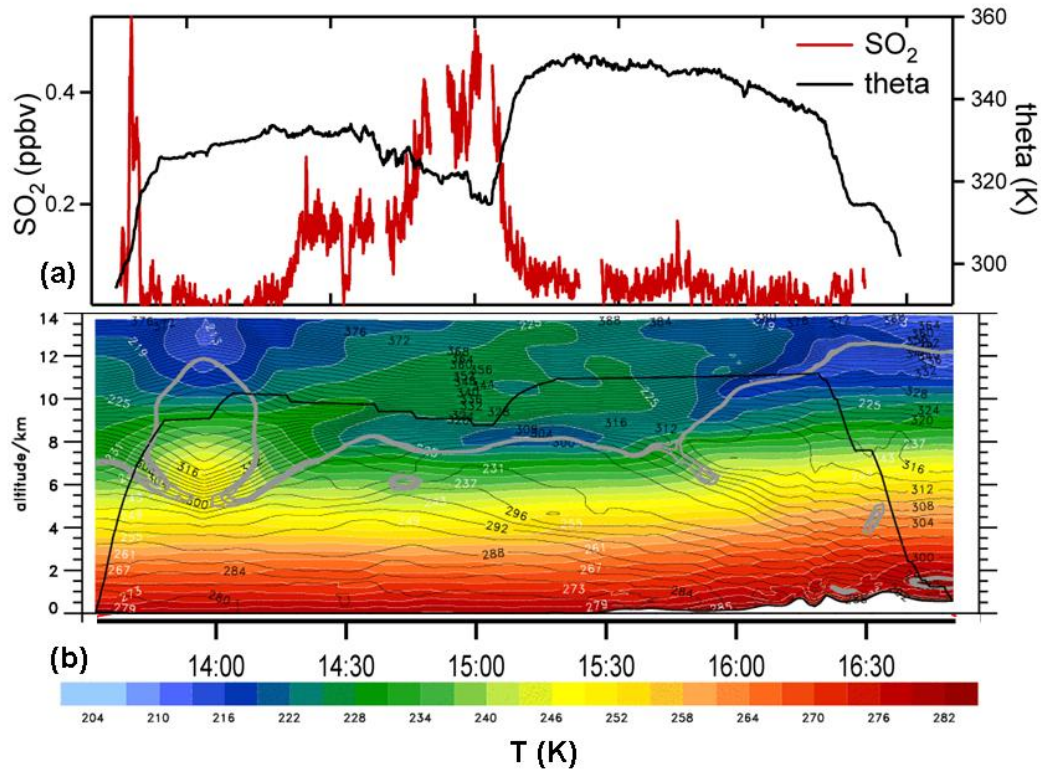


Figure 6.6: Time sequence of SO_2 mole fractions together with the potential temperature measured onboard the aircraft during flight B. The meteorological data were provided by the European Center of Medium Weather Forecast (ECMWF). (b): Flight altitude and temperature profile along the flight track (color coded) and potential temperature isotherms (black lines). The grey lines represent the height of the dynamical tropopause (given in 2, 3, and 4 potential vorticity units).

aboard the Falcon during the flight A and B are shown in Fig. 6.7. Also given are 10 s averages of the particulate sulfate concentrations, volume mixing ratios of O_3 , NO, NO_y and CO (all 1s time resolution) measured aboard the Falcon, the flight altitude and theta along the flight track. Gaps in the time sequence appear where calibration or background measurements were performed. The ITCIMS data are smoothed with a running mean over 10 spectra (30 spectra for HCl). The scatter in the HCl data are due to instrumental counting statistics near the detection limit. In the following paragraph flight B will be discussed in detail as the plume was most clearly observed during that flight. The aircraft cruised mostly between 9100 and 11600 m altitude and has spent considerable time (about 14:10 - 16:25 UTC) inside a plume with increased SO_2 mole fractions and enhanced sulfate. The measured SO_2 reached peak values of up to 0.51 ppbv. Background SO_2 ranged from the detection limit to approx. 0.05 ppbv. While HCl varied between values below the detection limit (0.044 ppbv, 2σ) to 0.32 ppbv throughout the whole flight, inside the plume HCl ranged from 0.065 ppbv to 0.32 ppbv. CO varies between 38 and 52 ppbv inside the plume with an average of 44.5 ppbv. Ozone showed peak values of 361 ppbv with an average of 259 ppbv in the stratospheric segment. The time sequences indicate a strong correlation between the measured HCl and O_3 mole fractions. Nitric oxide stays below 0.2 ppbv with the exception of pronounced spikes indicating occasional penetrations of aircraft exhaust plumes. NO_y stays between 1 and 2 ppbv in the stratosphere and is markedly enhanced during aircraft exhaust plume encounters. Nitric acid shows similar features as NO_y except for the aircraft plume penetrations, which is expected as aircraft emit only very little HNO_3 .

In the stratosphere, an average HNO_3/NO_y ratio of 0.78 ± 0.1 was observed for ozone concentrations > 100 ppbv, which is consistent with previous measurements in the lower stratosphere, not influenced by recent volcanic eruptions [Schneider et al., 1999; Neuman et al., 2001]. SO_2 and particulate sulfate reveal similar features during the two flights indicating a well mixed layer.

Fig. 6.8 shows the altitude profiles of SO_2 , HCl and HNO_3 along with O_3 , CO mole fractions and the temperature measured onboard the Falcon. The SO_2 layer was present at altitudes between 7000 and 11600 m, peaking at 9000 m (0.51 ppbv). A second SO_2 -rich layer was present at lower altitudes extending between about 6400 and 7000 m altitude.

6.7 Location of the air mass with respect to the tropopause

In contrast to the broad feature of the SO_2 and particulate sulfate enhancements in the stratospheric tongue with a horizontal extension of more than 440 km, the Falcon flew through another layer with increased SO_2 (up to 0.535 ppbv) during the

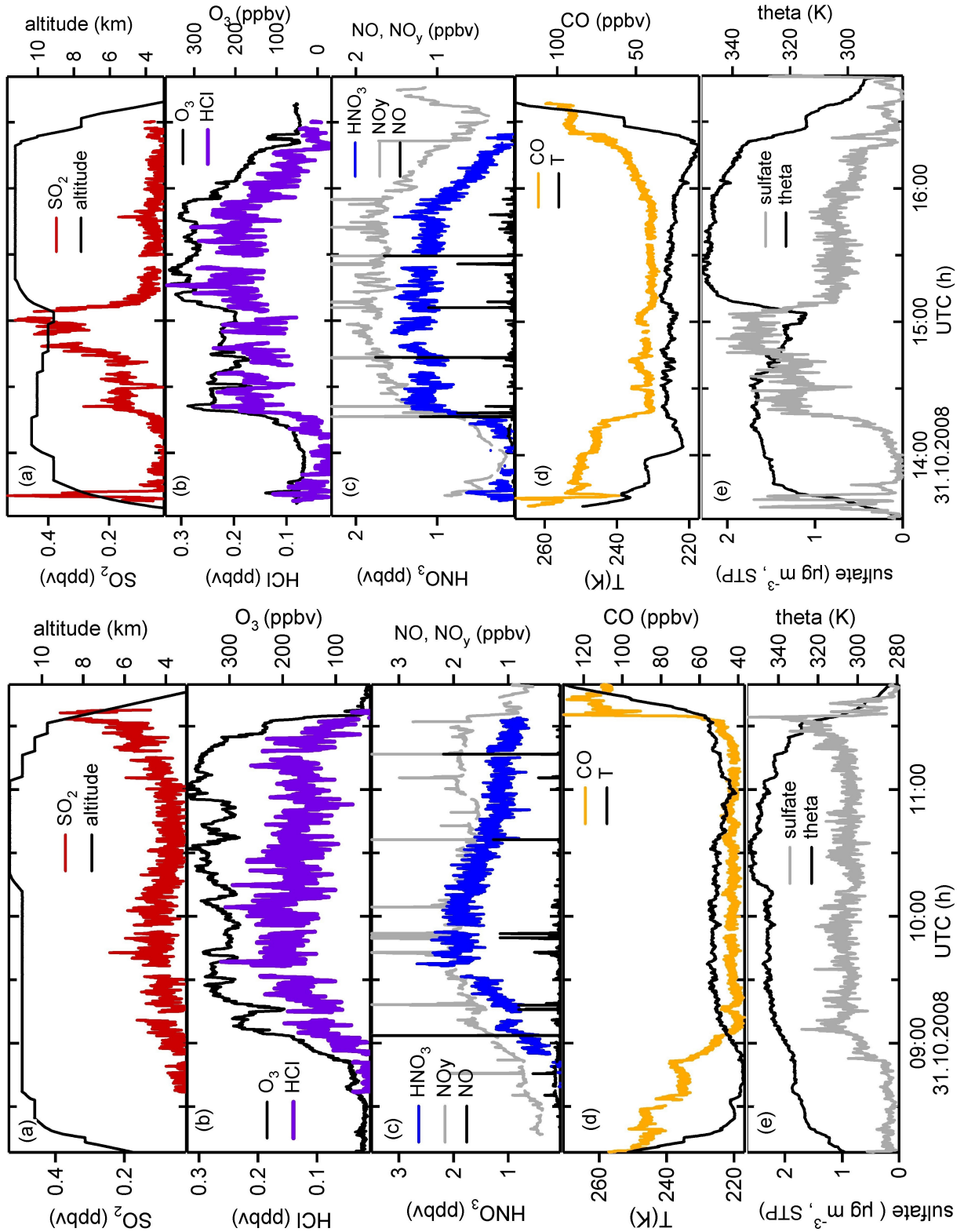


Figure 6.7: Time sequences of SO_2 , HCl , and HNO_3 mole fractions obtained by the ITCIMS instrument aboard the Falcon during flight A and B on 31 October 2008. Also given are particulate sulfate (STP) concentrations, O_3 , NO , NO_y and CO mole fractions as well as the flight altitude of the aircraft and the potential temperature.

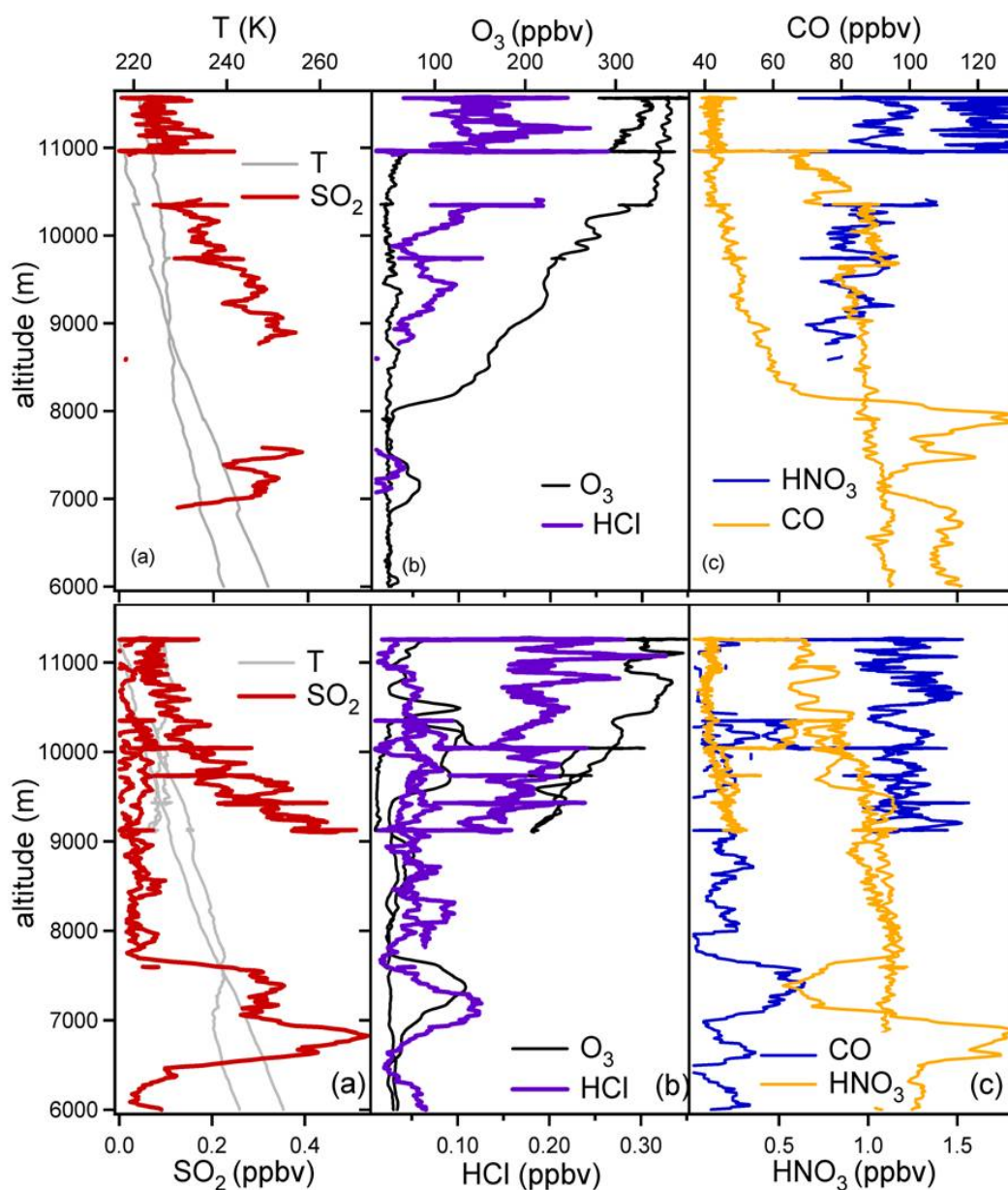


Figure 6.8: Altitude profiles of SO_2 , HCl and HNO_3 along with O_3 , CO and the temperature for flight A (upper panel) and B (lower panel).

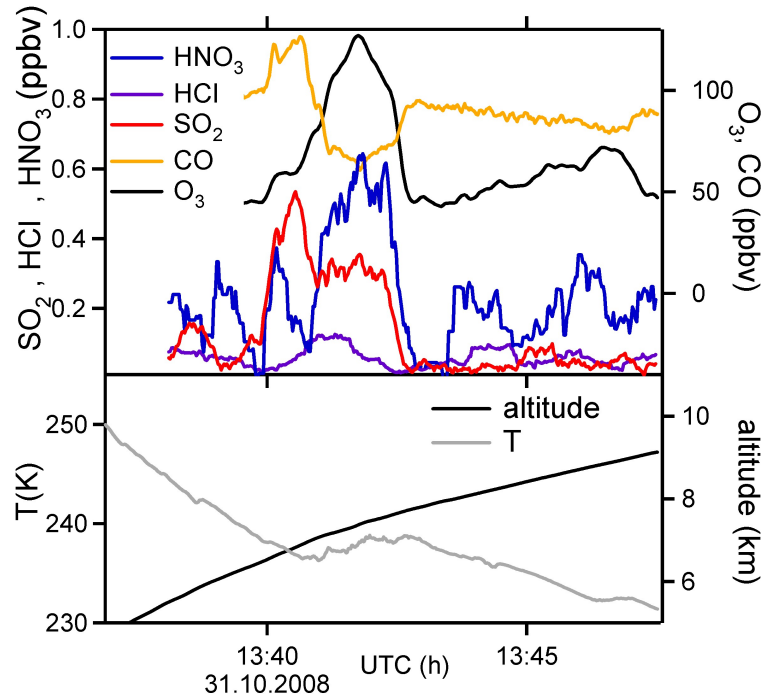


Figure 6.9: Blow up of the segment of Fig. 6.7, which contains the two SO_2 -rich air masses of different origin observed during ascent. HCl , HNO_3 and SO_2 together with O_3 , CO , T and the altitude are plotted versus time.

initial ascent from Shannon at 13:40 UTC (around 7000 m altitude) which is shown in more detail in Fig. 6.9. Two differently composed air masses both containing increased SO_2 and particulate sulfate were observed, the lower one between 13:40 and 13:41 UTC with enhanced CO but O_3 below 100 ppbv thus revealing tropospheric character. Between 13:41 and 13:42 UTC, an SO_2 layer with reduced CO but increased HCl (up to 0.05 ppbv) and O_3 up to 125 ppbv was penetrated, showing a stratospheric character. The stratospheric marker HCl implies that this air mass has been mixed downward from higher altitudes transporting ozone into the tropopause region. The upper tropospheric SO_2 layer may be of volcanic or anthropogenic origin.

An illustrative way of categorizing the two different air masses can be achieved by tracer-tracer correlations of O_3 and CO (Fig. 6.10) [Pan et al., 2004]. CO has mainly tropospheric sources such as anthropogenic combustion processes and biomass burning. Correlation with ozone as a stratospheric traces gives information on the location of the air mass with respect to the tropopause. SO_2 -rich air-masses were encountered in both regimes on the stratospheric and tropospheric branch. However in the transition region no enhancement of SO_2 was detected, thus no connection through mixing of the two air masses can be observed. The SO_2 found in the green marked area is of tropospheric origin, the SO_2 in the grey marked area of stratospheric origin.

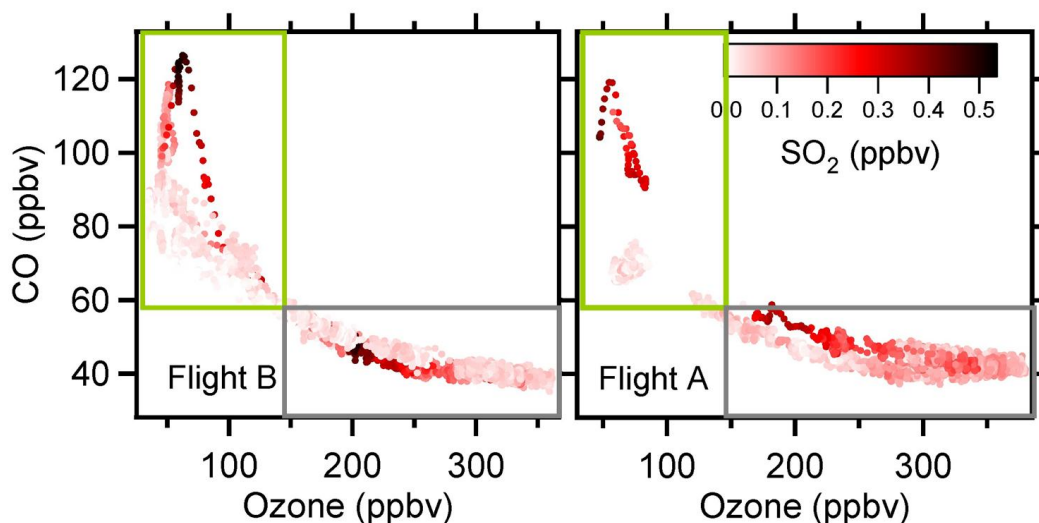


Figure 6.10: Scatterplot of CO versus ozone for the two flights on 31 October. The color code indicates where the SO_2 rich air mass was located in the tracer-tracer space. The marked area represent a tropospheric (green) and a stratospheric (grey) branch.

6.8 Evidence for volcanic origin

Drawing a direct connection between the eruption of volcano Kasatochi on 8 August and the measurement at the end of October is an impossible task. Therefore the line of argument will use the principle of exclusion of other sources such as air traffic, anthropogenic sources like smelters or other industries on the surface, long-range transport, natural sources such as plankton in the ocean or downward transport from the Junge-layer.

SO_2 was measured throughout the CONCERT campaign in flight corridors above Germany with a broad data set on background SO_2 (see chapter 7). Compared to SO_2 concentrations in the flight corridors over Germany and Western Europe, SO_2 showed short term peaks of similar magnitude (up to 6 ppbv) when intentionally chasing other aircraft and detecting the young aircraft exhaust plume. The SO_2 background values in the aircraft flight corridors reached 0.09-0.12 ppbv at maximum, thus air traffic can be ruled out for this broad SO_2 layer.

Six days backward trajectories were calculated with LAGRANTO [Stohl et al., 2001] and reanalysis data from the ECMWF. Calculations going further back in time were not initiated due to an increased uncertainty of the trajectory calculation. 6 trajectories were started inside the broad plume with elevated ozone and SO_2 . The SO_2 -mole fraction along the flight path is color-coded. One trajectory started in the second SO_2 -rich layer below 7 km (blue line). The position of the air parcels reveal a wide spread over the northern hemisphere with no focused location of one partic-

ular source. Except for the blue trajectory all trajectories resided at low pressures (< 350 hPa). Air parcels ending within the broad SO_2 -rich layer resided above the tropopause (here defined as potential vorticity > 2 PVU). The air parcel (blue trajectory) with longer residence times over industrial active areas around Chicago and the Hudson Bay may be influenced by other sources which can be associated to the elevated CO values in the measurements. Except for this air mass recent injection of SO_2 from lower altitudes can also be excluded for the broad stratospheric feature.

Natural sources such as dimethyl sulfide (DMS) emission from plankton which is oxidized to SO_2 would need strong, fast and continuous uplifting. Rapid OH-conversion and condensation in the form of H_2SO_4 is expected to reduce the initial concentration of emission. Such uplifting events could be in the form of strong convective systems which are usually observed at low latitudes. Ship-based mass spectrometric measurements in the marine boundary layer during the main plankton bloom showed exceptionally low SO_2 mole fractions [Jurkat, 2007] when compared to coastal regions. Only during ship exhaust encounters elevated SO_2 was observed. The source strengths is therefore negligible small.

The stratospheric layer of sulfate aerosol known as the Junge-layer which is mainly formed through volcanic injection of sulfur and transport of biogenic carbonyl sulfide (OCS) into the stratosphere is located between 20 and 30 km. Downward transport of the sulfate particles with a mass concentration of $0.03 \mu\text{g m}^{-3}$ [Roedel, 2000] could not explain the high sulfate concentrations of up to $2 \mu\text{g m}^{-3}$ encountered in the plume.

These combined evidence suggest that the sulfur layer originates from the August eruption of Mt. Kasatochi. Additional sources cannot be completely excluded but they appear to be less likely.

6.9 Correlation analysis

The following discussion is focused on the analysis of the trace gases HCl and HNO_3 together with NO_y inside the stratospheric SO_2 -rich plume observed during flight B. Both trace gases are abundant in the stratosphere with strong vertical gradients. Variations in their abundance can be compared to regions without volcanic influence when correlated with ozone. Ozone is produced in similar regions in the middle and upper stratosphere as HNO_3 and HCl therefore downward transport into the lower stratosphere should preserve their relative mixing state if tropospheric sources and chemical or photolytic processes can be neglected.

A somewhat conservative criterion of 0.2 ppbv SO_2 has been set to distinguish the air mass massively influenced by volcanic injection from the less perturbed stratospheric air. The SO_2 layer is of course not limited to values above this threshold and a latent sulfur enhancement appeared to be present practically everywhere in the

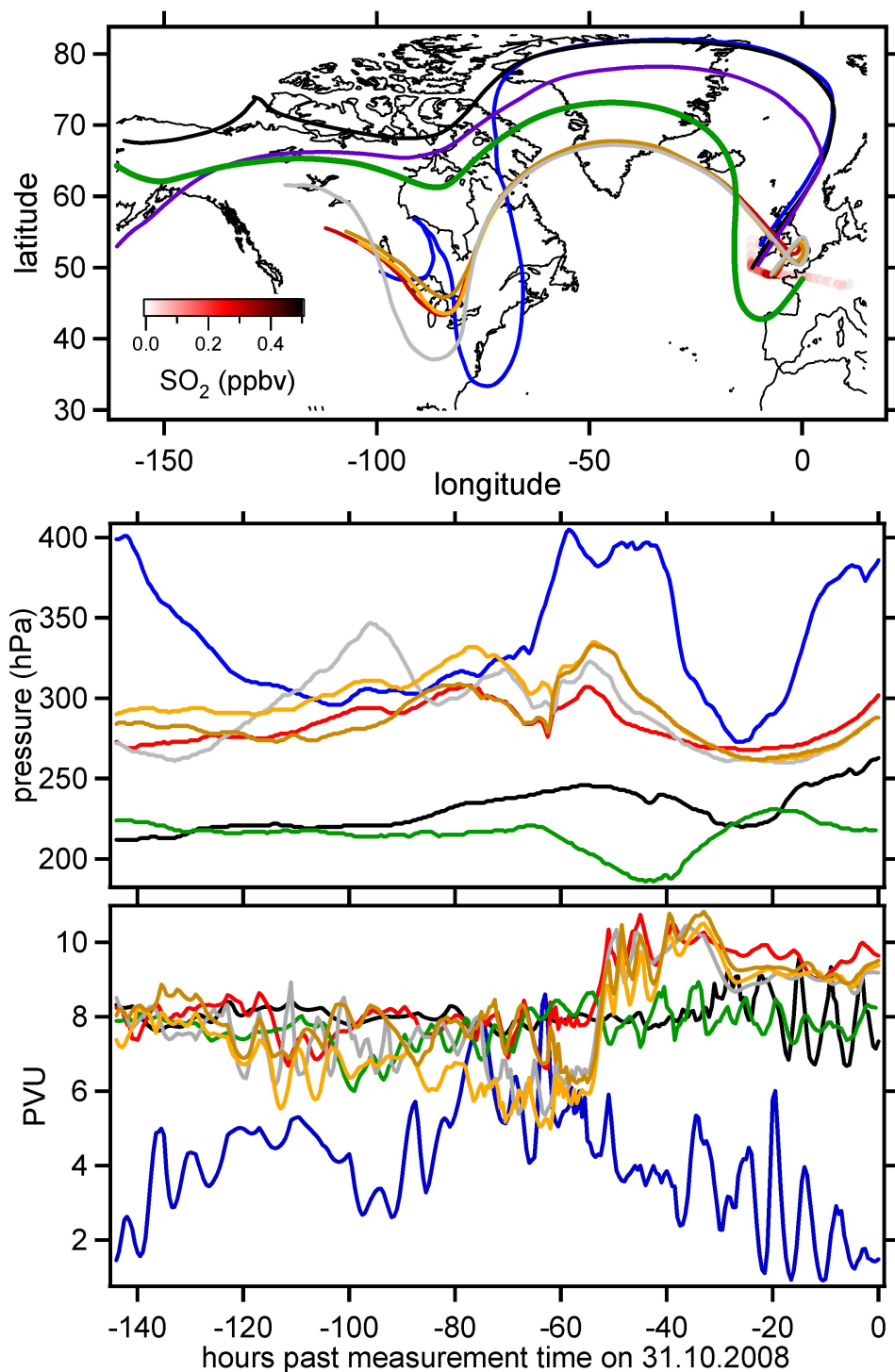


Figure 6.11: The upper panel shows the horizontal distribution of the backward trajectories ending on 31 October in the SO_2 -rich air mass. Pressure and potential vorticity along these trajectories as derived from ECMWF data are given in the lower two panels

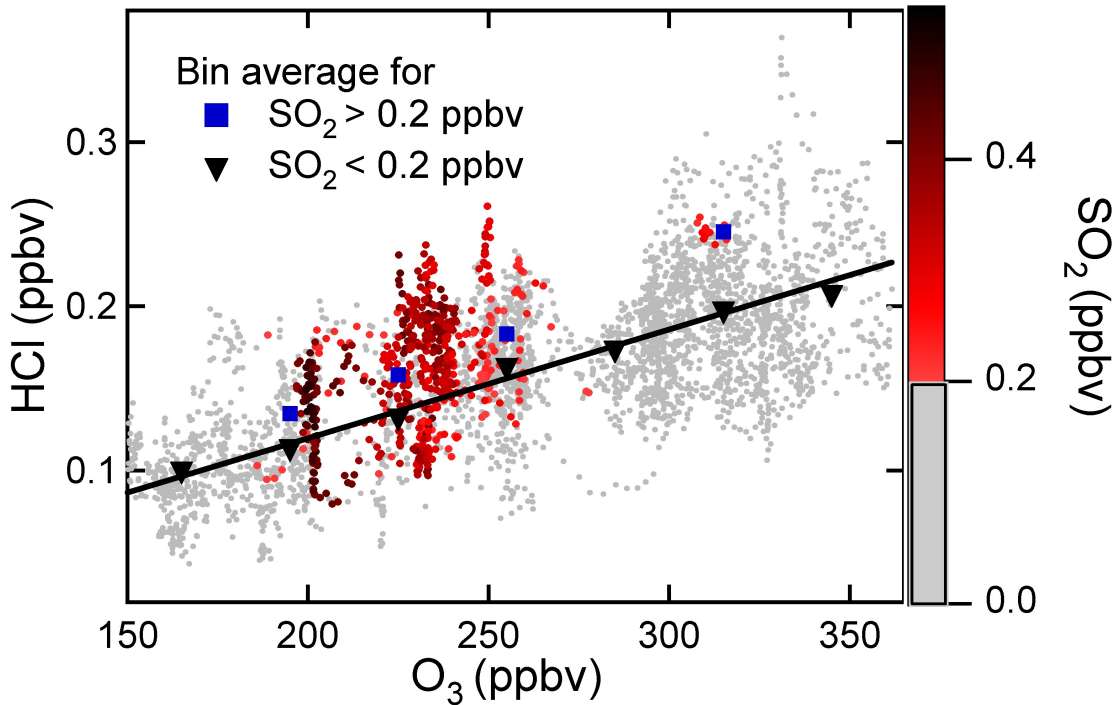


Figure 6.12: Scatterplot of HCl versus O₃ obtained on 31 October 2008 during mission flight B. The color code indicates the SO₂ mole fraction for data points where SO₂ > 0.2 ppbv while the grey dots represent HCl values for SO₂ < 0.2 ppbv. Bin averages (30 ppbv ozone bins) for SO₂ > 0.2 ppbv (blue squares) and SO₂ < 0.2 ppbv (black triangles) have been calculated. The fit (black line) for data points with SO₂ < 0.2 ppbv has a slope of $6.3 \cdot 10^{-4}$.

lower stratosphere. However only for measurements in the main plume with high SO₂ values a significant trend can be expected.

6.9.1 Correlation of HCl with ozone

A scatter plot of HCl versus O₃ for flight B with the color code indicating the SO₂ mole fraction above 0.2 ppbv is shown in Fig. 6.12. Bin averages for ozone bin widths of 30 ppbv have been calculated for air masses inside and outside of the main plume. For air masses with SO₂ mole fractions smaller than 0.2 ppbv (grey symbols), and for O₃ > 150 ppbv a linear correlation of $\text{HCl} = 6.3 \cdot 10^{-4} \times \text{O}_3 - 0.0036$ is found ($R=0.76$), that compares well within the measurement uncertainties with previous observations of Marcy et al. [2004] in stratospheric air not influenced by relatively recent major volcanic eruptions at lower latitudes. During two flights at latitudes between 24 and 39°N they found a slope of 4.4 and $5.1 \cdot 10^{-4}$. The larger slope of our data set may be due to a latitude dependence of the ratio [Marcy et al., 2004]. The slope of the curve is mainly determined by the calibration factor. A deviating

sensitivity of the instrument during flight as compared to laboratory measurements would result in a different value of the slope. The uncertainty of the calibration factor of 30 % therefore determines the error of the slope. Additional confirmation of the consistency of the measurement gives the data set obtained during another flight in the stratosphere on 28 October 2008 with a slope of $4.8 \cdot 10^{-4}$ (see Appendix (A)).

For plume parcels with SO_2 mole fractions > 0.2 ppbv (blue squares), the observed HCl bin-average tends to be increased by 0.025 ppbv. This suggests an enhancement of 19 % compared to plume parcels with SO_2 mole fractions < 0.2 ppbv (black triangles). The errors of the means (not included) are at maximum ± 6 %. The increase of the HCl mixing ratio of 19 % is within the instrumental errors of the measurements with an estimated accuracy of 20 %. However, all HCl bin averages in the plume with SO_2 mole fractions > 0.2 ppbv lie above their reference values outside of the plume. The possibility exists that the shift in the bin averages may additionally be caused by a significant ozone reduction of up to 40 ppbv. Some reduction should result from incomplete mixing of initially O_3 -poor tropospheric plume air with ambient O_3 -rich stratospheric air. With increasing plume age, the O_3 -deficit decreases due to entrainment of ambient O_3 -rich stratospheric air into the plume. A quantification of this O_3 -deficit requires detailed quantitative information on the initial plume dilution, which is not available. It is, at least, also conceivable that O_3 destruction may have occurred in the lower stratosphere. PSCs formed through transport of H_2O in the eruption plume into the stratosphere may have induced chlorine activation leading to significant ozone destruction [Rose et al., 2006]. The efficiency of this process is not well known in general and specifically for the Kasatochi eruption. It certainly depends on the local meteorological conditions. In addition, BrO measured in the eruption plume [Theys et al., 2009] may have caused some ozone destruction.

Hence, the excess HCl (dHCl) mole fractions of 0.025 ppbv in the Kasatochi main plume, represents at least an upper limit. Mechanisms discussed in chapter 6.1 may have contributed to this excess HCl: HCl increase may have occurred through direct injection of volcanic HCl into the stratosphere. Alternatively, it may reflect formation of secondary HCl in the stratosphere induced by sulfuric acid through conversion of injected NaCl. Little is known about the amount of NaCl particles injected into the stratosphere. Secondary HCl formation may take weeks and therefore secondary HCl may not be present in substantial amounts in the first days after the eruption but only after several months. An upper limit of particulate chloride in the aged plume can be derived from the AMS data. The 30 seconds detection limit of $0.03 \mu\text{g m}^{-3}$ (STP) for particulate chloride corresponds to a mixing ratio of 0.019 ppbv. Removal of HCl through condensation and activation are very unlikely to have played a role: Temperatures in the lower stratosphere in August to October may not have been low enough to allow for the dissolution of HCl in the already very acidic sulfate particles. For heterogeneous chlorine activation by reactions involving HCl, temper-

atures below 200 K are required [Borrmann et al., 1997]. Such low temperatures are usually not met in the mid-latitude lower stratosphere between August and October. In the following consideration ozone depletion caused by heterogeneous activation of HCl on SAP is therefore neglected.

Emission ratios and SO₂ conversion

The emission ratio of volcanoes for HCl is variable and different for explosive eruptions [Edmonds et al., 2002]. Still on a global scale volcanoes are thought not to contribute significantly to the stratospheric chlorine budget [Solomon, 1999]. There is still an unresolved question on the ratio of the two gases SO₂ and HCl at the point of emission and later in the stratosphere thus on the relative scavenging. Table 6.1 gives examples on SO₂/HCl ratios measured in volcanic clouds for recent eruptions. These ratios suggest that scavenging might not be as efficient as suggested by Tabazadeh and Turco [1993].

volcano	measure. techn.	dSO ₂ /dHCl	where	reference
Mt. Pinatubo	airb. IR spectr.	~10	strat.	[Mankin et al., 1992]
El Chichón	HR-FTIR spec.	dHCl = 0.04 Mt	strat.	[Mankin and Coffey, 1984]
Mt Hekla	CIMS	14.3	UTLS	[Hunton et al., 2005]
Soufriere Hills	OMI,MLS	10-33	strat.	[Prata and Bernardo, 2007]

Table 6.1: Measurements of emission ratios for recent volcanic eruptions

Shortly after the Kasatochi eruption, satellite measurements made by MLS (Microwave Limb Sounder) and OMI indicate an SO₂/HCl ratio of 70 at atmospheric pressure-levels of 147 hPa [Carn et al., 2008]. This ratio has been observed 3 days after the main eruptions, when tropospheric removal processes and loss of gaseous HCl have ceased and is larger than the ratio (~ 50) observed after the Okmok eruption. Under the assumption, that direct HCl injection can be considered as the principal mechanism leading to the observed ratio, the lifetime of SO₂ in the stratosphere with respect to OH induced conversion to H₂SO₄ can be determined using HCl as a volcanic tracer. The e-folding time depends mainly on the latitudinal residence of the air parcel during the last 85 days before the measurements, which is highly uncertain. The following assumptions have been made to estimate the stratospheric lifetime of SO₂: (1) The observed excess HCl is of volcanic origin mainly from the Kasatochi eruption and injected on 7/8 August 2008 into the stratosphere. (2) HCl loss after the 11 August 2008 on particles is neglected. (3) An initial dSO₂/dHCl of 70 as observed for the Kasatochi volcano on 10/11 August is considered. Hence, the measured dSO₂/dHCl of about 10 would imply that in the stratospheric plume

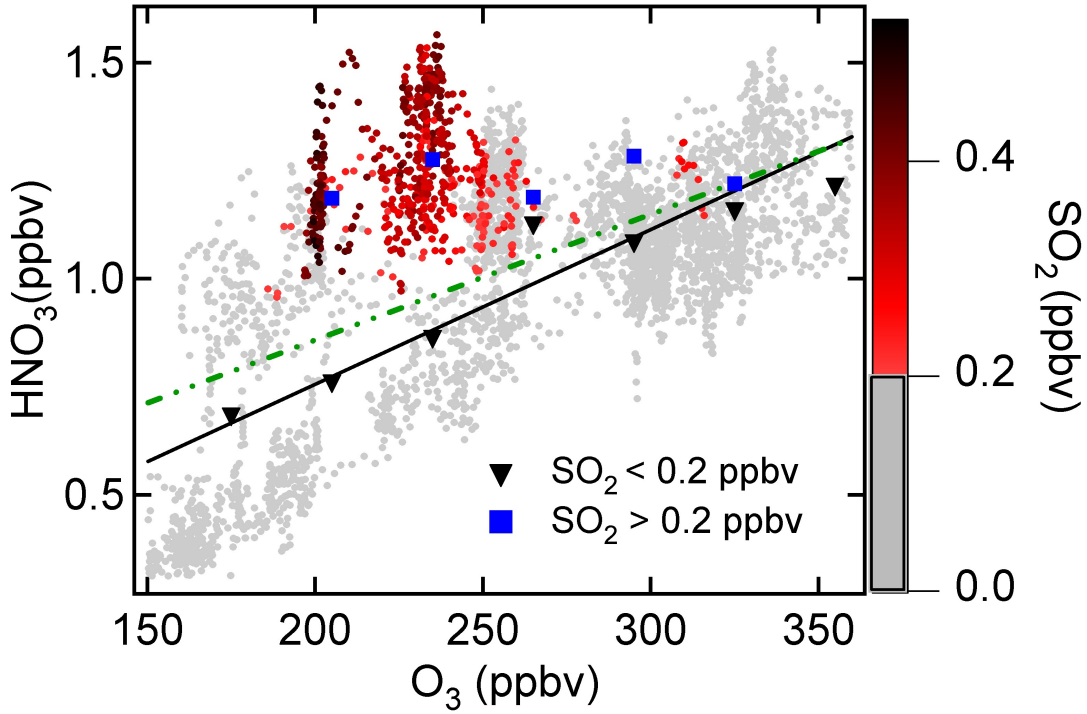


Figure 6.13: Scatter plot of HNO_3 versus O_3 . The color code indicates the SO_2 mole fraction. Two fits are included, one for all data > 150 ppbv O_3 (green dashed line) and one for data points > 150 ppbv O_3 and < 0.2 ppbv SO_2 (black line). Bin averages are calculated for inside ($\text{SO}_2 > 0.2$ ppbv) (blue squares) compared to outside plume conditions ($\text{SO}_2 < 0.2$ ppbv) (black triangles).

dSO_2/dHCl must have decreased by a factor of 7, or that only 14 % of the initial SO_2 was left. This would imply a mean e-folding lifetime of SO_2 of about 41 days. The SO_2 -lifetime in the lower stratospheric Kasatochi plume with respect to OH-induced conversion to H_2SO_4 is 47 days, as estimated by FLEXPART model simulations [Kristiansen, 2009]. A similar analysis with respect to particulate sulfate will be discussed in section 6.11. Regarding the contribution of the Okmok eruption to the dSO_2/dHCl ratio with a reduced value of 50 as compared to the Kasatochi value a maximal shift of 3 % is expected taking into account the relative SO_2 masses injected (Kasatochi 1.5 Tg and Okmok 0.1 Tg) by the two volcanos. It is however conceivable that the Okmok HCl and SO_2 emissions have contributed a small amount to the observed ratio.

6.9.2 Correlation of HNO_3 and NO_y with ozone

Fig. 6.13 shows a scatter plot of HNO_3 versus O_3 . The color code indicates the SO_2 mole fraction. The correlation analysis has been limited to a pure stratospheric branch ($\text{O}_3 > 150$ ppbv) with a fit $\text{HNO}_3 = 3.6 \cdot 10^{-3} \times \text{O}_3 + 0.04$ (all given in ppbv)

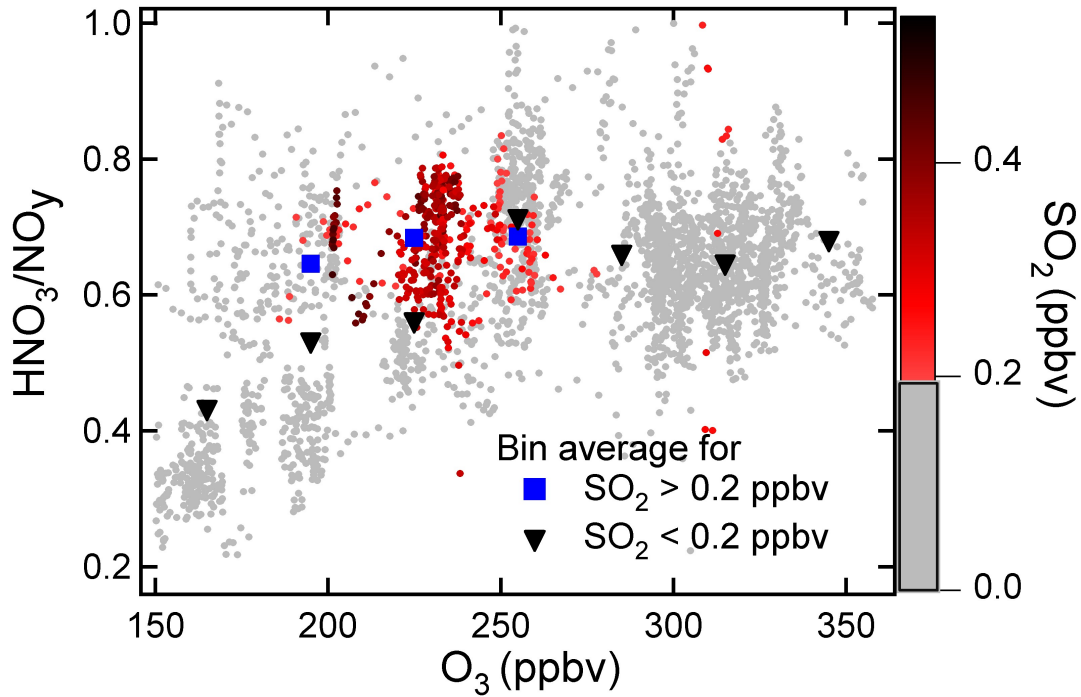


Figure 6.14: Abundance ratio HNO_3/NO_y versus O_3 and bin averages (30 ppbv ozone bins) with the color code indicating SO_2 for data points where $\text{SO}_2 > 0.2$ ppbv while the grey dots represent HNO_3/NO_y values for $\text{SO}_2 < 0.2$ ppbv.) (black triangles).

(black line). The comparison of the HNO_3/O_3 ratio to previous measurements in the lower stratosphere is complicated by the fact that latitudes of interest (47° to 54° N) are not covered by polar data from Schneider et al. [1999] and data for latitudes $> 68^\circ\text{N}$ and $< 43^\circ\text{N}$ from Popp et al. [2009]. Given an increasing slope of the HNO_3/O_3 ratio with increasing latitude, the measurements correspond well to previous results [Popp et al., 2009] and extend the detection region for northern mid latitudes. However the slope of the fit of HNO_3 versus O_3 is shifted towards a lower value ($2.9 \cdot 10^{-3}$, green line) if all data points are fitted, thus illustrating again a profound volcanic influence on the stratospheric inheritance of the HNO_3/O_3 relationship. A comparison of HNO_3/O_3 measurements should therefore only be made if no major volcanic influence is expected. Fig. 6.14 shows the abundance ratio HNO_3/NO_y versus O_3 with the color code indicating SO_2 . For stratospheric air masses ($\text{O}_3 > 150$ ppbv), the bin-averaged HNO_3 (Fig. 6.13) and HNO_3/NO_y (Fig. 6.14) ratio have been calculated, divided into air masses inside ($\text{SO}_2 > 0.2$ ppbv, blue squares) and outside of the plume ($\text{SO}_2 < 0.2$ ppbv, black triangles). HNO_3 is elevated by up to 50 % for inside plume conditions compared to the background (Fig. 6.13). The range of HNO_3/NO_y ratios from 0.51 to 0.72 compares well with the ratios previously measured [Schneider et al., 1999; Neuman et al., 2001]. Further

there might be a slight tendency for elevated HNO_3/NO_y in air masses with elevated SO_2 . For example for the bin corresponding to $\text{O}_3 = 225$ ppbv containing the largest number of data points for a statistical analysis, the ratio HNO_3/NO_y is 0.57 (for $\text{SO}_2 < 0.2$ ppbv) and 0.68 (for $\text{SO}_2 > 0.2$ ppbv), which corresponds to an increase by a factor of 1.19. The increase of the HNO_3/NO_y ratio is within the instrumental errors and natural variability while the increase of up to 50 % in the HNO_3 mixing ratios is statistically significant. Transport of air masses from higher latitudes might partially explain the HNO_3 increase. In addition, an increase of the HNO_3 and HNO_3/NO_y ratio could result from the increased efficiency of NO_x conversion to HNO_3 in the aerosol-rich volcanic plume. There are two stratospheric HNO_3 formation processes: (a) reaction of NO_2 with OH; (b) formation of N_2O_5 followed by N_2O_5 hydrolysis on $\text{H}_2\text{SO}_4\text{-H}_2\text{O}$ aerosols or PSCs. In most conditions process (b) is not very efficient in the stratosphere. However, in a volcanic plume or in polar air masses containing PSCs the efficiency of process (b) may be significantly increased, due to an increased surface area density of H_2O containing aerosols. Process (b) almost saturates when most N_2O_5 formed undergoes hydrolysis rather than photolysis, followed by reaction of NO_2 with OH [Arnold et al., 1990]. This is expected for an $\text{H}_2\text{SO}_4\text{-H}_2\text{O}$ surface area density larger than about $10 \mu\text{m}^2 \text{ cm}^{-3}$ [Fahey et al., 1993].

6.10 Aerosol composition

The AMS measured the relative mass fraction of the aerosol in the stratospheric plume and 71% were composed of particulate sulfate while 21 % of carbonaceous materia. The rest was mainly ammonia. Particularly the concentration of organic material in the volcanic layer was found to be a factor 1.4 higher than in the background UT/LS. However the increase was not significant within one standard deviation and uncertainties remain about a change in transmission efficiency due to the sulfate particles. A detailed discussion is given in Schmale et al. [2010].

The origin of the carbonaceous material is unclear: Either organic material was injected from the volcano or entrainment of ambient organic material occurred during the eruption and was transported into the stratosphere with the eruption plume. The presence of organics in the stratosphere may have a profound effect on particle growth and heterogeneous reaction taking place on these particles. Uptake coefficients are mostly assumed for sulfate-water particles and may be different for the present case. The particle size distributions measured by the AMS exhibited a mean mode diameter of 300 nm. Diameters of similar age were smaller as compared to the sulfate aerosols measured after the Pinatubo eruption [Wilson et al., 1993] which can be explained by the relatively smaller amount of injected Kasatochi-sulfur into the stratosphere. Sulfate particles from lower latitude eruptions furthermore experience higher water vapor content and lower temperatures in the stratosphere and can therefore grow faster. This in turn means comparably less surface area for heterogeneous reactions and may explain why no significant ozone depletion was observed

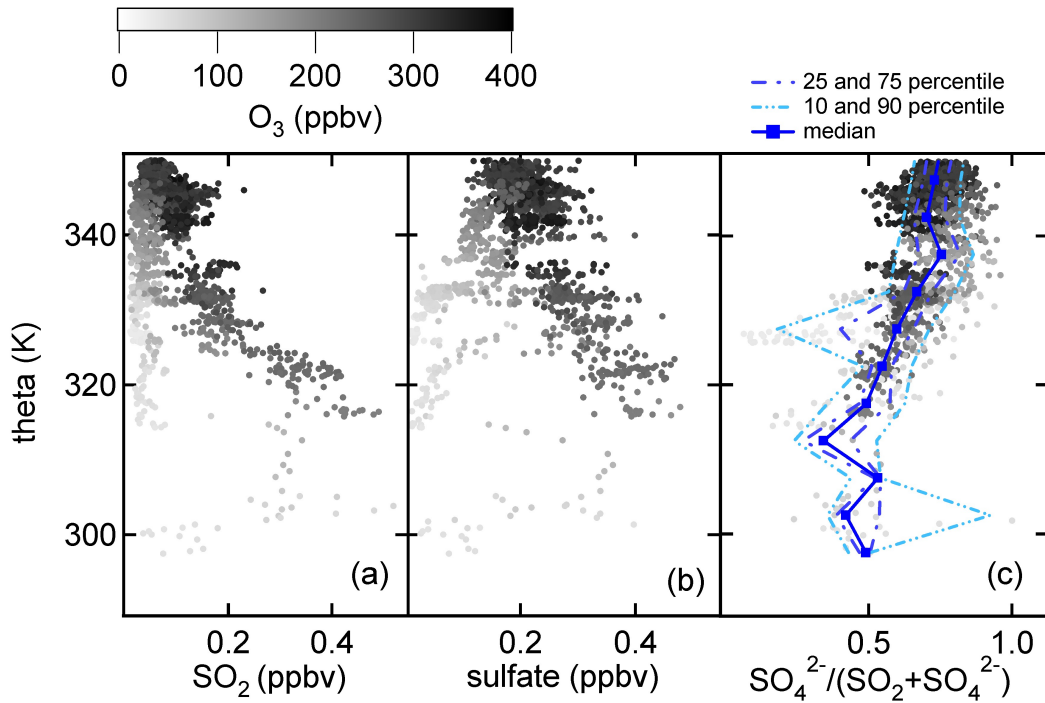


Figure 6.15: Potential temperature profiles of SO_2 (a), particulate sulfate (b), the fraction of converted sulfur ($\text{SO}_4^{2-}/(\text{SO}_2+\text{SO}_4^{2-})$) (c) with the ozone mole fraction color coded. Bin medians and percentiles for 5 K potential temperature bins for data points with $\text{O}_3 > 100$ ppbv have been calculated.

in the layer [Steinbrecht et al., 2008].

6.11 Partitioning of volcanic sulfur species

The lifetime of SO_2 in the stratosphere is highly uncertain and depends on OH, which in turn depends on various factors, such as water vapor and ozone abundance, photolysis rates and transport into the troposphere. One approach to address this problem was discussed above using HCl as a marker for air masses influenced by volcanic emissions. However the initial emission ratio and the scavenging in the eruption plume must be known for both species, HCl is only slightly enhanced above the stratospheric background, ozone depletion can not be neglected on longer time scales and HCl removal and activation is uncertain. Therefore an analysis for the conversion of SO_2 to particulate sulfate might give additional insight into the OH induced conversion that occurred during the 85 days of stratospheric residence. Taking into account the horizontally inhomogeneous field of the tropopause fold a more illustrative picture of the vertical trace gas distribution of SO_2 can be drawn with the data plotted against the potential temperature as air parcels tend to conserve their potential temperature under adiabatic conditions in the stratosphere. Fig. 6.15

shows a potential temperature - profile of SO_2 (a), particulate sulfate (b) and the sulfate mole fraction relative to the total sulfur mole fraction ($\text{SO}_2 + \text{SO}_4^{2-}$) for both flights A and B (c), the color code represents the ozone mole fraction. Elevated SO_2 and particulate sulfate accompanied by elevated O_3 is found in the theta range between 308 and 345 K. SO_2 and particulate sulfate accompanied by O_3 below 100 ppbv is found in the theta range between 300 and 308 K indicating two air masses with different histories, the lower one revealing tropospheric characteristics. The sulfur-rich stratospheric layer was encountered during both flights on 31 October with similar features and clearly enhanced above the tropospheric background ($\text{O}_3 < 100$ ppbv). The ratio ($\text{SO}_4^{2-} / (\text{SO}_2 + \text{SO}_4^{2-})$) reflects the fraction of sulfur that has been converted to sulfuric acid and condensed to particulate sulfate. It tends to show a dependence on potential temperature that seems to suggest a decreasing conversion at lower potential temperatures. Bin medians (blue squares) and percentiles (25 and 75 %, dash dotted, and 10 and 90 % dash double dotted) for 5 K theta bins have been calculated. Medians ranging from 0.34 to 0.76 are observed. Above a potential temperature of 335 K the median ranges from 0.70 and 0.76. An average of 0.76 ± 0.07 for these data is observed. This region is rather unperturbed with respect to tropospheric influence. It is at least conceivable, that the smaller ratio at lower potential temperatures is due to sulfate particle removal by cloud processes, particularly ice cloud processes. On the other hand, mixing of tropospheric SO_2 into the layer may have been a reason for the shifted ratio. Looking at thetas between 335 and 350 K the ratio of 0.76 leads to a stratospheric e-folding lifetime of 60 days for SO_2 , which represents an upper limit.

Comparison of the e-folding lifetime of 42 days inferred with the dSO_2/dHCl ratio, the above value is greater by a factor of approx. 1.5. The lower value represents a lower limit due to the fact that dHCl is an upper limit of enhanced HCl . The second value of 60 days represents an upper limit due to possible wash out effects of sulfate particles. The uncertainty of the dSO_2/dHCl -dilution method, though consistent with model calculations [Kristiansen, 2009], is however much larger than the uncertainty of the value inferred with the sulfur-partitioning method. The upper value is independent of additional satellite measurements in the volcanic eruption plume. Therefore the value of 60 days is regarded as a more likely measure of the e-folding lifetime of SO_2 with respect to OH induced conversion in the lower stratosphere at northern latitudes in late summer.

Chapter 7

Measurements of HONO and SO₂ in young aircraft exhaust plumes

This chapter deals with in situ ITCIMS measurements in the wake of commercial airliners. SO₂ and HONO were measured and HONO was compared to measurements of NO_y and NO by a chemiluminescence detector. A spatial and temporal evolution of the exhaust plume obtained during first measurements inside the wake of an A380 exhaust plume is discussed. An extensive data set on the nitrogen oxide partitioning in young exhaust plumes of 10 different commercial airliners is discussed with respect to its temporal and spatial distribution. The data are used to infer the efficiency of fuel sulfur conversion to gaseous H₂SO₄ for different aircraft and engine types. An introduction with a detailed overview on the scientific background is preceded.

7.1 Scientific background: HONO and SO₂ in aircraft exhaust plumes

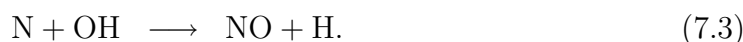
Aircraft engines emit trace gases and particles into the UT/LS region thereby affecting the local environment as well as climate on a global scale [Lee et al., 2009; Ponater et al., 1999; Schumann et al., 2000]. Aircraft emissions mainly comprise CO₂, H₂O, NO_x (NO₂ and NO), aerosols and their precursors, soot and sulfate. The greatest uncertainties lie in the estimates of the non-CO₂ effects such as the influence from NO_x emissions on the ozone budget [Sausen and Schumann, 2000] and aviation induced cloud modifications. Aircraft NO_x (NO₂ and NO) emissions, subsequent O₃ production and CH₄ destruction is thought to contribute positively to the radiative forcing (RF) but a factor of 2 less than CO₂. RF is the change in the energy budget of the system earth - atmosphere due to a perturbation. It is the current metric for comparing different influences from trace gases and particles that perturb the Earth's energy budget. Condensation trails, so called contrails, increase cloudiness. By trapping of long-wave radiation emitted from the surface and the atmosphere

and scattering of solar radiation back into space, the net RF of contrails is positive. Aviation is estimated to contribute up to 4.9 % to the total anthropogenic forcing (including aviation induced cirrus formation) with an uncertainty range of 2-14 % [Lee et al., 2009]. Considering the rate of airtraffic and RPK growths between 2000 and 2007 of 5.3 % per year it is concluded to be a significant and increasing contribution and a potential hazard for future generations [IPCC, 1999].

At present the level of scientific understanding of the RF of water, soot and sulfate is low [Lee et al., 2009] mainly due to few assessments on the subject. While sulfate particles in the upper troposphere induce a surface cooling they have diverse effects on the trace gas fields in the stratosphere, such as heterogeneous activation of ozone depleting substances [Meilinger et al., 2001]. These effects are thought to partly offset the ozone production induced by aviation produced NO_x [Pitari et al., 2001]. To assess these influences on a global scale the effective emissions of the aircraft and the subsequent processing in the young aircraft plume has to be known.

Nitrogen oxides in aircraft exhaust plumes

Nitrogen oxides from combustion processes inside of aircraft engines are predominantly present in the form of NO and NO₂. They are mainly produced through oxidation of the atmospheric nitrogen in the primary zone of the combustion chamber of the aircraft engine according to the Zeldovich-Mechanism



These processes are temperature dependent due to a high activation energy and can therefore be suppressed by either changing the combustion temperatures or reducing the residence time in the combustion chamber [IPCC, 1999]. The mass equivalent emission of NO_x in grams per kilogram of burned fuel is termed the NO_x emission index (EI NO_x). As compared to CO₂ and water, the EI NO_x is not exclusively a function of fuel flow but also depends on the thrust settings, the ambient atmospheric conditions and the combustor design mentioned above.

For the specific engine and operation mode it is tabulated in the International Civil Aviation Organization (ICAO) Engine Exhaust Emissions Database. The EI NO_x for aircraft are measured during a standardized landing and take-off cycle at the nozzle exit of the engine for four thrust settings (see Table 7.1). The ICAO imposed upper limits on the NO_x as well as on other gaseous and particulate emissions such as carbon monoxide and hydrocarbons to improve air quality around airports. The NO_x emission at cruise altitude is not regulated and therefore only few direct measurements exist. It is however an important information with respect to emission inventories for global airtraffic that are usually directly linked to an aircraft movement data-base.

operation mode	thrust settings (%)
Takeoff	100
Climb	85
Approach	30
Taxi/Idle	7

Table 7.1: The ICAO standardized thrust settings for EI NO_x measurements.

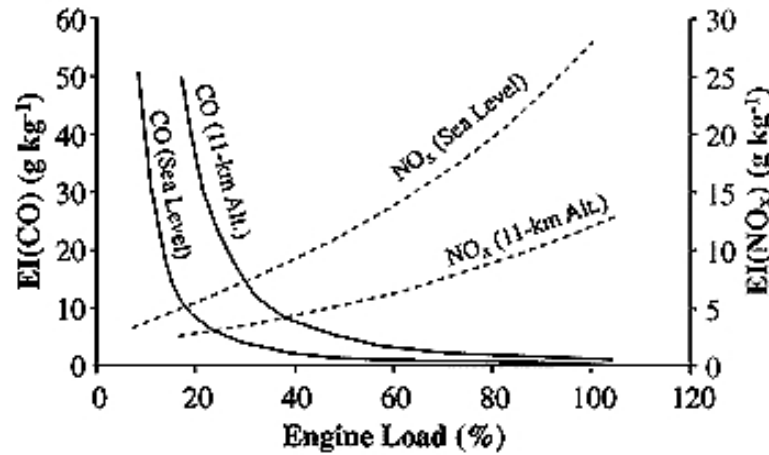


Figure 7.1: The EI NO_x as a function of the engine load (%) at sea level and 11 km altitude. At flight altitude the EI NO_x is approx. half of the EI NO_x measured at sea level. Taken from IPCC [1999].

One method to derive the EI NO_x at cruise altitude is the DLR-fuel-flow method. It uses the fuel flow during cruise as an input to calculate the EI NO_x at cruise altitude. In the first step the reference fuel flow at sea level pressure is derived from the actual fuel flow. Interpolation of the ICAO EI NO_x data for a given fuel flow gives the reference EI. This reference EI is then corrected for pressure and temperature by a linear scaling. Schulte et al. [1997] compared direct measurements at cruise altitude of the EI NO_x with the DLR-fuel-flow method and found good agreement. The greatest uncertainty as discussed by these authors are the reported fuel flows at cruise conditions. The dependence of the EI NO_x at flight altitude and during the LTO-cycle is shown in Fig. 7.1. The calculation is explained in detail in Döpelheuer and Lecht [1999].

NO_x emission indices for aviation ranges between 4 and 40 g/kg with an average of 13 g/kg.

Next to direct emissions of NO and NO₂, secondary products are an important component of aircraft emission. Near-field measurements in the exhaust plume of aircraft at cruise altitude that constrain the absolute amount of direct emission of HNO₃ and

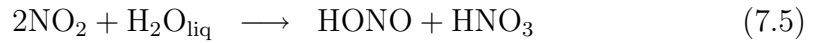
nitrous acid (HONO) and the relative amount with respect to their precursor gases NO₂ and NO are rare. First measurements of Arnold et al. [1992] measuring HONO and HNO₃ at plume ages of 60 and 72 s found a relative abundance 2.0 to 2.4 % for the HONO/NO ratio and 0.9 % for HNO₃/NO. In Fig. 7.2 the data are plotted versus plume age. Model simulations hereafter made by Tremmel et al. [1998]; Tremmel and Schumann [1999], focusing on the chemical evolution with time for the different exhaust species, are constrained by these measurements. OH is produced in the engine combustor and subsequently depleted in the turbine segment till the engine exit to a level of the order of 10¹² molecules cm⁻³ [Tremmel et al., 1998]. This occurs mainly due to reaction with NO and NO₂ and partly due to self-reaction. Concomitant reactions with SO₂ induce further depletion to background concentrations in the aging plume shortly behind the engine exit [Kärcher et al., 1996].

The chemical evolution of NO_x in the exhaust plume has been widely studied on the ground using dedicated engine tests on a stationary aircraft [Wood et al., 2008; Wormhoudt et al., 2007] or in advected plumes in the vicinity of airports [Herndon et al., 2008; Wood et al., 2008]. However comparison to cruise conditions can only be done with caution due the different environmental conditions and engine operations encountered at cruise altitude.

NO_x in the UT/LS has divers effects. While it contributes to the production of the greenhouse gas O₃ in the upper troposphere, it is involved in the catalytic destruction of ozone in the stratosphere [IPCC, 1999]. Photolysis of NO₂ generates atomic oxygen that forms ozone through reaction with molecular O₂. NO and NO₂ stand in a photochemical equilibrium during the day while NO₂ builds up during the night. On the long term NO_x is removed by gas phase oxidation to HNO₃, with subsequent wet deposition involving aerosol or cirrus clouds. This removal pathway can be enhanced in the stratosphere by heterogenous reaction on sulphate particles formed by e.g. aircraft emission or through volcanic sulfur injection [Fahey et al., 1993], a process which is discussed in chapter 6.1.

The altitude of emission of aircraft exhaust with respect to the tropopause has a profound impact on the conversion of NO_x into the reservoir species HNO₃ and HONO [Meilinger et al., 2005]. In the stratosphere NO_x is rapidly converted into HNO₃ while HONO formation plays a minor role. In the troposphere HONO is the main reservoir gas of aircraft-NO_x depending on the local meteorology and on contrail formation. Secondary HONO formation in aircraft exhaust plumes depends on the availability of hydroxyl radicals, mainly OH. Water vapor abundance is therefore a key aspect for HONO formation in aging plumes. Due to heterogeneous reaction of hydroxyl radicals on contrail ice particles so-called "dehydroxylation", HONO production is reduced in aging plumes. Additionally photolysis rates with a seasonal dependence are important for the lifetime of HONO as a reservoir gas. HONO is also known to be reservoir for OH radicals in polluted urban areas in gen-

eral and specifically in the upper troposphere where OH serves as a key component for ozone production and influencing the oxidation capacity of the atmosphere [Al-icke et al., 2003]. HONO is photolyzed at wavelengths of 300–405 nm with a lifetime of approx. 10 min in the upper troposphere. Heterogeneous reactions on soot or sulfate particles have been conducted in the laboratory but their effect on further HONO production in free troposphere remains illusive [Kleffmann et al., 1999, 1998]. The heterogeneous reaction of water with NO_x on surfaces are



and might be the dominant yet not the only source for HONO production in urban areas where high NO_x is available. For aircraft aerosols these processes have not been investigated yet.

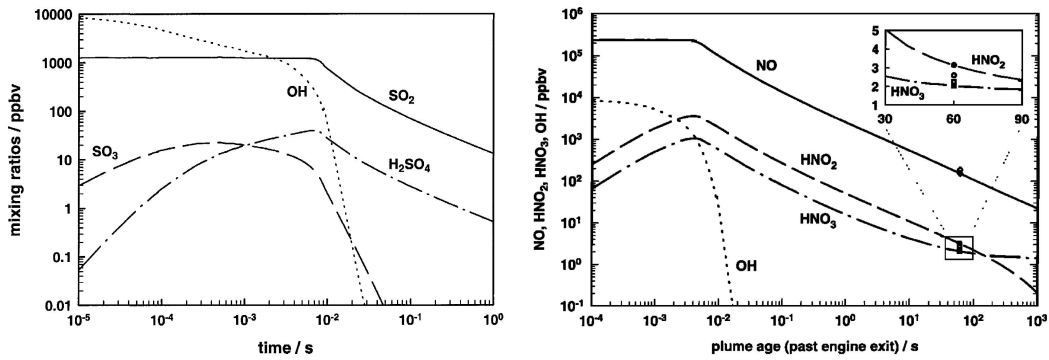
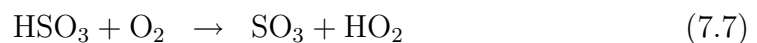
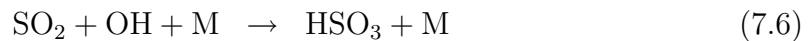


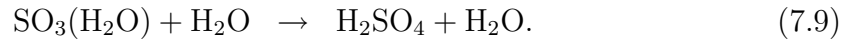
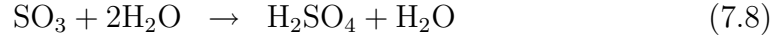
Figure 7.2: The temporal evolution of H₂SO₄, HNO₃ and HONO mole fractions starting at the combustor exit (left) and engine exit (right). The markers at plume ages around 70 s represent the measurements made by Arnold et al. [1992]. The model simulations are taken from Tremmel and Schumann, 1999 (left) and Tremmel et al., 1998 (right). The simulations were constrained by the measurement.

Sulfur oxides in aircraft exhaust plumes

The amount of sulfur oxide emissions is exclusively dependent on the fuel sulfur content (FSC) in the kerosene with an average value of 400 mg/kg. The effect of fuel sulfur on emission characteristics is summarized in Schumann et al. [2002]. SO₂ as the main emission product undergoes partly chemical conversion through OH-oxidation via the Stockwell and Calvert mechanism (1983) [Stockwell and Calvert, 1983]



The third reaction step with H₂O is sufficiently fast due to high water vapor concentrations in the atmosphere to form sulfuric acid H₂SO₄ [Reiner and Arnold, 1993]. There are two possible pathways, how H₂SO₄ could be formed from SO₃ and water [Reiner and Arnold, 1993][Reiner and Arnold, 1994]:



An additional oxidation reaction of SO₂ in the engine involves O to form directly SO₃, and relies on the availability of atomic oxygen formed through combustion of CO. SO₃ also reacts with atomic oxygen forming SO₂ and O₂.

The efficiency of conversion of the fuel sulfur to sulfuric acid is termed ε and defined as

$$\varepsilon = \frac{\text{H}_2\text{SO}_4 + \text{SO}_3}{\text{SO}_x} \quad (7.10)$$

where SO_x stands for the sum of all sulfur oxides. Between 0.5 and 2 % of the conversion of SO₂ is thought to take place in the expanding exhaust plume behind the engine exit however the major part of conversion occurs inside the engine [Kärcher et al., 1996; Somnitz et al., 2005]. ε is assumed to depend on the combustion pressure [Brown et al., 1996]. Recent developments in the engine design using higher bypass ratios and combustion temperatures to gain more over-all propulsion efficiency led to an increased combustion pressure thus differences in the conversion efficiency as compared to older engines are expected [IPCC, 1999].

Despite its low concentration in the atmosphere sulfuric acid plays an important role in nucleation processes with further potential effects on the climate. In the troposphere activation of new particle formation by homogeneous, heterogeneous or ion induced nucleation is triggered by H₂SO₄ due to its low vapor pressure ($< 10^{-4}$ hPa). In the wake of aircraft the amount of direct emission of sulfuric acid is important for particle formation and growth. Nucleation and condensation in the expanding and cooling plume rapidly depletes the gas phase component. In the young exhaust plume small volatile aerosol particles with typical emission indices of the order of 10¹⁷ per kg fuel burned with diameters > 1.5 nm are formed [Schumann et al., 2002]. The effect of these aerosol particles on the climate depend on the region of emission with respect to the tropopause: In the troposphere aerosols may act as cloud condensation nuclei (CN) and influence the climate through a change in the radiative forcing of clouds. Using NO_x as an aircraft emission tracer a mean CN/NO_x abundance ratio of 300 cm⁻³ ppbv⁻¹ was measured in airtraffic corridors. An increase in NO_x by 0.1 ppbv as observed during airborne measurements by Schlager et al. [1997] would result in an increase in CN of 30 cm⁻³. In the stratosphere sulfate particles have longer residence times and lower background concentrations. They may induce heterogeneous reactions activating ozone depleting substances, a subject which is discussed in chapter 6.1. Additionally H₂SO₄ changes the hygroscopicity of soot, thus possibly affecting contrail formation [Kärcher, 1998; Möhler et al., 2005].

Various methods have been employed to derive the sulfur conversion efficiency over the recent years. An overview of these activities is given in Table 7.2. Measurements of total sulfuric acid (gaseous and particulate) in aircraft exhaust plumes with a high time resolution and sufficient sampling efficiency are difficult to obtain. The low vapor pressure of the substance causes fast condensation and irreversible losses to the sampling line. First direct in-flight sulfuric acid measurements using CIMS in the wake of the DLR jet engine aircraft ATTAS have been performed by MPI-K ([Curtius et al., 1998][Arnold et al., 1998b]) with a lower limit of ε of 0.34 %. Particles up to 1 μm were sampled through a backward facing inlet and evaporated to at least 117°C and thereafter measured with a chemical ionization mass spectrometer. Later measurements with the same method in the wake of a B737 found an ε of 3.3 ± 1.8 % [Curtius et al., 2002]. Another method employs the depletion of SO₂ in the young exhaust plume thus the difference of the expected SO₂ derived from FSC and dilution and the measured SO₂ [Miake-Lye et al., 1998]. A more theoretical and indirect approach concludes the total sulfuric acid emission by modeling of nucleation and condensation to the measured particle size and number distributions. Strong increases of volatile particle number densities as a function of FSC and ε were measured in the young exhaust plumes (of a few seconds) but cannot be explained by binary nucleation of H₂SO₄ and H₂O. Chemi-ions, originally detected by MPI-K in aircraft exhaust [Arnold et al., 1998b][Arnold et al., 1998a][Kiendler and Arnold, 2002a][Kiendler and Arnold, 2002b], and organic vapors formed in the engine are thought to explain the discrepancy [Kärcher et al., 2000].

Modeling of the chemical evolution of nitrogen oxides and sulfur oxides inside jet engines is at present only possible with great uncertainties due to a lack of knowledge on the spatial distribution of pressure, temperature, trace gas concentration and the temperature and pressure dependent rate coefficients. Model studies addressing intra-engine chemical and dynamical features with simplified pressure and temperature distributions have been carried out by Lukachko et al. [1998], Tremmel and Schumann [1999] and Starik et al. [2002]. They only discuss the post-combustor flow due to lack of knowledge of the processes occurring inside the combustor. They discussed a number of factors that influence the sulfur conversion efficiency such as

- the initial OH and O concentration
- the efficiency of the second production pathway for the formation of SO₃ [Kärcher and Fahey, 1997]
- the pressure ratio and therefore the pressure in the combustor [Brown et al., 1996]
- the FSC
- the NO_x emission index

Time	ϵ_{meas}	ϵ_{model}	Measurements/Model Studies	Reference
1993			Flow reactor measurements of the reaction $SO_3 + H_2O + M \rightarrow H_2SO_4 + M$	Reiner and Arnold [1993]
1994			Rate constant measurement of the reaction $SO_3 + H_2O + M \rightarrow H_2SO_4 + M$	Reiner and Arnold [1994]
1994	>0.4%		Ground based mass spectrometric measurements	Frenzel and Arnold [1994]
1995	>12 %		Stratospheric measurements of volatile aerosol behind the Concorde	Fahy et al. [1995]
1996		<1 %	Model studies in the jet regime (start at engine exit plane)	Kärcher et al. [1996]
1996		2-10 %	Model studies on the Concorde, Atlas plume	Brown et al. [1996]
1997		36 %	Model studies on $\epsilon(s)$ where $s=[SO_3]/[SO_x]=0.2-0.6$, Concorde data	Kärcher and Fahy [1997]
1998		5.3-8 %	Model studies on turbine and exhaust nozzle aerodynamics	Lukachko et al. [1998]
1998	6-31 %		Measurements of depletion of gas phase SO ₂ by condensed phase	Mlake-Lye et al. [1998]
1998			Jet engine exhaust chemion measurements	Arnold et al. [1998a]
1998	1-2 %		Measurements on the time scale of gas to particle conversion	Arnold et al. [1998b]
1999		3.8-3.5 %	Model studies with focus on rate constants	Tremmel and Schumann [1999]
2000		0.5-5 %	Model studies on the aerosol emission index	Kärcher et al. [2000]
2002	3.3-4.8 %		In flight measurements of total sulfuric acid using CIMS	Curtius et al. [2002]
2002		8.4-9 %	Modeling of turbine + exhaust nozzle	Starik et al. [2002]
2004	2.3±1 %		Measurements of sulfur (VI) on simulated internal engine flow	Katragkou et al. [2004]
2004		2.3±1 %	Model studies starting at combustor exit	Sorokin et al. [2004]

Table 7.2: A chronological list of measurements and model studies contributing to an understanding of the sulfur conversion efficiency.

- the intra-engine fluid mechanics (blade cooling) [Lukachko et al., 1998]
- the rate coefficient of reaction 7.6

The greatest uncertainty lies in the last aspect due to a lack of measurements of the rate coefficient at such high pressure and temperature regimes as encountered inside the engine (combustor and turbine). Somnitz et al. [2005] performed quantum chemical dynamical calculations for this specific problem yet measurements are needed to confirm the inferred rate coefficient.

The availability of oxidants (first item on the list) draws a connection between the nitrogen oxides and the sulfur oxides. Investigations on the processing of the two categories of species, e.g. through simultaneous measurements of the precursor and oxidized gases, help to understand the oxidation potential inside the jet engine and the aircraft plume but are at present only limited available.

7.2 Measurements during the CONCERT-2-Contrails campaign

The CONCERT-2-Contrails campaign comprised the second half of the CONCERT campaign with a focus on aircraft emissions and contrail formation in flight corridors above Europe. The objective was to detect whether the aircraft type has an influence on contrail formation under similar meteorological conditions (e.g. temperature, pressure and relative humidity with respect to ice (RHi)), the emission of primary and secondary gaseous components and the plume processing. This was done by directing the Falcon into the wake of commercial airliners with the help of the German Air Traffic Control (ATC). The aim was to measure chemical and microphysical properties of the exhaust plumes and contrails at different ages and for different engines.

Contrails form when moist and hot exhaust air is mixed with drier and colder ambient air. When relative humidity has reached saturation with respect to water, droplets form, and when RHi decreases below the frost point ice nucleates in the liquid droplets. If the ambient air is supersaturated with respect to ice, the ice particles grow and may form a persistent contrail. A forecast for these regions was provided by ECMWF and accordingly was the flight plan chosen. The altitude for contrail tracking was adjusted in-flight by the pilots of the Falcon observing where persistent contrails are formed. They communicated with ATC to conduct commercial airliners into regions of ice supersaturation. Once the commercial airliner was positioned the Falcon dived into the contrail at a minimal distance of 5 nautical miles (NM) and followed the aircraft as long as possible, probing the plume at different ages and vertical positions with respect to the flight altitude of the chased aircraft. If no contrail was formed and the plume was visually undetectable, NO and NO_y served as exhaust tracers during the measurements. In addition the NO data were

used during analysis to distinguish between background and plume conditions and as a dilution marker. During the chase the pilots of the traced aircraft were asked to report their aircraft and engine type, the take-off and landing airport, the actual weight, the flight level (FL), the fuel flow (FF) and the true air speed (TAS, Mach number). Additionally ATC communicated the distance between the two aircraft. The Mach number is the aircraft speed divided by the speed of sound. The speed of sound increases with temperature therefore it decreases with altitude in the troposphere. Subsonic aircraft travel by definition at Mach numbers smaller than 1.

An overview on the measured aircraft plumes is given in Table 7.3. In total 22 contrails/plumes from 11 different aircraft were sampled with a total measurement time inside the wake of 1.7 hours. During 5 flights on the 17, 19 and 20 November 2008 over Western Europe 13 contrails were probed at altitudes between 8.5 and 11.6 km and temperatures above 212 K. Among these aircraft was the at present biggest commercial aircraft in use, the A380. Additionally an A319, two A340, a B737, B767 and smaller aircraft such as a Fokker 70 and a CRJ-2 were probed. The discussion will focus on these contrails/plumes. On 19 November 2008 the so-called "2-contrails-flight" pattern was performed: Two aircraft, an A319 and an A340, were instructed by ATC to fly side by side at a minimal safety distance of 5 NM at the same flight level. The Falcon was conducted into the contrail of the A340, changed after 3 min measurement time into the contrail of the A319 and again after 3 min back into the contrail of the A340. This procedure was chosen for direct comparison of contrail properties of different aircraft at similar meteorological conditions.

Temperature and pressure were measured by sensors aboard the Falcon. Water vapor was measured by the closed path Fast In-situ Stratospheric Hygrometer (FISH) [Zöger et al., 1999] with a time resolution of 1 s and an overall accuracy of 6 %. In combination with the Falcon temperature and pressure measurements the RH_i was inferred with an uncertainty of 15 %.

Particle concentrations and size distributions for particles with diameters between 0.3 and 19.5 μm were measured by a Forward Scattering Spectrometer Probe (FSSP100). The instrument measures the intensity of light scattered by contrail or cirrus particles passing through a light beam. These measurements were used to categorize the plume encounters into occasions when a contrail was formed or not. For the present consideration on gas phase emissions an arbitrary threshold of 100 particles cm^{-3} (standard conditions) with particle diameters between 0.65 and 3 μm was set. Particles in this diameter-range dominate the size spectrum in young contrails. Above this threshold the plume was associated with contrail formation.

7.3 Plume ages

Plume ages were calculated for 11 contrail encounters. The position (latitudinal and longitudinal coordinates and FL) of aircraft entering the control region of ATC is radar monitored and recorded for each aircraft in irregular but frequent time

No.	flight	regis- tration	type	FF (t/h/eng)	Weight (t)	FL	Mach	start of contrail	end of contrail	T (K)	p (hPa)	RHi (%)
17.11.2008												
1a	LH 492	DA1GB	A340-311	2.1	240	300	0.82	12:14:00	12:20:00	224	309	71
2	LOT 279	no data	B737-500	(1.2)	no data	340	0.79	15:08:41	15:17:39	216	253	75
3	LH 458	no data	A340-642	2.5	342.3	310	0.826	15:49:00	15:53:27	221	282	57
19.11.2008												
4a	HHI	D-AHIK	A319-111	1.15	51.1	340	0.895	07:18:01	07:27:37	220	254	64
4b	HHI	D-AHIK	A319-111	1.06	51.1	350	no data	08:07:19	08:13:33	213	238	81
4c	HHI	D-AHIK	A319-111	0.9	46.9	350	0.76	09:14:12	09:27:29	217	241	89
1b	LH 493	DAIGI	A340-311	1.25	150.3	350	0.737	08:45:00	08:47:59	217	242	94
1b	LH 493	DAIGI	A340-311	(1.58)	no data	351	0.737	08:56:12	08:58:06	218	245	73
5	LH 8PH	no data	CRJ-200	(0.52)	no data	328	no data	11:40:23	11:45:06	221	263	89
6	SIA317	9VSKC	A380-841	(3.6)	508.1	350	0.85	12:14:28	12:29:18	216	237	95
9	no data	no data	A320	no data	no data	no data	no data	12:34:20	12:40:24	214	227	95
20.11.2008												
7	AVA72GQ	OELFQ	Fokker 70	0.95	32.6	340	0.75	10:05:30	10:07:34	221	266	62
8	JAT240	YUAND	B 737-3H9	1.3	53.2	340	0.76	09:54:42	10:00:00	218	252	81

Table 7.3: Overview on the aircraft plumes and the aircraft parameters probed during 17, 19 and 20 November 2008: Flight No., aircraft type, registration, fuel flow (FF), weight, flight level (FL), Mach number, start and end of contrail measurement, averaged temperature (T), averaged pressure (p) and averaged relative humidity with respect to ice (RHi) measured onboard the Falcon. Values in brackets are estimated based on experienced data.



Figure 7.3: Picture taken from the cockpit of the Falcon. In the front the nose boom of the Falcon for the wind measurements can be seen. In the back two A340 aircraft flying at the same altitude both producing a contrail.

intervals (approx. every 1-5 min). Given the number of aircraft movements over Germany (approx. 9000/d) the right aircraft trail had to be selected. At the aircraft position the horizontal advection was calculated for a time step of 5 s using the wind vectors measured by the Falcon shortly after the aircraft crossed the region. The distance between the advected plume and the Falcon was then calculated for each time step. A minimal distance between the Falcon and the advected plume and an NO value above 1 ppbv was chosen as criteria for a plume encounter. The plume ages were interpolated for all data obtained during the quasi linear flight patterns of the Falcon. The contrail ages were compared to contrail ages derived with a different method using interpolated ECMWF wind fields. This method is explained in detail in Voigt et al. [2010]. Both calculations agree. The results of both methods are given in Fig. 7.6.

As an example the chase of an A380 is given in Fig. 7.5. Due to strong northern winds of maximal 41 m/s the plume with a contrail was rapidly advected to the south of the flight track. After a sequence of 265 s in the contrail the Falcon started a turn-around trying to probe the aged contrail in opposite direction. However it had drifted further south and was undistinguishable from other contrail-plumes in this region. Therefore a contrail of an A320 with ages of 520 to 570 s was probed instead.



Figure 7.4: The picture was taken inside the contrail of the A380. Clearly visible is the primary (two trailing vortices in the lower part) and secondary wake (upper part) of the contrail (see text for details).

7.4 The NO_x Emission Index

The EI NO_x was calculated by the Institute of Propulsion Technology (AT), DLR, employing the DLR Fuel Flow method [Schulte et al., 1997; Döpelheuer and Lecht, 1999], which was described in the introduction 7.1. In principle this method uses the sea level static measurements, adjusting the typical behavior of the engine to the emission indices. These characteristics are then considered for calculation of the EI NO_x at flight conditions. The results are listed in Table 7.4. The EI NO_x is given in g per kg fuel burned. The bypass ratio and the pressure ratio of the engine are taken from the ICAO data base.

The EI NO_x ranged from 8.35 to 19.69 g kg⁻¹ with an average of 12.8 g kg⁻¹. The highest EI NO_x was derived for the A380 with a Trent 970-84 engine, the lowest was for a B737 with the engine CFM56-3B1. All data are listed in the Tables 7.3 and 7.4. The data in brackets are estimated. The EI NO_x calculation of the A380 was based on an estimated lower fuel flow than the one reported by the pilots during cruise because the reported fuel flow of 4.75 t/(h engine) was exceptionally high. The higher fuel flow would result in an EI NO_x of 27.6 g kg⁻¹ and should be kept in mind for the following discussion.

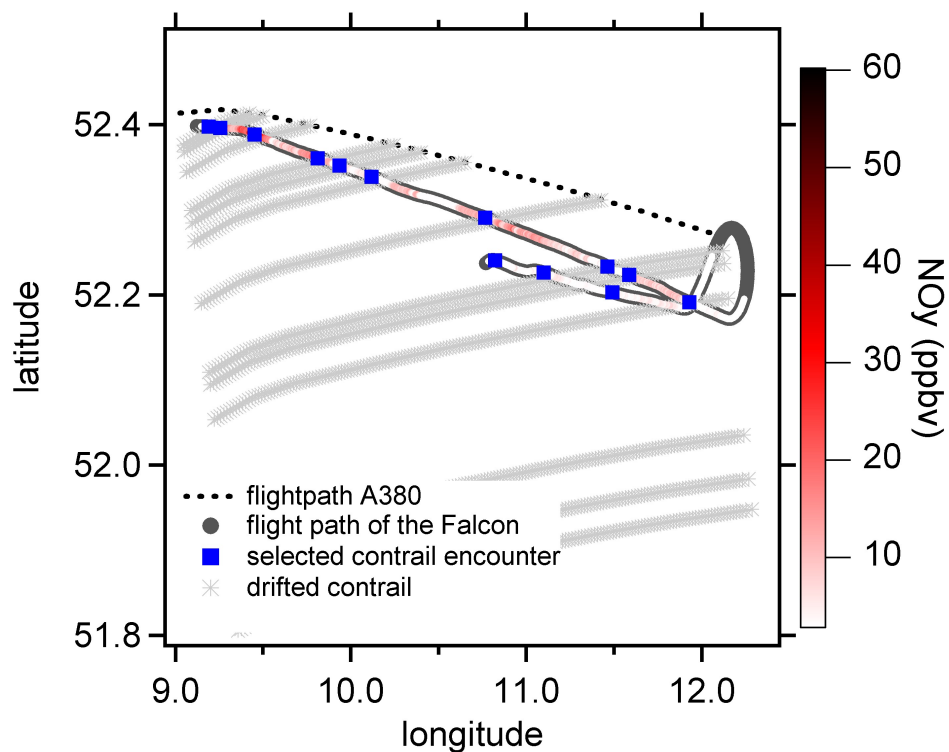


Figure 7.5: The advected contrail (grey) of the A380 at different ages. At a minimal distance between the Falcon flight path and the drifted contrails and for enhanced NO_y values the contrail age was determined.

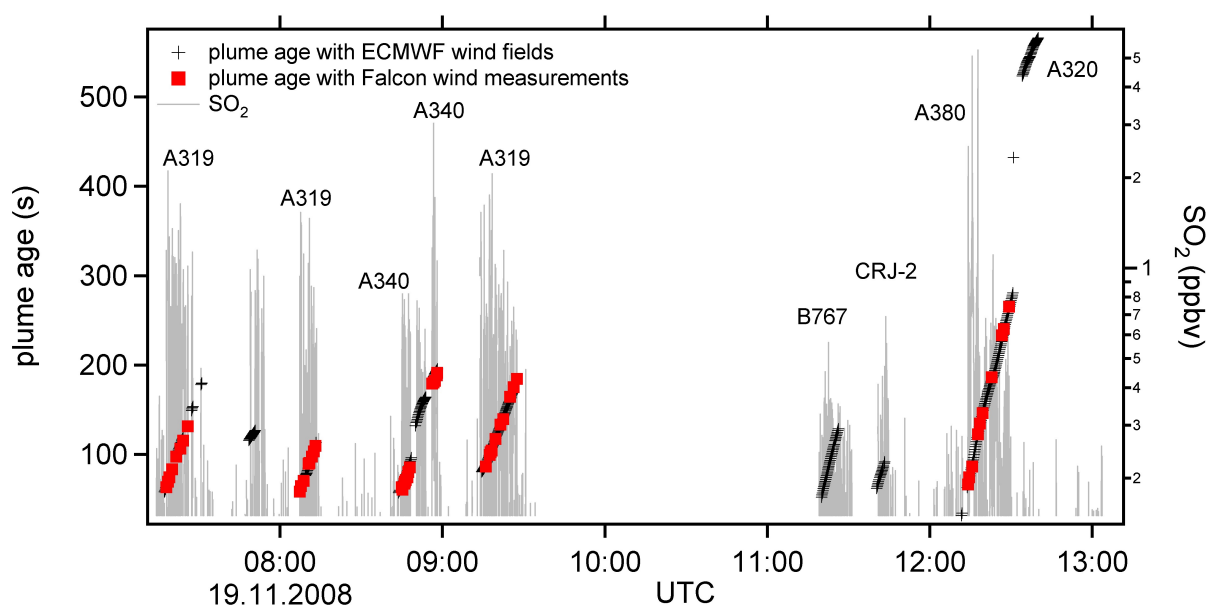


Figure 7.6: The plume ages derived for the measurement on 19 October 2008.

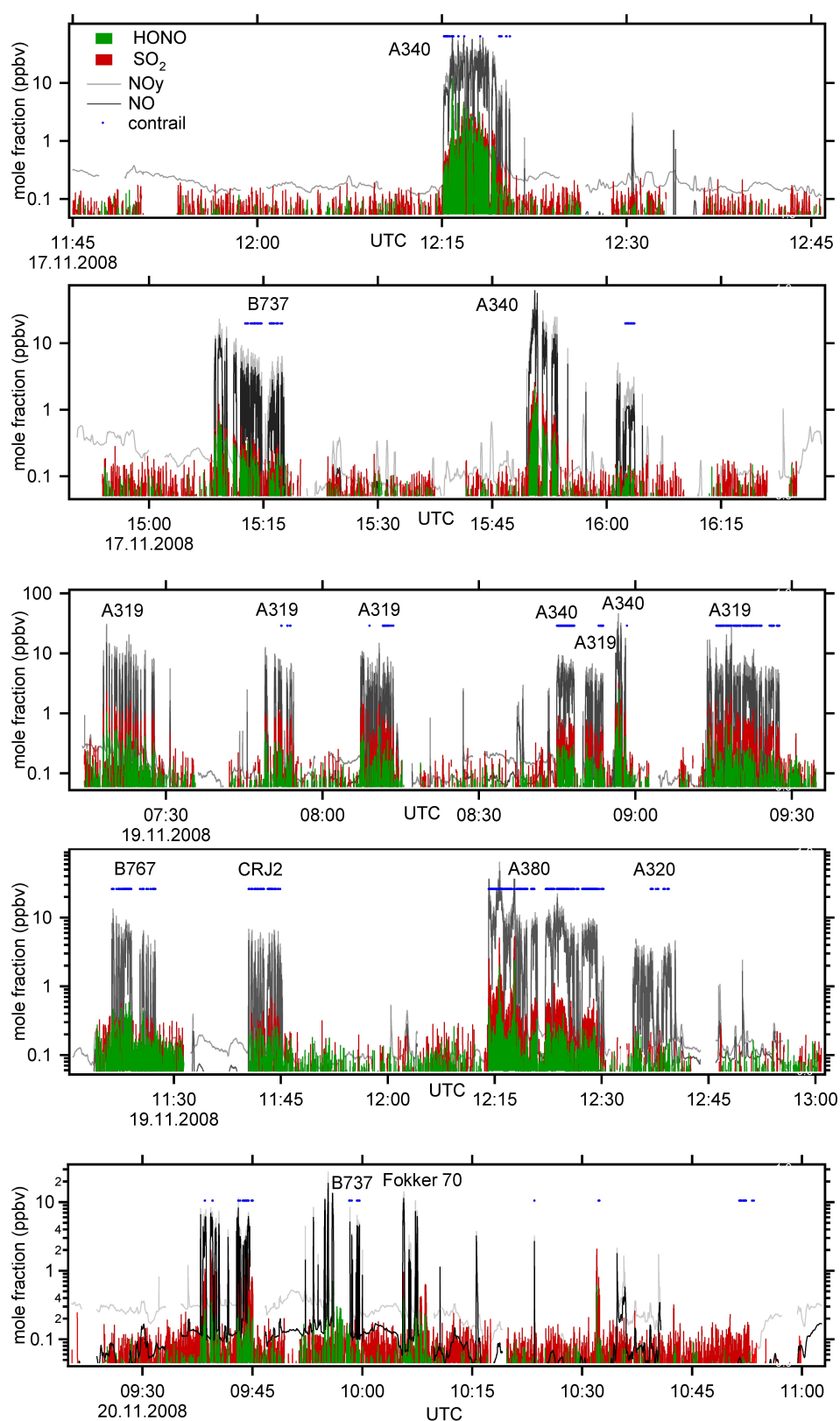


Figure 7.7: HONO, SO_2 (ITCIMS), NO and NO_y (CLD) mole fractions obtained during the flights on 17, 19 and 20 November. The plumes are labeled with the aircraft type. The blue dots show the time intervals when more than 100 particles cm^{-3} (STP) in the diameter range of 0.65-3 μm were measured.

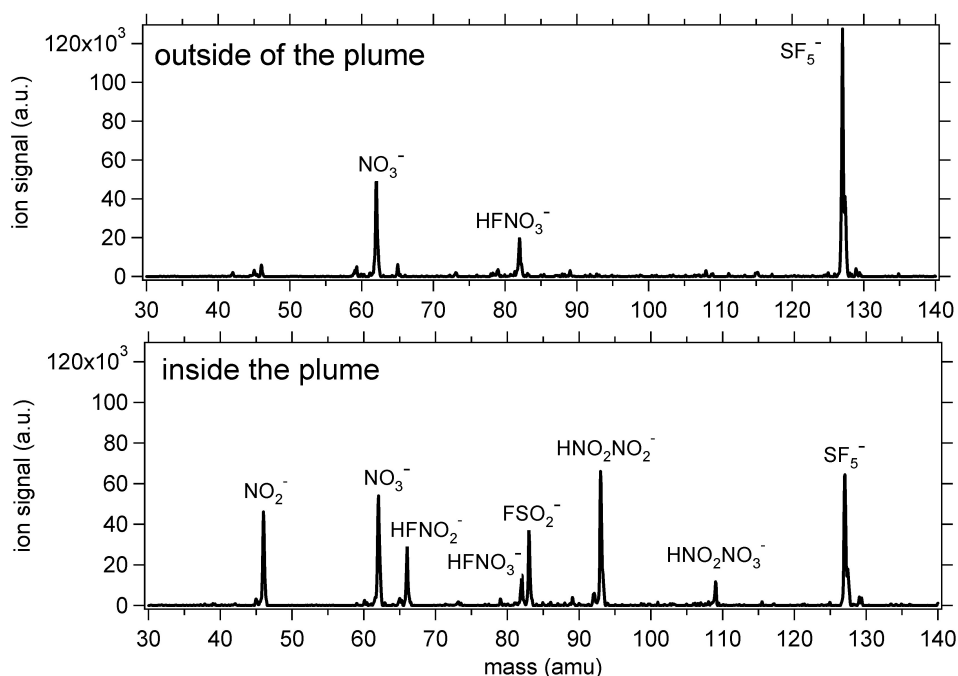


Figure 7.8: Negative ion mass spectra obtained by the ITCIMS at 9.7 km altitude outside (top) and inside (bottom) the exhaust plume of an A340, averaged over 10 spectra.

7.5 ITCIMS measurements in aircraft exhaust plumes

The ITCIMS instrument provided data of SO₂, HNO₃ and HONO measured during aircraft plume encounters to study the chemical evolution and spatial distribution inside the plume. The calibration procedures for measurements on the 17, 19 and 20 November 2008 are discussed in chapter 3.

During one flight on 2 November 2008 the bypass sampling line with passive flow configurations was deployed. However the background measurements were very noisy resulting in a high detection limit of a few hundred pptv. NO was not measured on that day therefore no further analysis was possible. Accordingly the data obtained on that day were not considered for the present discussion. An overview of the detection limits, flight paths and the time lines of the additional flights with no detailed discussion is given in the Appendix.

Measurements on the 17, 19 and 20 November 2008 used the same setup, flow configurations and operation mode thus the measurements obtained during these three days are comparable. A spectrum recorded during a plume interception of an A340 on 17 November 2008 is shown in Fig. 7.8. Outside the exhaust plume, the dominant ion is the de-clustered reagent ion SF₅⁻. In addition the product ion FHNO₃⁻ and its fragment NO₃⁻ are present. In the exhaust plume, the major product

ions of SO_2 (FSO_2^-) and HONO (FHONO^-) appear at a good signal to background ratio. In addition NO_2^- (fragment ion of FHONO^-) and NO_2HONO^- (reaction of FHONO^- with HONO) are formed. All three product masses were used after background correction to derive the HONO mole fraction.

Detection of HNO_3 in the exhaust plume was problematic. Due to a high HNO_3 abundance in the flow tube an elevated background of approx. 1 ppbv caused a high detection limit between 0.2 and 0.29 ppbv. Presumably due to the high detection limit no significant enhancement above the background concentrations for nitric acid during all plume encounters was observed.

This observation seems to contrast the measurements of Arnold et al. [1992]; Tremmel et al. [1998] in young aircraft exhaust plumes of similar ages. They detected HNO_3 mixing ratios of up to 1.32 ppbv above the background at plume ages of 60 s. The discrepancy might be explained by the absence of a contrail during their measurements in contrast to the present measurements in contrails. Popp et al. [2004] reported on a significant gas phase depletion of nitric acid due to condensation on $2\text{ }\mu\text{m}$ particles inside a contrail. HNO_3 is buried in growing contrail ice particles leading to a small but significant depletion of the gas phase abundance [Schäuble et al., 2009] of a few percent.

Another explanation might be the transmission of HNO_3 through the upper part of the sampling line that is not accounted for by the calibration procedure. Fast changes in the concentration of HNO_3 during plume interceptions suffer from losses to the unpassivated walls of the sampling line. This may explain the difference to measurements of Arnold et al. [1992], who used a different sampling line. Thus HNO_3 will not be addressed in the following discussion.

The HONO and SO_2 mole fractions measured during 5 flights on 17, 19 and 20 November 2008 are presented in Fig.7.7 together with the NO and NO_y data and dedicated aircraft types. Sequences when a contrail with more than 100 particles cm^{-3} with particle diameters between 0.65 and $3\text{ }\mu\text{m}$ was encountered are indicated by the blue dots.

The ITCIMS measurements constitute the first calibrated airborne HONO measurements in aircraft exhaust plumes. Mole fractions ranging from values below the detection limit up to 11.7 ppbv were measured at a time resolution of approx. 1.6 s. HONO and SO_2 detection limits were low, compared to the HNO_3 detection limit, ranging for both gases between 0.047 and 0.067 ppbv for two standard deviations of the background. The measurement benefits from the fast sampling and read-out of the ion trap when trace gas mole fractions may vary by an order of magnitude as observed at the edge of an aircraft exhaust plume. Additionally, the measurement benefits from the recording of all masses which are quasi simultaneously read-out. This was particularly important for systematic studies on interfering trace gases and for the parallel ACIMS method. Transmission of the trace gases through the sampling line was accounted for during calibration. Coating of the sampling line with soot was not observed and most of the time the water vapor concentration below

200 ppmv. Therefore heterogeneous processes on soot or PFA can be excluded [Kl-effmann et al., 1999, 2006].

7.6 Abundance ratios of HONO/NO and HONO/NO_y

NO proved to be a sensitive tracer for young aircraft exhaust plumes. Due to its broad dynamical measurement range (background - 65 ppbv), its fast acquisition (1 s) and unproblematic transmission of the trace gas within the sampling line the chemiluminescence detector was particularly suited for exhaust measurements. A short overview of the measurement technique is given in chapter 5.

The ratio of HONO to NO was derived for each plume sequence for contrail ages between 60 and 120 s. These ages were chosen for two reasons: The dilution did not decrease the HONO mole fraction to background values. And secondly, removal and processing of HONO or NO is negligible. The most important removal process for HONO is photolysis [Alicke et al., 2003]. The e-folding time with respect to photolysis of HONO is of the order of 10 min at noon in the lower troposphere. Photolysis rates at these altitudes are still highly uncertain but were discussed in Dix [2007]. They are of the order of $2.5 \cdot 10^{-3} \text{s}^{-1}$ with an error of 40 % which would result in a decrease of the initial concentration to 75 % after 120 s. High NO mole fractions in the young exhaust plume may however react with ambient OH to form HONO.

According to the model results of Tremmel et al. [1998], which considers entrainment and dilution, no significant changes of the HONO/NO ratio within the first two minutes of the plume (see Fig. 7.2) is expected. The temporal evolution of the HONO/NO value for the A380 plume is shown in Fig. 7.9. The longest measurement sequence inside this plume was used to study the temporal evolution of the HONO/NO ratio. NO was synchronized to the time resolution of the HONO measurements. The scatter plot shows a reasonable correlation for the two measurements with a correlation coefficient $R^2=0.68$. Only data above the threshold of 3 ppbv for NO and above a 1σ detection limit for HONO were used to assure that the data are not affected by non-plume conditions. The ratio of HONO/NO reveals no dependence on the plume age. It is conceivable that the contrail particles may have decreased the photolysis rate in the contrail. The slope is close to zero, thus HONO depletion through photolysis or other removal processes that affect the NO and HONO abundance within the measured time sequences are neglected. The data support the model results by Tremmel et al. [1998] and stand in good agreement with Arnold et al. [1992]. Under the assumption of a constant ratio and to avoid problems arising from sampling statistics, HONO/NO ratios were derived by integrating all data points above the pre-defined threshold and then dividing the integrated mole

No	flight	engine	aircraft-type	B/P ratio	p-ratio	EI NOx	HONO/NO	HONO/NO _y	ε
17.11.2008									
1a	LH 492	CFM56-5C2	A340-311	6.8	28.8	18.53	0.054	0.041	0.041
2	LOT 279	CFM56-3C1	B737-500	5.1	25.5	8.43	0.050	0.030	0.039
3	LH 458	Trent 556-61	A340-642	7.5	36.63	16.56	0.035	0.026	0.027
19.11.2008									
4a	HHI	CFM56-5B6/P	A319-111	6.0	24.64	11.24	0.058	0.036	0.044
4b	HHI	CFM56-5B6/P	A319-111	6.0	24.64	no data	0.047	0.036	0.036
4c	HHI	CFM56-5B6/P	A319-111	6.0	24.64	8.69	0.043	0.028	0.033
1b	LH 493	CFM56-5C2	A340-311	6.8	28.8	11.6	0.039	0.032	0.030
1b	LH 493	CFM56-5C2	A340-311	6.8	28.8	11.64	0.038	0.032	0.029
5	LH 8PH	CF34-3B	CRJ-200	no data	no data	(9)	0.037	0.029	0.035
6	SIA317	Trent 970-84	A380-841	7.5	38.97	(19.69)	0.021	0.021	0.017
9	no data	no data	A320	no data	no data	no data	0.045	0.032	0.035
20.11.2008									
7	AVA72GQ	RR Tay Mk620-15	Fokker 70	3.0	16.1	9.85	0.034	0.025	0.026
8	JAT240	CFM56-3B1	B 737-3H9	5.1	22.44	8.35	0.045	0.034	0.037

Table 7.4: Overview on the measurements performed during 17, 19 and 20 November 2008. Flight No., engine, aircraft type, bypass pressure ratio, pressure-ratio (ICAO), NO_x emission index (g kg⁻¹), HONO/NO, HONO/NO_y and ε are listed. Values in brackets are derived with estimated fuel flow.

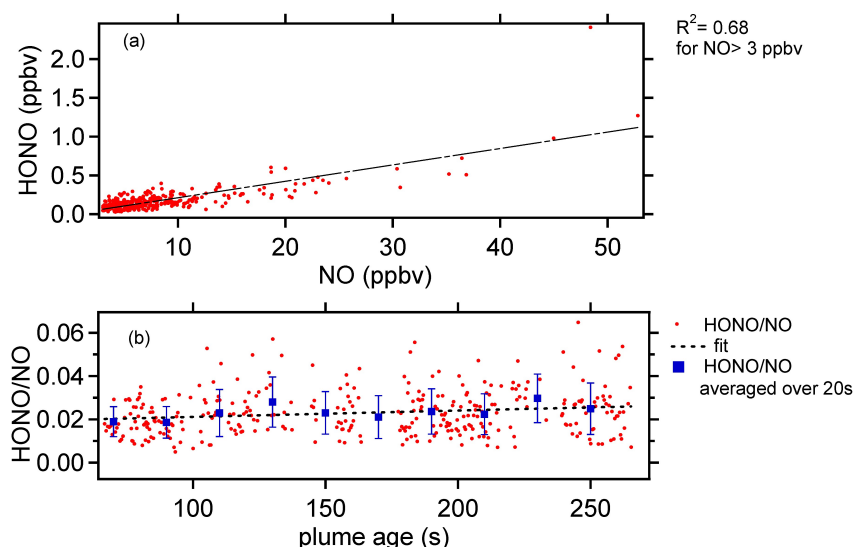


Figure 7.9: (a) A scatter plot of HONO versus NO in the plume of the A380 for plume ages up to 265 s. The fit has a correlation coefficient of $R^2=0.68$ and a slope of 0.021 ± 0.001 . (b) The HONO/NO ratio plotted versus the plume age. The blue squares represent the 20 s averaged data and the standard deviation of the values within the bin are represented by the error bars. No significant changes for plume ages up to 265 s are observed.

fractions. This was done for 13 exhaust plumes from 10 different airliners listed in Table 7.4. For HONO/NO_y the same procedure was applied.

An average ratio of 0.042 ± 0.010 for HONO/NO ratios for all plumes was obtained. HONO/NO_y ratios had an average of 0.031 ± 0.006 . The uncertainty of the ratios is dominated by the uncertainty of the HONO measurements with an estimate of ± 50 %.

The engine specific ratios are plotted as a function of the EI NO_x in Fig. 7.10. The two error bars plotted exemplarily result from the accuracy of the trace gas measurements. Except for the A380 with the highest EI NO_x, no marked tendency of the HONO/NO ratio with the EI NO_x is observed, that means that for every emission index the same amount of NO is converted into HONO. The observation may suggest that for most engines there is no or not yet an OH-limitation acting on the NO_x conversion. Only the value of the HONO/NO ratio of the A380 with a very high EI NO_x appears to be systematically lower. The reaction of HSO₃ with O₂ (7.6) yields HO₂ as the second product which can in turn react with NO to form NO₂ and OH with a similar reaction rate as for the reaction of NO with OH. For high NO mole fractions the SO₂ conversion is not an OH-consuming reaction. Recycled OH is therefore available for NO-conversion.

The value of the A380 may suggest that in the case of a new engine with high EI

NO_x an OH-limitation causes a reduced NO conversion. NO and OH production depends on the combustion-temperature and the combustion chamber design and may be different for new engines [Katragkou et al., 2004]. These temperatures are proprietary to the engine designer. Compared to the other plume measurements the A380 produced the biggest contrail. It was flying in regions with high relative humidity near ice saturation. This may have also contributed to a significantly lower HONO production. A well-founded explanation may be obtained from model simulations taking the engine parameters and the meteorological conditions into account.

There are only few measurements available in-flight for ratios of HONO/NO and HONO/NO_y which makes comparison difficult. Ratios of 0.025 were found for HONO/NO in the exhaust plumes of a B747 at 60 and 75 s [Tremmel et al., 1998; Arnold et al., 1992]. This value is 40 % below the present average but still in good agreement considering the uncertainties and statistical variability.

On the ground HONO/NO ratios were measured for different rated thrust settings using a tunable diode laser spectrometer (TDL) [Wormhoudt et al., 2007]. HONO/NO ratios exhibit a decreases from low rated thrust to higher rated thrust settings. The average values of 0.03 are found at a rated thrust between 60-100 % for the DC-8 CFM-56-2C1 engine. At the lowest rated thrust (4 %) the HONO/NO ratios were high with an average of 0.07. They also discussed the dependence on aircraft type revealing that the B757 RB211-535E4 engine has a significantly lower HONO/NO ratio for all power settings with average values around 0.01. This might also explain the difference to the in-flight ratios of a similar engine [Tremmel et al., 1998] discussed above. The dedicated engine tests were performed at three different distances from the engine exhaust (1 m, 10 m, 30 m) and no marked variations in the HONO emission index were detected. Wood et al. [2008] measured HONO/NO_y ratios behind a CFM-56-2C1 engine at 30 m distance on the ground. The ratios ranged from 0.04 to 0.005 but were distinct for other engines. Given the uncertainties of both measurements, these values agree well with our measurements, however no significant difference in the HONO/NO ratios for the probed engines were observed in the present measurements.

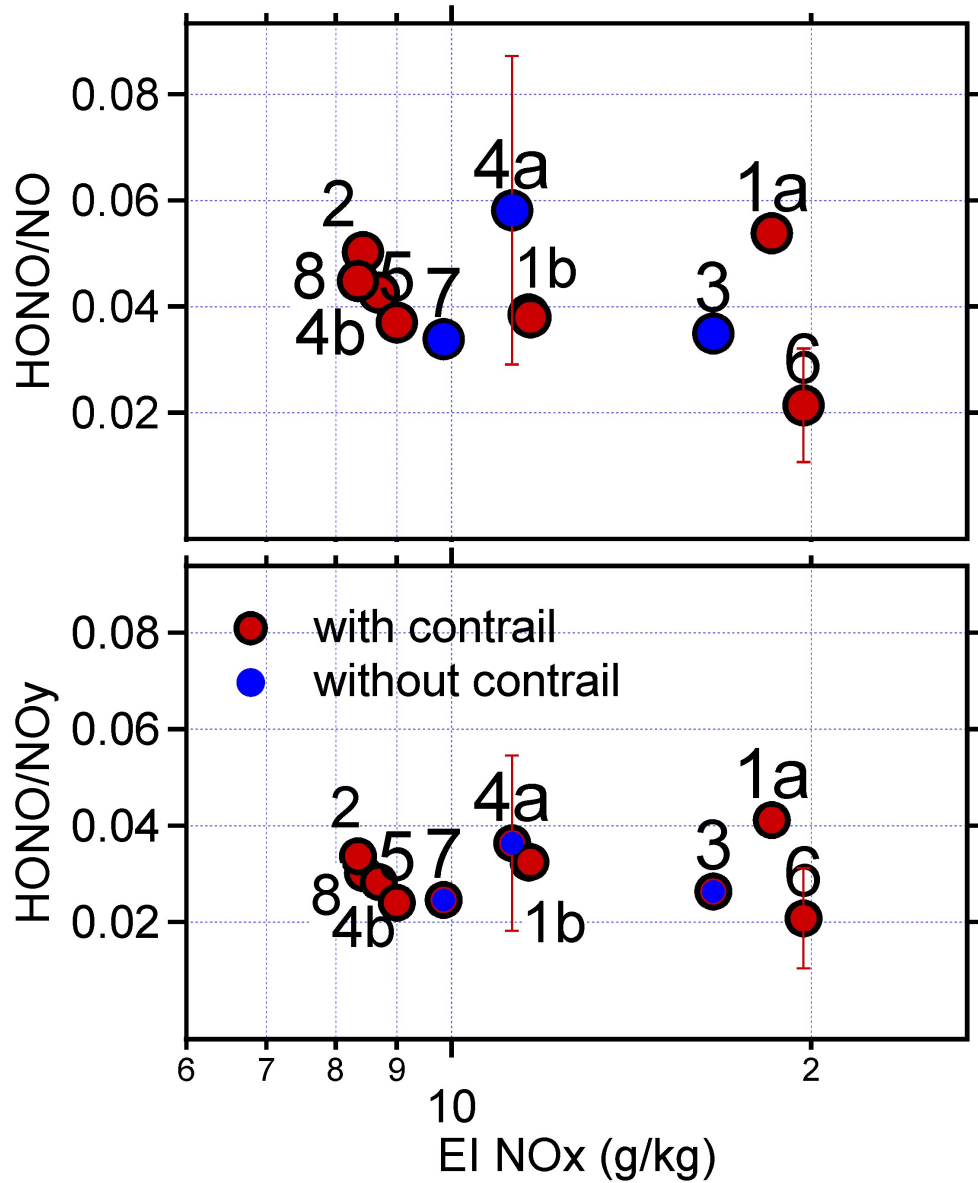
The chemistry of young exhaust plumes is mainly governed by the exhaust chemistry. After the brake up of the vortices entrainment of ambient air starts. The plume development is conveniently divided into three phases: the "jet"-regime where the circulation around the wings forms two counter-rotating vortices which trap the aircraft emission, shielding it from the surrounding atmosphere. During the second phase, the so called "vortex"-regime, the vortices propagate downward due to mutual velocity induction, transporting most of the exhaust emissions downward. The two regimes were clearly observed as for example in the vortex of the A380 7.4. The vertical extension of the plume is proportional to the weight and span of the aircraft and inversely proportional to the velocity. This part is called the primary

vortex. Partial detrainment forms a secondary wake at the original flight level. The "dispersion"-regime is the ultimate stage where the vortices have broken up and dispersion and entrainment of ambient air starts. The effect of plume chemistry with contrail and without contrail on the HONO mole fraction are particularly important for plumes in the dispersion regime. Here NO is converted by ambient hydroxyl radicals to form HONO. The efficiency of this process depends on the availability of hydroxyl radicals thus on the water vapor mole fraction. In the case of persistent contrails dehydration leads to dehydroxylation. Heterogeneous self-reaction of HO_x causes additional depletion of OH. Thus less HONO is produced in the aging plume [Meilinger et al., 2005].

An aged plume of an A320 on 19 October 2008 was measured in the dispersion regime. No further information on the engine data or fuel flow were obtained because the aircraft pilots were not contacted. Therefore no EI NO_x is available. The plume ages derived with the ECMWF wind fields were 520-570 s and due to dilution few data were above the threshold of 3 ppbv NO. To gain a statistically significant data set a lower threshold of 1 ppbv was chosen. Despite the high dilution of the plume, HONO reached maximum mole fractions of 0.21 ppbv. HONO/NO ratios of 0.045 and HONO/NO_y was 3.2 % were measured. These values lie within one standard deviation of the ratios obtained for younger plumes. This observation is striking because the plume age is of the same magnitude as the e-folding time of HONO with respect to photolysis. The NO/NO_y ratio was significantly lower in this plume as compared to younger plumes. A ratio near unity was measured in the plume of the A380 at plume ages of 60 s while NO/NO_y was 71 ± 0.4 % in the plume of the A320 with plume ages between 520 and 570 s. This reduction can be explained by oxidation of NO to NO₂. It may partly explain the evolution of the ratio yet a lower ratio of HONO/NO was expected when photolysis is the dominant removal process of HONO. Alternatively entrainment of ambient OH may have induced NO conversion thus secondary production of HONO which was not originally emitted by the aircraft. Further investigation regarding heterogeneous processes that influence the ratio in aging plumes are needed but cannot be addressed in this work.

7.7 Sulfur conversion efficiency

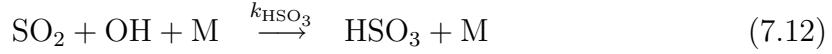
The sulfur conversion efficiency ε was inferred by comparison of the rate of conversion of NO to HONO with the rate of conversion of SO₂ to H₂SO₄ by reaction with OH. The rate limiting step for the latter conversion is the reaction of SO₂ with OH. The reaction rate constant depends on the pressure gradients and temperature inhomogeneities [Lukachko et al., 1998] in the aircraft engine where most of the conversion takes place. These parameters are highly uncertain. However under the assumption of a similar T,p-dependence of the two rate coefficients a lower limit of ε can be inferred using the ratio of the effective rate coefficients.



1 (a+b) A340-311	1 (a+b) CFM56-5C2
2 B737-500	2 CFM56-3C1
3 A340-642	3 Trent 556-61
4 (a+b) A319-111	4 (a+b) CFM56-5B6/P
(5 CRJ-200)	(5 CF34-3B)
6 A380-800	6 Trent 970-84
7 Fokker 70	7 RR Tay Mk620-15
8 B737-3H9	8 CFM56-3B1

Figure 7.10: (a) HONO/NO_y and (b) HONO/NO ratios plotted versus the EI NO_x derived with the DLR Fuel- Flow method. The numbers refer to the different aircraft and engine types. Exemplarily plotted are the error bars for two aircraft.

NO and SO₂ are oxidized by OH in the engine given the three-body collision reaction



At a residence time t_{eng} between 2 and 3 ms behind the combustor exit (see Fig. 7.11) the two reactions yield

$$[\text{HSO}_3](k_{\text{HSO}_3}t_{\text{eng}})^{-1} = [\text{SO}_2][\text{OH}] \quad (7.13)$$

$$[\text{HONO}](k_{\text{HONO}}t_{\text{eng}})^{-1} = [\text{NO}][\text{OH}] \quad (7.14)$$

where k_{HSO_3} and k_{HONO} are the effective rate coefficients. Division of the two equation yields the $[\text{HSO}_3]$ concentration

$$[\text{HSO}_3] = \frac{k_{\text{HSO}_3}}{k_{\text{HONO}}} \frac{[\text{HONO}]}{[\text{NO}]} [\text{SO}_2]. \quad (7.15)$$

Assuming that most of the HSO₃ and SO₃ is converted to H₂SO₄ at plume ages > 3 s [Katragkou et al., 2004] the conversion efficiency is given by

$$\begin{aligned} \varepsilon &= \frac{[\text{H}_2\text{SO}_4] + [\text{SO}_3]}{[\text{SO}_x]} \triangleq \frac{[\text{H}_2\text{SO}_4]}{[\text{SO}_2] + [\text{H}_2\text{SO}_4]} \\ &= \frac{\alpha \frac{[\text{HONO}]}{[\text{NO}]} [\text{SO}_2]}{[\text{SO}_2] + \alpha \frac{[\text{HONO}]}{[\text{NO}]} [\text{SO}_2]} = \frac{\alpha \frac{[\text{HONO}]}{[\text{NO}]}}{1 + \alpha \frac{[\text{HONO}]}{[\text{NO}]}} \\ &= \frac{1}{1 + \frac{[\text{NO}]}{\alpha [\text{HONO}]}} \end{aligned} \quad (7.16)$$

with $\alpha = \frac{k_{\text{HSO}_3}}{k_{\text{HONO}}}$. Thus ε depends only on the ratio of HONO to NO and α .

7.7.1 The ratio of effective reaction rate coefficients

The ratio of the reaction rate coefficients has to be derived for the given temperature and pressure conditions encountered in the engine. The two reaction rate coefficients for the high (k_{∞}) and low (k_0) pressure regime for a termolecular reaction is given by

$$k(T) = A \cdot T^n \cdot \exp(-E_a/RT). \quad (7.17)$$

The values for A, n and E_a/R are taken from Tremmel and Schumann [1999] to allow for a comparison with their model results. Additionally the uncertainty of the rate coefficients which are the same from the present consideration are discussed in their work. Reaction rate coefficients for the two reactions lack measurements at temperatures and pressures encountered in the engine.

	A	n	E_a/R
k_{HSO_3}			
k_0	1.97 e -32	0	-867.3
k_∞	2.0 e -12	0	0
k_{HONO}			
k_0	1.4 e -24	-2.51	-34
k_∞	3.30 e -12	-0.05	-363

Table 7.5: Reaction rate coefficients taken from Tremmel and Schumann [1999]. Reaction rate coefficients k_0 are given in $\text{cm}^6 \text{ molecule}^{-2} \text{ s}^{-1}$ and k_∞ in $\text{cm}^3 \text{ molecule}^{-1} \text{ s}^{-1}$

For the forward reaction rate coefficients the values given in Table 7.5 were applied, assuming a normal Arrhenius behavior for k_0 thus a linear extrapolation to higher temperatures.

The effective reaction rate coefficient k is given by the Troe-equation and depends on the high and low pressure reaction rate coefficients in the following way

$$k = (k_0 \cdot [M] / (1 + k_0 \cdot [M] / k_\infty)) \cdot F_c^{(1 + (\log_{10}(k_0[M]/k_\infty))^2)^{-1}} \quad (7.18)$$

where F_c is 0.6 for k_{HSO_3} and 0.62 for k_{HONO} . The pressure and temperature profile in the post-combustor flow is highly uncertain and may vary in three dimensions. For simplicity uniformity of the engine cross section perpendicular to the flow direction is assumed. While Tremmel and Schumann [1999](Fig. 7.11 (a)) used a hyperbolic pressure gradient and a linear temperature decrease along the axis of flow direction from combustor exit to engine exit, Starik et al. [2002] (Fig. 7.11 (b)) divided the turbine into 4 segments: the high-pressure turbine (HPT), the duct between high-pressure and low-pressure turbine, the medium-pressure turbine (MPT), the three-stage low-pressure turbine (LPT) and the exhaust nozzle.

For these two T,p-profiles the rate coefficients were calculated. The absolute values of the rate coefficient vary by more than an order of magnitude within the post-combustor flow. The temperature and pressure dependence may even deviate from a normal Arrhenius behavior as recently calculated by Somnitz et al. [2005]. They used quantum chemical dynamical calculations to derive a reaction rate coefficient for the oxidation of SO_2 by OH which differs by an order of magnitude from the extrapolated reaction rate coefficient used above. Ergo absolute values of these reaction rate coefficients are uncertain. The method employed in this work profits from the fact that the ratio of the two reaction rate coefficients α is relatively stable ranging from 0.4 to 1.2 in the post-combustor flow. It only relies on the assumption

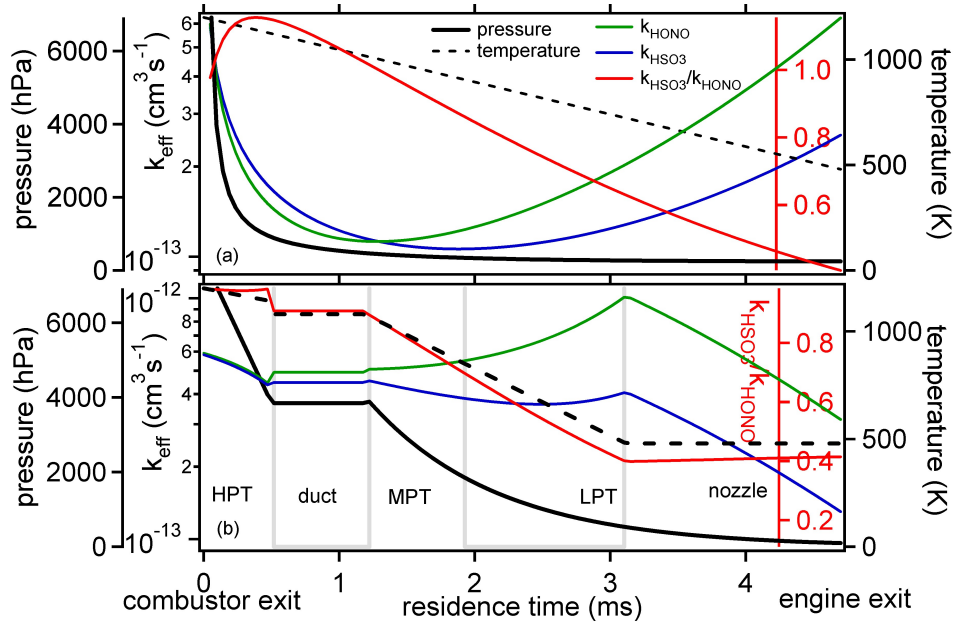


Figure 7.11: The rate coefficient for the reactions of NO and SO₂ with OH and their ratios in the post-combustor flow were derived for two pressure and temperature profiles along the flow axis: (a) Tremmel and Schumann [1999] and (b) Starik et al. [2002]

that the temperature dependence of the two reaction rate coefficients is given by equation 7.17. Average values of 0.6 (case (b)) and 0.8 (case (a)) \pm 30% were derived from the two models. For comparison of ε with the model by Tremmel and Schumann [1999] the latter value will be used. The dependence of ε on HONO/NO and α will be discussed critically later in this section.

Results

The values of ε for the different plumes, engines and aircraft are given in Table 7.4 and plotted as a function of the EI NO_x in Fig. 7.12. The error bars represent the uncertainty given by the HONO and NO measurements. Uncertainties of the rate coefficients are not included. Furthermore uncertainties in the EI NO_x originating from imprecisely reported fuel flow may be as high as 30 %. The data are compared to the model simulations of Tremmel and Schumann [1999] with the results for three different rate coefficients (lower $9.23 \cdot 10^{-14}$ and upper $9.27 \cdot 10^{-13}$ cm³ molecules⁻¹ s⁻¹ limit). The EI NO_x dependence was calculated with their model for one engine (JT9D-7A) thus comparison with other engines is limited. It is conceivable that the decrease in ε with EI NO_x is similar for other engines.

An average value of 3.2 ± 0.7 % for all plumes was inferred. The data agree well within the errors with the model studies. Except for the plumes 4a and 1a, the trend of ε with increasing EI NO_x is well represented: ε tends to decrease with increasing

EI NO_x due to the competing reactions of NO with OH and SO_2 with OH. The two plumes of the A340 (1b) measured on 19 November within a short time interval of 8 min compare well: The difference in the HONO/NO and EI NO_x values are only around 3 %, reflecting the consistency and reproducibility of the measurement. The plume of the second A340 (1a) had the same engine but was measured on the 17 November with the highest HONO values observed during the campaign of 11.7 ppbv. It was a fully loaded, heavy aircraft and starting for a transatlantic flight from Frankfurt.

The plumes 4a and 4b were produced by the same A319 aircraft measured several times during the flight on 19 November 2008 with 2 h time difference. The aircraft was chartered for a 3 to 4 h measurement flight. A reduction in aircraft-weight (4.2 t of fuel have been burned) and speed and a higher flight level resulted in a decreased fuel flow. The HONO/NO ratio decreased from 0.058 to 0.043 and accordingly ε from 4.4 to 3.3 %.

The difference in ε , and similarly in HONO/NO for the two higher values 1a and 4a is not significant with respect to the systematical errors. Again model calculations taking into account the meteorological conditions and engine properties are needed to explain this.

Non-contrail plumes as for example plume 3 of the A340-642 do not seem to deviate from the plumes with contrail. This implies that the trace gas abundances and measurements are not or at least not efficiently affected by the contrail ice particles at these plume ages. Direct sulfuric acid measurements of Curtius et al. [2002] found a difference of more than a factor of 2 for contrail as compared to non-contrail plumes (2.2 % with contrail and 4.8 % without contrail). This was attributed to the uptake of sulfuric acid on contrail particles larger than 1 μm that cannot be sampled by the backward facing inlet. In contrast to H_2SO_4 and HNO_3 , SO_2 and HONO are less soluble in water and have less affinity to ice [Huthwelker et al., 2006]. Thus removal of these emissions from the gas phase in young contrails is not expected.

Discussion of the method

The indirect method presented here to derive ε has several advantages over other methods partly discussed in chapter 7.1:

- It benefits from reliable trace gas measurements. HONO and NO are less susceptible to sampling effects occurring on the walls of the sampling tube than H_2SO_4 .
- It is independent of dilution. The dilution can be inferred using the passive tracer CO_2 and the reported fuel flow. While CO_2 can be measured very precisely the fuel flow reported depends on the accurate reading of the pilot.
- It is independent of the initial OH concentration. OH concentrations in the

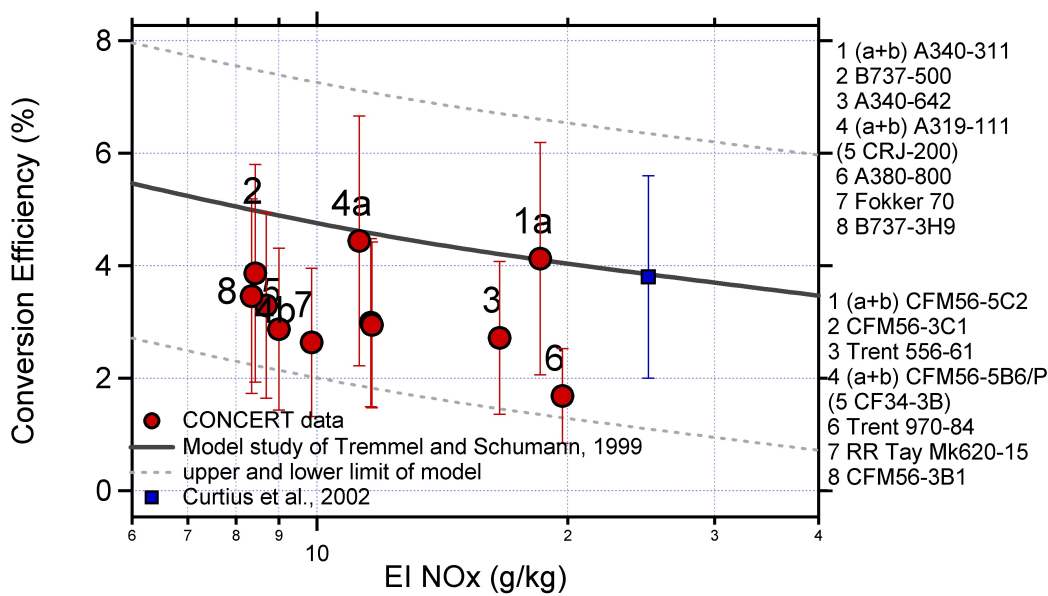


Figure 7.12: The sulfur conversion efficiency for different aircraft is plotted as a function of EI NO_x. ε shows a decline with increasing EI NO_x. The curves represent model simulations by Tremmel and Schumann [1999]. The measured ε by Curtius et al. [2002] is represented by the blue square.

post-combustor flow are still highly uncertain but are not needed for the present consideration because it cancels out.

- The trace gas measurements of NO and HONO are independent of contrail formation for young plumes.

The uncertainties of the indirect method lie in the relative p,T-dependence of the effective reaction rate coefficients and their ratio and the region of the main conversion in the engine. The dependence of ε as a function of HONO/NO for different values of the factor α is shown in Fig. 7.13. The present ε scales linearly with α for the measured HONO/NO ratios. The uncertainty of the reaction rate coefficients is immanent to all chemical models dealing with aircraft engine combustion processes. Further investigation in this field is needed for validation of these reaction rate coefficients.

Furthermore the inferred ε is only a lower limit since only OH oxidation is considered. SO₂ oxidation by O leading to the direct product SO₃ may possibly play an important role in the H₂SO₄ production [Kärcher, 1998]. Conversion in the combustor is not considered, due to an even greater uncertainty of the conversion processes. Other effects like backward reaction, thermal decomposition etc. are also not included. Additionally the uncertainty of the HONO measurements with an estimated uncertainty of $\pm 50\%$ contributes to the overall uncertainty of the method.

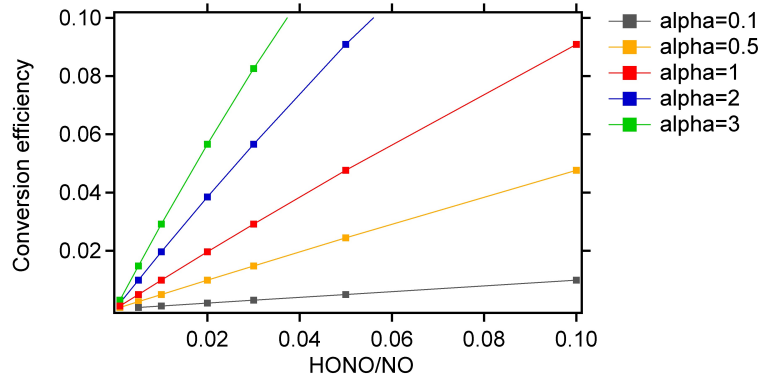


Figure 7.13: The theoretical dependence of the conversion efficiency ε on the HONO/NO ratio and the ratio of effective reaction rate coefficients α .

7.8 Spatial distribution of trace gases inside the exhaust wake

The time resolution of the HONO, SO₂ and NO measurements allowed for a high resolution image of the temporal and spatial trace gas distribution in the plume. Meilinger et al. [2005] discuss the importance of emission altitude with respect to the tropopause which influences NO_x processing in the aging plume. The changes of meteorological parameters encountered by the downward sinking vortex pair may have profound influence on the evolution of the nitrogen oxide partitioning. The downward motion scales with the wingspan, weight and inversely with the speed of the aircraft and may be a few hundred meters for big aircraft [Gerz et al., 1998; Holzäpfel, 2003]. All contrail measurements performed during the 17, 19 and 20 November were in the upper troposphere. Therefore comparison of stratospheric and tropospheric conditions on the engine and plume chemistry was not possible. However the following discussion focuses on the potential effect of a vertical distribution of trace gases e.g. from stratosphere to troposphere.

A case study of the exhaust plume of the A380 was chosen to illustrate the effect of redistributions of trace gases to lower altitudes. The altitude profile of the trace gases is shown in Fig. 7.14. The aircraft is at present the biggest commercial aircraft in use therefore the effects described above are particularly pronounced. In panel (a) and (b) the flight path of the Falcon is plotted as a function of the contrail age and color-coded with the HONO and SO₂ mole fractions. The flight altitude of the A380 is represented by the dashed line with an estimated uncertainty of ± 20 m. The Falcon entered the contrail at an age of 66 s. The contrail was very pronounced with a great horizontal and vertical extension, easily distinguishable from the background atmosphere. Two trailing vortices formed and separated from the secondary wake at flight altitude (see also Fig. 7.3). A detailed description of theoretical and measured wake-vortex separation is given in Sussmann and Gierens [1999]. Separation of the

two contrail parts preferably happens at sub-saturated conditions. However trace gas distributions are not directly governed by relative humidity and therefore show a different profile. A vertical scan inside the plume was performed at contrail ages from 110 to 160 s marked by the grey shaded area. The three panels (c,e,f) on the right show the averaged trace gas distributions (altitude bins of 10 m) with the 10 and 90 percentile derived from measurements within the sequence. A curtain-like distribution starting at the flight altitude of the A380 with a vertical extension of approx. 270 m developed. The decent rate was confirmed by calculations with the P2P model [Holzäpfel, 2003]. The primary wake was not entirely scanned mainly due to high turbulence that troubled the aircraft steering. The maximal trace gas mole fractions are observed in the lower part, the primary wake with 49 ppbv NO, 5.3 ppbv SO₂ and 2.4 ppbv HONO as compared to the upper secondary wake of 1.7 to 5.7 ppbv for NO, 0.07 to 0.13 ppbv for HONO and 0.15 to 0.27 ppbv for SO₂. The ratio of the HONO and NO profiles is shown in panel (d) in Fig. 7.14. The black squares represent values for NO > 3 ppbv. The values scatter around the mean of 0.029 with $\sigma = 0.01$. This is still in good agreement with the value derived at younger contrail ages and demonstrates that the ratio of HONO/NO is not changing within the vertical profile of the contrail, at least not for the considered plume ages. Thus a descent of the primary wake of 270 m as observed in the present case implicates an altitude and meteorological dependent most variable processing of NO.

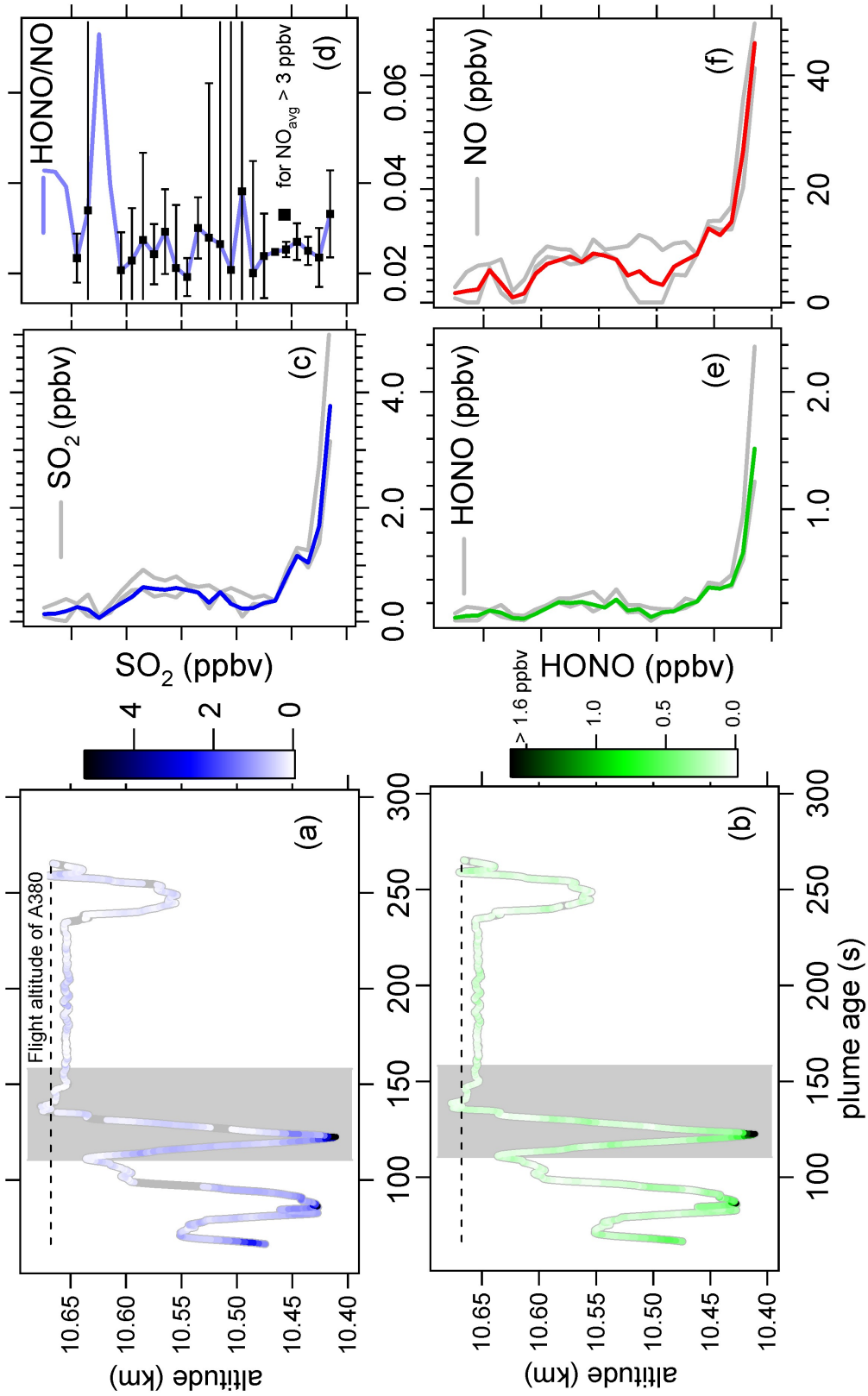


Figure 7.14: Panel (a) and (b): The vertical flight path of the Falcon inside the contrail of the A380 is plotted versus contrail age. Color coded are the trace gas abundances of HONO and SO₂. Also given is the flight altitude of the A380 (dashed line). Panel c, d, e, f show the vertical profile of averaged trace gas distributions obtained from measurements inside the shaded area. The grey lines represent the 10 and 90 percentile profiles. Ratios of HONO/NO are very stable throughout the contrail.

date	aircraft	FSC (mg kg ⁻¹)
17.11.2008	A340-642	103
19.11.2008	A319-111	1155
19.11.2008	A340-300	940

Table 7.6: Fuel sulfur content of three different aircraft.

7.9 Dilution of SO₂

The SO₂ data can be compared to earlier flight measurements when the fuel sulfur content (FSC) is known. Or expressed from a different perspective: Assuming SO₂ to be a passive tracer the dilution of the plume can be inferred. The dilution describes the mixing state of the exhaust air mass, produced by burning a unit mass of fuel, which is mixed per unit flight distance within the bulk of the plume. For a known emission index EI_A of the species A and a measured mole fraction of the trace gas $[A](t)$ at a plume age t the dilution ratio N is given by

$$N(t) = \frac{EI_A M_{air}}{[A](t) M_A} \quad (7.19)$$

where M_{air} is the molar mass of the air and M_A is the molar mass of the species. The dependence on plume age was empirically derived by Schumann et al. [1998] for a set of measurements of CO₂, SO₂, NO_x, NO_y, H₂O in aircraft exhaust plumes performed by different groups and is given by

$$N(t) = 7000(t/t_0)^{0.8} \quad (7.20)$$

where N is the dilution ratio, t_0 is 1 s and t is the contrail age.

During CONCERT kerosine probes from three aircraft were taken after landing and analyzed on their fuel sulfur content. The FSC of the A380 was estimated. The values are given in Table 7.6. The SO₂ emission index (EI SO₂) is 2·FSC. The results are shown in Fig. 7.15. The A319 was probed several times on the same day. The plume ages were derived as explained in section 7.3. The dilution ratio for the present measurements is somewhat overestimated as compared to the approximated fit curve by Schumann et al. [1998]. Except for the A340-642 with the lowest FSC the values lie at least a factor of 2 above the fit curve.

This observation might be explained by the inhomogeneous trace gas distribution within the young exhaust plume in the vortex regime as demonstrated in section 7.8. The primary wake contains the bulk of the trace gases and is transported to lower altitudes. It is less diluted than the secondary wake due to efficient trapping of trace gases in the vortex pairs. Therefore it is important to differentiate where and when

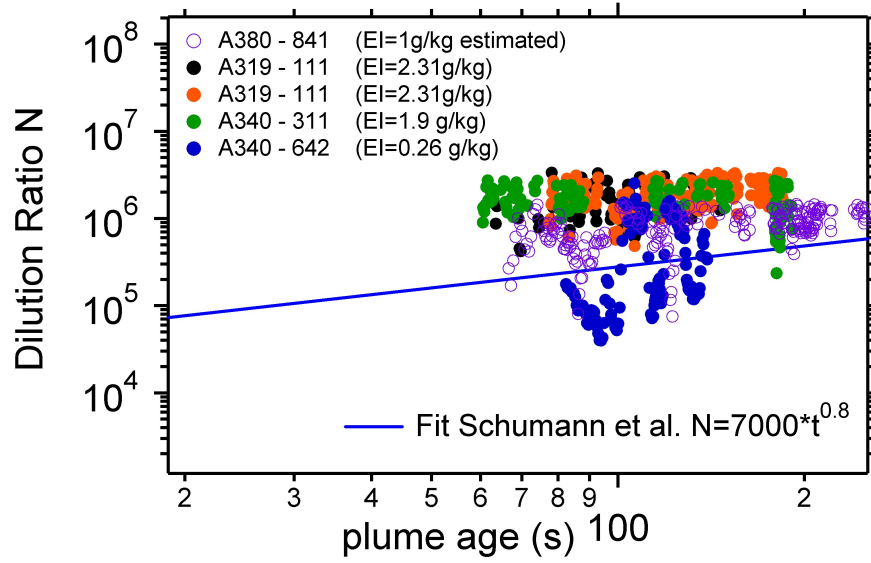


Figure 7.15: The dilution ratio N of SO_2 as a function of the plume age (after Schumann et al. [1998]) for four different aircraft probed during CONCERT as well as the fit from former measurements in aircraft exhaust plumes (time t in s).

(jet, vortex or dispersion regime) the measurements inside the plume took place. The trace gas measurements used for the fit were performed in all regimes. Earlier measurements used to derive the fit curve scatter similarly as the present data with 3 times higher or lower dilution ratios than predicted by the fit. Measurements in the primary wake cannot be compared to measurements in the secondary wake which has a higher dilution ratio. In the wake of the A340-642 the highest SO_2 mole fractions were observed, presumably measured in the primary wake. These data are in good agreement with the fit curve. The method can only be considered as a rough validation of the present measurements.

Chapter 8

Conclusion and outlook

A novel method using a previously introduced ion trap mass spectrometer was for the first time combined with SF_5^- reagent ions for the detection of SO_2 , HCl , HNO_3 and HONO during this thesis. The instrument with a newly designed inlet was calibrated and characterized. The system has been successfully deployed on the research aircraft Falcon and was operated during the CONCERT campaign in October/November 2008. Measurements have been performed in the tropopause region and in aircraft exhaust plumes at cruise altitude. Two major aspects regarding the atmospheric chemistry of the tropopause region were discussed based on the ITCIMS measurements: What are the effects of sulfate particles of volcanic origin on the HCl , HNO_3 and NO_y budget in the lowermost stratosphere? And how large are the effective emissions of the oxidation products of NO and SO_2 of commercial aircraft at cruise altitude?

Instrumental achievements and future work

The combination of an ion trap chemical ionization mass spectrometer with SF_5^- reagent ions has been employed for the first time during airborne measurements. The system was characterized with respect to sensitivity, detection limit, systematic and statistical errors, transmission of the sampling line and response time. Furthermore potentially interfering trace gases were tested. Water vapor mole fractions of up to 200 ppmv, O_3 up to 500 ppbv, NO and NO_2 up to 150 ppbv and 8 ppbv, respectively, did not affect the present measurements at altitudes above 7 km. An in-flight calibration system using a newly designed permeation oven was built and deployed during airborne measurements to account for wall effects of HNO_3 . Calibration procedures for SO_2 , HCl and HONO were introduced and discussed regarding their application to the aircraft measurements. In particular the reactions of HONO and SO_2 with SF_5^- was for the first time employed for atmospheric measurements. HONO calibration of the instrument was performed with the LOPAP instrument in the laboratory and gave important insight into the reaction mechanism. Water vapor dependencies of the ion molecule reactions have been assessed qualita-

tively, because only low water vapor mole fractions (below 200 ppmv) were encountered during the flights and did not affect the measurements. Future work with the detection scheme will have to address this problem in detail.

Furthermore a fast and effective background measurement would be desirable. The present work employed dry nitrogen that was added in the upper part of the sampling line, with long response times. Water vapor dependent background measurements cannot be performed with this method. Alternatively filters or NaCO₃-coated denuder tubes may be used for background measurements.

A servo-controlled valve has been developed, with all wetted parts fabricated of PFA to improve the transmission of the sampling line. The transmission was significantly improved compared to a stainless steel valve however more effort into a surface reduction of the relevant parts is needed. Sampling of HNO₃ in the troposphere is still problematic and needs further improvements of the sampling technique. A reduction of the HNO₃ background produced by the ion source is desirable. The use of isotopically labeled standards should be pursued. The present work suggests different isotopic labels that were not installed for the present measurements but may improve the accuracy significantly if employed in future measurements.

Results from measurements in the stratospheric volcanic sulfur plume

First airborne measurements with the ITCIMS instrument measuring HCl, HNO₃ and SO₂ in the tropopause region have been successfully performed.

On 31 October 2008, a layer with strongly increased SO₂ (> 500 %) and substantially increased HCl (19 %) was detected over Europe in the lowermost stratosphere at altitudes between 7000 and 11600 m. The plume originated most likely from the eruption of the Aleutian volcano Kasatochi, since other potential sources have been ruled out. For the molar ratio HNO₃/NO_y an upper limit increase of 19 % was obtained. Correlation of HNO₃ with ozone shows an enhancement of up to 50 % for inside plume conditions compared to outside plume conditions. The observation can be explained by large sulfate aerosol surface areas that can enhance NO_x-conversion to HNO₃ via N₂O₅ hydrolysis. Excess SO₂ (dSO₂) and excess HCl (dHCl) reached up to about 500 and 25 pptv in the volcanic plume. The average ratio dSO₂/dHCl of about 10 measured in the plume on 31 October was about 7 times smaller than the dSO₂/dHCl observed by satellite measurements on 10/11 August in the young volcanic eruption plume in the lower stratosphere. This indicates that ~ 86 % of the initial SO₂ has been converted to particulate sulfate within 85 days after the eruption. A similar conclusion can be drawn from the fraction of particulate sulfate to total sulfur (SO₄²⁻/(SO₂+SO₄²⁻)) that ranges around 0.76 for stratospheric air masses. This implies an e-folding SO₂-lifetime of about 41 to 60 days.

The measurements represent a new independent approach to estimate the SO₂ life-

time in the lower stratosphere at northern latitudes. The inherent stratospheric trace gas relations of HCl and O₃, HNO₃ and O₃ and HNO₃ and NO_y can be altered through volcanic sulfur injection.

Results from measurements in the wake of commercial airliners

SO₂ and HONO measurements have been successfully performed with the ITCIMS in the wake of commercial airliners at cruise altitude with a time resolution of 1.6 s and a detection limit of approx. 70 pptv. The HONO-CIMS measurements comprised for the first time laboratory-calibrated airborne measurements in young aircraft exhaust plumes. 10 airliners with 13 plume encounters were probed. Simultaneous measurements of NO and HONO revealed good correlation of the two trace gases. HONO/NO and HONO/NO_y molar ratios have been derived. An average ratio of 0.042 ± 0.01 for HONO/NO ratios for all plumes was obtained. HONO/NO_y ratios had an average of 0.031 ± 0.006 for young aircraft exhaust plumes. The uncertainty of the ratios is dominated by the error of the HONO measurements with an estimated error of 50 %. In addition the spatial distribution of SO₂, NO and HONO inside the plume of the A380 was determined.

Based on these measurements a comparison of the two oxidation processes of SO₂ with OH and NO with OH an attempt was made to infer a lower limit of the fuel sulfur conversion efficiency. An average value of 3.2 ± 0.7 % for all plumes was derived and compares to model studies and earlier measurements. The data agree well within the measurement errors with earlier direct CIMS measurements of total sulfuric acid made by MPI-K.

Outlook

Future work may concentrate on the dependence of the HONO/NO ratio and the conversion efficiency on meteorological parameters such as relative humidity, temperature and pressure (see also the Appendix). Contrail formation may influence the ratio of HONO/NO. In addition consideration of aircraft parameters such as combustion temperature, pressure ratios and engine design may help to understand the effective emission ratios.

Model simulation dealing with particle formation and growth in the stratospheric SO₂ plume of Mt. Kasatochi may help to understand and support the measured particle concentrations and sizes and the heterogeneous processes taking place on these particles. The particle concentrations and diameters presumably changed over the three months residence time in the stratosphere due to nucleation, condensation and coagulation. Future work may focus on the influence of light absorption and scattering of the aerosol particles in the layer over the 3 months time period.

List of Figures

2.1	Relative ion abundance versus trace gas concentration	7
2.2	The ion trap mass spectrometer	9
2.3	Difference spectrum at SO ₂ injection	12
2.4	Reaction scheme of SF ₅ ⁻	16
2.5	Dependence of ion signal on N ₂ and SCF ₈	19
2.6	Dependence of ion signal on the pressure	20
3.1	Calibration of HCl	25
3.2	The profile of the in-flight calibration oven	26
3.3	Calibration of the HNO ₃ standard	27
3.4	Calibration of HNO ₃	28
3.5	Calibration of SO ₂	29
3.6	The scheme of the LOPAP instrument	31
3.7	Calibration spectrum with HONO and SO ₂	32
3.8	Product ions of the reaction SF ₅ ⁻ with HONO	33
3.9	Derivation of $kt_r T$	34
3.10	Fragmentation studies	36
3.11	Fragmentation of primary products	37
3.12	Relative errors of the ion signals	38
3.13	Nitric acid background measurements	41
3.14	Laboratory tests with DCl	44
3.15	Calibration spectrum with isotopically labeled standards	45
4.1	Dependence of SF ₅ ⁻ on the water vapor mole fraction	49
4.2	Spectrum with high water vapor	50
4.3	SO ₂ and HNO ₃ product ion versus H ₂ O	51
4.4	HONO product ion signal versus H ₂ O	52
4.5	Ion abundance ratios versus NO ₂ and NO	53
4.6	Ion abundance ratios versus O ₃	54
5.1	Photo of the ion trap	59
5.2	Schematic diagrams of passive and active flow configurations	60
5.3	Tests with coated flow tube	61
5.4	Calibration flow diagram	64

6.1	Effects of explosive volcanic eruptions	70
6.2	GOME-2 and OMI SO ₂ satellite measurements	74
6.3	Tropopause height on 31 October 2008	76
6.4	GOME-2 satellite measurements on 30 October 2008	77
6.5	In-flight ion mass spectrum	78
6.6	Vertical cross section of the temperature on 31 October 2008	79
6.7	Time sequences during flight A and B on 31 October 2008	81
6.8	Altitude profile of flight A and B	82
6.9	Mixture of air masses during ascent	83
6.10	Tracer-tracer correlation	84
6.11	Backward trajectories	86
6.12	Scatterplot of HCl versus O ₃	87
6.13	Scatter plot of HNO ₃ versus O ₃	90
6.14	Abundance ratio HNO ₃ /NO _y versus O ₃	91
6.15	Potential temperature profiles of converted sulfur	93
7.1	The EI NO _x versus engine load	97
7.2	Temporal evolution of secondary oxidation products	99
7.3	Photo obtained during contrail measurement on 19 November 2008	106
7.4	Photo taken inside the contrail of an A380	107
7.5	Advected contrail of the A380	108
7.6	Plume ages for measured plumes on 19 October 2008	108
7.7	Overview on contrail encounter	109
7.8	Spectrum inside an aircraft plume	110
7.9	HONO versus NO in the A380 plume	114
7.10	HONO/NO and HONO/NO _y versus EI NO _x	117
7.11	Ratio of reaction rate coefficient	120
7.12	Epsilon versus EI NO _x	122
7.13	Epsilon dependence on HONO and α	123
7.14	Distribution of trace gases in the contrail	125
7.15	Dilution ratio of SO ₂	127
A.1	HCl versus O ₃ on 28 October 2008	139
A.2	Outlook: HONO/NO versus RHi	139
A.3	Flight path campaign overview	140
A.4	Flight 27 October 2008	142
A.5	Flight 28 October 2008	143
A.6	Flight 29 October 2008	144
A.7	Flight 02 October 2008	145
A.8	Flight 07 October 2008	146

List of Tables

2.1	Measured mass discrimination values	11
2.2	Compilation of ion mass numbers and identification of detected ions .	17
3.1	Permeation rates of HCl	24
3.2	Abundance ratios of SO ₂ and HCl isotopes	30
3.3	Gas phase acidities and proton affinities	36
3.4	Estimated contributions to the accuracy of the measurement	40
3.5	Detection limits	43
5.1	Ion trap MS settings during CONCERT	58
5.2	Temperature, pressure and flow parameters in the sampling lines . . .	62
6.1	Measurements of emission ratios for recent volcanic eruptions	89
7.1	ICAO LTO cycle	97
7.2	A chronological list of measurements and model studies contributing to an understanding of the sulfur conversion efficiency.	102
7.3	Overview of contrail plumes during CONCERT	105
7.4	Overview of CONCERT results	113
7.5	Reaction rate coefficients	119
7.6	Fuel sulfur content of three different aircraft.	126
A.1	Detection limits for 5 flights	138
A.2	Overview of the CONCERT missions	141

Appendix A

This chapter presents all additional flights performed during the CONCERT-chemistry and CONCERT-2-contrails campaign. Additional measurements of CO, O₃, NO_y (DLR) and particulate sulfate (MPI-C) mole fractions are also plotted.

During the missions on 2 November 2008 and 7 November 2008 the bypass sampling line was deployed. A shorter 1/4" PFA sampling line with a Swagelok 1/4" valve for pressure control was used. The second flight employed a reduced pressure of 30 hPa in the flow tube due to technical problems. HONO and HCl were not calibrated for these setups. The detection limits for the 2 flights are given in Table A.1 together with the 3 additional flights with the actively pumped sampling line which were not shown before. In general the high detection limit during the flight on the 2 November 2008 and the reduced pressure during the flight on the 7 November 2008 make a comparison of the two sampling setups difficult. A direct comparison cannot be done because the bypass sampling line was not calibrated. The dilution (of the order of 10³) for the HNO₃ standard would be too high to achieve reasonable concentrations for the detection with the ITCIMS instrument. The high detection limits may originate from a turbulent flow in the bypass sampling line that may have caused continuous attachment to and detachment from the walls. A final conclusion on the comparison of both sampling techniques with a recommendation for either sampling line cannot be done. Both sampling lines were adequate for measurements of HNO₃ in the stratosphere. Further effort is needed for a judgement based on quantitative measures.

The principle aims and achievements of the 12 mission flights are listed in Table A.2 and an overview on the flight paths for the 12 missions is given in Fig. A.3.

As example of the dependence of the HONO/NO ratio on the meteorological conditions the ratio is plotted versus the RHi in Fig. A.2. The RHi values are averaged over the whole measurement sequence therefore comprise measurements inside and outside of the contrail/plume. The HONO/NO ratio shows a decrease with increasing RHi, thus it is lower if a contrail forms behind the aircraft. Heterogeneous processes that influence either the HO_x (dehydroxylation) or the HONO

date	HCl	HNO ₃	SO ₂	HONO
27 October 2008	35 (20)	126 (20)	31 (10)	-
28 October 2008	38 (20)	106 (20)	47 (10)	-
29 October 2008	23 (20)	27 (20)	19 (10)	-
02 November 2008	-	150 (20)	80 (2)	134 (2)
07 November 2008	-	32 (20)	31 (10)	-

Table A.1: Detection limits in pptv for 5 additional flights with the ITCIMS instrument. The number in brackets represents the number of spectra that were averaged (running mean).

(trapping) abundance may explain the observed trend. Model studies are needed to understand the chemistry in the young exhaust plumes and their dependence on the meteorological conditions.

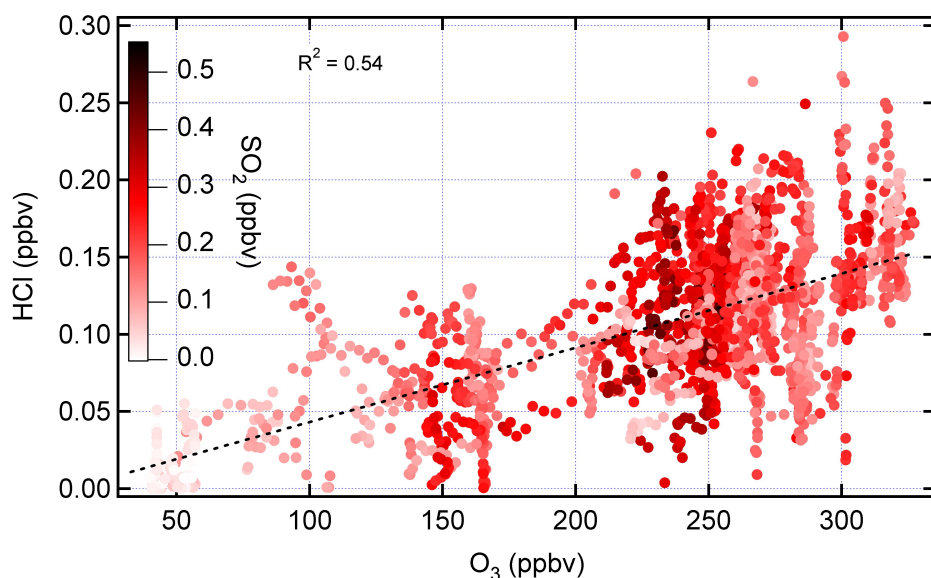


Figure A.1: Mole fractions of HCl versus O₃ on 28 October 2008. A slope of $4.8 \cdot 10^{-4}$ was obtained which compares well to former measurements of Marcy et al. [2004] with a slope of $4.4 \cdot 10^{-4}$

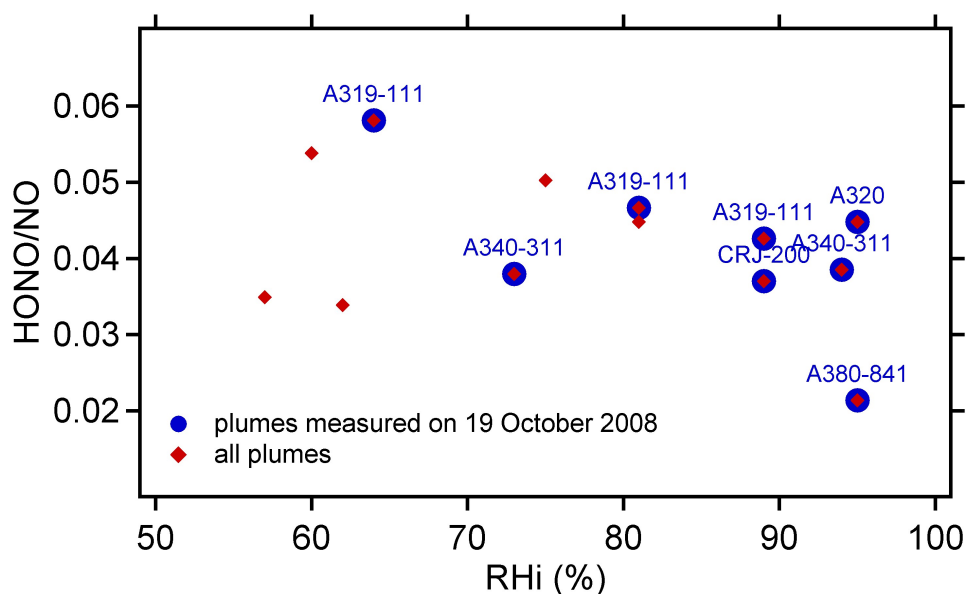


Figure A.2: The HONO/NO ratios are plotted versus the relative humidity with respect to ice (RHi) for all aircraft probed during CONCERT (red circles). The blue circles represent the measurements on the 19 November 2008 where the A319 was probed three times, the A340 two times and additionally a CRJ2, an A320 and an A380 were probed. These data reveal a trend of a decreasing HONO/NO ratio with RHi.

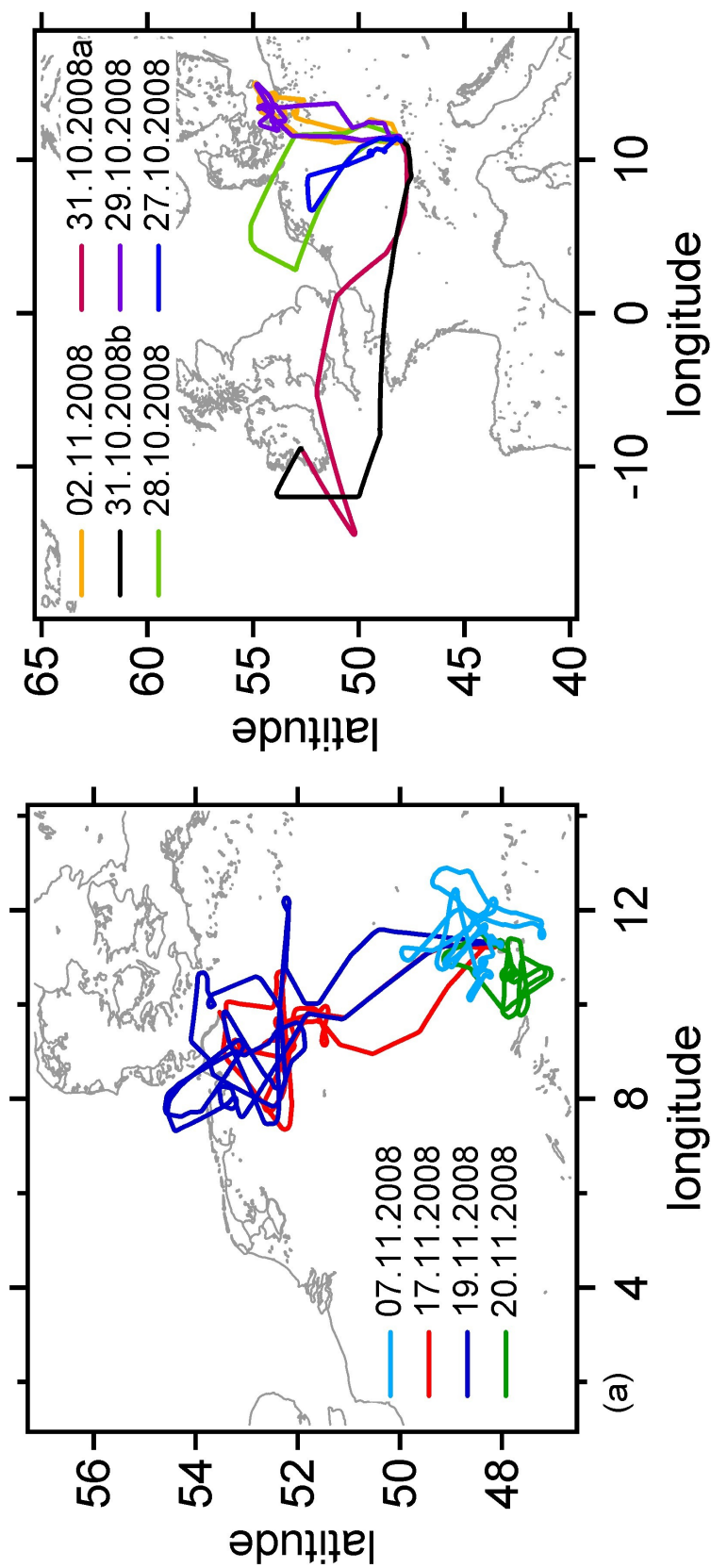


Figure A.3: Flight path of the Falcon for all flights during the CONCERT - chemistry (b) and the CONCERT-2-contrails (a) campaign.

date	take-off	landing	mission
CONCERT-chemistry			
27.10.2008	OP	OP	instrument test flight
28.10.2008	OP	OP	stratospheric intrusion over Northern Germany, UT/LS chemistry
29.10.2008	OP	OP	contrail measurements in the tra-region over Meckl.-Vorpom.
31.10.2008a	OP	SNN	stratospheric intrusion, Western Europe flight corridors (see chapter 6)
31.10.2008b	SNN	OP	stratospheric intrusion, Western Europe flight corridors (see chapter 6)
02.11.2008	OP	OP	contrail measurements in the tra-region over Meckl.-Vorpom., BP
CONCERT-2-contrails			
07.11.2008	OP	OP	instrument test flight, cirrus probing over Southern Germany, BP
11.11.2008	OP	OP	engine break down
17.11.2008a	OP	HH	contrail measurements, see chapter 7
17.11.2008b	HH	OP	contrail measurements, see chapter 7
19.11.2008a	OP	HH	contrail measurements: A319, A340, "two-contrails-flight", see chapter 7
19.11.2008b	HH	OP	contrail measurements: A380, B767, CRJ2, see chapter 7
20.11.2008	OP	OP	contrail and cirrus measurements, see chapter 7

Table A.2: An overview of all mission flights during the CONCERT-chemistry and CONCERT-2-contrails campaign. (OP=Oberpfaffenhofen, HH=Hamburg, SNN=Shannon). BP refers to measurements with the bypass tubing (see chapter 5).

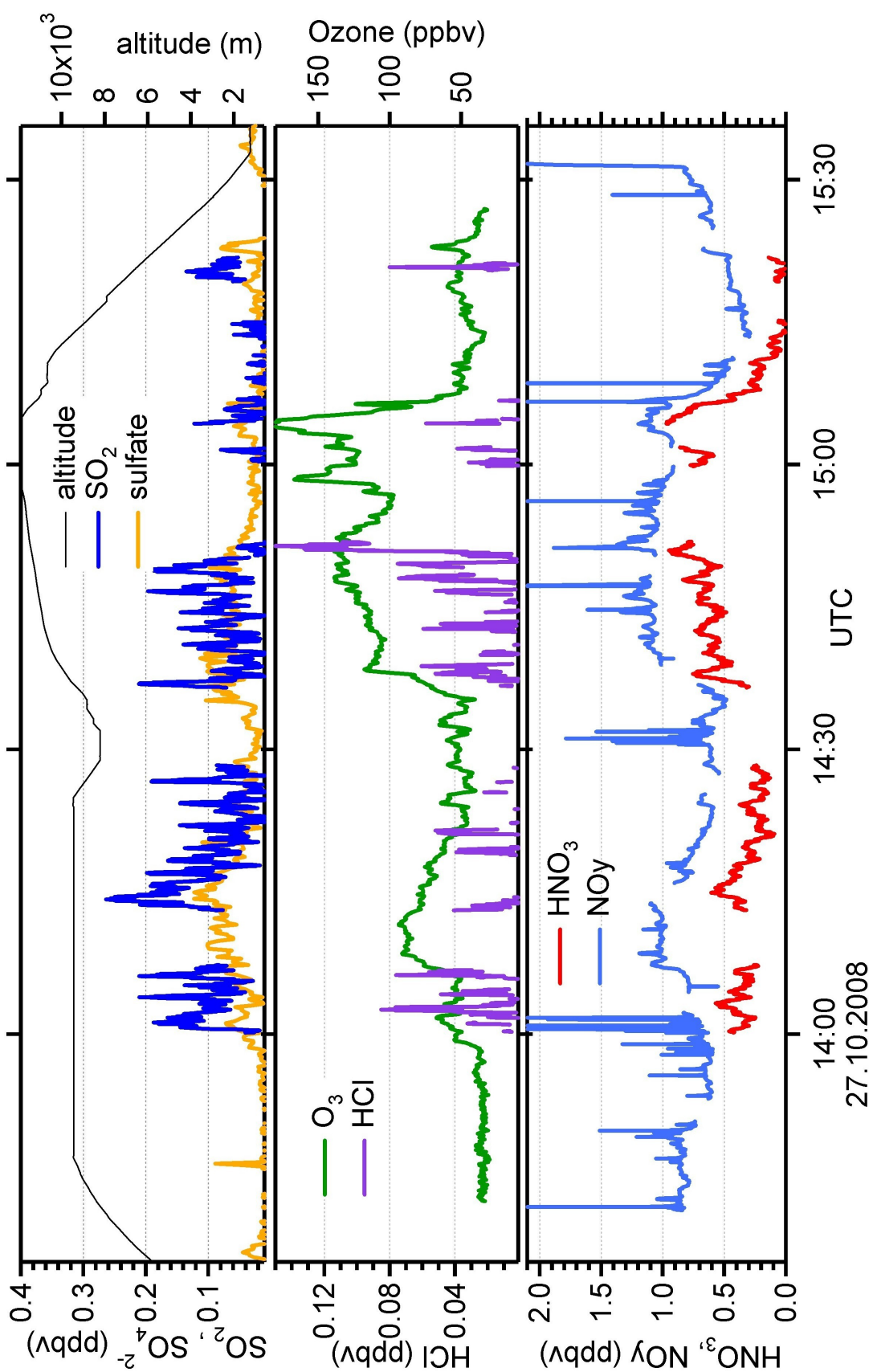


Figure A.4: Instrument test flight with take-off and landing in Oberpfaffenhofen.

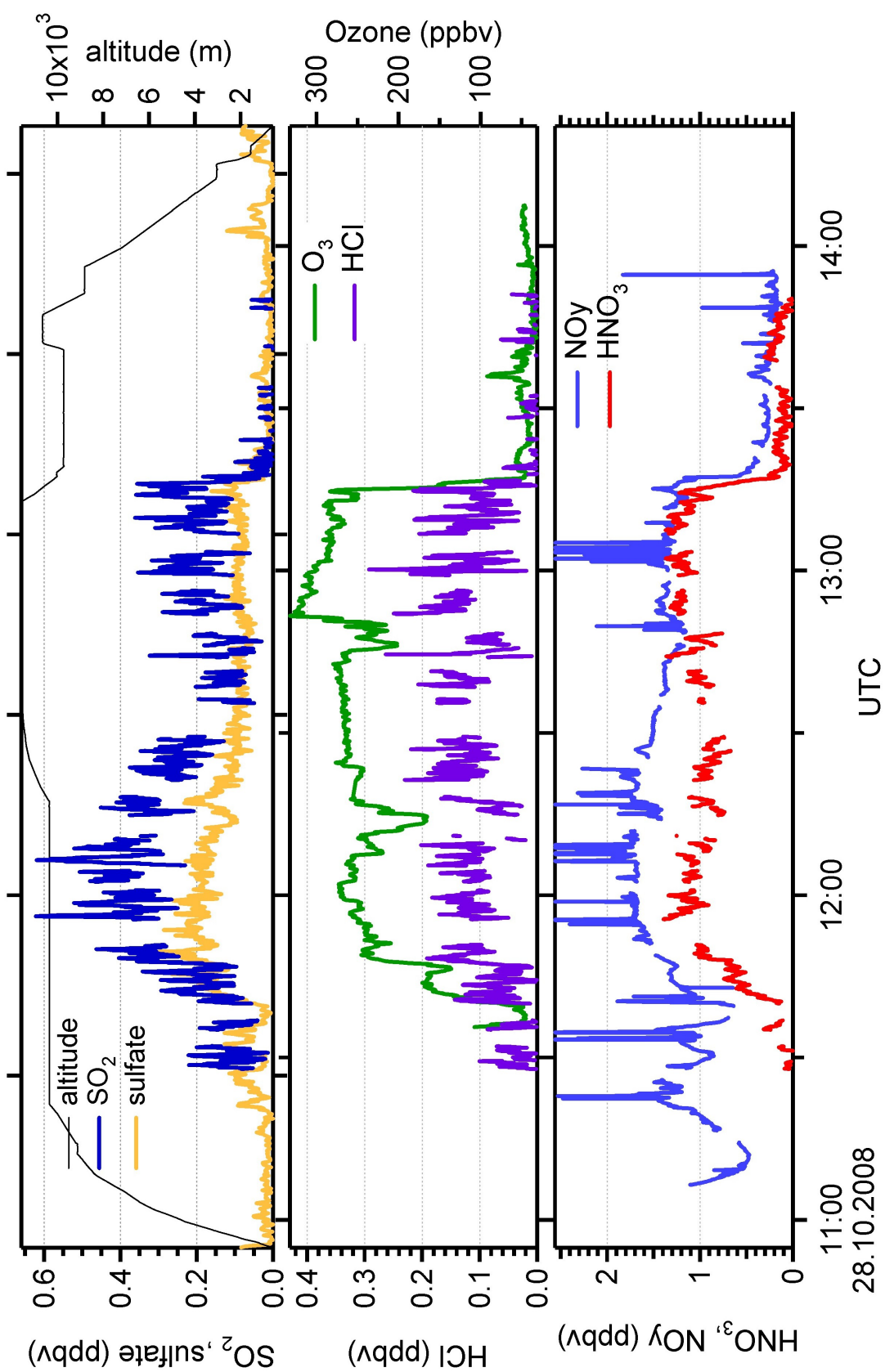


Figure A.5: Measurement in a stratospheric intrusion.

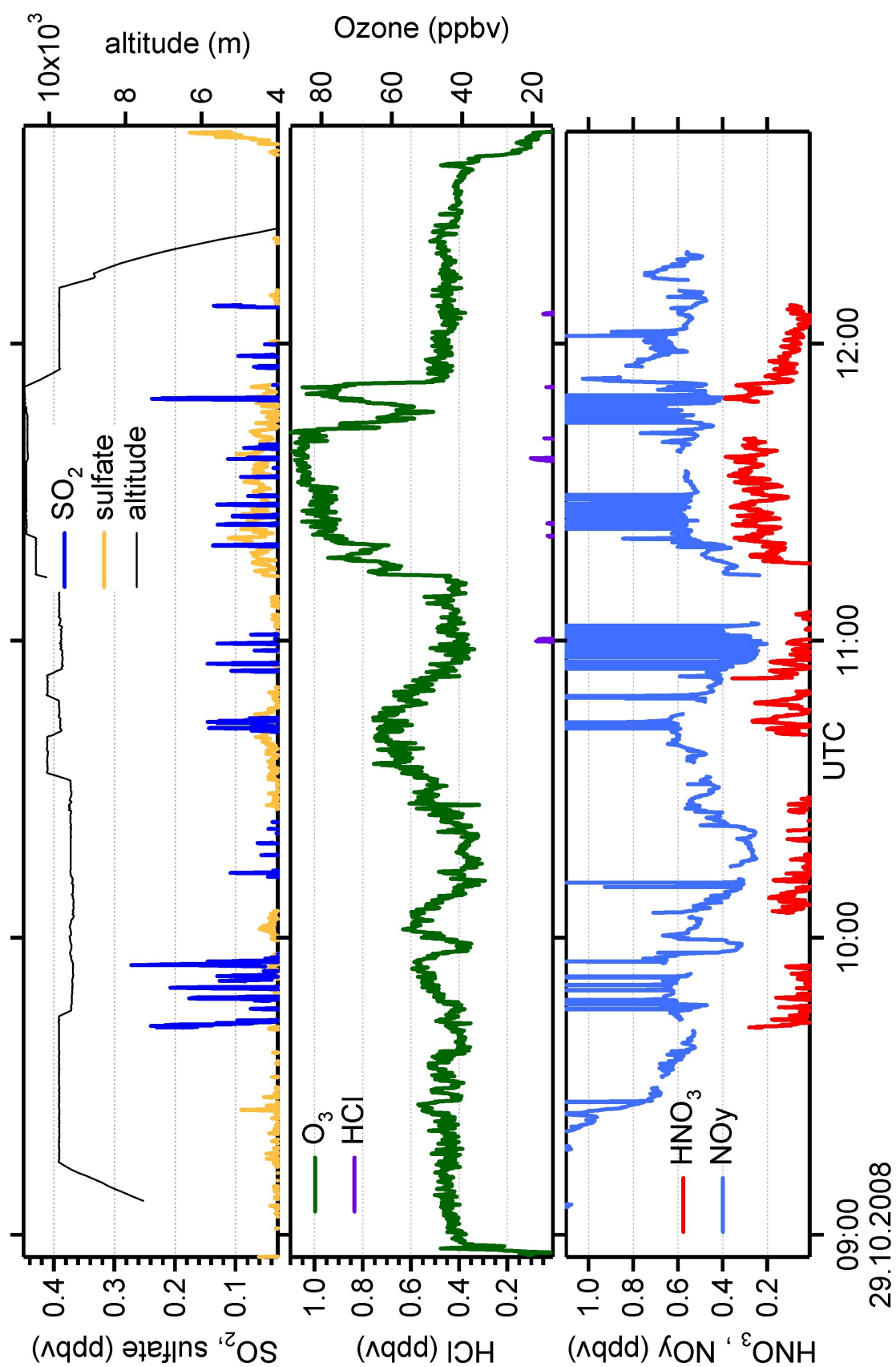


Figure A.6: Contrail measurements over Northern Germany.

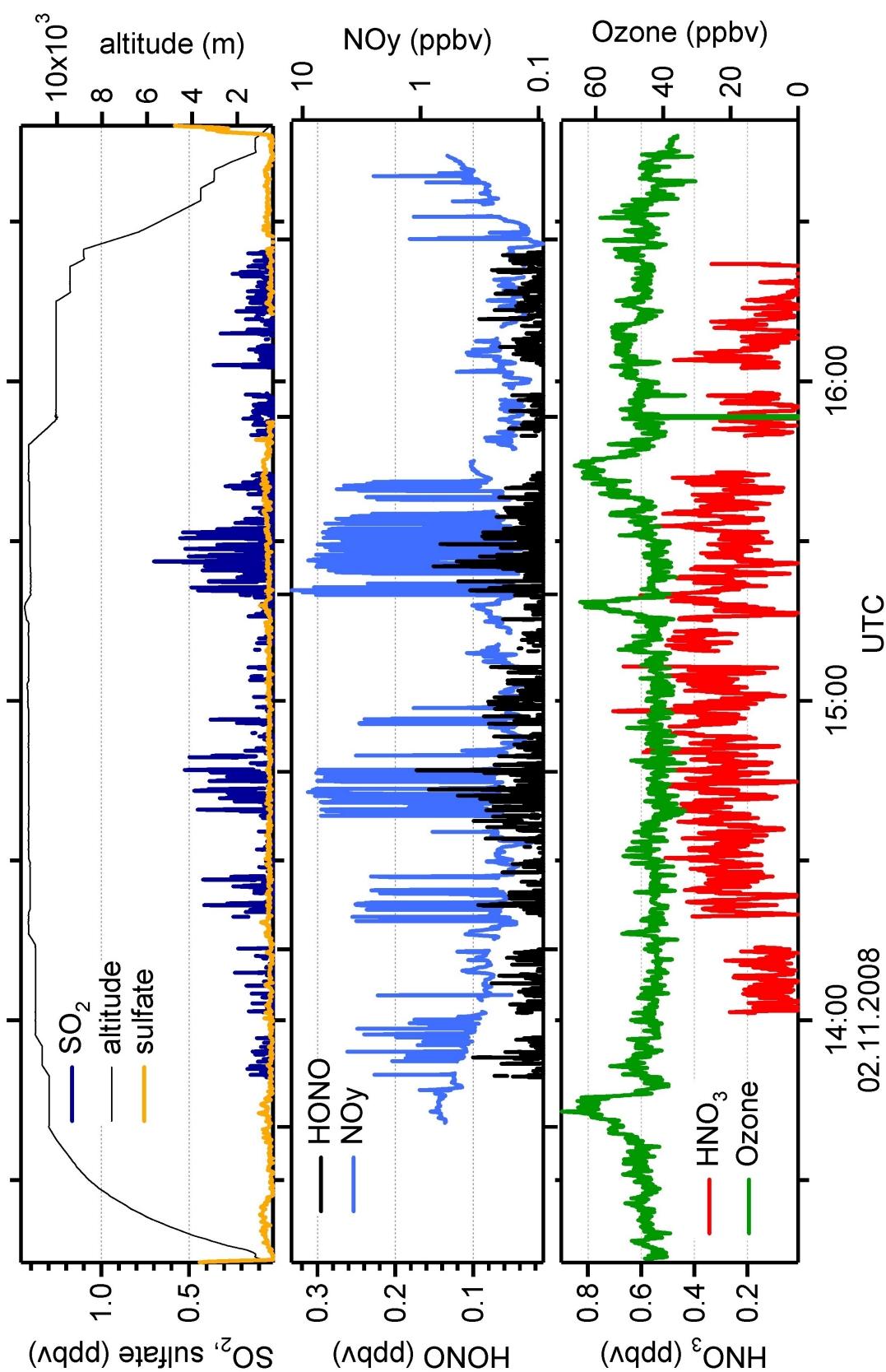


Figure A.7: Contrail measurement over Northern Germany. Measurements performed with the bypass sampling line.

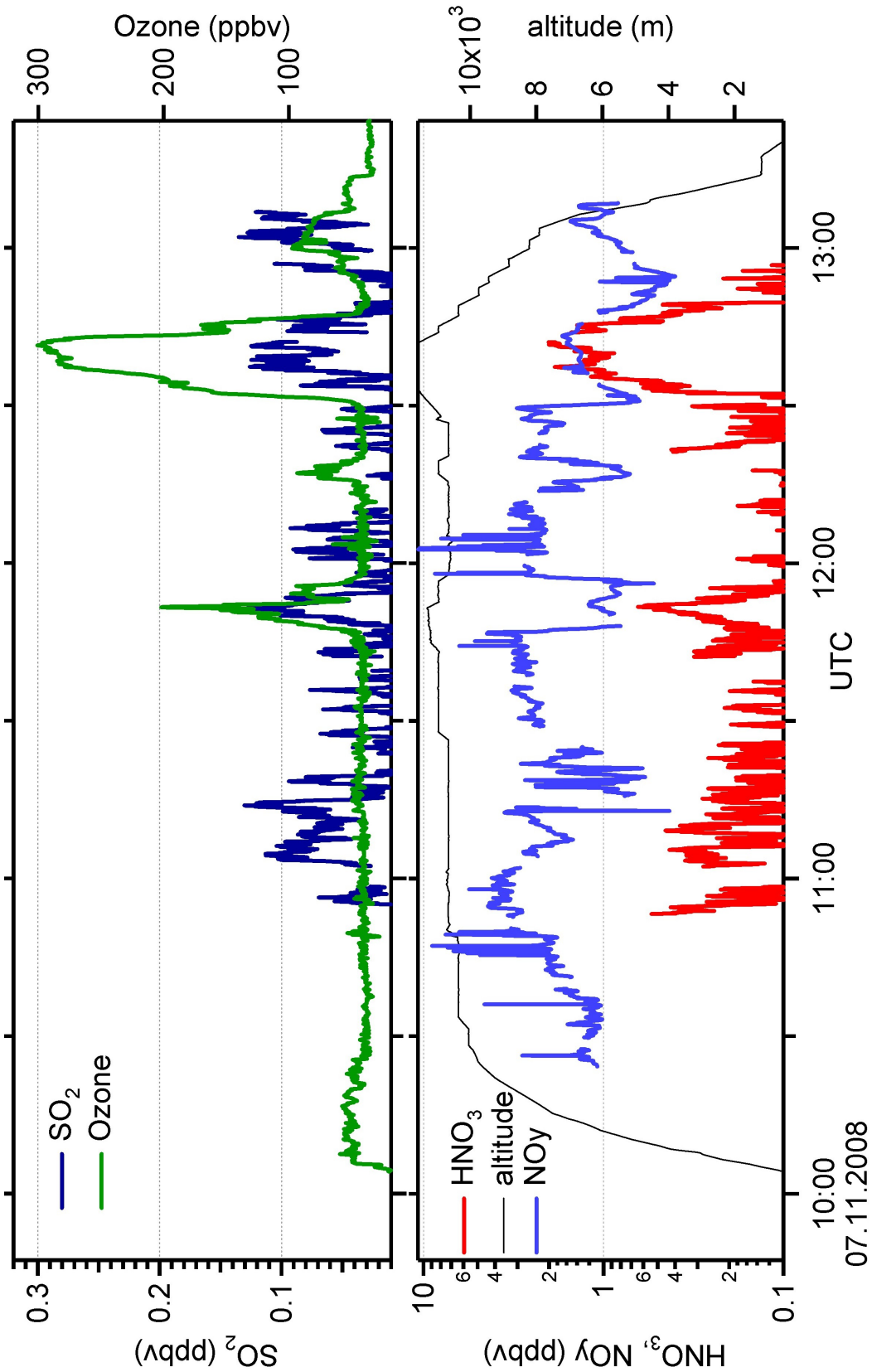


Figure A.8: Instrument test flight for the second part of the campaign. Measurement with the bypass sampling line at reduced pressure (30 hPa) in the flow tube.

Bibliography

- B. Alicke, A. Geyer, A. Hofzumahaus, F. Holland, S. Konrad, H. W. Pätz, J. Schäfer, J. Stutz, A. Volz-Thomas, and U. Platt. OH formation by HONO photolysis during the BERLIOZ experiment. *J. Geophys. Res.*, 108(D4):8247, 2003.
- A. Ansmann, F. Wagner, U. Wandinger, I. Mattis, U. Gärdsdorf, H.-D. Dier, and J. Reichardt. Pinatubo aerosol and stratospheric ozone reduction: Observations over central Europe. *J. Geophys. Res.*, 101(D13):18775–18785, 1996.
- F. Arnold and R. Fabian. First measurements of gas phase sulfuric acid in the stratosphere. *Nature*, 283:55–57, 1980.
- F. Arnold and G. Hauck. Lower stratospheric trace gas detection using aircraft-borne active chemical ionization mass spectrometry. *Nature*, 315:307–309, 1985.
- F. Arnold and S. Spreng. Balloon-borne mass spectrometer measurements of HCL and HF in the winter arctic stratosphere. *Geophys. Res. Lett.*, 21(13):1255–1258, 1994.
- F. Arnold, Th. Bührke, and S. Qiu. Evidence for stratospheric ozone-depleting heterogeneous chemistry on volcanic aerosols from El Chichón. *Nature*, 348:49–50, 1990.
- F. Arnold, J. Scheid, Th. Stilp, H. Schlager, and M. E. Reinhardt. Measurements of jet aircraft emissions at cruise altitude: The odd-nitrogen gases NO, NO₂, HNO₂ and HNO₃. *Geophys. Res. Lett.*, 19(24):2421–2424, 1992.
- F. Arnold, T. Stilp, R. Busen, and U. Schumann. Jet engine exhaust chemiion measurements: implications for gaseous SO₂ and H₂SO₄. *Atmospheric Environment*, 32(18):3073–3077, 1998a.
- F. Arnold, K.-H. Wohlfrom, M.W. Klemm, J. Schneider, K. Gollinger, U. Schumann, and R. Busen. First gaseous ion composition measurements in the exhaust plume of a jet aircraft in flight: Implications for gaseous sulfuric acid, aerosols, and chemiions. *Geophys. Res. Lett.*, 25(12):2137–2140, 1998b.
- P.W. Atkinson and J. de Paula. *Physikalische Chemie*. Wiley-VCH, 2006.
- H. Aufmhoff. *Atmosphärische gasförmige Vorläufer von Aerosol and Ozon: Messungen mit CIMS-Methoden auf einem Flugzeug und am Boden*. PhD thesis, University of Heidelberg, 2004.
- A. Bandy, D.C.Thornton, and A.R.Driedger. Airborne measurements of sulfure dioxide, dimethyl sulfide, carbon disulfide, and carbonyl sulfide by isotope dilution gas chromatography/mass spectrometry. *J. Geophys. Res.*, 98:23423–23433, 1993.

- H. Berresheim, T. Elste, H. G. Tremmel, A. G. Allen, H.-C. Hansson, K. Rosman, M. Dal Maso, J. M. Mäkelä, M. Kulmala, and C. D. O'Dowd. Gas-aerosol relationships of H₂SO₄, MSA, and OH: Observations in the coastal marine boundary layer at Mace Head, Ireland. *J. Geophys. Res.*, 107(D19)(8100), 2002.
- N. Bobrowski, R. von Glasow, A. Aiuppa, S. Inguaggiato, I. Louban, O. W. Ibrahim, and U. Platt. Reactive halogen chemistry in volcanic plumes. *J. Geophys. Res.*, 112:D06311, 2007.
- S. Borrmann, S. Solomon, J. E. Dye, D. Baumgardner, K. K. Kelly, and K. R. Chan. Heterogeneous reactions on stratospheric background aerosols, volcanic sulfuric acid droplets, and type I polar stratospheric clouds: Effects of temperature fluctuations and differences in particle phase. *J. Geophys. Res.*, 102(D3):3639–3648, 1997.
- G.P. Brasseur, J.J. Orlando, and G.S. Tyndall. *Atmospheric Chemistry and Global Change*. 1999.
- N. Brough, C. E. Reeves, S. A. Penkett, D. J. Stewart, K. Dewey, J. Kent, H. Barjat, P. S. Monks, H. Ziereis, P. Stock, and H. Schlager. Intercomparison of aircraft instruments on board the C-130 and Falcon 20 over southern Germany during EXPORT 2000. *Atmos. Chem. Phys.*, 3:2127–138, 2003.
- R.C. Brown, M.R. Anderson, R.C. Mielke-Lye, and C.E. Kolb. Effects of aircraft exhaust sulfur emissions on near field plume aerosols. *Geophys. Res. Lett.*, 23(24):3607–3610, 1996.
- K. Caldeira and L. Wood. Global and Arctic climate engineering: Numerical model studies. *Philosophical Transactions of the Royal Society A: Mathematical, Physical and Engineering Sciences*, 366(1882):4039–4056, 2008.
- M. R. Canagaratna, J. T. Jayne, J. L. Jimenez, J. D. Allan, M. R. Alfarra, Q. Zhang, T. B. Onasch, F. Drewnick, H. Coe, and A. Middlebrook. Chemical and microphysical characterization of ambient aerosols with the aerodyne aerosol mass spectrometer. *Mass Spectrom. Rev.*, 26(2):185–222, 2007.
- S. A. Carn, N.A. Krotkov, V. Fioletov, K. Yang, A.J. Krueger, and D. Tarasick. Emission, transport and validation of sulfur dioxide in the 2008 Okmok and Kasatochi eruption clouds. In *AGU Fall Meeting; Fall Meet. Suppl., Abstract A51J-07*, 2008.
- P.J. Crutzen. Albedo enhancement by stratospheric sulfur injections: A contribution to resolve a policy dilemma? *Climatic Change*, 77(3):211–220, 2006.
- P.J. Crutzen and F. Arnold. Nitric acid cloud formation in the cold Antarctic stratosphere: a major cause for the springtime 'ozone hole'. *Nature*, 324:651–655, 1986.

- J. Curtius, B. Sierau, F. Arnold, R. Baumann, R. Busen, P. Schulte, and U. Schumann. First direct sulfuric acid detection in the exhaust plume of a jet aircraft in flight. *Geophys. Res. Lett.*, 25:923–926, 1998.
- J. Curtius, F. Arnold, and P. Schulte. Sulfuric acid measurements in the exhaust plume of a jet aircraft in flight: Implications for the sulfuric acid formation efficiency. *Geophys. Res. Lett.*, 29(7):17–1 – 17–4, 2002.
- B. Dix. *Spectroscopic Measurements of Atmospheric Trace Gases on Long-Distance Flights*. PhD thesis, University of Heidelberg, 2007.
- A. Döpelheuer and M. Lecht. *Influence of engine performance on emission characteristics*, volume Gas Turbine Engine Combustion, Emissions and Alternative Fuels. Canada Communication Group. Inc., 1999.
- E.G. Dutton and J.R. Christy. Solar radiative forcing at selected locations and evidence for global lower tropospheric cooling following the eruptions of El Chichón and Pinatubo. *Geophys. Res. Lett.*, 19(23):2313–2316, 1992.
- M. Edmonds, D. Pyle, and C. Oppenheimer. HCl emissions at Soufriere Hills Volcano, Montserrat, West Indies, during a second phase of dome building: November 1999 to October 2000. *Bulletin of Volcanology*, 64(1):21–30, 2002.
- D. W. Fahey, S. R. Kawa, E. L. Woodbridge, P. Tin, J. C. Wilson, H. H. Jonsson, J. E. Dye, D. Baumgardner, S. Borrmann, D. W. Toohey, L. M. Avallone, M. H. Proffitt, J. Margitan, M. Loewenstein, J. R. Podolske, R. J. Salawitch, S. C. Wofsy, M. K. W. Ko, D. E. Anderson, M. R. Schoeber, and K. R. Chan. In situ measurements constraining the role of sulphate aerosols in mid-latitude ozone depletion. *Nature*, 363(6429):509–514, 1993.
- D. W. Fahey, E. R. Keim, K. A. Boering, C. A. Brock, J. C. Wilson, H. H. Jonsson, S. Anthony, T. F. Hanisco, P. O. Wennberg, R. C. Miake-Lye, R. J. Salawitch, N. Louisnard, E. L. Woodbridge, R. S. Gao, S. G. Donnelly, R. C. Wamsley, L. A. Del Negro, S. Solomon, B. C. Daube, S. C. Wofsy, C. R. Webster, R. D. May, K. K. Kelly, M. Loewenstein, and J. R. Podolske. Emission measurements of the Concorde supersonic aircraft in the lower stratosphere. *Science*, 270(5233):70–74, 1995.
- D.W. Fahey, C.S. Eubank, G. Hubler, and F.C. Fehsenfeld. Evaluation of a catalytic reduction technique for the measurement of total reactive odd-nitrogen NO_y in the atmosphere. *J. Atmos. Chem.*, 3:435–468, 1985.
- A. Febo, C. Perrino, M. Gherardi, and R. Sparapani. Evaluation of a high-purity and high-stability continuous generation system for nitrous acid. *Environ. Sci. Technol.*, 29:2390–2395, 1995.

- C. Feigl, H. Schlager, H. Ziereis, J. Curtius, F. Arnold, and C. Schiller. Observation of NO_y uptake by particles in the Arctic tropopause region at low temperatures. *Geophys. Res. Lett.*, 26:2215–2218, 1999.
- V. Fiedler, M. Dal Maso, M. Boy, H. Aufmhoff, J. Hoffmann, T. Schuck, W. Birmili, M. Hanke, J. Uecker, F. Arnold, and M. Kulmala. The contribution of sulphuric acid to atmospheric particle formation and growth: A comparison between boundary layers in Northern and Central Europe. *Atmos. Chem. Phys.*, 5(7):1773–1785, 2005.
- V. Fiedler, R. Nau, S. Ludmann, F. Arnold, H. Schlager, and A. Stohl. East Asian SO₂ pollution plume over Europe - Part 1: Airborne trace gas measurements and source identification by particle dispersion model simulations. *Atmos. Chem. Phys. Discuss.*, 9(1):4717–4728, 2009.
- A. Frenzel and F. Arnold. Sulfuric acid cluster ion formation by jet engines: Implications for sulfuric acid formation and nucleation. *Proceedings of Int. Colloquium on Impact of Emissions from Aircraft and Spacecraft upon the Atmosphere, Köln, Germany, April 18-20*, pages 106–112, 1994.
- T. Gerz, T. Dürbeck, and P. Konopka. Transport and effective diffusion of aircraft emissions. *J. Geophys. Res.*, 103, D20:25,905–25,913, 1998.
- H.-F. Graf, J. Feichter, and B. Langmann. Volcanic sulfur emissions: Estimates of source strength and its contribution to the global sulfate distribution. *J. Geophys. Res.*, 102:10,727–10,738, 1997.
- M.M. Halmer, H.-U. Schmincke, and H.-F. Graf. The annual volcanic gas input into the atmosphere, in particular into the stratosphere: a global data set for the past 100 years. *Journal of Volcanology and Geothermal Research*, 115:511–528, 2002.
- M. Hanke. *Development of a Novel Method for Measuring Atmospheric Peroxy Radicals : Calibration, Aircraft-Borne Measurements and Speciated Measurements of HO₂ and RO₂*. PhD thesis, University of Heidelberg, 1999.
- J. Heland, J. Kleffmann, R. Kurtenbach, and P. Wiesen. A new instrument to measure gaseous nitrous acid (HONO) in the atmosphere. *Environmental Science & Technology*, 35(15):3207–3212, 2001.
- S.C. Herndon, J.T. Jayne, P. Lobo, T.B. Onasch, G. Fleming, D.E. Hagen, P.D. Whitefield, and R.C. Miao-Lye. Commercial aircraft engine emissions characterization of in-use aircraft at Hartsfield-Jackson Atlanta International Airport. *Environmental Science and Technology*, 42(6):1877–1883, 2008.
- K.-P. Heue, C. A. M. Brenninkmeijer, T. Wagner, K. Mies, B. Dix, U. FrieSS, B. G. Martinsson, F. Slemr, and P. F. J. van Velthoven. A comparison of DOAS

- observations by the CARIBIC aircraft and the GOME-2 satellite of the 2008 Kasatochi volcanic SO₂ plume. *Atmos. Chem. Phys. Discuss.*, 10(1):523–558, 2010.
- D. J. Hofmann, S. J. Oltmans, W. D. Komhyr, J. M. Harris, J. A. Lathrop, A. O. Langford, T. Deshler, B. J. Johnson, A. Torres, and W. A. Matthews. Ozone loss in the lower stratosphere over the United States in 1992-1993: Evidence for heterogeneous chemistry on the Pinatubo aerosol. *Geophys. Res. Lett.*, 21:65–68, 1994.
- F. Holzäpfel. Probabilistic two-phase wake vortex decay and transport model. *Journal of aircraft*, 40:323–331, 2003.
- L. G. Huey. Measurement of trace atmospheric species by chemical ionization mass spectrometry: Speciation of reactive nitrogen and future directions. *Mass Spectrom. Rev.*, 26(2):166–184, 2007.
- L. G. Huey, P. W. Villalta, E. J. Dunlea, D. R. Hanson, and C. J. Howard. Reactions of CF₃O- with atmospheric trace gases. *J. of Phys. Chem.*, 100(1):190–194, 1996.
- L.G. Huey, D.J. Tanner, D.L. Slusher, J.E. Dibb, R. Arimoto, G. Chen, D. Davis, M.P. Buhr, J.B. Nowak, R.L. Mauldin III, F.L. Eisele, and E. Kosciuch. CIMS measurements of HNO₃ and SO₂ at the South Pole during ISCAT 2000. *Atmospheric Environment*, 38(32):5411–5421, 2004.
- D.E. Hunton, A.A. Viggiano, T.M. Miller, J.O. Ballenthin, J.M. Reeves, J.C. Wilson, S.H. Lee, B.E. Anderson, W.H. Brune, H. Harder, J.B. Simpas, and N. Oskarsson. In-situ aircraft observations of the 2000 Mt. Hekla volcanic cloud: Composition and chemical evolution in the Arctic lower stratosphere. *Journal of Volcanology and Geothermal Research*, 145(1-2):23–34, 2005.
- Th. Huthwelker, M. Ammann, and Th. Peter. The uptake of acidic gases on ice. *Chemical Reviews*, 106(4):1375–1444, 2006.
- IPCC. Aviation and the global atmosphere. In: E Penner, J., Lister, D.H., Griggs, D.J., Dokken, D.J., McFarland, M. (Eds.), Intergovernmental Panel on Climate Change. *Cambridge University Press, Cambridge, UK*, 1999.
- C. Jost. Calibration with permeation devices: is there a pressure dependence of the permeation rates? *Atmospheric Environment*, 28, Issue 21:3535–3538, 2004.
- T. Jurkat. Atmospheric gaseous sulfuric acid and methanesulfonic acid in the marine boundary layer: Mass spectrometric measurements on a research ship cruise. Master’s thesis, University of Heidelberg, 2007.
- B. Kärcher and D. W. Fahey. The role of sulfur emission in volatile particle formation in jet aircraft exhaust plumes. *Geophys. Res. Lett.*, 24:389–392, 1997.

- B. Kärcher. On the potential importance of sulfur-induced activation of soot particles in nascent aircraft exhaust plumes. *Atmospheric Research*, 46:293–305, 1998.
- B. Kärcher, M. M. Hirschberg, and P. Fabian. Small scale chemical evolution of aircraft exhaust species at cruising altitudes. *J. Geophys. Res.*, 101:–, 1996.
- B. Kärcher, R.P. Turco, F. Yu, M.Y. Danilin, D.K. Weisenstein, R.C. Miake-Lye, and R. Busen. A unified model for ultrafine aircraft particle emissions. *J. Geophys. Res. D: Atmospheres*, 105(D24):29379–29386, 2000.
- E. Katragkou, S. Wilhelm, F. Arnold, and C. Wilson. First gaseous Sulfur (VI) measurements in the simulated internal flow of an aircraft gas turbine engine during project PartEmis. *Geophys. Res. Lett.*, 31(2):L02117–, 2004.
- A. Kiendler and F. Arnold. First composition measurements of positive chemiions in aircraft jet engine exhaust: detection of numerous ion species containing organic compounds. *Atmospheric Environment*, 36(18):2979–2984, 2002a.
- A. Kiendler and F. Arnold. Unambiguous identification and measurement of sulfuric acid cluster chemiions in aircraft jet engine exhaust. *Atmospheric Environment*, 36(11):1757–1761, April 2002b.
- A. Kiendler, S. Aberle, and F. Arnold. Positive ion chemistry in the exhaust plumes of an air craft jet engine and a burner: investigations with a quadrupole ion trap mass spectrometer. *Atmospheric Environment*, 34(28):4787–4793, 2000.
- S. Kim, L.G. Huey, R.E. Stickel, R.B. Pierce, G. Chen, M.A. Avery, J.E. Dibb, G.S. Diskin, G.W. Sachse, C.S. McNaughton, A.D. Clarke, B.E. Anderson, and D.R. Blake. Airborne measurements of HCl from the marine boandary layer to the lower stratosphere over the North Pacific Ocean during INTEx-B. *Atmos. Chem. Phys. Discuss.*, 8(1):3563–3595, 2008.
- J. Kleffmann and P. Wiesen. Technical note: Quantification of interferences of wet chemical HONO measurements under simulated polar conditions. *Atmos. Chem. Phys.*, 8:6813–6822, 2008.
- J. Kleffmann, K. H. Becker, and P. Wiesen. Heterogeneous NO₂ conversion processes on acid surfaces: Possible atmospheric implications. *Atmos. Environ.*, 32:2721–2729, 1998.
- J. Kleffmann, K.H. Becker, M. Lackhoff, and P. Wiesen. Heterogeneous conversion of NO₂ on carbonaceous surfaces. *Phys. Chem. Chem. Phys.*, 1(24):5443–5450, 1999.
- J. Kleffmann, J.C. Lörzer, P. Wiesen, C. Kern, S. Trick, R. Volkamer, M. Rodenas, and K. Wirtz. Intercomparison of the DOAS and LOPAP techniques for the detection of nitrous acid (HONO). *Atmospheric Environment*, 40:3640–3652, 2006.

- B. Kärcher and F. Yu. Role of aircraft soot emissions in contrail formation. *Geophys. Res. Lett.*, 36(1):L01804, 2009.
- N. I. Kristiansen. Determination of the emission height profile of volcanic emissions using inverse modelling. Master’s thesis, University of Oslo, 2009.
- D. S. Lee, D.W. Fahey, P. M. Forster, P.J. Newton, R. C.N. Wit, L. L. Lim, B. Owen, and R. Sausen. Aviation and global climate change in the 21st century. *Atmospheric Environment*, 43:3520–3537, 2009.
- E. R. Lovejoy and R. R. Wilson. Kinetic studies of negative ion reactions in a quadrupole ion trap: Absolute rate coefficients and ion energies. *J. of Phys. Chem.*, 102(13):2309–2315, 1998.
- S.P. Lukachko, I.A. Waitz, R.C. Miake-Lye, R.C. Brown, and M.R. Anderson. Production of sulfate aerosol precursors in the turbine and exhaust nozzle of an aircraft engine. *J. Geophys. Res. D: Atmospheres*, 103(D13):16159–16174, 1998.
- NIST J. A. Manion, R. E. Huie, R. D. Levin, D. R. Burgess Jr., V. L. Orkin, W. Tsang, W. S. McGivern, J. W. Hudgens, V. D. Knyazev, D. B. Atkinson, E. Chai, A. M. Tereza, C.-Y. Lin, T. C. Allison, W. G. Mallard, F. Westley, J. T. Herron, R. F. Hampson, and D. H. Frizzell. NIST chemical kinetics database, NIST standard reference database 17, version 7.0 (web version), release 1.4.3, data version 2008.12, 12 2008.
- W. Mankin and M. T. Coffey. Increased stratospheric hydrogen chloride in the El Chichon cloud. *Science*, 226(4671):170–172, 1984.
- W. G. Mankin, M. T. Coffey, and A. Goldman. Airborne observations of SO₂, HCl and O₃ in the stratospheric plume of the Pinatubo volcano in July 1991. *Geophys. Res. Lett.*, 19:179–182, 1992.
- R. March and R. Hughes. *Quadrupole Storage Mass Spectrometry*. John Wiley and Sons, New York, 1989.
- T.P. Marcy, D.W. Fahey, R.S. Gao, P.J. Popp, E.C. Richard, T.L. Thompson, K.H. Rosenlof, E.A. Ray, R.J. Salawitch, C.S. Atherton, D.J. Bergmann, B.A. Ridley, A.J. Weinheimer, M. Loewenstein, E.M. Weinstock, and M.J. Mahoney. Quantifying stratospheric ozone in the upper troposphere with in situ measurements of HCl. *Science*, 304(5668):261–265, 2004.
- T.P. Marcy, R.S. Gao, M.J. Northway, P.J. Popp, H. Stark, and D.W. Fahey. Using chemical ionization mass spectrometry for detection of HNO₃, HCl, and ClONO₂ in the atmosphere. *International Journal of Mass Spectrometry*, 243:63–70, 2005.

- B. G. Martinsson, C. A. M. Brenninkmeijer, S. A. Carn, M. Hermann, K.-P. Heue, P. F. J. van Velthoven, and A. Zahn. Influence of the 2008 Kasatochi volcanic eruption on sulfurous and carbonaceous aerosol constituents in the lower stratosphere. *Geophys. Res. Lett.*, 36:L12813, 2009.
- M. P. McCormick, L. W. Thomason, and C. R. Trepte. Atmospheric effects of the Mt Pinatubo eruption. *Nature*, 373(6513):399–404, 1995.
- S. K. Meilinger, B. Kärcher, and Th. Peter. Microphysics and heterogeneous chemistry in aircraft plumes - high sensitivity on local meteorology and atmospheric composition. *Atmos. Chem. Phys.*, 5(2):533–545, 2005.
- S.K. Meilinger, B. Kärcher, R. von Kuhlmann, and T. Peter. On the impact of heterogeneous chemistry on ozone in the tropopause region. *Geophys. Res. Lett.*, 28:515–518, 2001.
- R.C. Miake-Lye, B.E. Anderson, W.R. Cofer, H.A. Wallio, G.D. Nowicki, J.O. Ballenthin, D.E. Hunton, W.B. Knighton, T.M. Miller, J.V. Seeley, and A.A. Viggiano. SO_x oxidation and volatile aerosol in aircraft exhaust plumes depend on fuel sulfur content. *Geophys. Res. Lett.*, 25(10):1677–1680, 1998.
- D. V. Michelangeli, M. Allen, and Y.. L. Yung. Heterogeneous reactions with NaCl in the El Chichón volcanic aerosols. *Geophys. Res. Lett.*, 18:673–676, 1991.
- P. Minnis, U. Schumann, D. R. Doelling, K. M. Gierens, and D. W. Fahey. Global distribution of contrail radiative forcing. *Geophys. Res. Lett.*, 26(13):1853–1856, 1999.
- O. Möhler and F. Arnold. Flow reactor and triple quadrupole mass spectrometer investigations of negative ion reactions involving nitric acid: Implications for atmospheric HNO₃ detection by chemical ionization mass spectrometry. *Journal of Atmospheric Chemistry*, 1991:33–61, 1991.
- O. Möhler, S. Büttner, C. Linke, M. Schnaiter, H. Saathoff, O. Stetzer, R. Wagner, M. Krämer, A. Mangold, V. Ebert, and U. Schurath. Effect of sulfuric acid coating on heterogeneous ice nucleation by soot aerosol particles. *J. Geophys. Res.*, 110: D11210, 2005.
- M. J. Molina and F.S. Rowland. Stratospheric sink for chlorofluoromethanes: Chlorine atom catalyzed destruction of ozone. *Nature*, 249:820–812, 1974.
- R. Nau. *Weiterentwicklung eines flugzeuggetragenen CIMS - Instruments: Spurengasmessungen in der Atmosphäre und in einem Blitzlabor*. PhD thesis, University of Heidelberg, 2008.

- J. A. Neuman, R. S. Gao, M. E. Schein, S. J. Ciciora, J. C. Holecek, T. L. Thompson, R. H. Winkler, R. J. McLaughlin, M. J. Northway, E. C. Richard, and D. W. Fahey. A fast-response chemical ionization mass spectrometer for in situ measurements of HNO₃ in the upper troposphere and lower stratosphere. *Rev. Sci. Instrum.*, 71 (10):3886–3894, 2000.
- J.A. Neuman, R.S. Gao, D.W. Fahey, J.C. Holecek, B.A. Ridley, J.G. Walega, F.E. Grahek, E.C. Richard, C.T. McElroy, T.L. Thompson, J.W. Elkins, F.L. Moore, and E.A. Ray. In situ measurements of HNO₃, NO_y, NO and O₃ in the lower stratosphere and upper troposphere. *Atmos. Environ.*, 35:5789–5797, 2001.
- L.G. Neuman, J.A. and. Huey, T.B. Ryerson, and D. W. Fahey. Study of inlet materials for sampling atmospheric nitric acid. *Environ. Sci. Technol.*, 33:1133–1136, 1999.
- L. L. Pan, W. J. Randel, B. L. Gary, M. J. Mahoney, and E. J. Hints. Definitions and sharpness of the extratropical tropopause: A trace gas perspective. *J. Geophys. Res.*, 109(D23):D23103–, 2004.
- J. E. Penner, D. H. Lister, D. J. Griggs, D. J. Dokken, and M. McFarland. Aviation and the global atmosphere - a special report of IPCC working groups I and III. intergovernmental panel on climate change. *Intergovernmental Panel on Climate Change, Cambridge University Press*, page 365 pp., 1999.
- G. Pitari, E. Mancini, A. Bregman, H.L. Roget, J.K. Sander, V. Grewe, and O. Dessens. Sulphate particles from subsonic aviation: Impact on upper tropospheric and lower stratospheric ozone. *Phys. Chem. Earth*, 26:563–569, 2001.
- U. Platt. *Differential optical absorption spectroscopy (DOAS), in Air Monitoring by Spectroscopic Techniques. Chem. Anal.* Number 127. John Wiley, New York, 1994.
- U. Platt, D. Perner, G. W. Harris, A. M. Winer, and J. N. Pitts. Observations of nitrous acid in an urban atmosphere by differential optical absorption. *Nature*, 285:312–314, 1980.
- R. Alan Plumb and Malcolm K. W. Ko. Interrelationships between mixing ratios of long-lived stratospheric constituents. *J. Geophys. Res.*, 97(D9):10145–10156, 1992.
- M. Ponater, R. Sausen, B. Feneberg, and E. Roeckner. Climate effect of ozone changes caused by present and future air traffic. *Climate Dynamics*, 15(9):631–642, 1999.
- P. J. Popp, R. S. Gao, T. P. Marcy, D. W. Fahey, P. K. Hudson, T. L. Thompson, B. Kärcher, B. A. Ridley, A. J. Weinheimer, D. J. Knapp, D. D. Montzka,

- D. Baumgardner, T. J. Garrett, E. M. Weinstock, J. B. Smith, D. S. Sayres, J. V. Pittman, S. Dhaniyala, T. P. Bui, and M. J. Mahoney. Nitric acid uptake on subtropical cirrus cloud particles. *J. Geophys. Res.*, 109(D6):D06302, 2004.
- P.J. Popp, T.P. Marcy, R.S. Gao, L.A. Watts, D.W. Fahey, E.C. Richard, S.J. Oltmans, M.L. Santee, N.J. Livesey, L. Froidevaux, B. Sen, G.C. Toon, K.A. Walker, C.D. Boone, and P.F. Bernath. Stratospheric correlation between nitric acid and ozone. *J. Geophys. Res. D: Atmospheres*, 114(3):D03305, 2009.
- A. J. Prata and C. Bernardo. Retrieval of volcanic SO₂ column abundance from Atmospheric Infrared Sounder data. *J. Geophys. Res.*, 112:D20204, 2007.
- W. G. Read, L. Froidevaux, and J. W. Waters. Microwave Limb Sounder measurement of the stratospheric SO₂ from the Mt. Pinatubo volcano. *Geophys. Res. Lett.*, 20:1299–1302, 1993.
- Th. Reiner and F. Arnold. Laboratory flow reactor measurements of the reaction $\text{SO}_3 + \text{H}_2\text{O} + \text{M} \rightarrow \text{H}_2\text{SO}_4 + \text{M}$: Implications for gaseous H₂SO₄ and aerosol formation in the plumes of jet aircraft. *Geophys. Res. Lett.*, 20(23):2659–2662, 1993.
- Th. Reiner and F. Arnold. Laboratory investigations of gaseous sulfuric acid formation via $\text{SO}_3 + \text{H}_2\text{O} + \text{M} \rightarrow \text{H}_2\text{SO}_4 + \text{M}$: Measurement of the rate constant and product identification. *Chemical Physics*, 101:7399–7407, 1994.
- M. Rix, P. Valks, N. Hao, J. van Geffen, C. Clerbaux, L. Clarisse, P.-F. Coheur, D. Loyola, T. Erbertseder, W. Zimmer, and S. Emmadi. Satellite monitoring of volcanic sulfur dioxide emissions for early warning of volcanic hazards. *IEEE Journal of Selected Topics in Applied Earth Observations and Remote Sensing*, 2: 196–206, 2009.
- W. Roedel. *Physik unserer Umwelt, Die Atmosphäre*. Springer, 2000.
- W. I. Rose, G. A. Millard, T. A. Mather, D. E. Hunton, B. Anderson, C. Oppenheimer, B. F. Thornton, T. M. Gerlach, A. A. Viggiano, Y. Kondo, T. Miller, and J. O. Ballenthin. Atmospheric chemistry of a 33-34 hour old volcanic cloud from Hekla volcano (Iceland): Insights from direct sampling and the application of chemical box modeling. *J. Geophys. Res.*, 111:D20206, 2006.
- R. Sausen and U. Schumann. Estimates of the climate response to aircraft CO₂ and NO_x emissions scenarios. *Climatic Change*, 44(1):27–58, 2000.
- D. Schäuble, C. Voigt, B. Kärcher, P. Stock, H. Schlager, M. Krämer, C. Schiller, R. Bauer, N. Spelten, M. de Reus, M. Szakáll, S. Borrmann, U. Weers, and Th. Peter. Airborne measurements of the nitric acid partitioning in persistent contrails. *Atmos. Chem. Phys.*, 9(3):8189–8197, 2009.

- H. Schlager, P. Konopka, P. Schulte, U. Schumann, H. Ziereis, F. Arnold, M. Klemm, D.E. Hagen, P.D. Whitefield, and J. Ovarlez. In situ observations of air traffic emission signatures in the North Atlantic flight corridor. *J. Geophys. Res. D: Atmospheres*, 102(9):10739–10750, 1997.
- J. Schmale, J. Schneider, T. Jurkat, C. Voigt, H. Eichler, Rautenhaus, M. Lichtenstern, H. Schlager, G. Ancellet, F. Arnold, M. Gerding, I. Mattis, M. Wendisch, and S. Borrmann. Aerosol layers from the 2008 eruptions of Mt. Okmok and Mt. Kasatochi: In-situ UT/LS measurements of sulfate and organics over Europe. *submitted to J. Geophys. Res.*, 2010.
- J. Schneider, F. Arnold, V. Bürger, B. Droste-Franke, F. Grimm, G. Kirchner, M. Klemm, T. Stalp, K.-H. Wohlfrom, P. Siegmund, and P. F. J. van Velthoven. Nitric acid (HNO₃) in the upper troposphere and lower stratosphere at midlatitudes: New results from aircraft-based mass spectrometric measurements. *J. Geophys. Res.*, 103(D19):25337–25343, 1998.
- J. Schneider, F. Arnold, J. Curtius, B. Sierau, H. Fischer, P. Hoor, F. G. Wienhold, U. Parchatka, Y. C. Zhang, H. Schlager, H. Ziereis, Ch. Feigl, J. Lelieveld, H. A. Scheeren, and O. Bujok. The temporal evolution of the ratio HNO₃/NO_y in the Arctic lower stratosphere from January to March 1997. *Geophys. Res. Lett.*, 26(8):1125–1128, 1999.
- J. Schreiner, C. Voigt, A. Kohlmann, F. Arnold, K. Mauersberger, and N. Larsen. Chemical analysis of polar stratospheric cloud particles. *Science*, 283:968–970, 1999.
- P. Schulte, H. Schlager, H. Ziereis, U. Schumann, S. Baughcum, and F. Deidewig. NO_x emission indices of subsonic long-range jet aircraft at cruise altitude: In situ measurements and predictions. *J. Geophys. Res.*, 102(D17):21431–21442, 1997.
- U. Schumann, H. Schlager, F. Arnold, R. Baumann, P. Haschberger, and O. Klemm. Dilution of aircraft exhaust plumes at cruise altitudes. *Atmospheric Environment*, 32(18):3097–3103, 1998.
- U. Schumann, H. Schlager, F. Arnold, J. Ovarlez, H. Kelder, O. Hov, G. Hayman, I.S.A. Isaksen, J. Staehelin, and P.D. Whitefield. Pollution from aircraft emissions in the North Atlantic flight corridor: Overview on the POLINAT projects. *J. Geophys. Res. D: Atmospheres*, 105(D3):3605–3631, 2000.
- U. Schumann, F. Arnold, R. Busen, J. Curtius, B. Kärcher, A. Kiendler, A. Petzold, H. Schlager, F. Schröder, and K.-H. Wohlfrom. Influence of fuel sulfur on the composition of aircraft exhaust plumes: The experiments SULFUR 1-7. *J. Geophys. Res.*, 107:AAC 2–1–2–27, 2002.

- D.L. Slusher, S.J. Pitteri, B.J. Haman, D.J. Tanner, and L.G. Huey. A chemical ionization technique for measurement of pernitric acid in the upper troposphere and the polar boandary layer. *Geophys. Res. Lett.*, 28(20):3875–3878, 2001.
- S. Solomon. Stratospheric ozone depletion: A review of concepts and history. *Rev. Geophys.*, 37(3):275–316, 1999.
- H. Somnitz, G. G. Gleitsmann, and R. Zellner. Novel rates of OH induced sulfur oxidation: Implications to the plume chemistry of jet aircraft. *Meteorologische Zeitschrift*, 14:459–464, 2005.
- A. Sorokin, E. Katragkou, F. Arnold, R. Busen, and U. Schumann. Gaseous SO₃ and H₂SO₄ in the exhaust of an aircraft gas turbine engine: measurements by CIMS and implications for fuel sulfur conversion to sulfur (VI) and conversion of SO₃ to H₂SO₄. *Atmospheric Environment*, 38(3):449–456, 2004.
- M. Speidel, R. Nau, F. Arnold, H. Schlager, and A. Stohl. Sulfur dioxide measurements in the lower, middle and upper troposphere: Deployment of an aircraft-based chemical ionization mass spectrometer with permanent in-flight calibration. *Atmospheric Environmental Science & Technology*, 41:2427–2437, 2007.
- A.M. Starik, A.M. Savel’ev, N.S. Titova, and U. Schumann. Modeling of sulfur gases and chemiions in aircraft engines. *Aerospace Science and Technology*, 6(1):63–81, 2002.
- W. Steinbrecht, H. Claude, and U. Köhler. Kasatochi Vulkanaerosol über Europa. *Ozone Bulletin des DWD*, 121, 2008.
- W.R. Stockwell and J.G. Calvert. The mechanism of the HO-SO₂ reaction. *Atmos. Environ.*, 17:2231–2235, 1983.
- A. Stohl, L. Haimberger, M. P. Scheele, and H. Wernli. An intercomparison of results from three trajectory models. *Meteorological Applications*, 8(2):127–135, 2001.
- R. Sussmann and K. Gierens. Lidar and numerical studies on the different evolution of vortex pair and secondary wake in young contrails. *J. Geophys. Res.*, 104(D4): 2131–2142, 1999.
- A. Tabazadeh and R.P. Turco. Stratospheric chlorine injection by volcanic eruptions: HCl scavenging and implications for ozone. *Science*, 260:1082–1086, 1993.
- Ch. Textor, H.-F. Graf, M. Herzog, and J. M. Oberhuber. Injection of gases into the stratosphere by explosive volcanic eruptions. *J. Geophys. Res.*, 108(D19):ACH 5–1 – 5–17, 2003.

- N. Theys, M. Van Roozendaal, B. Dils, F. Hendrick, N. Hao, and M. De Mazière. First satellite detection of volcanic bromine monoxide emission after the Kasatochi eruption. *Geophys. Res. Lett.*, 36:L03809, 2009.
- S. Tilmes, R. Garcia, R. Douglas, E. Kinnison, A. Gettelman, and P. Rasch. Impact of geoengineered aerosols on the troposphere and stratosphere. *J. Geophys. Res.*, 114:D12305, 2009.
- H. G. Tremmel, H. Schlager, P. Konopka, P. Schulte, F. Arnold, M. Klemm, and B. Droste-Franke. Observations and model calculations of jet aircraft exhaust products at cruise altitude and inferred initial OH emissions. *J. Geophys. Res.*, 103(D9):10803–10816, 1998.
- H.G. Tremmel and U. Schumann. Model simulations of fuel sulfur conversion efficiencies in an aircraft engine: dependence on reaction rate constants and initial species mixing ratios. *Aerospace Science and Technology*, 3:417–430, 1999.
- C. Voigt, J. Schreiner, A. Kohlmann, P. Zink, K. Mauersberger, N. Larsen, T. Deshler, C. Kröger, J. Rosen, A. Adriani, F. Cairo, G. di Donfrancesco, M. Viterbini, J. Ovarlez, H. Ovarlez, C. David, and A. Dörnbrack. Nitric acid trihydrate (NAT) in polar stratospheric clouds. *Science*, 290:1756–1758, 2000.
- C. Voigt, H. Schlager, H. Ziereis, B. Kärcher, B. P. Luo, C. Schiller, M. Krämer, P. J. Popp, H. Irie, and Y. Kondo. Nitric acid in cirrus clouds. *Geophys. Res. Lett.*, 33(5):L05803, 2006.
- C. Voigt, B. Kärcher, H. Schlager, C. Schiller, M. Krämer, M. De Reus, H. Vössing, S. Borrmann, and V. Mitev. In-situ observations and modeling of small nitric acid-containing ice crystals. *Atmos. Chem. Phys.*, 7(12):3373–3383, 2007.
- C. Voigt, U. Schumann, T. Jurkat, D. Schäuble, H. Schlager, J.F. Gayet, C. Gourbeyre, J. Krämer, M. Schneider, J. Schmale, S. Borrmann, W. Frey, F. Arnold, P. Jessberger, A. Petzold, T. Hamburger, M. Lichtenstern, M. Scheibe, J. Meyer, M. Kübbeler, H. Eichler, M. Wendisch, T. Butler, M. Lawrence, F. Holzäpfel, R. Baumann, K. Gottschaldt, M. Rautenhaus, and A. Dörnbrack. Detection of contrails, cirrus clouds and volcanic aerosol - Overview from the CONCERT campaign. *submitted to Atmos. Chem. Phys. Discuss.*, 2010.
- R. von Glasow, N. Bobrowski, and C. Kern. The effects of volcanic eruptions on atmospheric chemistry. *Chemical Geology*, 263:131–142, 2009.
- J. C. Wilson, H. H. Jonsson, C. A. Brock, D. W. Toohey, L. M. Avallone, D. Baumgardner, J. E. Dye, L. R. Poole, D. C. Woods, and R. J. Decoursey. In-situ observations of aerosol and chlorine monoxide after the 1991 eruption of Mount Pinatubo - Effect of reactions on sulfate aerosol. *Science*, 261:1140–1143, 1993.

- WMO. SPARC assessment of stratospheric aerosol properties. *SPARC Report No.4, WCRP-124, WMO/TD-No. 1295, Toronto, Canada.*, 2006.
- K.-H. Wohlfrom. *Measurements of atmospheric trace gases and ions by aircraft-based mass spectrometers*. PhD thesis, University of Heidelberg, 2000.
- E. C. Wood, S. C. Herndon, M. T. Timko, P. E. Yelvington, and R. C. Miake-Lye. Speciation and chemical evolution of nitrogen oxides in aircraft exhaust near airports. *Environmental Science & Technology*, 42(6):1884–1891, 2008.
- D. C. Woods, R. L. Chuan, and W. I. Rose. Halite particles injected into the stratosphere by the 1982 El Chichón eruption. *Science*, 230(4722):170–172, 1985.
- J. Wormhoudt, S.C. Herndon, P.E. Yelvington, R.C. Miake-Lye, and C. Wey. Nitrogen oxide (NO/NO₂/HONO) emissions measurements in aircraft exhausts. *Journal of Propulsion and Power*, 23(5):906–911, 2007.
- X. Zhou, Y. He, G. Huang, T. D. Thornberry, M. A Carroll, and S. B. Bertman. Photochemical production of nitrous acid on glass sample manifold surface. *Geophys. Res. Lett.*, 29(14):1681, 2002.
- H. Ziereis, H. Schlager, H. Fischer, C. Feigl, P. Hoor, R. Marquardt, and V. Wagner. Aircraft measurements of tracer correlations in the Arctic subvortex region during the Polar Stratospheric Aerosol Experiment (POLSTAR). *J. Geophys. Res.*, 105(D19):24,305–24,313, 2000.
- H. Ziereis, A. Minikin, H. Schlager, J.F. Gayet, F. Auriol, P. Stock, J. Baehr, A. Petzold, U. Schumann, A. Weinheimer, B. Ridley, and J. Ström. Uptake of reactive nitrogen on cirrus cloud particles during INCA. *Geophys. Res. Lett.*, 31(5):L05115 1–4, 2004.
- M. Zöger, A. Afchine, N. Eicke, M.-T. Gerhards, E. Klein, D. S. McKenna, U. Mörschel, U. Schmidt, V. Tan, F. Tuitjer, T. Woyke, and C. Schiller. Fast in situ stratospheric hygrometers: A new family of balloon-borne and airborne lyman α photofragment fluorescence hygrometers. *J. Geophys. Res.*, 104(D1):1807–1816, 1999.
- M. A. Zondlo, R. L. Mauldin, E. Kosciuch, C. A. Cantrell, and F. L. Eisele. Development and characterization of an airborne-based instrument used to measure nitric acid during the NASA transport and chemical evolution over the Pacific field experiment. *J. Geophys. Res.*, 108:8793, 2003.

Acknowledgment

Many people have contributed to the work presented in this thesis and supported me during my Ph.D. studies. I would like to take this opportunity to thank them all.

I would like to thank my advisor Prof. Frank Arnold for giving me the opportunity to write this thesis, for his support and experienced advise. I am thankful for many hours of helpful discussions in Munich and Heidelberg on many aspects of mass spectrometry and atmospheric physics.

I also would like to thank my DLR-advisor Prof. Christiane Voigt for giving me the opportunity to conduct research in this very exciting field as part of the AEROTROP Nachwuchsgruppe. I am grateful for her guidance in many aspects of atmospheric research, her support and encouragement and her generous availability.

I also would like to thank the second referee of this thesis Prof. Ulrich Platt for stepping in in the last minute and writing the advisory's report.

Prof. Ulrich Schumann supported, encouraged and inspired me in many ways during my time at the Institut für Physik der Atmosphäre, DLR. I would like to thank him for that. I also would like to thank Dr. Hans Schlager for giving me the opportunity to work in his department.

Thanks to the whole CONCERT-Team! Particularly to Julia Schmale and Johannes Schneider (MPI-C) and the Flight Department of DLR. Michael Lichtenstern, Monika Scheibe, Paul Stock and Bernhard Preissler have provided valuable technical support before and during the campaign. Thanks to all of you!

I would like to express my gratitude to Dr. Jörg Kleffmann from the University of Wuppertal who helped with the HONO calibration and operated the LOPAP instrument.

I have gained a lot of support and valuable discussions from all CIMS-people of department 2 of the IPA: First of all I would like to thank Heinfried Aufmhoff, who supported me during the setup of the instrument, and taught me many things in the laboratory. Thanks to Anke Roiger and Verena Fiedler, who have always been there

for advise and encouragement. Thanks to all AEROTROPs: Dominik Schäuble for many discussions on measurement techniques and PhD-life, Philipp Jessberger for great advise, Klaus Gottschald for company during late working hours and to the new ones Stefan and Alexander.

Many thanks also to my other IPA colleagues: Andreas M., Sebastian, Ingo, Vera, Greta, Marc, Lisa, Jan, Kathi, Simon, Andreas D., Lucas, Thomas, Thomas, Bernadett, Andreas P., Helmut... - I feel honored having worked with you.

I would like to thank Henning Christ, Christiane Voigt, Heinfried Aufmhoff, Dominik Schäuble, Anke Roiger, Philipp Jessberger and Ingo Sölch for proof reading (parts of) this thesis.

Vielen Dank an meine Freunde in Heidelberg, München und Hessen: Allen voran an die "Angels": Sabrina - meinem Lieblingsengel seit mittlerweile 10 Jahren, Verena (Verenika), Ulrike, PAnke und Tanja. Ein Dank geht an besondere Menschen: Alex G., Ute, Amir, Simone, Alex S., Theresa, Anna, Helga, Johanna, Leonie und Jens, Tina und Markus, und die ODW-WG. Danke an meine MESSER's-Highlights, an alle Westsideler und die Musicalmagier - let the music do the talking!

Ein besonderer Dank geht an Henning, der mich schon so lange durch alle Höhen und Tiefen begleitet hat, von dem ich so viel gelernt habe und der immer für mich da war. Danke für all das, und dass Du immer noch da bist!

Zum Schluss möchte ich meiner Familie danken, meiner Großmutter, meiner Schwester und besonders meinen Eltern, die mir ein Studium ermöglicht und mich immer bestärkt und ermutigt haben. Ich schätze mich sehr glücklich so wundervolle Eltern zu haben und danke Euch!